Cooling High Heat Flux Micro-Electronic Systems using Refrigerants in High Aspect Ratio Multi-Microchannel Evaporators

THÈSE N^O 5225 (2011)

PRÉSENTÉE LE 25 NOVEMBRE 2011
À LA FACULTÉ DES SCIENCES ET TECHNIQUES DE L'INGÉNIEUR
LABORATOIRE DE TRANSFERT DE CHALEUR ET DE MASSE
PROGRAMME DOCTORAL EN ENERGIE

ÉCOLE POLYTECHNIQUE FÉDÉRALE DE LAUSANNE

POUR L'OBTENTION DU GRADE DE DOCTEUR ÈS SCIENCES

PAR

Etienne COSTA-PATRY

acceptée sur proposition du jury:

Prof. D. Favrat, président du jury
Prof. J. R. Thome, directeur de thèse
Prof. D. Atienza Alonso, rapporteur
Prof. G. P. Celata, rapporteur
Dr D. Wen, rapporteur

ÉCOLE POLYTECHNIQUE
FÉDÉRALE DE LAUSANNE

Suisse
2011

"Heavier-than-air flying machines are impossible."
- Lord Kelvin, president, Royal Society, 1895.

Pour Judit, Vincent et Milena…

Acknowledgements

This study has been carried out at the Laboratory of Heat and Mass Transfer (LTCM), École Polytechnique Fédérale de Lausanne, under the direction of Prof. John R. Thome. This work has been supported by the Swiss Federal Office for Professional Education and Technology (KTI) under contract No. 6862.2 DCS-NM and by financial contributions of IBM and Embraco.

I would like to express my gratitude to Prof. John R. Thome for his time, constructive advice, and willingness to share his insight and wisdom. I thank Prof. David Atienza Alonso (EPFL), Dr. Gian Piero Celata (ENEA), Dr. Dongsheng Wen (Queen Mary, University of London) and Prof. Daniel Favrat (EPFL) for their constructive comments, suggestions and for their time.

Without the discussions and exchanges with my colleagues at the LTCM and the people of IBM Zurich, this experimental work could not have been a success. Thank you for your inputs, ideas and the good time spent together. I would also like to thank Wolverine Tube Inc. for providing a MicroCool copper multi-microchannel cooling element made to our specifications.

Finally, I would like to thank my wife and my kids for their support, patience and their smiles.

Abstract

Improving the energy efficiency of cooling systems can contribute to reduce the emission of greenhouse gases. Currently, most microelectronic applications are air-cooled. Switching to two-phase cooling systems would decrease power consumption and allow for the reuse of the extracted heat. For this type of application, multi-microchannel evaporators are thought to be well adapted. However, such devices have not been tested for a wide range of operating conditions, such that their thermal response to the high non-uniform power map typically generated by microelectronics has not been studied.

This research project aims at clarifying these gray areas by investigating the behavior of the two-phase flow of different refrigerants in silicon and copper multi-microchannel evaporators under uniform, non-uniform and transient heat fluxes operating conditions. The test elements use as a heat source a pseudo-chip able to mimic the behavior of a CPU. It is formed by 35 independent sub-heaters, each having its own temperature sensor, such that 35 temperature and 35 heat flux measurements can be made simultaneously. Careful measurements of each pressure drop component (inlet, microchannels and outlet) found in the micro-evaporators showed the importance of the inlet and outlet restriction pressure losses. The overall pressure drop levels found in the copper test section were low enough to possibly be driven by a thermosyphon system.

The heat transfer coefficients measured for uniform heat flux conditions were very high and typically followed a V-shape curve. The first branch was associated to the slug flow regime and the second to the annular flow regime. By tracking the minimum level of heat transfer, a transition criteria between the regimes was established, which included the effect of heat flux on the transition. Then for each branch, a different prediction method was used to form the first flow pattern-based prediction method for two-phase heat transfer in microchannels.

A non-uniform heat flux creates important temperature gradients in the evaporator, such that the data reduction procedure needs to be adapted to include heat spreading within the evaporator. To do so, a robust multi-dimensional thermal conduction scheme was developed. Once these effects were taken into consideration, the local heat transfer coefficients provided by two-phase flow were found to be the same for uniform and non-uniform heat fluxes, allowing the flow pattern-based method to be extended to non-uniform heat flux conditions. Lastly, with proper control of the mass flow, transient heat flux situations were well handled by the micro-evaporators.

KEYWORDS: Hot-spots, non-uniform heat flux, refrigerants, two-phase flow cooling, thermal management, micro-cooling

Résumé

Améliorer l'efficacité énergétique des systèmes de refroidissement peut contribuer à réduire les émission de gas à effet de serres. Aujourd'hui la majorité des applications microélectroniques sont refroidies avec l'air. En utilisant un système de refroidissement biphasique, la consommation énergétique serait réduite et la réutilisation de l'énergie thermique deviendrait possible. Pour ce type d'applications, les micro-évaporateurs à multi-canaux semblent être particulièrement bien adaptés. Cependant, ces systèmes n'ont pas encore été testés pour une large gamme de conditions d'opérationelles, de sorte que leur réponses thermiques à des profils de puissances non-uniformes typiques aux systèmes microélectroniques n'ont pas été étudiées.

Ce projet de recherche cherche à clarifier ces zones grises en étudiant la réaction de l'écoulement diphasique de différents réfrigérants dans des micro-évaporateurs faits en silicium et en cuivre pour des conditions opérationelles de flux thermiques uniformes, non-uniformes et transients. Pour ce, une source de chaleur simulant les propriétés d'un microprocesseur est utilisée. Elle est divisée en 35 sous-unités, chacune ayant sa propre sonde thermique. Ainsi sont faites simultanément 35 mesures de température et 35 mesures de flux thermique. Des mesures précises de chaque composant (entré, micro-canaux et sortie) formant la perte de pression totale dans un micro-évaporateur ont montré l'importance des pertes de pressions d'entrées et de sorties. Les pertes de pression totales dans l'évaporateur de cuivre étaient suffisamment basses pour envisager utiliser un système de thermosyphon pour générer l'écoulement.

Les coefficients de transferts thermiques mesurés pour des condition de flux thermique uniformes sont très élevés et suivent une forme caractéristique en V. La première branche est associée à un écoulement intermittent et la seconde, à un écoulement annulaire. En suivant le déplacement du minimum sur les courbes de transfert thermique, un critère de transition entre les deux écoulements a été établi et inclu l'effet du flux thermique sur la transition. Ensuite, une méthode de prédiction a été sélectionnée pour chaque branche pour former la première méthode de prediction basée sur les régimes d'écoulement pour les écoulements diphasiques en micro-canaux.

Un flux thermique non-uniforme crée d'important gradient thermique dans l'évaporateur, de sorte que la réduction des données doit inclure les effects de conductions thermiques dans l'évaporateur. À cette fin, un modèle robuste calculant la conduction thermique multi-dimensionelles a été développé. Lorsque que ces effects sont pris en considération, les coefficients locaux de transfert thermique sont les mêmes pour un flux thermique uniforme et non-uniforme. Dans cette situation, la méthode de prédiction basée sur les régimes d'écoulement est utilisée pour des flux thermiques non-uniformes. Finalement, avec un système de contrôle du débit, les flux thermiques transitoires ne présentent pas de difficulté particulière pour les micro-évaporateurs.

MOTS-CLÉS: Flux thermique non uniforme, réfriérants, refroidissement biphasique, micro-refroidissement

Contents

Acknowledgements **iii**

Abstract **v**

1 Introduction **1**

2 State of the art review **5**

2.1 Single-phase liquid flow heat transfer in microchannels 6
2.2 Two-phase flow boiling 8
2.3 Two-phase flow transition from macroscale to microscale 9
2.4 Two-phase flow boiling stability 11
2.5 Two-phase flow patterns 13
2.6 Two-phase pressure drop in microchannels 19
2.7 Two-phase heat transfer coefficient 22
2.8 Critical heat flux in microchannel 30
2.9 Non-uniform and transient heat flux cooling 30

3 Experimental facility and data reduction **35**

3.1 Refrigerant flow loop 35
3.2 Test sections 36
  3.2.1 Thermal chip and the printed circuit board 39
  3.2.2 Thermal interface material 42
  3.2.3 Evaporators 42
  3.2.4 Manifolds 44
3.3 Test fluid 45
3.4 Measurement and accuracy 46
  3.4.1 Dimension 47

3.4.2 Signal acquisition 47
3.4.3 Flow rate 48
3.4.4 Temperature 49
3.4.5 Absolute pressure 49
3.4.6 Differential pressure 50
3.4.7 Heat flux losses 51
3.4.8 Fluid and material properties 52
3.5 Data reduction and error propagation 53
3.5.1 Heat conduction 53
3.5.2 Fluid-side parameters 55
3.5.3 Heat transfer coefficient 59

4 Pressure drop 61
4.1 Inlet restriction pressure drop 61
4.2 Outlet restriction pressure drop 63
4.3 Channel pressure drop 66
4.3.1 Single-phase validation 66
4.3.2 Flow distribution 67
4.3.3 Results 69
4.3.4 Temperature 72
4.3.5 Comparison with prediction methods 72
4.4 Total pressure drop 77
4.4.1 Pressure drop ratios 80

5 Uniform heat flux: Heat transfer coefficients 83
5.1 Validation 83
5.1.1 Single-phase Nusselt number 83
5.1.2 Thermal conduction data reduction scheme 88
5.1.3 Lateral heat transfer coefficients uniformity 89
5.1.4 Repeatability of the results 90
5.2 Uniform heat flux heat transfer coefficients 90
5.3 Comparison with prediction methods 104

6 Non-uniform heat flux 111

6.1 Power and temperature maps . . . 111

6.2 Base heat flux and package thermal resistance without heat spreading . . . 112

6.3 Footprint heat flux and wall temperatures with heat spreading . . . 118

6.3.1 Thermal conduction data reduction scheme . . . 118

6.3.2 Footprint heat flux and wall temperature maps . . . 119

6.4 Heat transfer coefficient under non-uniform heat flux . . . 123

6.4.1 Pressure drop model . . . 123

6.4.2 Mass flux variation due to non-uniform heat flux . . . 124

6.4.3 Wall heat transfer coefficients . . . 125

6.5 Comparison with prediction methods . . . 138

7 Transient response 141

7.1 Constant base heat flux . . . 141

7.2 Varying base heat flux . . . 144

8 Conclusions 149

A Error propagation 153

A.1 Heat flux . . . 153

A.2 Thermal conductivity . . . 153

A.3 Wall temperature . . . 154

A.3.1 1-D thermal conduction . . . 154

A.3.2 Multi-dimensional thermal conduction . . . 154

A.4 Fluid . . . 154

A.4.1 Fluid properties . . . 154

A.4.2 Mass flux . . . 155

A.4.3 Pressure . . . 156

A.4.4 Enthalpy and vapor quality . . . 157

A.5 Heat transfer coefficient . . . 157

B Further results 159

B.1 Pressure drop ratios . . . 159

B.2 Uniform heat flux heat transfer coefficients . . . 161

B.3 Non-uniform heat flux . . . 172

  - B.3.1 Base heat flux and package thermal conductance 172
  - B.3.2 Wall heat transfer coefficients for the silicon test section 176
  - B.3.3 Wall heat transfer coefficients for the copper test section 181
- B.4 Transient response 189

List of Figures

2.1 Required α_b to maintain the chip temperature below 85°C for different heat fluxes. 5

2.2 Results for R-134a from Agostini *et al.* (2006). 7

2.3 α_w and pressure drop rate for water and R-134a at 30°C, Re=300. 8

2.4 Scale effect of hydraulic diameter on various forces, based on Kandlikar (2010). 10

2.5 Elongated bubbles for R-134a for (a)2.0mm channel; (b)0.8mm channel; (c)0.5mm channel. From Revellin *et al.* (2006) 11

2.6 Channel and restriction demand curve: pressure drop vs. mass flux for constant heat flux, adapted from Zhang *et al.* (2009). 12

2.7 Liquid to vapor density ratio of different fluids. 12

2.8 Schematic of flow pattern and transitions: (a)bubbly flow; (b)bubbly/slug flow; (c)slug flow; (d)slug/semi-annular flow; (e)semi-annular flow; (f)annular flow. From Revellin *et al.* (2006). 14

2.9 FC-72 bubble growth in 400×4000μm channel. G=32kg/m^{2}s, T=52°C, 4.25kW/m^2. From Barber *et al.* (2010). 15

2.10 Schematic channel frame sequence of the intermittent dewetting-dryout process for elongated bubbles, with the liquid and vapour regions represented by gray and white, respectively. From Borhani *et al.* (2010). 16

2.11 Comparison between Revellin *et al.* (2006) and Kattan *et al.* (1998) flow pattern maps. From Revellin *et al.* (2006). 17

2.12 Comprehensive flow regime map for FC-77, from Harirchian & Garimella (2010). 17

2.13 Heat transfer coefficient vs. quality for mass flux of 300kg/m^{2}sfor R-134a at P$_{sat}$=6bar in a 0.52mm tube. From Karyiannis *et al.* (2010). 18

2.14 Two-phase frictional pressure drop for R134a and R245fa. D=0.509mm, T$_{sat}$=35°C, G=700kg/m^{2}s. From Revellin & Thome (2007a). 19

2.15 Test section of Agostini & Bontemps (2005), dimension in mm. 20

2.16 Heat transfer coefficient results for different studies. 23

2.17 Heat transfer coefficient results for different studies. 25

2.18 Heat transfer coefficient results from Ong & Thome (2011b). 26

2.19 Heat transfer coefficient results for different studies. 27

2.20 Schematic of three-zone model of Thome *et al.* (2004). 29

2.21 Schematic of dry-out of Revellin & Thome (2008). 31

2.22 Thermal maps of two UltraSPARC T1 (Niagara) chips stacked one on the top of the other (Case A in Section VI-E). From A. *et al.* (2012) 31

2.23 Liquid film thickness and wave heights for R-134a, G=500kg/m^{2}s, T$_{sat}$=30°C. Hot-spot at 10mm. From Revellin *et al.* (2008). 32

2.24 CPU usage history from a laptop. 32

2.25 Laptop microprocessor temperature evolution during bootup. Time-step between each image 10s. From Hamann *et al.* (2007). 33

3.1 Schematic of the flow loop. 35

3.2 Assembled test sections without insulation. 37

3.3 Schematic of the test sections. Cut views along the channel axis. Blue: Sections filled with refrigerant. 38

3.4 Position of test section dimensions. 39

3.5 Heater subdividing process. 41

3.6 Heater notation. 41

3.7 TIM thermal characteristics. 43

3.8 Thermal interface spreading on copper test section. 44

3.9 Silicon evaporator. 44

3.10 Copper evaporator. 45

3.11 Surface roughness measurements. 48

3.12 Silicon test section, heater 11 calibration. 50

3.13 Comparison between heat losses based on measurement across the copper test section and between the preheater and the test section. 51

3.14 Saturation pressure from temperature and pressure measurements for uniform heat flux at T$_{sat}$=30°C. 52

3.15 Schematic of the temperaturees and heat fluxes. 54

3.16 Two-dimensional heat conduction data reduction scheme. 55

3.17 Base temperature evolutions for R-236fa at G=963kg/m^{2}s in silicon test section. 57

3.18 Single-phase pressure profile for R-134a at 502kg/m^{2}s in copper test section. 58

4.1 Inlet restriction pressure drops in the silicon and the copper test sections. . 62

4.2 Comparison between Δp_1 and equation 4.1 for R-134a at T_{sat}=30°C for the copper test section. 63

4.3 Outlet restriction pressure drop in silicon test section, T_{sat}=30°C. 64

4.4 Outlet restriction pressure drop in copper test section. 65

4.5 Prediction of outlet restriction pressure drop. 67

4.6 Frictional pressure drop factor for copper test section. 68

4.7 Pressure drop from the inlet plenum to Row 5 for silicon test section. . . . 68

4.8 Comparison between Δp_2 measured along Columns 2 and 6 for copper test section. 69

4.9 Channel pressure drops in silicon test section. 70

4.10 Channel pressure drops in copper test section. 71

4.11 Fluid temperature drop versus pressure drop. 72

4.12 Comparison with best channel pressure drop prediction methods. 76

4.13 Comparison with best channel pressure drop prediction methods. 77

4.14 Total pressure drop in silicon test section. 78

4.15 Total pressure drop in copper test section. 79

4.16 Pressure drop ratios for silicon test section, T_{sat}=30°C. 81

4.17 Pressure drop ratios for copper test section, T_{sat}=30°C. 82

5.1 Single-phase validation of Nusselt number in the silicon test section. 85

5.2 Single-phase validation of Nusselt number in the copper test section. 87

5.3 Comparison between the one-dimensional thermal conduction data reduction and COMSOL Multiphysics' results for the silicon test section: R-236fa, 933kg/m^{2}s, Column 4, q_b=96.4W/cm^2. 88

5.4 Comparison between the two-dimensional thermal conduction data reduction and COMSOL Multiphysics' results for the copper test section: R-1234ze(E), 411kg/m^{2}s, Column 6, q_b=136.3W/cm^2. 89

5.5 Heat transfer coefficients in all columns. 90

5.6 Reproductibility of α_w at different wall heat fluxes. 91

5.7 Base temperatures. 92

5.8 α_w for different q_w. Silicon test section R-236fa. 93

5.9 α_w for different q_w. Silicon test section R-245fa. 94

5.10 Comparison between R-236fa and R-245fa at 703kg/m^{2}s in the silicon test section. 95

5.11 α_w for R-236fa for increasing mass fluxes in the silicon test section. . . . 95

5.12 α_w for R-245fa for increasing heat fluxes in the silicon test section. 96

5.13 α_w for different q_w. Copper test section R-134a, 569kg/m^{2}s. 97

5.14 α_w for different q_w. Copper test section R-1234ze(E), 346kg/m^{2}s. 98

5.15 α_w for different q_w. Copper test section R-245fa. 99

5.16 Comparison between R-134a, R-1234ze(E) and R-245fa around 350kg/m^{2}s and T_{sat}=31°C, in the copper test section. 100

5.17 α_w for R-134a for increasing mass fluxes in the copper test section. 100

5.18 α_w for R-1234ze(E) for increasing mass fluxes in the copper test section. . . 101

5.19 α_w for R-245fa for increasing mass fluxes and q_w=130kW/m^2 in the copper test section at T_{sat}=31.0°C. 101

5.20 α_w versus q_w at all mass fluxes in the copper test section. 102

5.21 α_w versus q_w for R-236fa at all mass fluxes in the silicon test section. . . . 103

5.22 Vapor quality at the minimum heat transfer coefficients for R-134a in copper test section 103

5.23 Comparison with heat transfer prediction methods for silicon test section. Red:R-236fa, Blue:R-245fa. 106

5.24 Comparison with heat transfer prediction methods for copper test section. Red:R-134a, Blue:R-1234ze(E), Green:R-245fa. 107

5.25 Comparison with the new flow pattern based heat transfer model. 109

5.26 Predicted α_w by the new flow pattern based heat transfer model. 110

6.1 Power maps configuration. 112

6.2 Copper test section: Thermal conductance for row hot-spots in the package R-1234ze(E), T_{sat}=30°C, 350kg/m^{2}s, assuming one-dimensional conduction. 113

6.3 Copper test section: Thermal conductance for point hot-spots in the package for R-134a, T_{sat}=30°C, 364kg/m^{2}s, assuming one-dimensional conduction. 114

6.4 Copper test section: Thermal conductance for column hot-spot in the package for R-245fa, T_{sat}=30°C, 280kg/m^{2}s, assuming one-dimensional conduction. 115

6.5 Thermal conductance over the hot-spot versus local heat flux for R-245fa in the silicon test section. 116

6.6 Thermal conductance over the hot-spot versus local heat flux in the copper test section. 117

6.7 Comparison between the two-dimensional thermal conduction data reduction and COMSOL Multiphysics numerical results for the silicon test section with R-245fa along Column 4. 119

6.8 Comparison between the two-dimensional thermal conduction data reduction and COMSOL Multiphysics numerical results for the copper test section with R-134a along Column 4 for T_{sat}=30°C. 119

6.9 Comparison between the three-dimensional thermal conduction data reduction and COMSOL Multiphysics numerical results for the silicon test section with R-245fa for hot-spot at 14H, q_b[kW/m^2] 2100:400, 507kg/m^2s. 120

6.10 Wall temperature and footprint heat flux for R-245fa with hot-spot at heater 34 in the silicon test section using a three-dimensional thermal conduction reduction method, q_b[kW/m^2] 2020:400, T_{sat}=30°C, 713kg/m^2s. . . 120

6.11 Wall temperature and footprint heat flux for R-1234ze(E) with hot-spot at Row 1 in the copper test section using a three-dimensional thermal conduction reduction method, q_b[kW/m^2] 2100:400, T_{sat}=30°C, 350kg/m^2s. 121

6.12 Mean lateral heat spreading for R-1234ze(E) with hot-spot at Row 1 in the copper test section using a three-dimensional thermal conduction reduction method, T_{sat}=30°C, 350kg/m^2s. 121

6.13 Heat spreading for R-245fa with hot-spot at heater 34 in the silicon test section along Column 4 using a three-dimensional thermal conduction reduction method, T_{sat}=30°C, 713kg/m^2s. 122

6.14 Pressure drop model correction. 123

6.15 Mass flux variation due to hot-spot. 124

6.16 Vapor quality variation at Row 5 due to hot-spot. 125

6.17 α_w for row hot-spot in the silicon test section at 701kg/m^2s, T_{sat}=30°C. . . 127

6.18 α_w along Column 4 in the silicon test section for point hot-spot at 712kg/m^2s, T_{sat}=30°C. 128

6.19 α_w for R1H at 701kg/m^2s, T_{sat}=30°C, calculated using the three-dimensional conduction scheme. 129

6.20 Comparison between the cooling for R1H and 14H at similar heat fluxes and mass flux along Column 4. 130

6.21 Comparison between the cooling for uniform heat flux and row hot-spots for R-245fa around 500kg/m^2s, in the silicon test section for similar heat fluxes. 131

6.22 α_w for row hot-spots with R-134a in the copper test section, T_{sat}=30°C. . 133

6.23 α_w for row hot-spots with R-1234ze(E) in the copper test section, T_{sat}=30°C.134

6.24 α_w for row hot-spots with R-245fa in the copper test section, T_{sat}=30°C. . 135

6.25 Base temperature, wall heat transfer coefficients and heat flux for R3H, q_b[kW/m^2]2212:499, 366kg/m^2s. 136

6.26 Comparison between some results obtained with the copper test section for R3H hot-spots and uniform heat flux results at T_{sat}=30°C. 137

6.27 Comparison between the cooling for uniform heat flux and row hot-spots for R-245fa in the copper test section for 290kg/m^{2}s and T$_{sat}$=30°C, at similar heat fluxes. 138

6.28 Impact of the multiplier for the bubble frequency in the silicon test section for R1H, q$_b$[kW/m^2] 1550:553, 503kg/m^{2}s. 139

6.29 Comparison of non-uniform heat flux results with the new flow pattern based heat transfer model. 140

6.30 Comparison of non-uniform heat flux results with the method of Bertsch *et al.* (2009). 140

7.1 Signal to noise ratio for the copper test section with R-245fa. 142

7.2 Power spectral density for R-134a in the copper test section at T$_{sat}$=30°C . 143

7.3 Evolution of the optimum frequency identified for each series of test versus heat flux for different fluid and tube diameter. From Dupont *et al.* (2004). 144

7.4 Base temperature signal at heater 34 for sudden change in base uniform heat flux. 146

7.5 Thermal response at heater 34 of the copper test section to a square change in base uniform heat flux for R-134a, 453kg/m^{2}s, T$_{sat}$=30°C. 147

7.6 Response of the copper test section to a sudden change in base uniform heat flux from single-phase condition for R-134a, 453kg/m^{2}s, T$_{sat}$=30°C. . 147

B.1 Pressure drop ratios for copper test section, T$_{sat}$=50°C. 160

B.2 α_w for different q$_w$. Silicon test section R-236fa. 161

B.3 α_w for different q$_w$. Silicon test section R-236fa, T$_{sat}$: 31.0°C, 1051kg/m^{2}s, Error in α_w: 5.7%, RMS: 8.5%. 162

B.4 α_w for different q$_w$. Silicon test section R-245fa. 163

B.5 α_w for different q$_w$. Silicon test section R-245fa, T$_{sat}$: 31.1°C, 902kg/m^{2}s, Error in α_w: 7.2%, RMS: 8.6%. 164

B.6 α_w for different q$_w$. Copper test section R-134a, 292kg/m^{2}s. 165

B.7 α_w for different q$_w$. Copper test section R-134a, 367kg/m^{2}s. 166

B.8 α_w for different q$_w$. Copper test section R-134a, 473kg/m^{2}s. 167

B.9 α_w for different q$_w$. Copper test section R-1234ze(E), 205kg/m^{2}s. 168

B.10 α_w for different q$_w$. Copper test section R-1234ze(E), 275kg/m^{2}s. 169

B.11 α_w for different q$_w$. Copper test section R-1234ze(E), 412kg/m^{2}s. 170

B.12 α_w for different q$_w$. Copper test section R-245fa, 365kg/m^{2}s. 171

B.13 Silicon test section: Thermal conductance for row hot-spots in the package for R-245fa, T$_{sat}$=31°C, 703kg/m^{2}s. 172

B.14 Silicon test section: Thermal conductance for point hot-spots in the package for R-245fa, T$_{sat}$=31°C, 909kg/m^{2}s. 173

B.15 Silicon test section: Thermal conductance for column hot-spots in the package for R-245fa, T$_{sat}$=30°C, 702kg/m^{2}s. 174

B.16 Comparison between the three-dimensional thermal conduction data reduction and COMSOL Multiphysics numerical resulzs for the silicon test section with R-245fa for hot-spot at heater 34, q$_b$[kW/m^2] 1200:400, 909kg/m^{2}s.174

B.17 Comparison between the three-dimensional thermal conduction data reduction and COMSOL Multiphysics numerical results for the silicon test section with R-245fa for hot-spot at heater 54, q$_b$[kW/m^2] 1600:400, 715kg/m^{2}s.175

B.18 α_w for row hot-spot in the silicon test section at 503kg/m^{2}s, T$_{sat}$=30°C. . . 177

B.19 α_w for row hot-spot in the silicon test section at 900kg/m^{2}s, T$_{sat}$=30°C. . . 178

B.20 α_w along Column 4 for point hot-spot in the silicon test section at 507kg/m^{2}s, T$_{sat}$=30°C. 179

B.21 α_w along Column 4 for point hot-spot in the silicon test section at 908kg/m^{2}s, T$_{sat}$=30°C. 180

B.22 α_w for row hot-spots with R-134a in the copper test section, T$_{sat}$=30°C. . 182

B.23 α_w for row hot-spots with R-134a in the copper test section, T$_{sat}$=30°C. . 183

B.24 α_w for row hot-spots with R-134a in the copper test section, T$_{sat}$=50°C. . 184

B.25 α_w for row hot-spots with R-1234ze(E) in the copper test section, T$_{sat}$=30°C.185

B.26 α_w for row hot-spots with R-1234ze(E) in the copper test section, T$_{sat}$=30°C.186

B.27 α_w for row hot-spots with R-1234ze(E) in the copper test section, T$_{sat}$=50°C.187

B.28 α_w for row hot-spots with R-245fa in the copper test section, T$_{sat}$=30°C. . 188

B.29 Power spectral density for R-1234ze(E) in the copper test section at T$_{sat}$=30°C189

B.30 Power spectral density for R-245fa in the copper test section at T$_{sat}$=30°C 190

List of Tables

2.1 Macro- to microscale transition diameters for R-134a at 30°C. 11

3.1 Test section dimensions. 40

3.2 Refrigerant saturation properties at 30°C and 50°C. 46

3.3 Systematic measurement errors. 47

3.4 Results of the error propagation analysis. 60

4.1 Pressure loss coefficients ξ from Idelcik (1999). 64

4.2 Mean average error for silicon test section. 74

4.3 Mean average error for copper test section. 75

5.1 Mean average error and accuracy for single-phase Nusselt number 86

5.2 Ratio of lateral standard deviation over lateral mean value of the local heat transfer coefficient. 90

5.3 Prediction of the vapor quality at minimum heat transfer coefficient using three-zone model. 104

5.4 Mean average error for local heat tranfer coefficients in the silicon test section. 108

5.5 Mean average error for the local heat tranfer coefficients in the copper test section. 108

6.1 Mean average error and percentage of data within ±30% for the local heat tranfer coefficients for non-uniform heat flux. 139

Nomenclature

Latin

A	Area (m^2)
AF	Annular flow
$AF-PD$	Annular flow to post dry-out
B	Evaporator width (m)
C	Coefficient
c	Constant
c_p	Specific heat (J/kgK)
CB	Coalescing bubbles
$CB-AF$	Coaslescing bubble to annular flow
D	Diameter (m)
dB	Total channel width (Channel and Fins)(m)
$dP, \Delta P$	Differential pressure (Pa)
dz	Length increment (m)
e	Thickness (m)
F	Force (N)
f	Friction factor, Frequency (Hz)
G	Mass flux (kg/m^{2}s)
g	Earth gravity: 9.81 m/s^2
H	Channel height (m)
h	Enthalpy (kJ/kg)
IB	Isolated bubbles

$IB - CB$	Isolated bubble to coaslescing bubble
L	Length (m)
l	Heater size(m)
L_{PTap}	Pressure tap position (m)
L_{tp}	Channel evaporating length (m)
m	Mass flow(kg/s)
N	Number
n	Exponent
$onset$	Evaporation starting point
PCB	Printed circuit board
Per	Perimeter
PSD	Power spectral density
q	Heat flux (W/m^2)
R	Resistance (Ω)
R_χ	Random error)
S_χ	Systematic error)
SP	Single-phase
T	Temperature (°C)
TIM	Thermal interface material
TP	Two-phase
U	Velocity (m/s)
UHF	Uniform heat flux
V	Voltage (V)
W	Channel width (m)
x	Vapor quality
z	Channel flow length position (m)
z^*	Dimensionless channel position $\left(z^* = \frac{z}{RePrD}\right)$
z_+	Dimensionless channel position $\left(z_+ = \frac{z}{ReD}\right)$

Greek

α	Heat transfer coefficient, Thermal conductance (W/m^{2}K)
β	Surface to bubble contact angle
χ	Parameter
χ^2	Liquid only pressure drop over vapor only pressure drop $\left(\frac{\frac{dP}{dz}_{lo}}{\frac{dP}{dz}_{vo}}\right)$
δ	Thickness (m)
$\delta\chi$	Measurement error
η	Fin efficiency
Γ	Function
γ	Aspect ratio W/H
λ	Thermal conductivity (W/mK)
μ	Dynamic viscosity (Pas)
ψ_s	Separate flow multiplier
ρ	Density (kg/m^3)
σ	Surface tension (Nm)
τ	Characteristic time (s)
θ	Temperature difference (°C)
υ	Specific volume (m^3/kg)
ξ	Pressure loss coefficient

Subscripts

0	Initial
$1-2$	From point 1 to point 2
$3Z$	Three zone model
AF	Annular flow
$AF-PD$	Annular flow to post dry-out
ave	Average
b	Base

c	Contraction
$CB-AF$	Coaslescing bubble to annular flow
ch	Channel
$ch-end$	Channel end
$chip$	Thermal chip
$conv$	Convective
cu	Copper
e	Exit
$evap$	Evaporator
f	Fluid
FB	Flow boiling
fin	Fins
fr	Frictional
i	Integer
$IB-CB$	Isolated bubble to coaslescing bubble
in	Inlet plenum
l	Liquid
lam	Laminar
lo	Liquid only
lv	Liquid-vapor
min	Minimum
n	number
NB	Nucleate boiling
nom	Nominal
$onset$	Evaporation starting point
out	Outlet plenum
$preh$	Preheater outlet
ref	Reference

rem	Remaining
$restr-in$	Inlet restriction
$restr-out$	Outlet restriction
sat	Saturation
si	Silicon
sp	Single phase
sub	Subcooling
TIM	Thermal interface material
$total$	Two phase
tp	Two phase
$turb$	Turbulent
v	Vapor
vo	Vapor only
vt	Laminar film - turbulent core
vv	Laminar film - laminar core
w	Wall
xy	Each local heater

Dimensionless numbers

Bi	Biot number $\left(Bi = \frac{h\delta}{\lambda}\right)$
Bl	Boiling number $\left(Bl = \frac{q}{Gh_{lv}}\right)$
Bo	Bond number $\left(Bo = \frac{g(\rho_l-\rho_v)D^2}{\sigma}\right)$
Co	Confinement number $\left(Co = \sqrt{\frac{\sigma}{g(\rho_l-\rho_v)D^2}}\right)$
Fr	Froude number $\left(Fr = \frac{m}{\rho^2 gD}\right)$
Nu	Nusselt number $\left(Nu = \frac{\alpha D}{\lambda}\right)$
Pr	Prandtl number $\left(Pr = \frac{c_p\mu}{\lambda}\right)$
Re	Reynolds number $\left(Re = \frac{GD}{\mu}, Re = \frac{\rho UD}{\mu}\right)$
We	Weber number $\left(We = \frac{\rho U^2 D}{\sigma}\right)$

Chapter 1

Introduction

Germany, France and California have set 75–80% reduction targets for carbon dioxide emissions for 2050 (Weaver *et al.* (2007)). This ambitious goal requires an annual drop of 4% over 40 years. While switching electricity generation towards renewable energy sources and using hydrid engines or electrical motors in vehicles are well-advertised methods for potentially reducing such emissions, improving energy efficiency is a less discussed, but a crucial contribution to achieve these objectives.

Cullen & Allwood (2010) pointed out in a global map of energy conversion efficiency that currently low-temperature waste heat was the main product coming from energy conversion systems. Most engines, burners, motors and heaters are air-cooled, because air is cheap and accessible. The resulting waste heat is rarely reused and is very often released to the environment. The development of better heat management systems able to recover this heat is often slowed down by financial considerations.

Electronic applications offer the economical backing to develop low temperature ($\leq$100°C) waste recovery, because they generate a very large amount of heat. Currently air-cooled systems are commonly used for computers and IGBTs (Insulated Gate Bipolar Transistors), used for example in AC/DC converters. However for these applications, air-cooling is expensive. Koomey *et al.* (2009) have calculated that the annual cost of running an air-cooled data center is currently as high as its annualized equipment costs. Air has a low specific heat, such that large volumes have to be moved and chilled before entering the data center. In turn, the power needed to operate a data center is rising rapidly and approaches close to 3% of the total American electricity production (EPA (2007)).

As long as air remains the cooling medium, options for improvement are limited. Changing to liquid-based cooling, which has better heat removal capacities, would decrease power consumption, improve the system's efficiency and allow recovery of waste heat. Regarding increasing efficiency, the latter advantage is particularly interesting: it is possible to design a liquid-based cooling system to have an output temperature over 50°C which for example could enable saving on building heating costs. Moreover, liquid-based systems would raise the ceiling for applications combining high heat fluxes and low operating temperatures; in these situations air cannot dissipate much more than 50W/cm^2.

Among liquid-base cooling systems, two-phase cooling is optimal: the latent heat of evaporation of a refrigerant ($\approx$150kJ/kg) is much greater than the sensible heat of liquid water (4.2kJ/kg). Therefore, it requires a much lower flow rate and pumping power to remove the same amount of heat. In addition, the fluid temperature of two-phase flow can be almost constant over the whole surface whilst using a dielectric refrigerant removes the risk associated with water in an electrical circuit. Finally, two-phase cooling can be integrated in a heat pump cycle, which can efficiently increase the value of the waste heat for further use by raising the system's output temperature.

Any such heat recovery system starts from the evaporator mounted on the heat generating chip. Park & Thome (2010) have shown that with a copper micro-evaporator, an evaporating flow of refrigerant can successfully dissipate heat fluxes over 350W/cm^2 while maintaining the operating temperature under a given temperature limit, typically 85°C for CPUs and 125°C for IGBTs. Current high-end CPU applications have a heat load of around 35W/cm^2 which is expected to rise in the next generation of chips to about 100-150W/cm^2, while IGBTs have local heat fluxes above 120W/cm^2. The temperature limitation is principally set to reduce risk of failure by electro-migration in micro-electronics nanometer-sized wires. Electro-migration is mostly a function of the electrical current and temperature (Black (1969)) and as a consequence improved cooling by two-phase flow would allow higher currents and faster clock speed.

Typically, CPUs have "hot-spots" (highly localized heat fluxes) in the cores and lower heat fluxes in the cache and interconnect zones. The heat load also varies rapidly depending on the demand for computational power. These characteristics have not been studied in two-phase flow microchannel boiling experiments so far, although it is accepted that two-phase flow will be suitable for non-uniform heat flux conditions. Testing refrigerant flow boiling in multi-microchannels for non-uniform and transient heat flux is an important step needed in order to assess the feasibility of an on-chip two-phase refrigerant cooled data center.

The present investigation aims at studying the behavior of two-phase cooling of micro-electronics using a test setup mimicking the thermal behavior of a CPU. Two multi-microchannels evaporators are used to investigate uniform, non-uniform and transient heat flux situations. The objectives are to answer the following questions:

- What is the respective importance of the inlet and outlet pressure losses with respect to the diabatic channel pressure drop and how can the outlet pressure losses be evaluated?
- What are the heat transfer coefficients in microchannels of hydraulic diameter less than 300μm and how can they be predicted accurately?
- What is the response of a two-phase multi-microchannel evaporator to non-uniform heat fluxes and what are the interactions between the power dissipation maps and two-phase cooling?
- How fast can two-phase flow stabilize the chip temperature after a sudden change in heat flux?

To answer these questions, a large experimental database will be presented for four different refrigerants and a wide range in heat fluxes, for eight power map configurations and at different refrigerant mass fluxes. As a result, it will be possible to predict all relevant thermal and hydraulic quantities, needed to design and optimize micro-evaporators from the cooler's inlet to outlet connecting pipes.

The thesis will be organized as follows:

- Chapter 1: Introduction
- Chapter 2: State of the art review
- Chapter 3: Experimental facility
- Chapter 4: Pressure drop
- Chapter 5: Uniform heat flux results
- Chapter 6: Non-uniform heat flux results
- Chapter 7: Transient heat flux results
- Chapter 8: Conclusions

Chapter 2

State of the art review

The design of micro-coolers for CPUs is constrained by the size of the chip. It usually has a "footprint" of less than 2cm^2 and has high aspect ratio channels to multiply the actual heat transfer surface area. The thermal package typically has a thermal resistance of about 10×10^{-6}m^{2}K/W, so that the wall temperature is about 80°C. Fig 2.1 plots the required base (or "footprint") heat transfer coefficients for different heat fluxes for a CPU. The values vary between 5000 and 80'000W/m^{2}K. Based on the information compiled by Lin *et al.* (2002), there are three cooling methods which can be expected to reach these values using fins but without heat spreaders: water pool and flow boiling, refrigerant flow boiling and single-phase water flow.

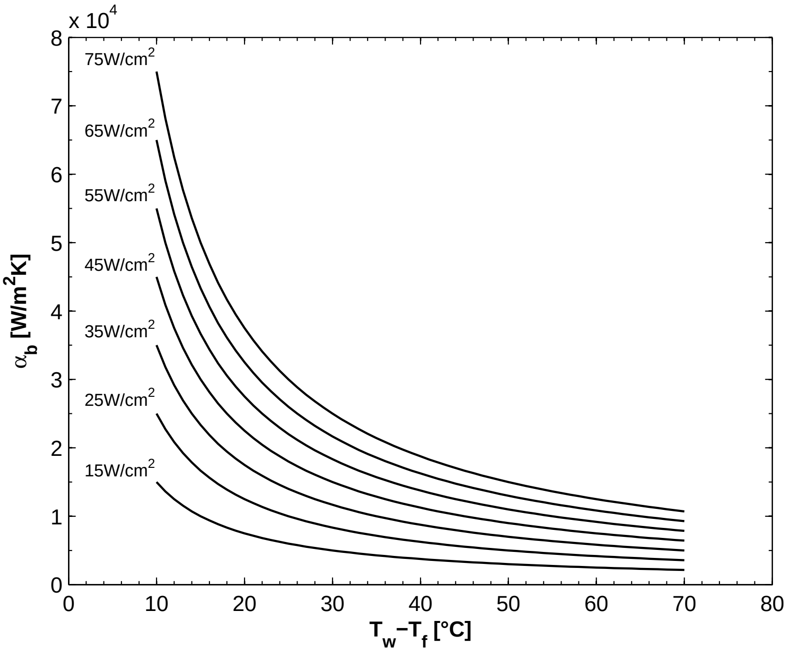

Figure 2.1: Required α_b to maintain the chip temperature below 85°C for different heat fluxes.

The resulting heat sink will be composed of several channels, which will need to be smaller than 1mm. At this scale, it was not certain that thermal and hydraulic prediction methods derived from experiments and simulations made at larger scales were valid, especially for two-phase processes. This led many researchers to study flow in microchannels and when needed to define new methods for microscales.

This review will have eight sections pertaining to the development of two-phase micro-coolers. First, the state of the research in heat transfer with single-phase liquid flow in microchannels will be covered to provide a point of comparison with the capabilities of two-phase flow cooling. Then the definition of the transition from macro- to microscale two-phase flow will be discussed. Next, the behavior of two-phase flow in microchannels will be presented in the flow patterns and flow stability sections. Important design parameters for micro-coolers such as the pressure drop and heat transfer coefficient will also be covered in detail. Finally, research made on critical heat flux in microchannels and non-uniform and transient heat flux in microchannels will be presented.

2.1 Single-phase liquid flow heat transfer in microchannels

The behavior of single-phase fluid flow in microchannels, often called microfluidics, is well studied. Several journals and books focus on the subject, for which Bruus (2008) is a good introduction. Unfortunately, microfluidics does not always answer directly the need of the heat transfer community that is concerned with much higher flow rates and the prediction of pressure drops and heat transfer coefficients, aspects discussed in detail by Kandlikar *et al.* (2006).

Since the channel sizes used are several orders of magnitude larger than the molecular mean free path of liquid coolants, the Navier-Stokes and Nusselt equations can be expected to be valid. This was however not always observed in early experiments on the subject and discrepancies were attributed to new micro-effects. In fact, as explained by Morini (2005), once conjugate heat transfer and viscous heating are correctly taken into account, the traditional well-known theories are proven and do not need modification.

Results presented by Agostini *et al.* (2006), reproduced in Fig 2.2(a), confirm that the experimental laminar single-phase frictional factors in microchannels follow well the correlation of Shah & London (1978) for laminar flow in rectangular channels:

$$f = \frac{24}{Re}\left(1 - 1.3553\gamma + 1.9467\gamma^2 - 1.7012\gamma^3 + 0.9564\gamma^4 - 0.2537\gamma^5\right) \tag{2.1}$$

for which γ is the channel aspect ratio, W/H. The equation gives a slope of 4f=57/Re for a channel aspect ratio of one. Agostini *et al.* (2006) also showed that Blasius (1908) correlation is adequate for single friction factor of fully-developped turbulent flows. Other methods are more appropriate for developing flows. Biber & Belady (1997) used the following correlation to calculate single-phase developing flow pressure drop:

$$f = \left(\frac{3.44}{\sqrt{z_+}} + \frac{24 + \frac{0.674}{z_+} - \frac{3.44}{\sqrt{z_+}}}{1 + \frac{2.9\times10^{-5}}{z_+^2}}\right)\frac{\Gamma(\gamma)}{Re} \tag{2.2}$$

The function $\Gamma(\gamma)$ is defined as:

$$\Gamma\left(\gamma\right) = 1 - 1.3553 \cdot \gamma + 1.9467 \cdot \gamma^2 - 1.7012 \cdot \gamma^3 + 0.9564 \cdot \gamma^4 - 0.2537 \cdot \gamma^5 \tag{2.3}$$

and

$$z_+ = \frac{z}{ReD_h}. \tag{2.4}$$

On the thermal side, Agostini *et al.* (2006) showed in Fig 2.2(b) that the results for fully-developed flow presented by Shah & London (1978) for laminar flow and Gnielinski (1976)'s one for turbulent flows were precise. For thermally and hydro-dynamically developing flow, Olivier (2008) used a Taylor series expansion to approximate the tabulated results of Shah & London (1978):

$$Nu_x = 3.04 + \frac{0.0244}{z^*} + \frac{0.448}{\gamma} - \frac{2.69 \times 10^{-5}}{z^{*2}} + \frac{0.02}{\gamma^2} - \frac{6.78 \times 10^{-4}}{z^*\gamma} \tag{2.5}$$

where

$$z^* = \frac{\pi}{4}\frac{z}{RePrD_h} \tag{2.6}$$

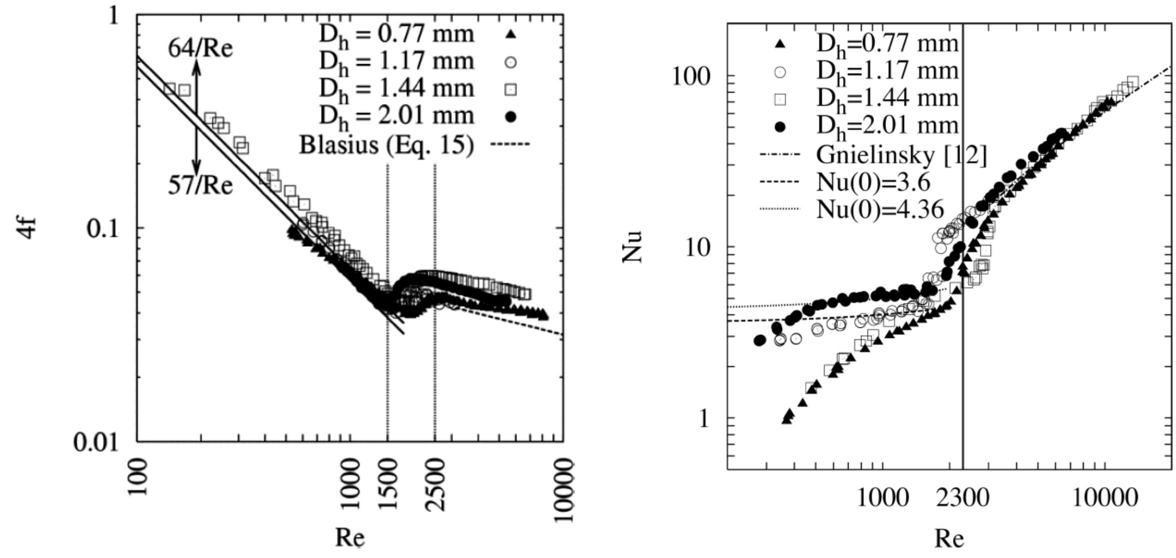

(a) f versus Re

(b) Nu_m versus Re average

Figure 2.2: Results for R-134a from Agostini *et al.* (2006).

Using these correlations, it is possible to evaluate typical single-phase pressure drops and heat transfer coefficients in microchannels. Since turbulent pressure drop rates are difficult to sustain in microchannels, most single-phase cooling applications operate in the laminar flow regime. For fully developed flows, the Nusselt number is for these conditions constant and the heat transfer coefficient depends only on the liquid thermal conductivity and the hydraulic diameter.

Setting the Nusselt number to 4.36, the variation of the wall heat transfer coefficient and pressure drop with respect to the hydraulic diameter is plotted in Fig 2.3 for liquid R-134a and water. Passing from 1 mm to 400μm, α_w does not change much, but the pressure drop rate decuples. Comparing Fig 2.3 to Fig 2.1, water cooling of microelectronics is possible with channels smaller than 500μm. For a heat load of 35W/cm^2, a laminar flow of 30°C single-phase water must pass in 300μm channels and the corresponding channel pressure drop is 5bar/m. The same comparison for R-134a shows that single phase flow of refrigerants is not a valid solution for high heat flux applications.

More complex geometries can be thermally beneficial for single-phase flow. Agostini *et al.* (2006) reviewed single-phase cooling through microchannels, porous media and jet impingement. The review showed that with improved geometries and using entrance or jet impingement effects, the Nusselt number can be increased, as it was done by Colgan *et al.* (2007), but at the cost of an increase in pressure drop and mechanical complexity. More detailed information on single-phase microchannel methods is found in Thome (2010).

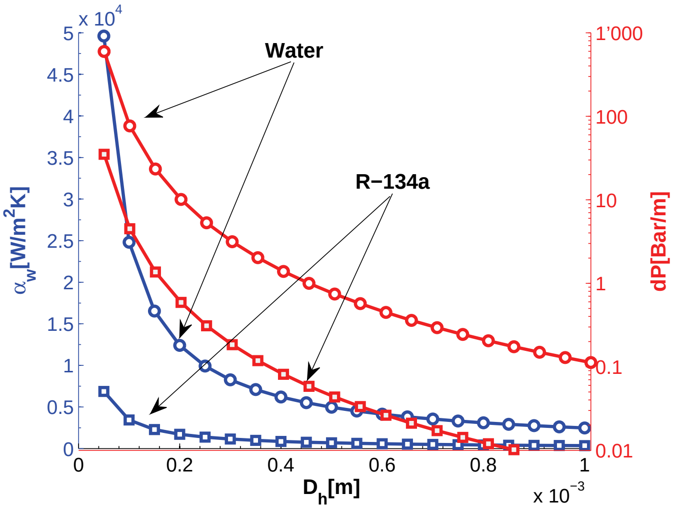

Figure 2.3: α_w and pressure drop rate for water and R-134a at 30°C, Re=300.

2.2 Two-phase flow boiling

Two-phase flow boiling is a very effective cooling mechanism. Several books cover the different aspects of two-phase flow boiling. For this work, Collier & Thome (1994), Thome (2010) and Carey (2008) were used as reference. Specific chapters on two-phase microscale flows have been written by, Kandlikar *et al.* (2006) and Bergles *et al.* (2003). For this review, two-phase flow is divided into seven subsections:

- Microscale transition
- Flow boiling stability

- Flow patterns
- Pressure drop in microchannels
- Heat transfer coefficients in microchannels
- Critical heat flux in microchannels
- Non-uniform and transient heat flux cooling

2.3 Two-phase flow transition from macroscale to microscale

Before studying microscale two-phase flow pressure drop and heat transfer, it is important to know where the transition between macro- and microscale two-phase flow lies. A simple criterion was given by Kandlikar & Grande (2003), although not specifically for two-phase flows. Conventional channels were defined as having a diameter larger than 3mm, minichannels between 200μm and 3mm and microchannels between 10μm and 200μm. Smaller channels where the molecular mean free path could come close to the diameter size were called transitional and molecular.

This estimate can be improved for two-phase flows. The objective is to determine when channel dimension does modify the flow behavior. This certainly happens when a bubble, once released, immediately fills the channel. As an approximate estimate, nucleate pool boiling methods for predicting the bubble departure diameter can be used to define a microscale lower bound limit. Fritz (1935)'s correlation, shown below, gives a value of 98 μm for refrigerant R134a at 30°C.

$$D = 0.0208\beta \left(\frac{\sigma}{g\left(\rho_l - \rho_v\right)} \right)^{0.5} \tag{2.7}$$

where β is the contact angle between the surface and the bubble. The contact angle, 5.8°, was taken from Vadgama & Harris (2007) for a copper surface. If the channel is larger than this value, the flow can still differ from macroscale, since the viscous, surface tension and buoyancy forces remain more important at small scales.

Kandlikar (2010) has evaluated the relative importance of each force affecting the flow as follows:

- Inertia force: $F_i \approx \frac{G^2 A}{\rho}$
- Surface tension force: $F_\sigma \approx \frac{\sigma A}{D_h}$
- Viscous shear force: $F_\tau \approx \frac{\mu G A}{\rho D_h}$
- Gravity (buoyancy) force: $F_g \approx \mu(\rho_l - \rho_v) D_h A$

- Evaporation momentum force: $F_M \approx \left(\frac{q}{h_{lv}}\right)^2 \frac{A}{\rho_v}$

where A is the channel cross-sectional area.

Kandlikar (2010) also plotted the diameter dependence of these forces per unit area for water and R-123. The same analysis for R-134a with a heat flux of 200kW/m^2 and a mass flux of 500kg/m^{2}s is repeated in Fig 2.4, using the recommended approximation for the two-phase properties. Buoyancy forces decrease in importance with the hydraulic diameter and has the same magnitude as surface tension around 800μm and as viscous force around 80μm. The diameter must go down to 60μm before inertia and surface tension have the same magnitude.

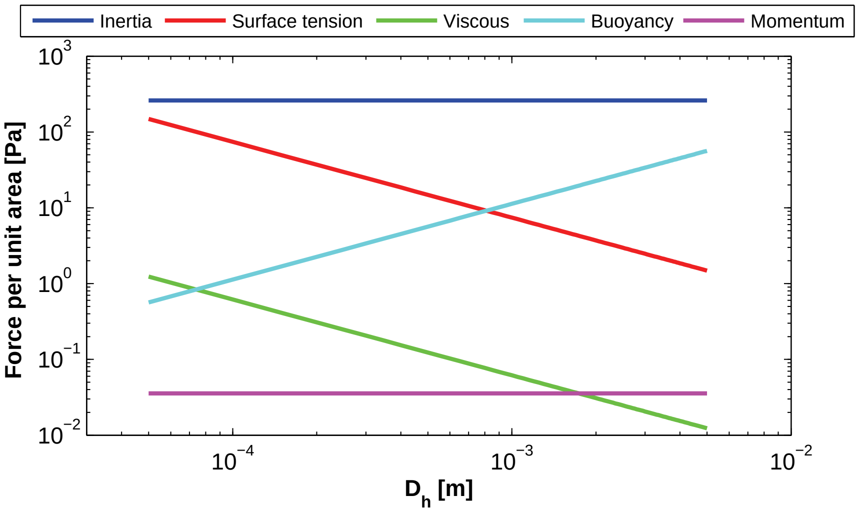

Figure 2.4: Scale effect of hydraulic diameter on various forces, based on Kandlikar (2010).

The strength of each force can be assessed by non-dimensional numbers. Buoyancy to surface tension forces ratio is represented by the Bond number, $Bo = \frac{g(\rho_l - \rho_v)D^2}{\sigma}$, the inertia to surface tension by the Weber number, $We = \frac{\rho U^2 D}{\sigma}$, and the inertia to viscous forces by the Reynolds number, $Re = \frac{\rho U D}{\mu}$. All three will decrease in smaller channel.

Based on Fig 2.4, tracking changes in bubble's buoyancy experimentally can be used to describe the transition. Pictures taken by Revellin *et al.* (2006) for R134a in 0.5, 0.8 and 2 mm tubes, presented in Fig 2.5, point to a transition around 0.8 mm, when the bubble is much less affected by buoyancy and flows in the middle of the tube. This is close to where surface tension becomes greater than buoyancy in Fig 2.4. The Bond number is thus a good indicator for the macro- to microscale transition.

Several authors defined transition criteria. Harirchian & Garimella (2010) used the Bond and Reynolds number to define a transition from unconfined to confined flow as

$$Bo^{0.5}Re = \frac{1}{\mu_l}\left(\frac{g\left(\rho_l - \rho_v\right)}{\sigma}\right)^{0.5} GD^2 = 160 \tag{2.8}$$

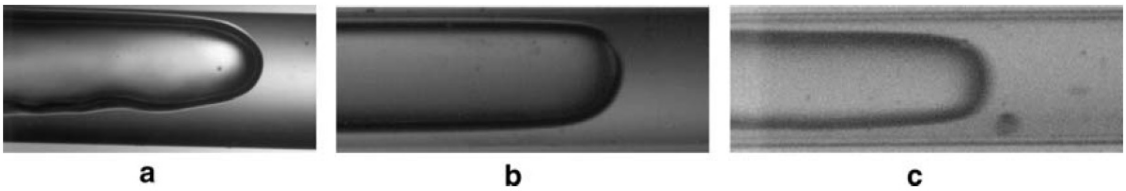

Figure 2.5: Elongated bubbles for R-134a for (a)2.0mm channel; (b)0.8mm channel; (c)0.5mm channel. From Revellin *et al.* (2006)

They noted that, at low heat flux, bubbles are smaller and many can be found in the channel cross-section; thus the flow is not confined. In such a case, the macro to microscale transition is also a function of the heat flux, even though this parameter is not present in their transition criteria.

Ong & Thome (2011a) and Cheng & Wu (2006) used the Confinement and Bond numbers ($Bo = Co^{-2}$) respectively as transition criteria from microscale (Co>1 and Bo<0.05) to a transition scale (0.3-0.4≤Co≤1 and 0.05≤Bo≤3) to macroscale (Co<0.3 and Bo<3).

Table 2.1 presents the expected transition diameters for R-134a at 30°C and based on these values, a 300μm channel lies somewhere between micro and the transition scales, far away from macroscale.

Table 2.1: Macro- to microscale transition diameters for R-134a at 30°C.

	Microscale	Transition	Macroscale
Kandlikar & Grande (2003)	D<200μm	200μm≤D≤3mm	D>3mm
Harirchian & Garimella (2010)	D<101μm	–	D>101μm
Ong & Thome (2011a)	D<825μm	825μm≤D≤2.7mm	D>2.7mm
Cheng & Wu (2006)	D<175μm	175μm≤D≤1.45mm	D>1.45mm

2.4 Two-phase flow boiling stability

Two-phase flow instabilities are common to both macro- and microscale flow boiling. Boure *et al.* (1973) classified them in static and dynamic instabilities. The most important one observed in microchannels are called Ledinegg instabilities.

Looking at Fig 2.6, when boiling starts, the rate of pressure drop with respect to mass flux becomes negative, which means that the channel demands more external pressure for a smaller mass flux. The flow loop characteristic also has a negative slope, as it can provide more pressure to the evaporator at a smaller mass flux. However, if the channel's slope is steeper than the loop's slope, pressure cannot be balanced and the system becomes unstable. To ensure stability, the loop's slope must be steeper than that of the channel. This is achieved by adding a throttling device at the inlet of each channel. This device will make the supply curve vary rapidly with mass flux and free the system of Ledinegg instabilities, but in turn will increase the loop pressure drop.

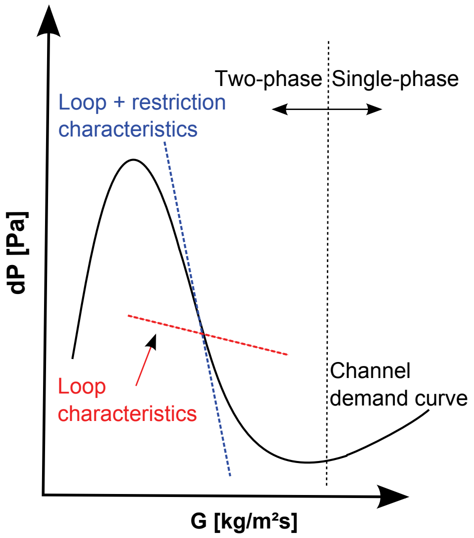

Figure 2.6: Channel and restriction demand curve: pressure drop vs. mass flux for constant heat flux, adapted from Zhang *et al.* (2009).

Microchannels restrict the volume in which a bubble axially expand. If water is used for the evaporation, the acceleration process can be dramatic and almost explosive, as reported by Hestroni *et al.* (2005). In their experiment, the time needed from the onset of boiling somewhere in the tube to a fully developed vapor core or post dryout regime was less than 0.1s. Zhang *et al.* (2009) also studied these instabilities in microchannels. They showed that boiling water was much more prone to be unstable than refrigerant HFE-7100 and suggested that the very large difference in kinematic viscosity ratio between vapor and liquid phase for both fluids were the cause of it. This explanation gives too much importance to dynamic viscosity: the main factor is most probably the liquid to vapor density ratio of water under 100°C shown in Fig 2.7. In order to respect the conservation of mass, water bubbles will create a pressure peak and accelerate in some cases to sonic velocities. It is thus very difficult to work with water in microscale evaporators under 100°C. In comparison, the density ratio for refrigerants is 1000 times smaller than that of water and consequently much easier to handle.

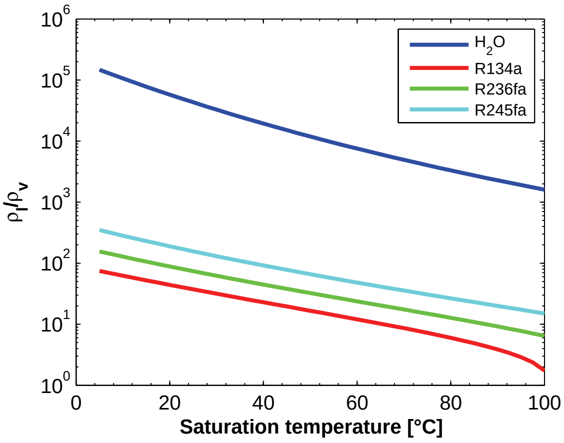

Figure 2.7: Liquid to vapor density ratio of different fluids.

If the instability problem is not tackled in an experimental setup, the validity of the heat transfer and pressure drop results is questionable. As a remedy, an adequate size of the inlet restriction must be defined. For water, Wang *et al.* (2008) found that 3mm long area restrictions of 20% at the inlet of their channels of 186μm hydraulic diameter stabilized the flow. Kosar *et al.* (2006), for similar experiments, needed an orifice of D_h=37μm in front of a channel of D_h=227μm, at least 100μm long to stabilize their test section up to an exit quality of x_e=0.5. They also found that the inlet restriction increased the pressure drop by at least 100%.

For refrigerants, Park *et al.* (2009) used a special insert with individual orifices and another one with a slit placed at the beginning of the channels. Both setups prevented back flows in the inlet reservoir and multi-channels instability. Back flows in the channels themselves were still observed, but were contained within the channel where they occurred. The time-averaged performance of the evaporator was uniform for all channels. A different type of restriction was used by Agostini *et al.* (2008a). The flow was forced through a slit machined in channel cover and made a 90° turn as it entered the channels. This configuration was shown to bring excellent stability and had the advantage to be easily integrated in the test section. It also decreased the proportion of the inlet restriction pressure drop to only about 10% of the total pressure drop.

2.5 Two-phase flow patterns

The study of two-phase flow patterns describes how the liquid and vapor phases are distributed. Each specific flow configuration will affect its thermal and hydraulic characteristics. Once the flow patterns are determined, the information can be later used to develop pressure drop and heat transfer flow pattern-based prediction methods.

Microscale two-phase flow patterns differ from those observed in macrochannels, due to the increased importance of surface tension. Several microscale flow pattern maps have been proposed based on water, refrigerant and water-air two-phase flow. Most share approximately the same pattern description, but the transition criteria can differ from one to another. For this review, the focus will be on studies which covered refrigerant flow patterns.

Flow observations are the first step needed toward the development of flow pattern maps. Revellin *et al.* (2006) divided microscale flow regimes using visual and statistical methods into six different subsets: bubbly flow, bubbly-slug flow, slug flow, slug/semi-annular flow, semi-annular flow and annular. This division is represented in Fig 2.8. The bubbly flow regime is still affected by buoyancy, whereas the other are axisymmetric.

Most flow pattern studies used circular tubes larger than 500μm for their visualization and some authors pointed out that there are differences in non-circular geometries. For example, Barber *et al.* (2010) have observed that the flow evolution in high aspect ratio channel can differ, especially when the bubbles grow. In Fig 2.9, at a low mass flux, the bubble grows initially in all directions and once it is almost as large as the channel width, it mostly grows laterally. Only when it reaches all walls, does the cross-section view look like the view in a circular pipe.

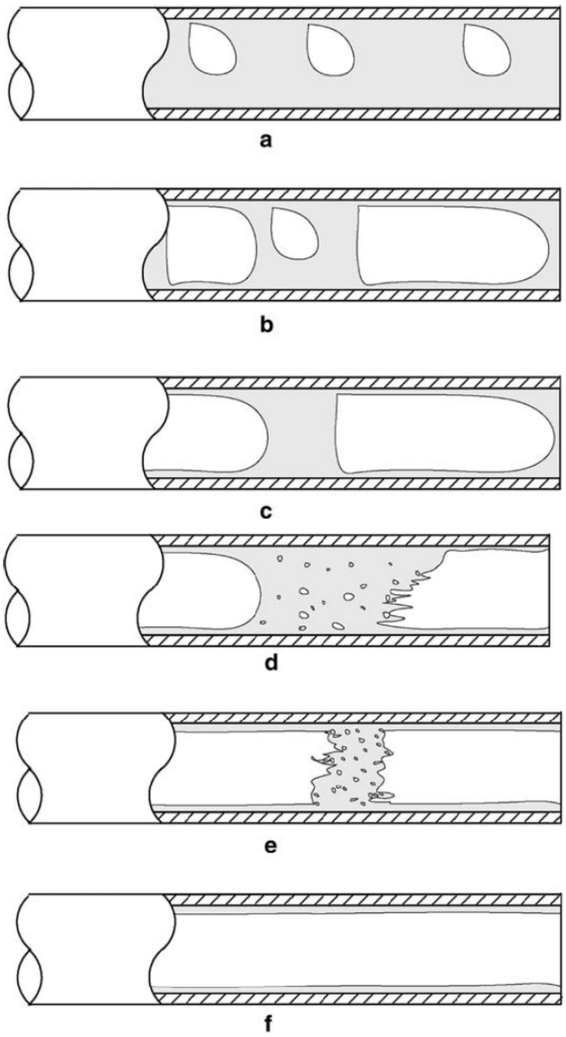

Figure 2.8: Schematic of flow pattern and transitions: (a)bubbly flow; (b)bubbly/slug flow; (c)slug flow; (d)slug/semi-annular flow; (e)semi-annular flow; (f)annular flow. From Revellin *et al.* (2006).

In a multi-microchannel evaporator of $D_h = 336\mu m$, Borhani *et al.* (2010) observed that under diabatic conditions, two-phase flow in microchannels can be affected by intermittent dry-out. Fig 2.10 graphically described the dewetting process after a pertubation at the tail of a bubble occurs. After a certain time, the perturbation breaks the liquid annular film and grows upstream. At that point, the surface is completely dewetted. This process occurs in a few milliseconds and rewetting of the wall is done by the arrival of the next liquid slug. It is however not clear if these dry-out zones are part of a transition between two stable flow patterns or a permanent feature of two-phase flow in channels smaller than $500\mu m$.

Two-phase flow observation can be collected into a flow pattern map. In Fig 2.11 Revellin *et al.* (2006)'s map is shown. It is compared to a macroscale map developed by Kattan *et al.* (1998). There are several differences between both maps. The stratified flow regimes disappear in the microscale map due to the effect of surface tension, as

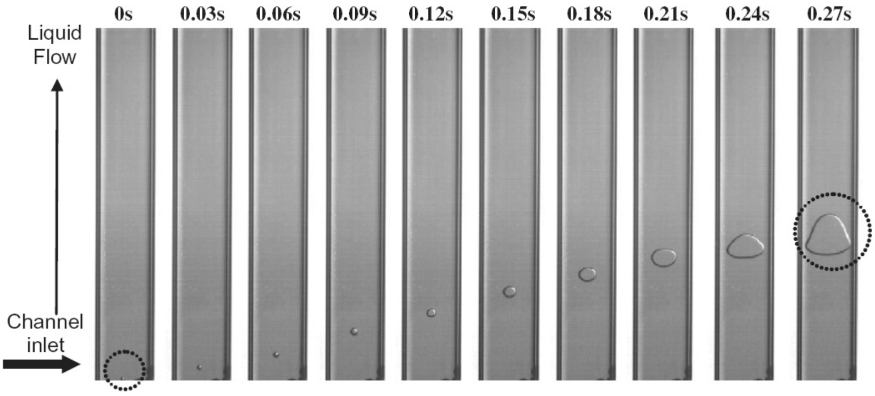

Figure 2.9: FC-72 bubble growth in 400×4000μm channel. G=32kg/m^{2}s, T=52°C, 4.25kW/m^2. From Barber *et al.* (2010).

highlighted in Fig 2.5. The microscale transition to annular flow is a function of the mass flux, whereas it happens at a fix vapor quality for macroscale. This transition also happens at lower quality in microscale channels for high mass fluxes.

On the microscale map, three flow regimes can be considered as transitional and the count can be reduced to four stable flow regimes: IB, isolated bubble regime; CB, coalescing bubble regime; AF, annular flow regime (completely coalesced regime) & PD, post-dryout regime, as done by Revellin & Thome (2007b). The transitions were described by the following equations:

IB–CB, isolated bubble to coalescing bubble regime transition

$$x_{IB-CB} = 0.763\left(\frac{Re_{lo}Bo}{We_{vo}}\right)^{0.41} \tag{2.9}$$

CB–AF, coalescing bubble to annular flow regime transition

$$x_{CB-AF} = 0.00014\frac{Re_{lo}^{1.47}}{We_{lo}^{1.23}} \tag{2.10}$$

AF–PD, annular flow to post-dryout regime transition

$$x_{AF-PD} = 0.437\left(\frac{\rho_v}{\rho_l}\right)^{0.073}\frac{Gh_{lv}}{We_{lo}^{0.24}\left(\frac{L}{D}\right)^{0.72}} \tag{2.11}$$

Ong & Thome (2011b) proposed different transition equations at microscales, based on a large database, including many fluids. He included the effect of the Confinement number, $Co = \sqrt{\frac{\sigma}{g(\rho_l-\rho_v)D^2}}$, and that of the liquid to vapor phase viscosity and density ratios. The dry-out zone was not directly observed but was predicted via critical heat flux correlations. The IB–CB transition is thus:

$$x_{IB-CB} = 0.36Co^{0.3}\left(\frac{\mu_v}{\mu_l}\right)^{0.65}\left(\frac{\rho_v}{\rho_l}\right)^{0.9}\frac{Re_{vo}^{0.75}Bo^{0.25}}{We_{lo}^{0.91}}; \tag{2.12}$$

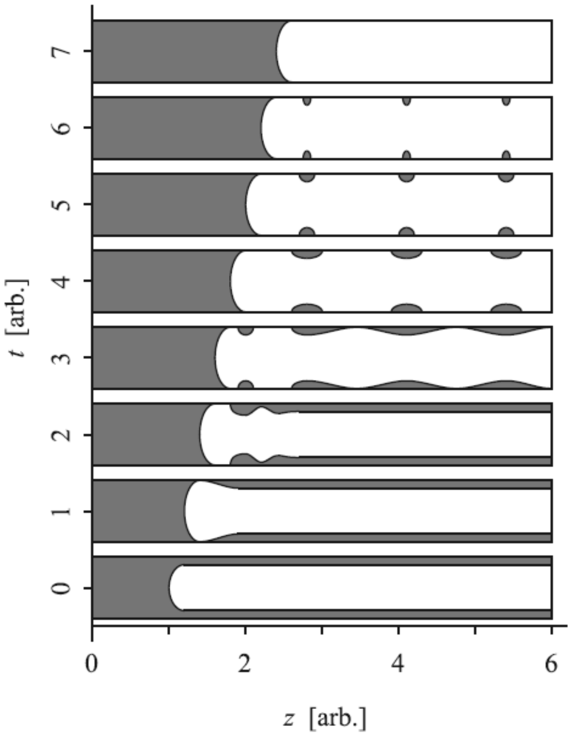

Figure 2.10: Schematic channel frame sequence of the intermittent dewetting-dryout process for elongated bubbles, with the liquid and vapour regions represented by gray and white, respectively. From Borhani *et al.* (2010).

and that for CB–AF is:

$$x_{CB-AF} = 0.047 Co^{0.05} \left(\frac{\mu_v}{\mu_l}\right)^{0.7} \left(\frac{\rho_v}{\rho_l}\right)^{0.6} \frac{Re_{vo}^{0.8}}{We_{lo}^{0.91}}; \tag{2.13}$$

Harirchian & Garimella (2010) used their unconfined to confined transition criteria to create a comprehensive flow regime map shown in Fig 2.12. They found that the slug to annular transition both in confined and unconfined flow was:

$$Bl = 0.017 \left(\frac{Bo^{0.4}}{Re^{0.3}}\right) \tag{2.14}$$

It should be noted that their flow regime map does not include information about the local flow evolution (vapor quality, void fraction or velocity).

It is also possible to infer flow pattern transition from heat transfer results, by following the change in trends. Karyiannis *et al.* (2010) found that in a 0.52 mm tube, four different trends in heat transfer could be associated with flow pattern change, as shown in Fig 2.13. In zone I, a confined bubble regime could exist, which would peak when dry-patches start to occur in zone II. The results in zone III may depend on the interaction between nucleation sites and the changing flow regime. In zone IV, the flow is annular, based on observation at the microchannel outlet.

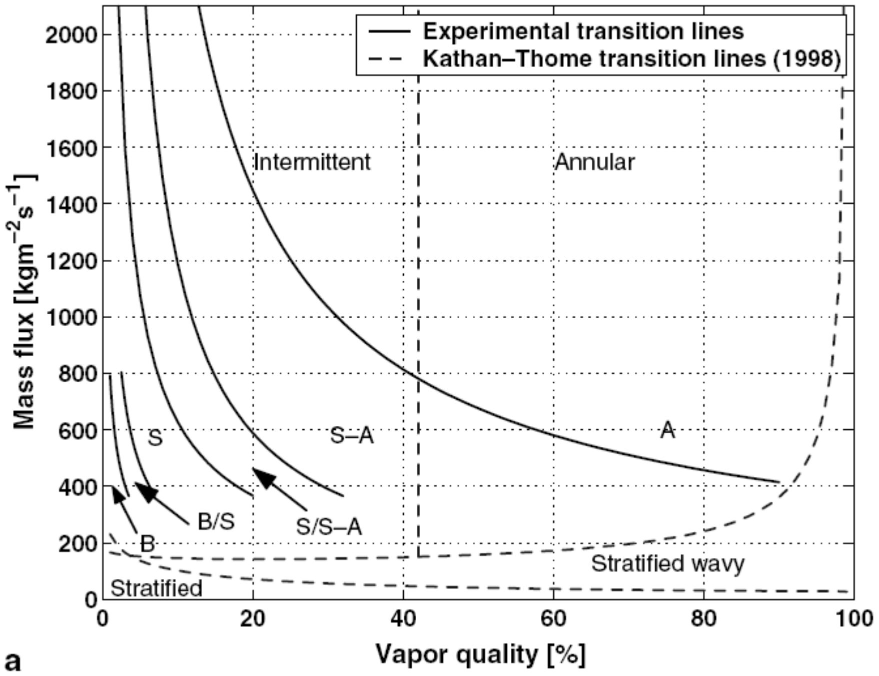

Figure 2.11: Comparison between Revellin *et al.* (2006) and Kattan *et al.* (1998) flow pattern maps. From Revellin *et al.* (2006).

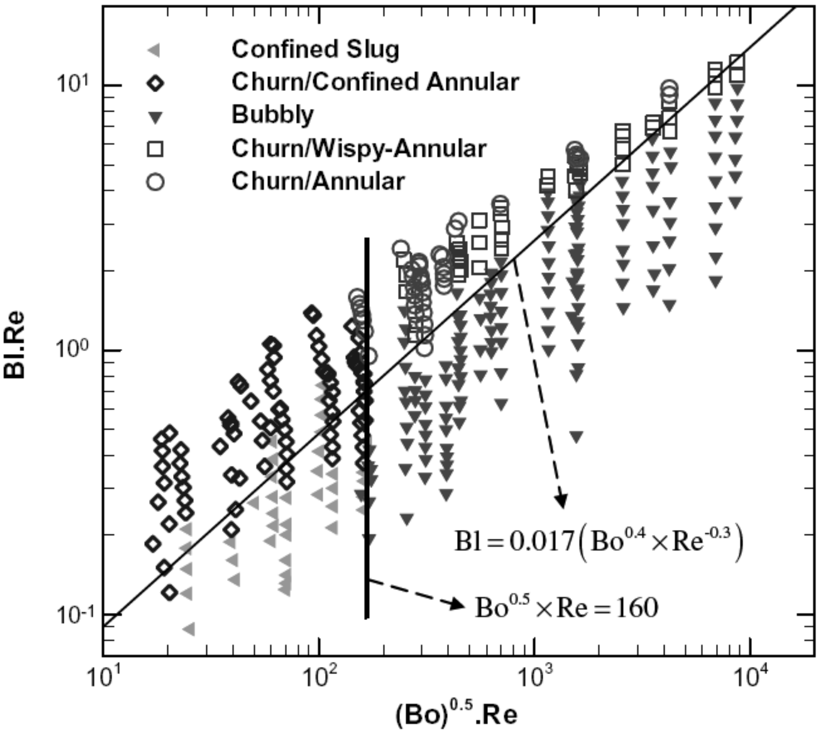

Figure 2.12: Comprehensive flow regime map for FC-77, from Harirchian & Garimella (2010).

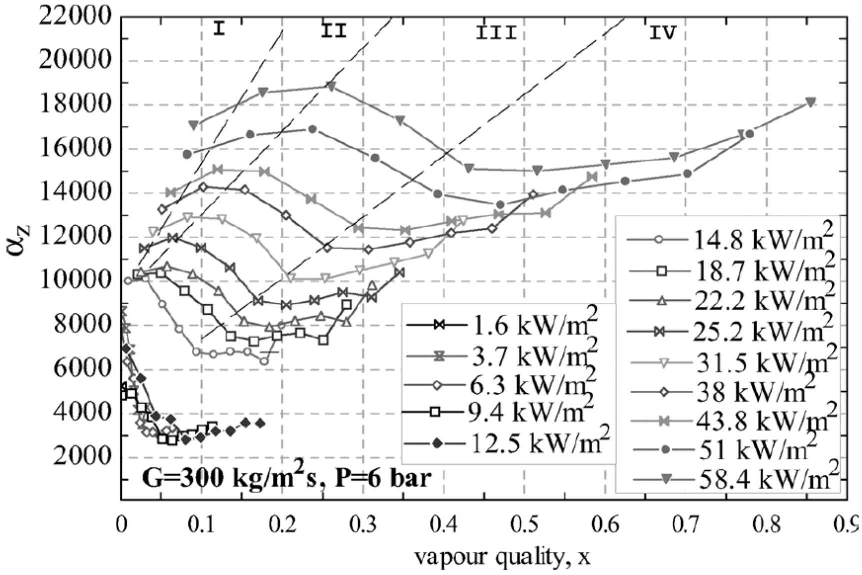

Figure 2.13: Heat transfer coefficient vs. quality for mass flux of 300kg/m^{2}sfor R-134a at P$_{sat}$=6bar in a 0.52mm tube. From Karyiannis *et al.* (2010).

2.6 Two-phase pressure drop in microchannels

In a two-phase system, pressure drop is used both to define the hydraulic and thermal characteristics. Accurate pressure measurements are thus important to develop efficient micro-evaporators. In single-pipe microchannels, which typically have a diameter over 500μm, pressure measurement techniques are well developed. Revellin & Thome (2007a) showed (graph repeated in Fig 2.14) that the two-phase frictional pressure drop of R-245fa was more than twice larger than that of R-134a, reaching 10 bar/m for a vapor quality of 0.6.

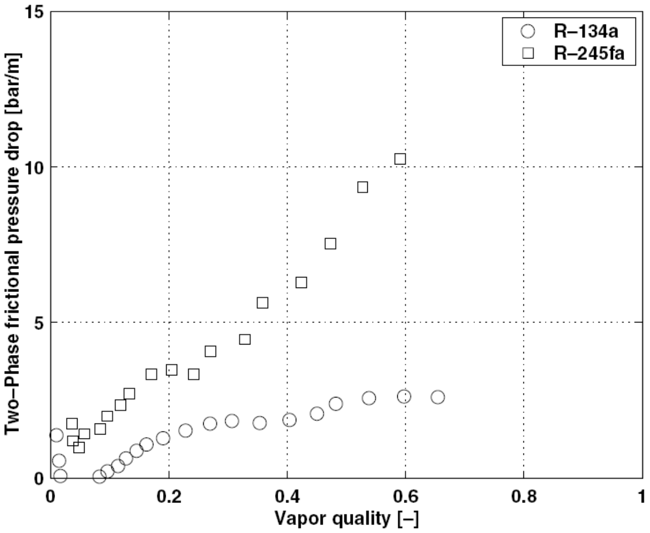

Figure 2.14: Two-phase frictional pressure drop for R134a and R245fa. D=0.509mm, T$_{sat}$=35°C, G=700kg/m^{2}s. From Revellin & Thome (2007a).

Helped by micro-machining techniques, multi-microchannels usually have a hydraulic diameter smaller than 500μm. In such a configuration, accurate pressure measurements are difficult. These are usually made in the larger inlet and outlet plenums and not directly in the channel.

The pressures at the channel extremities are determined by the pressure measurements using pressure loss correlations, as explained by Lee & Garimella (2008). Single-phase losses can in principle be accurately determined by using design tables, such as those provided in Idelcik (1999). In comparison, predicting the two-phase losses in a sudden reduction or expansion is difficult and many articles eluded the subject. For example, Agostini & Bontemps (2005) presented two-phase pressure drop results in an evaporator composed of 11 square channels of 3.28mm × 1.47mm, a schematic of the test section is shown in Fig 2.15, but did not discuss the pressure difference that exists between the measurement point in the outlet manifold and the end of the evaporator (L$_j$).

Chen *et al.* (2010) studied pressure in sudden contraction and expansion for macroscale pipes and showed that existing prediction methods for a sudden expansion were not accurate and that the best method for sudden contraction was the homogeneous method described in Collier & Thome (1994), which had a mean average error of 49.2%. The

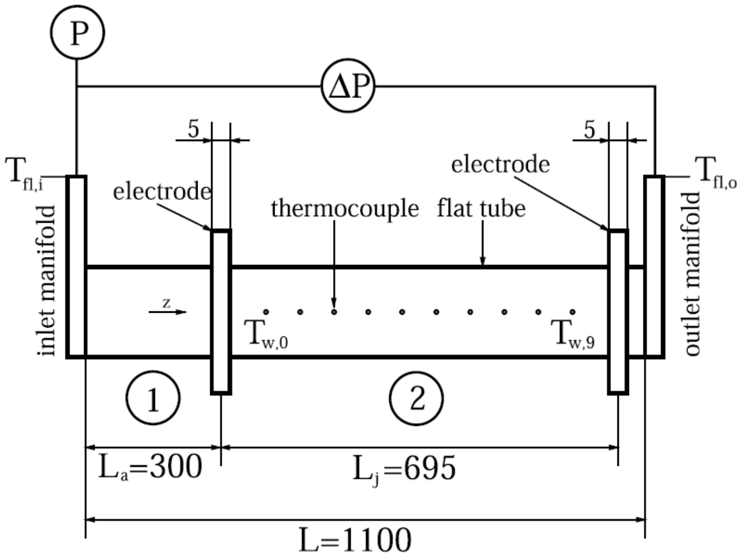

Figure 2.15: Test section of Agostini & Bontemps (2005), dimension in mm.

static pressure change expression for a sudden contraction from point 1 to 2 given by Collier & Thome (1994) is:

$$\Delta p_{1-2} = \frac{G_2^2 \upsilon_l}{2} \left[\left(\frac{1}{C_c} - 1 \right)^2 + \left(1 - \left(\frac{A_2}{A_1} \right)^2 \right) \right] \left[1 + \frac{\upsilon_{lv}}{\upsilon_l} x \right] \tag{2.15}$$

where G_2 is the outcoming mass flux and C_c a contraction coefficient, for which tabulated results are provided.

For sudden enlargement, Collier & Thome (1994) give

$$\Delta p_{1-2} = G_1^2 \frac{A_1}{A_2} \left(1 - \frac{A_1}{A_2} \right) \upsilon_l \left(1 + \frac{\upsilon_{lv}}{\upsilon_l} x \right) \tag{2.16}$$

where G_1 is the incoming mass flux.

In microchannel, Garimella *et al.* (2002) included two-phase singularity losses in the pressure drop calculation of a condensing flow of R-134a by first measuring the pressure drop in a short test section. The losses were estimated by using the models recommended by Hewitt *et al.* (1993) and validated against pressure measurements. The model for contraction is the same as equation 2.15. For enlargement the equation differs from equation 2.16 by using a separate flow multiplier instead of a homogenous flow one:

$$\Delta p_{1-2} = G_1^2 \frac{A_1}{A_2} \left(1 - \frac{A_1}{A_2} \right) \upsilon_l \psi_s \tag{2.17}$$

where G_1 is the incoming mass flux and ψ_s the separated flow multiplier.

To evaluate the two-phase channel pressure drop itself, numerous prediction methods are available. Classical methods, presented in Collier & Thome (1994), include:

- The homogeneous model with two-phase viscosity modelled using McAdams *et al.* (1942), Cicchitti *et al.* (1960) and Dukler *et al.* (1964).
- The separated flow model of Lockhart & Martinelli (1949)
- The correlation of Baroczy (1965), adapted by Chisholm (1973)
- The correlation of Friedel (1979)

Ribatski *et al.* (2006) reviewed 12 methods against 1800 pressure measurements taken from 9 experimental microchannel databases and found that the most accurate methods were those of:

- Mueller-Steinhagen & Heck (1986), which proposed an asymptotic fit based on the single-phase liquid and vapor frictional pressure drop
- Mishima & Hibiki (1996), which modified a parameter in the Chisholm (1973) method
- The homogeneous model used with the Cicchitti *et al.* (1960) two-phase viscosity expression.

Ribatski *et al.* (2006) also noted that at high vapor quality, where annular and mist flow can be expected, the methods worked poorly.

Cioncolini *et al.* (2009) proposed a new one-dimensional turbulence model for macro and microscale annular two-phase flow, typically occuring at higher vapor quality. It can be used to predict the frictional pressure gradients, the liquid velocity profile in the annular film, the film thickness, the fraction of liquid entrained in the vapor core and the void fraction.

Three further other studies have come up with new expressions specific to microchannels. One, Tran *et al.* (1999), modified the method of Baroczy (1965) and the later two changed the definition of the C coefficient in the method of Lockhart & Martinelli (1949) based on their experimental results. Lee & Mudawar (2005a) proposed two new definitions:

$$C_{vv} = 2.16 Re_{lo}^{0.047} We_{lo}^{0.60} \tag{2.18}$$

for laminar liquid and laminar vapor flow.

$$C_{vt} = 1.45 Re_{lo}^{0.25} We_{lo}^{0.23} \tag{2.19}$$

for laminar liquid and turbulent vapor flow.

Lee & Garimella (2008) evaluate the coefficient as:

$$C = 2566 G^{-0.5466} D^{0.8819} \left(1 - e^{-319D}\right) \tag{2.20}$$

2.7 Two-phase heat transfer coefficient

Many studies have examined two-phase heat transfer in microchannels. This section of the review will focus on stable flow experiments using refrigerants (i.e. which did not report an instability problem) that used a single tube or multi-microchannel test section. Although the data reduction for single tube experiments is simpler, especially regarding the flow distribution assumption, both types of test sections provide precise results, once proper care is taken. In fact, to achieve the level of heat transfer required in Fig 2.1, multiplying the cooling channels is the only solution and multi-microchannels studies are probably closer to future applications.

Thome & Consolini (2009) placed experimental trends reported for microscale heat transfer coefficients in several groups. In some studies, the heat transfer coefficient was found to be unaffected by the vapor quality or the mass flux, but strongly dependent on the heat flux. One of the first studies on the subject was made by Lazarek & Black (1982) using R-113 in 123mm and 246mm long tubes of a diameter of 3.1mm. An example of their results is shown in Fig 2.16(a). A simple expression for the Nusselt number, using the liquid fluid properties, fits their results well:

$$Nu = 30Re^{0.857}Bl^{0.714} \tag{2.21}$$

Tran *et al.* (1996) used R-12 in 870mm long, round and rectangular single channels. They also found a strong link between the heat flux and the heat transfer coefficient, as shown in Fig 2.16(b), and fitted their experimental data with:

$$\alpha = 8.4 \times 10^{-5} \left(Bl^2 We_l\right)^{0.3} \left(\frac{\rho_l}{\rho_v}\right)^{-0.4} \tag{2.22}$$

Hamdar *et al.* (2010) used HFC-152a in a 1mm tube and found that equation 2.22 with modified exponents fitted their results well, an example of which is shown in Fig 2.16(c). Bao *et al.* (2000) repeated the same type of experiment, this time with R-11 and R-123 in a 1.95 mm copper tube. Their experimental heat transfer coefficients for both fluids at a given saturation pressure can be accurately predicted by a power law fit of the heat flux, given in Fig 2.16(d), with n=0.735. Based on this and not on any visual observation, they deduced that nucleate boiling was the dominant mechanism and recommended using the pool boiling method of Cooper (1984) for heat transfer prediction. However linking microchannel flow boiling to pool boiling is problematic because according to Collier & Thome (1994), the exponent value n in $T_w - T_{sat} = Cq^n$ for pool boiling is normally in the range 0.25–0.5, far from n=0.735.

Harirchian & Garimella (2008) used FC-77 in silicon multi-microchannels of different cross section and obtained results similar to Bao *et al.* (2000), as shown in Fig 2.16(e), and also found that the Cooper (1984) nucleate pool boiling correlation was the most accurate method to predict their results. In their test section, the heat flux was provided by a 5 × 5 array heater, each having its own temperature sensor, but their results were derived from measurements made with only one heater, making it impossible to assess if the reported heat transfer trends are constant along the channel.

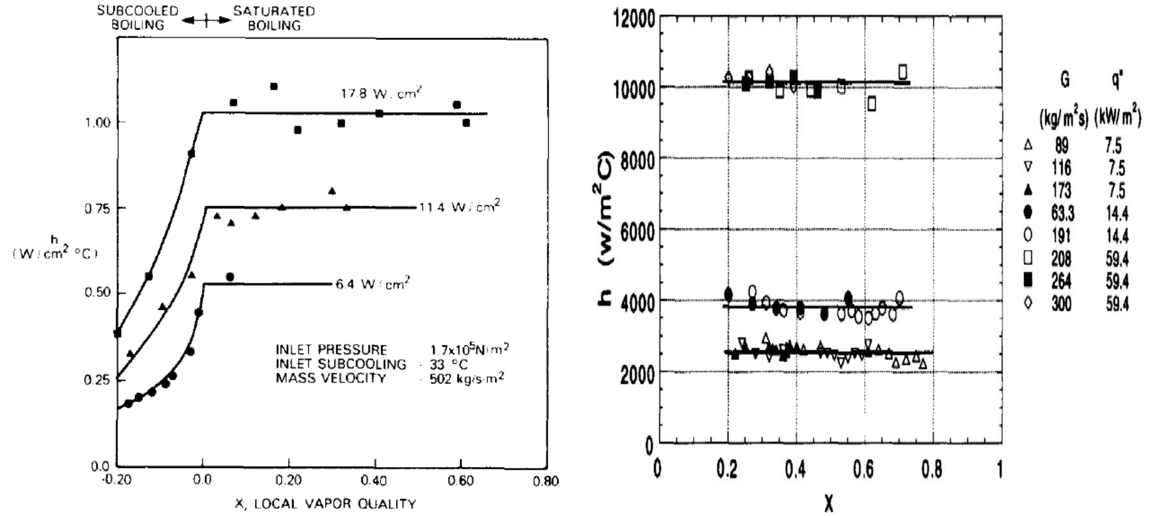

(a) Lazarek & Black (1982), R-113, D= 3.1mm (b) Tran *et al.* (1996), R-12, D= 2.46mm

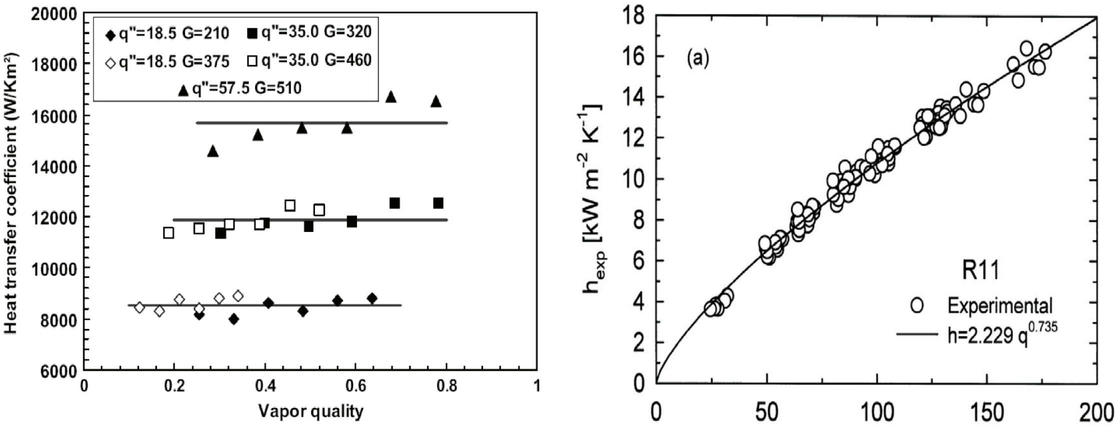

(c) Hamdar *et al.* (2010), HFC-152a, D= 1mm (d) Bao *et al.* (2000), R-11, D= 1.95mm

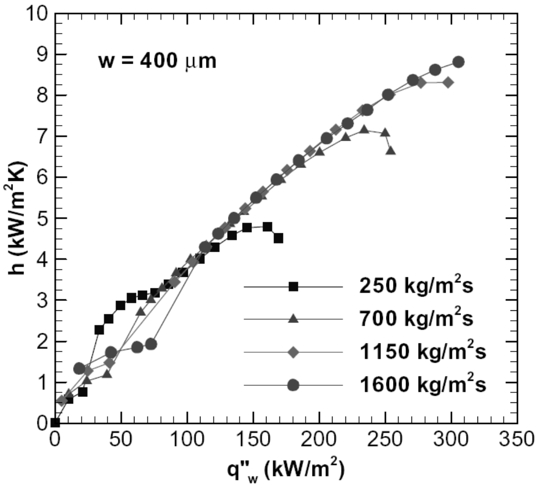

(e) Harirchian & Garimella (2008), FC-77, Multi-microchannels

Figure 2.16: Heat transfer coefficient results for different studies.

In the microchannel flow pattern observation of Fig 2.11, nucleate boiling is not seen, but could be linked to the isolated bubbles flow regime, described in Fig 2.8, which exists only at very low vapor qualities since the bubbles quickly become confined by the channel which then promotes thin film evaporation. Thus, extending this heat transfer mechanism to all vapor quality does not correspond to what is observed in two-phase microchannel flows. In fact, Mukherjee (2009) showed in his numerical simulations of elongated bubble growth in microchannels, that thin-film evaporation, which directly increases with heat flux, is the dominant heat transfer mechanism, confirming a point already made by Jacobi & Thome (2002). He also stressed that thin-film evaporation can create heat transfer-wise the apparence of nucleate boiling.

In a second group of studies, heat transfer coefficients were found to be a function of the vapor quality and the heat flux. Graphs by Lin *et al.* (2001) for R-141b in a 1mm tube and Agostini *et al.* (2008a) for R-236fa in a silicon 680μm × 223 μm multi-microchannel evaporator, reproduced in Fig 2.17, show the variation of heat transfer coefficient with respect to heat flux and vapor quality. As the heat flux increases, the mean heat transfer increases. First the local heat transfer tends to be higher towards the end of the channel, at high vapor qualities, but at higher heat flux, the shape of the curve changes. It flattens and later has a decreasing trend with vapor quality.

The two first trends are clearly seen in the results of Ong & Thome (2011b). His heat transfer coefficient experimental database is extensive, covering three fluids (R-134a, R-236fa and R-245fa) and three tubes (1.03mm, 2.20mm and 3.04mm) for mass fluxes varying from 200 to 1400 kg/m^{2}s, and wall heat fluxes from 5 to 180kW/m^2. Fig 2.18 presents an excerpt of his results. Using a reference case (Fig 2.18(a)), the change in trends due to variation in diameter (Fig 2.18(b)), mass flux (Fig 2.18(c)) and by changing the fluid (Fig 2.18(d)) are highlighted. For example Fig 2.18(c) displays a 50% increase in heat transfer at 39.8 kW/m^2 from inlet to outlet, whereas in Fig 2.18(d), heat transfer coefficient curves are almost flat and the graph ressembles the one of Lazarek & Black (1982). It is then possible that, by having a relatively narrow experimental range, the studies presented in Fig 2.16 could have observed only a fraction of the two-phase microchannel heat transfer coefficient trends.

More authors observed variation of heat tranfer coefficients with respect to vapor quality. Kew & Cornwell (1997) used R-141b in 500 mm long tubes with diameters 1.39–3.69mm. The heat transfer coefficients increasing and flattening trends are clear in Fig 2.19(a). Karyiannis *et al.* (2010) used five different tube diameters and also observed that the heat transfer trends changed with diameter. An example of their results is shown in Fig 2.13.

Yan & Lin (1998) tested R-134a in an array of 2.00mm tubes with a heated length of 100mm and found that the heat transfer mostly decreased with increasing vapor quality (Fig 2.19(b)). Heat transfer results by Lee & Mudawar (2005b), shown in Fig 2.19(c), also display this decreasing trend. They performed their experiments in a 25.3 mm long copper multi-microchannel evaporator with 231μm × 714μm channels and obtained the highest wall heat transfer coefficients values seen in this review (50'000W/m^{2}K).

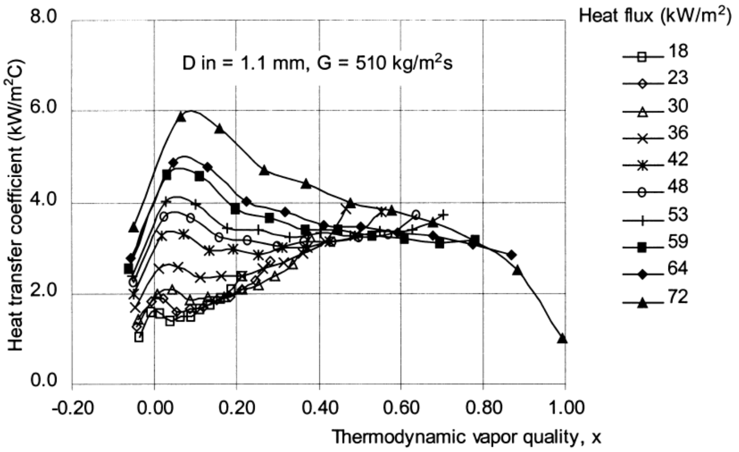

(a) Lin *et al.* (2001), R-141b, D= 1mm

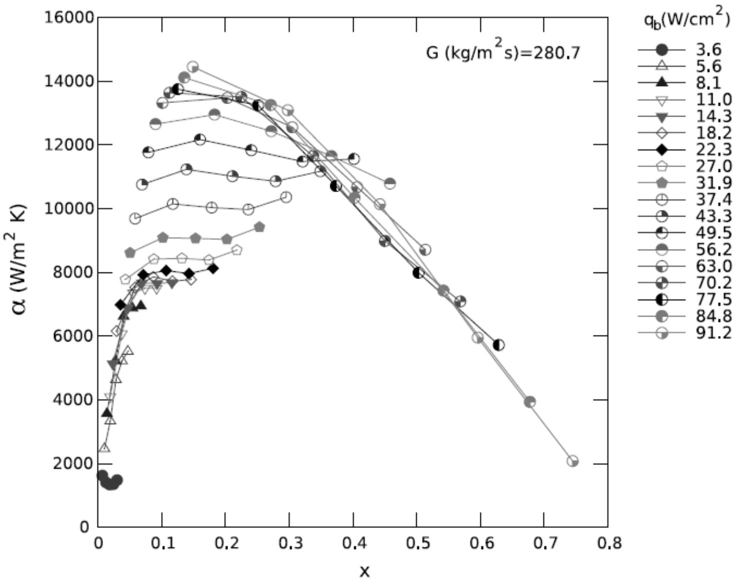

(b) Agostini *et al.* (2008a), R-236fa, Multi-microchannels

Figure 2.17: Heat transfer coefficient results for different studies.

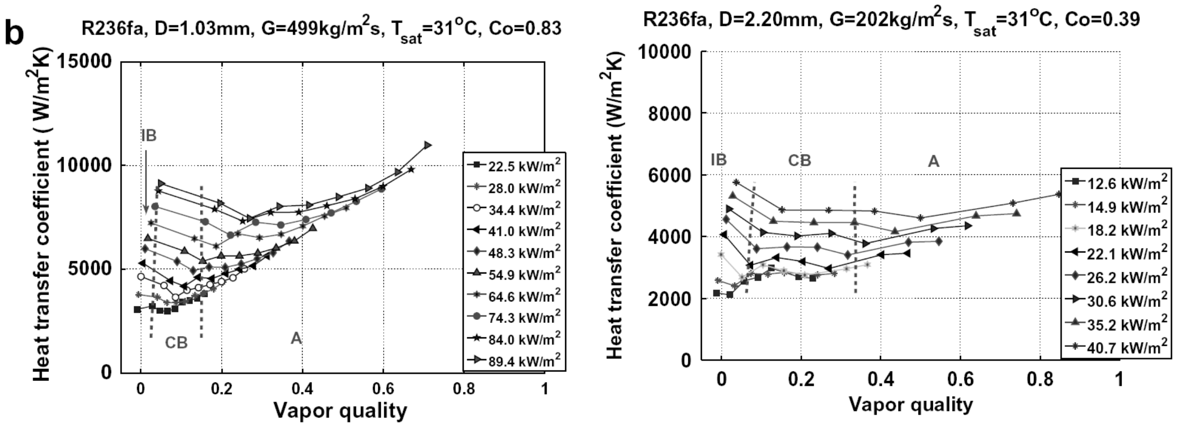

(a) R-236fa, D=1.03mm, G=499kg/m^{2}s, T$_{sat}$=31°C

(b) R-236fa, D=2.20mm, G=503kg/m^{2}s, T$_{sat}$=31°C

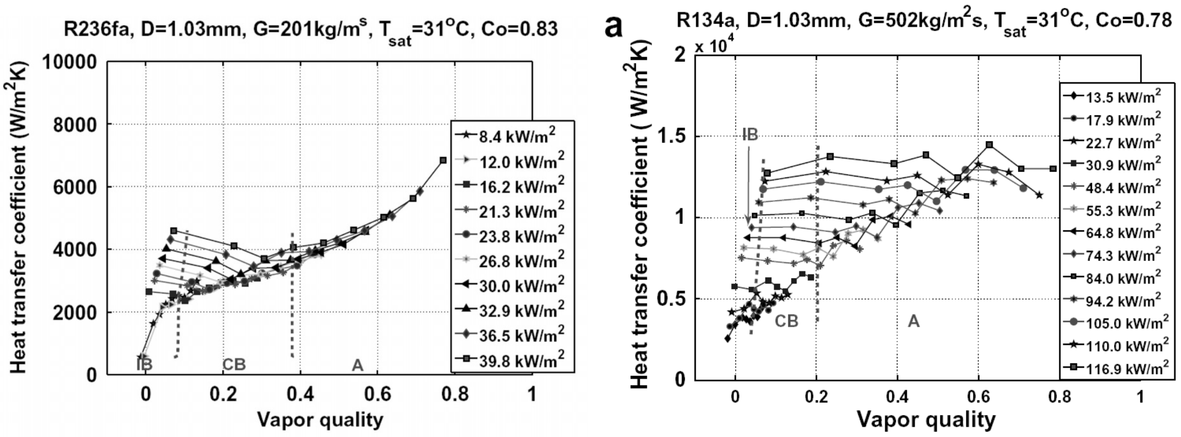

(c) R-236fa, D=1.03mm, G=201kg/m^{2}s, T$_{sat}$=31°C

(d) R-134a, D=1.03mm, G=499kg/m^{2}s, T$_{sat}$=31°C

Figure 2.18: Heat transfer coefficient results from Ong & Thome (2011b).

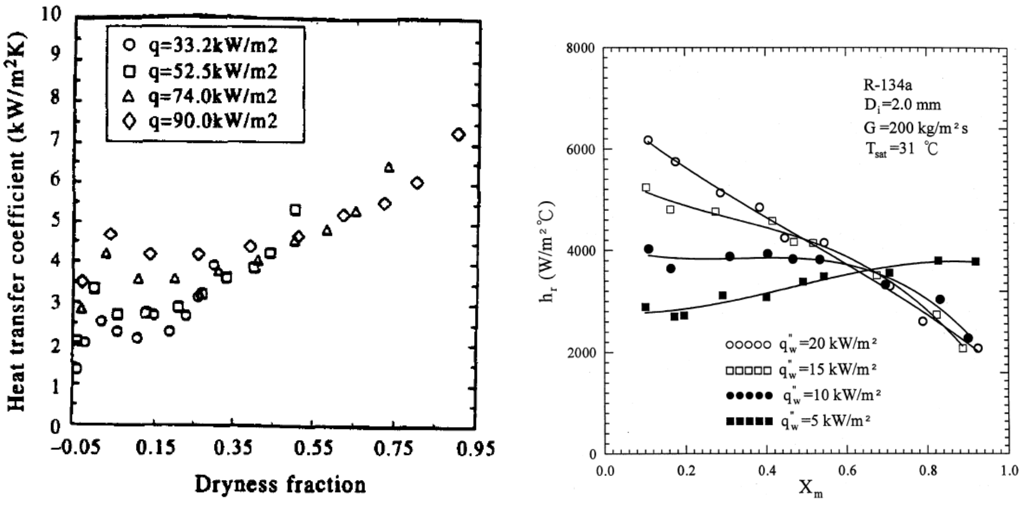

(a) Kew & Cornwell (1997), R-141b, D= 3.69mm, G= 212kg/m^{2}s

(b) Yan & Lin (1998), R-134a, D= 2.00mm

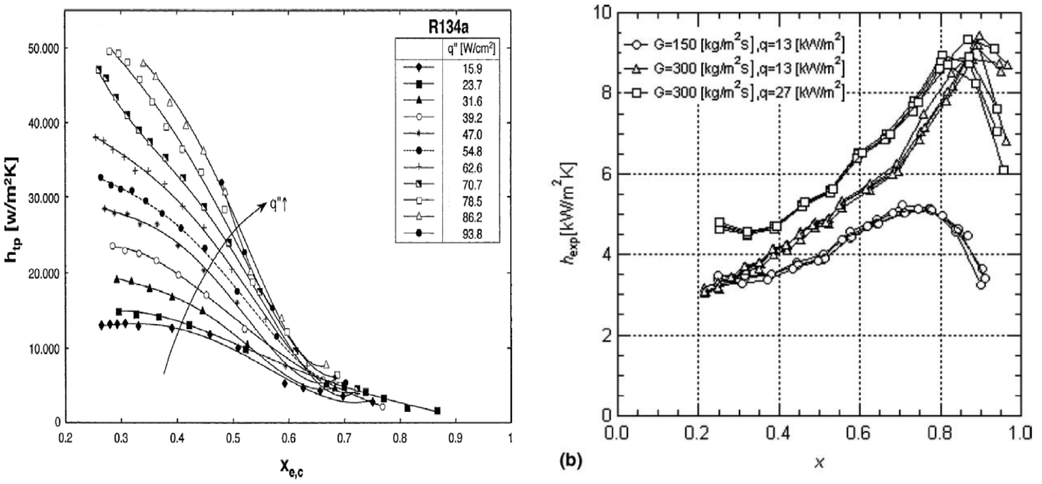

(c) Lee & Mudawar (2005b), R-134a, Multi-microchannels

(d) Saitoh *et al.* (2005), R-134a, D= 1.12mm

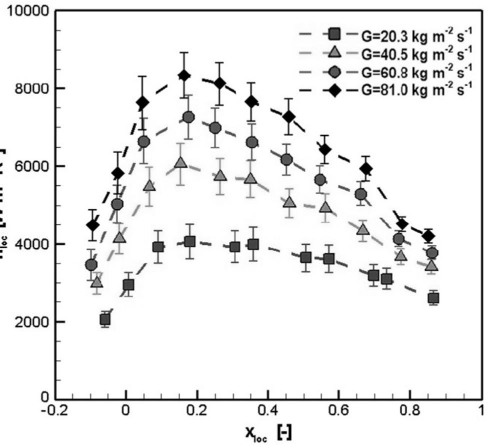

(e) Bertsch *et al.* (2008), R-134a, Multi-microchannels

Figure 2.19: Heat transfer coefficient results for different studies.

Saitoh *et al.* (2005) found that a higher mass flux had a positive influence on heat transfer. In Fig 2.19(d), heat transfer coefficients for q=13kW/m^2 increase faster for G=300kg/m^{2}s after a vapor quality of 0.3 than for G=150kg/m^{2}s. Finally, Bertsch *et al.* (2008) observed that going from 20.3kg/m^{2}s to 81.0kg/m^{2}s in a copper multi-microchannel composed of 17 channels, D$_h$=1089μm, 9.9 mm long, doubles the heat transfer, as shown in Fig 2.19(e).

Predicting experimental two-phase heat transfer coefficient in microchannels, which vary from 2000 to 50'000W/m^{2}K, and their trends is a complicated task. Nevertheless, several prediction methods have been proposed. The most interesting ones were written with the insight from several studies, fluids and geometries. Some studies adapted macroscale methods, such as Bertsch *et al.* (2009), who developed a new formulation of the Chen (1966) correlation. They assumed that heat transfer was the combined result of nucleate boiling and two-phase convective heat transfer.

$$\alpha_{FB} = \alpha_{NB} S + \alpha_{conv-tp} F \tag{2.23}$$

where S and F are the suppression and multiplication factors.

For the nucleate boiling part, α_{NB}, they used the correlation of Cooper (1984) and for the convective part, they used a single-phase laminar developing flow correlation, combining the liquid and vapor component by the vapor quality fraction (respectively (1-x) and x). Once their fit for S and F are included, equation 2.23 reads as follows:

$$\alpha_{FB} = \alpha_{NB}(1-x) + \alpha_{conv-tp}\left[1 + 80\left(x^2 - x^6\right)e^{-0.6Co}\right] \tag{2.24}$$

Kandlikar & Balasubramanian (2004) also used the idea of combining nucleate and convective boiling components. They extrapolated a previously developed macroscale correlation to microscale, effectively removing the effect of the Froude number $\left(Fr_l = \frac{m^2}{\rho_l^2 gD}\right)$ found in the macroscale correlation. In this method, the microscale two-phase heat transfer is set to the larger value between the nucleate and convective boiling component.

Moving away from nucleate boiling, Thome *et al.* (2004) developed a semi-mechanistic model, the three-zone model, to describe the evaporation of elongated bubbles in microchannels. Fig 2.20 shows the schematic of their model. Bubbles form at a given frequency (f) and are separated by liquid slugs. The bubbles grow and form a film with an initial thickness δ_0. The rate of vapor formation is tracked and if, as the bubble grows, the liquid film surrounding the bubble reaches a minimum value (δ_{min}), the evaporating film is assumed to dry out and form a vapor slug (dry zone) behind the elongated bubble.

The heat transfer coefficient in the liquid and vapor slug are evaluated using laminar and turbulent developing flow correlations. Heat transfer in the elongated bubble happens through thin film evaporation, which is modeled by one-dimensional conduction through the film. Finally, the cyclical variation of the heat transfer due to the different zones is used to obtain a time-averaged heat transfer coefficient. The method requires f, δ_0 and δ_{min} to be modeled. Agostini *et al.* (2008a) and Ong & Thome (2011b) showed that setting the minimum film thickness to the channel wall roughness improved the accuracy of the method. The mechanisms described in the three-zone method are intermittent and can be associated to the isolated bubbles and coaslescing bubbles flow regimes of Revellin *et al.* (2006) and Ong & Thome (2011a).

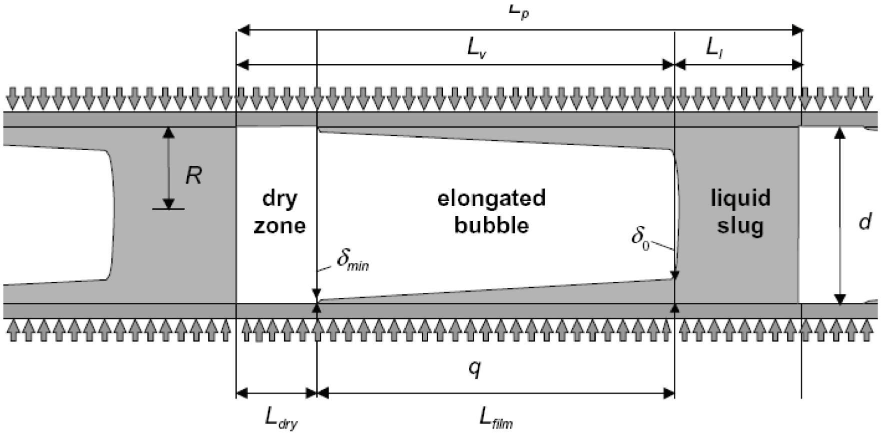

Figure 2.20: Schematic of three-zone model of Thome *et al.* (2004).

Although heat transfer in annular flow appears at first look to be similar in macro- and microscale, since the liquid film thickness in both cases are much smaller than the channel diameter, they nevertheless differ in some aspects. In microchannels, the liquid film is thinner and can thus be laminar, which affects the liquid-vapor interface interactions. Moreover, since the surface tension is more important in microchannels, a non-circular channel will proportionally concentrate more liquid in its corners, thin the film and increase heat transfer, as it was shown by Nebuloni & Thome (2010) through numerical simulation of condensing laminar annular flow.

The annular flow heat transfer prediction method of Cioncolini & Thome (2011) covers macro and microscales. It is derived from a mechanistic analysis of the annular flow and used experimental results from 1.03mm to 14.4mm test sections to optimize the method's accuracy. It provides information about the film velocity and temperature profiles, the average film thickness, the void fraction, the entrainment and the heat transfer coefficient. With an intermittent to annular flow transition criteria, it could be used in combination with the three-zone model to create a flow pattern-based method.

Another approach almost developing a flow pattern-based prediction method, is proposed by Lee & Mudawar (2005b). They proposed an empirical heat transfer method for each trend, based on the vapor quality. For vapor qualities from 0 to 0.05, their expression for heat transfer is.

$$\alpha_{tp} = 3.856\chi^{0.267}\alpha_{sp,l} \tag{2.25}$$

where χ^2 is the ratio the liquid only and vapor only pressure drop. For x=0.05 to 0.55:

$$\alpha_{tp} = 436.48Bl^{0.522}We_{lo}^{0.351}\chi^{0.665}\alpha_{sp,l} \tag{2.26}$$

Finally, for x=0.55 to 1:

$$\alpha_{tp} = max\left[\left(108.6\chi^{1.665}\alpha_{sp,v}\right), \alpha_{sp,v}\right] \tag{2.27}$$

2.8 Critical heat flux in microchannel

The critical heat flux (CHF) in microchannels represents the upper boundary beyond which the heat transfer coefficients drop rapidly, as there is no liquid film left on the channel wall to evaporate. In turn, the wall temperatures increase to a level that can damage what was being cooled. For two-phase experiments, it represents the upper heat flux limit at which experiments can be performed. Flow pattern-wise, it can be associated to the microchannel dry-out zone as done by Revellin & Thome (2007b).

Since staying under the critical heat flux is a thermal safety criterion, defining it has received a lot of attention. For example, in single tube microchannels, Ong & Thome (2011b) and Wojtan *et al.* (2006) made together 215 critical heat flux measurements with R-134a, R-236fa and R-245fa. Basu *et al.* (2011) made 113 measurements with R-134a. Park & Thome (2010) made 323 measurements in copper multi-microchannels. Using the same multi-microchannel in slit flow configuration, Mauro *et al.* (2010) made 78 measurements. Also 25 measurements were made by Agostini *et al.* (2008b) with R-236fa and 30 with R-113 by Kosar & Peles (2007) in silicon multi-microchannels.

There are probably as many prediction methods for critical heat flux in microchannels as there are experimental studies on the subject. Overall, two empirical prediction methods stand out as the most accurate. The first is given Katto & Ohno (1984) which combines five different correlations, differentiated by the fluid's density ratio. The second one is that of Ong & Thome (2011b) who modified Wojtan *et al.* (2006) method, itself a modified and simplified version of Katto & Ohno (1984) method. Note that these methods predict wall critical heat flux and for multi-microchannels, this value needs to be transformed onto the base ("footprint") critical heat flux, using the area ratio and the fin efficiency.

A mechanistic CHF model was proposed by Revellin & Thome (2008). The model starts from the observation that dry-out occurs when the liquid film in the annular flow regime dryouts at the trough of the waves in the film. On the other hand, if evaporation is the only factor influencing the film thickness, dry-out will occur at a vapor quality of 1. Since critical heat flux has been seen to occur at much lower vapor qualities, the shear force imposed by vapor core on the liquid film must play a role on the dry-out by creating interfacial waves.

A schematic of both phenomena is shown in Fig 2.21. If the wave amplitude exceeds the mean liquid film thickness, the channel will be directly in contact with vapor. By using conservation of mass and energy, the mean liquid thickness along the channel can be determined. It is then compared to the size of the interfacial waves, calculated based on the one dimensional Kelvin-Helmholtz critical wavelength. If the wave size exceeds the local film thickness, critical heat flux is said to occur.

2.9 Non-uniform and transient heat flux cooling

Many devices, such as CPUs or IGBTs, generate a non-uniform heat flux, with hot-spots several times greater than their background heat flux. Actual hot-spot signatures for a stacked UltraSPRAC T1 (Niagara) chip are reproduced in Fig 2.22. The hot-spot to

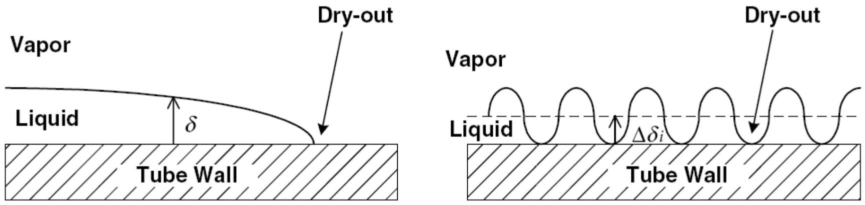

Figure 2.21: Schematic of dry-out of Revellin & Thome (2008).

background heat flux ratios presented by Hamann *et al.* (2007) were around 10 to 1 and the hot-spot covered 5 to 25% of the chip's area. Precise information regarding power maps is usually not disclosed by manufacturers, but the IBM Research Center in Zurich confirmed for this work that these values were typically found in micro-processors.

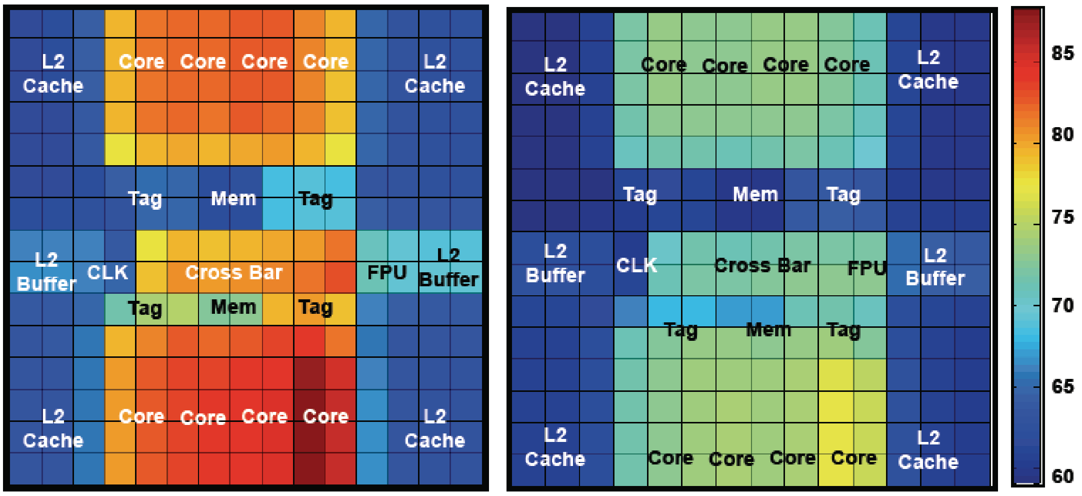

(a) Bottom Die (b) Top Die

Figure 2.22: Thermal maps of two UltraSPARC T1 (Niagara) chips stacked one on the top of the other (Case A in Section VI-E). From A. *et al.* (2012)

Under non-uniform heat flux conditions, the cooling method will influence both the junction temperature and the size of the region affected by the hot-spot, setting respectively the maximum hot-spot heat flux and the maximum number of hot-spots possible on the unit. These two aspects are particularly important to microelectronic design, which aims to pack more power on an ever smaller surface. Two-phase flow cooling has been often seen as an excellent candidate for non-uniform heat flux cooling, because the heat transfer coefficients are a function of the heat flux. Moreover, its very high heat transfer coefficients should help contain the spread of the hot-spot to surrounding areas.

Experimental studies on microchannel flow boiling in non-uniform heat flux situations have been performed with water as the cooling fluid. Koo *et al.* (2002) presented results for several silicon micro-evaporators, but did not reduce their data and present heat transfer coefficient results. As it was previously noted, due to the large difference between the vapor and liquid densities, flow boiling of water in microchannels is difficult to control.

The relation between those water-induced instabilities and non-uniform heat flux were the subject of a study by Bogojevic *et al.* (2011).

On the modeling side, Revellin *et al.* (2008) extended their critical heat flux prediction method for uniform heat flux to non-uniform heat flux situations. The hot-spot's effect is included in the local energy balance along the channel. In this model, both the hot-spot and the background heat flux can generate the critical heat flux. For example, in Fig 2.23(a), the wave height meets the film thickness at 20mm, under q= 386kW/m^2, and critical heat flux is assumed to happen there, while in Fig 2.23(b), this point is first reached at the hot-spot position.

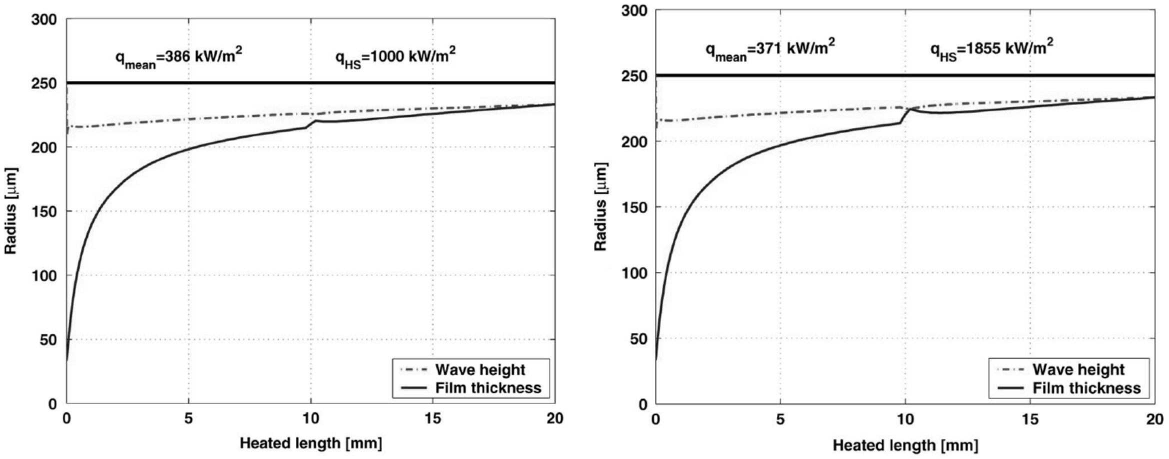

(a) Dry-out at outlet (b) Dry-out at hot-spot and outlet position

Figure 2.23: Liquid film thickness and wave heights for R-134a, G=500kg/m^{2}s, T_{sat}=30°C. Hot-spot at 10mm. From Revellin *et al.* (2008).

One last important aspect remains to be addressed on in the heat load variation in microelectronics. In CPUs, the heat generation follows the computational duty. Since CPU clock speeds are on the order of mega- and gigahertz, instantaneous local heat flux variations are very fast. However, from a cooling requirement point of view, the time scale is longer. The CPU usage history of a normal computer provides an idea for the cooling requirements. A typical example is shown in Fig 2.24. The CPU usage changes suddenly, but is otherwise mostly stable. Hamann *et al.* (2007) also measured the temperature signature evolution of a laptop microprocessor during bootup (Fig 2.25). Temperature maps follow the CPU power jumps. Thus as a primary requirement, a two-phase cooling system for microelectronics must be able to handle a step increase in heat flux.

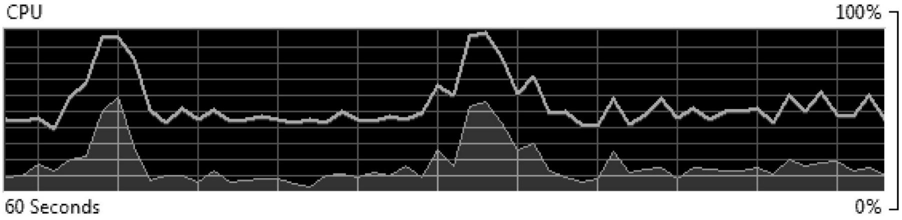

Figure 2.24: CPU usage history from a laptop.

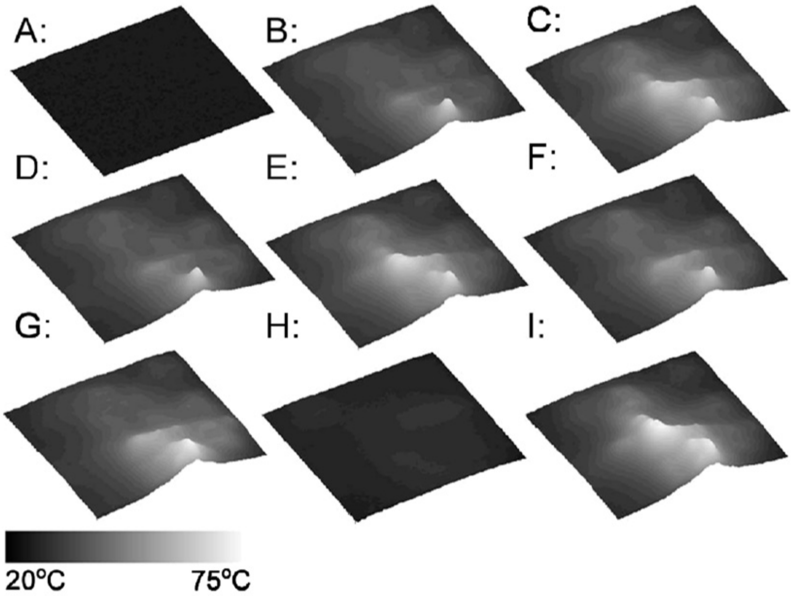

Figure 2.25: Laptop microprocessor temperature evolution during bootup. Time-step between each image 10s. From Hamann *et al.* (2007).

Chapter 3

Experimental facility and data reduction

3.1 Refrigerant flow loop

The flow loop used for the experiments is shown in Fig 3.1. It was previously used by Park & Thome (2010) and was modified by adding instrumentation and expanding the data acquisition capabilities for the present tests.

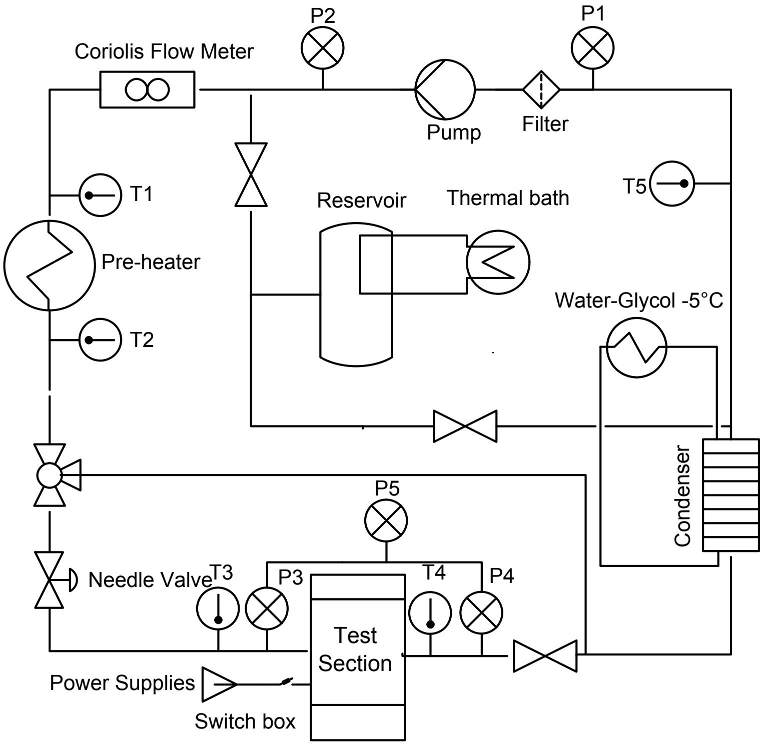
P2
P1
Coriolis Flow Meter
Pump
Filter
T1
T5
Reservoir
Thermal bath
Pre-heater
Water-Glycol -5°C
T2
Condenser
P5
Needle Valve
T3
P3
T4
P4
Test Section
Power Supplies
Switch box

Figure 3.1: Schematic of the flow loop.

The flow is driven by an oil-free magnetic-driven gear pump and its mass flow rate is measured using a Coriolis mass flow meter. The pre-heater is used to bring the fluid temperature close to the experimental saturation point. The fluid temperature is never increased in the pre-heater by more than 20°C, a limit beyond which sub-cooled boiling was found to happen. It was also important to maintain the pressure in the pre-heater above the saturation pressure, since the target level of subcooling was typically lower than 1°C. For this purpose, a needle valve was placed between the pre-heater and test section. It was set to decrease the pressure enough to reach the desired conditions at the inlet of the test section.

Sight glasses were placed before and after the test section to visualize if the flow was single or two-phase. After passing through the test section, the flow is condensed in a plate heat exchanger. The cold fluid is a water-glycol solution normally at 5°C. The system pressure is set by keeping the refrigerant in the reservoir in a two-phase condition. The saturation point is adjusted through the temperature of the reservoir, connected to a computer controlled thermal bath. The fluid is always single-phase from the exit of the condenser to the inlet of the test section. The system is loaded with about 5kg of refrigerant, most of which remained in the reservoir. Before filling the loop, it is carefully vacuumed to remove any trace of air or moisture in the test loop.

The test loop is instrumented with thermocouples, placed across the pre-heater and after the condenser. Pressure measurements are made in the reservoir and across the pump. These measurements are not directly used to study the multi-microchannel evaporator, but are needed to monitor the flow loop's operation and to evaluate the heat losses.

3.2 Test sections

Two different test sections were used for the experiments. In one, the evaporator was made of silicon, in the other copper. Fig 3.2 shows each test section assembled on the test stand. The main visible differences are the pressure ports placed on top of the copper test section, which were used to measure pressure drops directly along the channels.

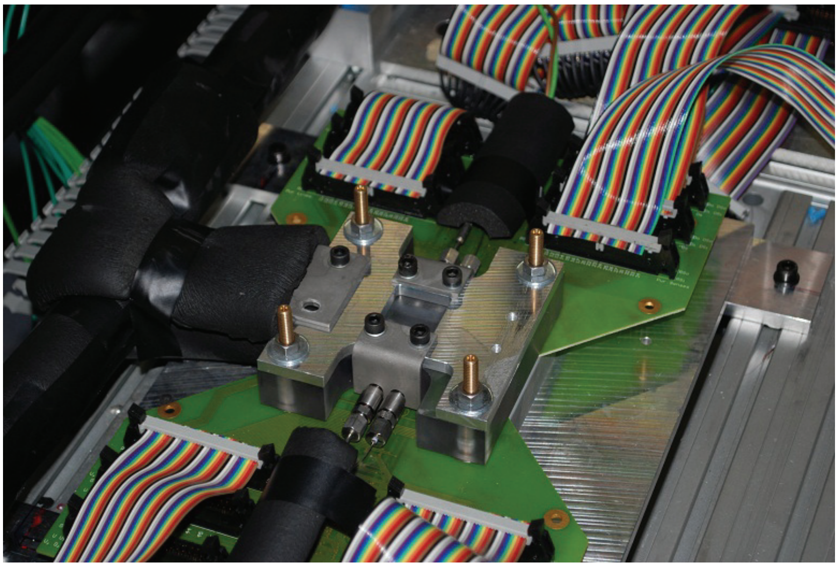

(a) Silicon test section

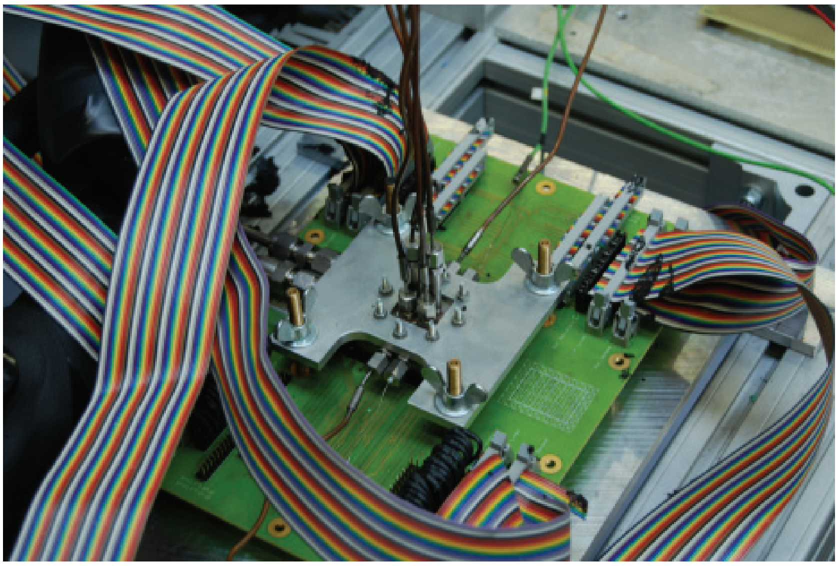

(b) Copper test section

Figure 3.2: Assembled test sections without insulation.

The general design and operation of both test sections was similar. Cut views of each test section along the channels, shown in Fig 3.3, are useful to visualize how the thermal packages were built and what the flow paths were. Fig 3.4 gives schematically the position of the relevant test section dimensions, which are later needed for calculations. Their values are listed in Table 3.1.

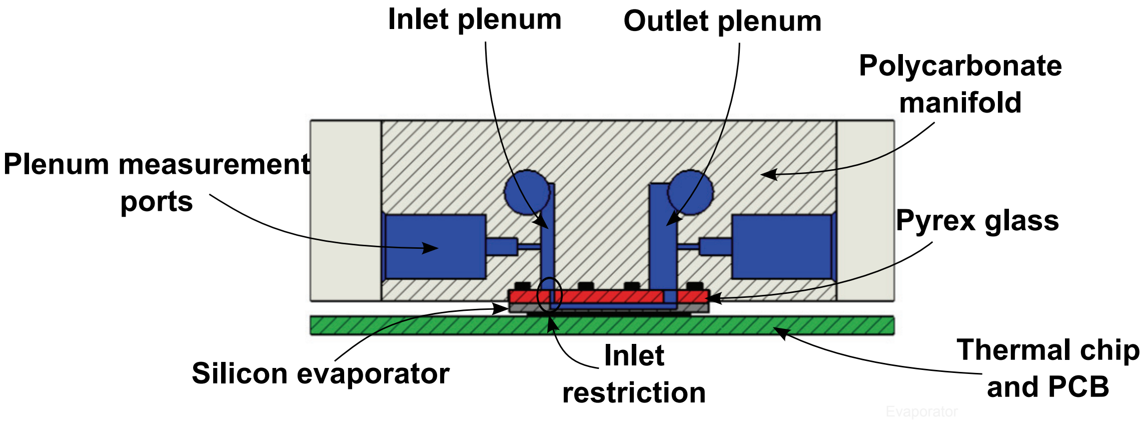
Inlet plenum
Outlet plenum
Polycarbonate manifold
Plenum measurement ports
Pyrex glass
Thermal chip and PCB
Silicon evaporator
Inlet restriction
Evaporator

(a) Silicon test section

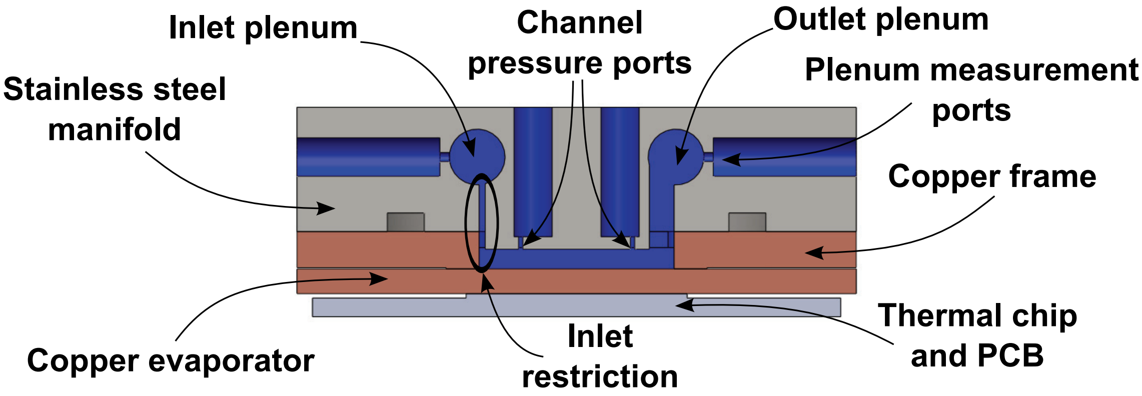
Inlet plenum
Channel pressure ports
Outlet plenum
Plenum measurement ports
Stainless steel manifold
Copper frame
Thermal chip and PCB
Copper evaporator
Inlet restriction

(b) Copper test section

Figure 3.3: Schematic of the test sections. Cut views along the channel axis. Blue: Sections filled with refrigerant.

The test sections' description will be divided into four sub-groups:

- The thermal chip and the printed circuit board (PCB)
- The thermal interface material (TIM)
- The evaporator
- The manifold

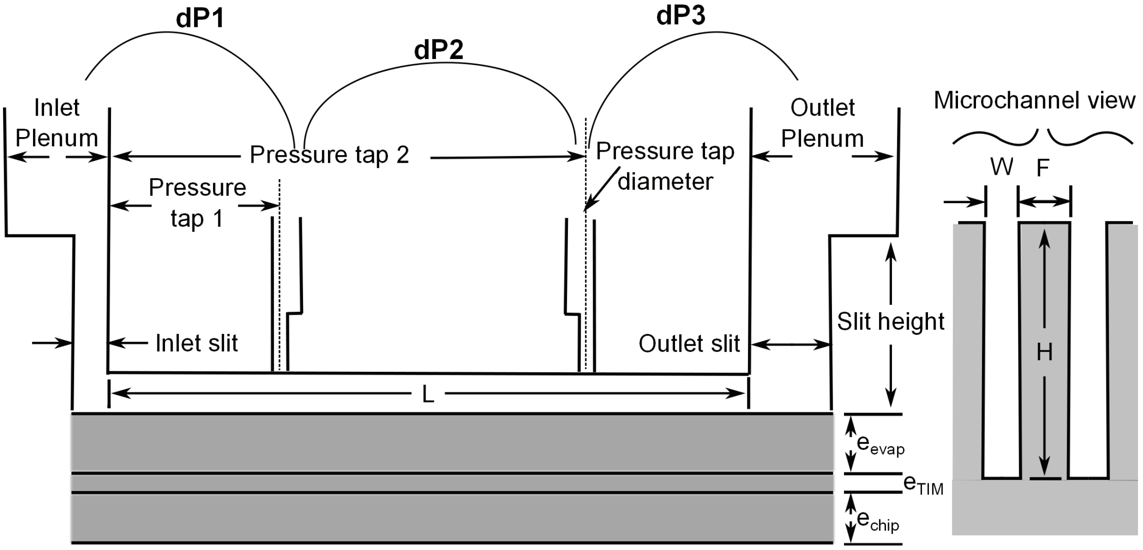

Figure 3.4: Position of test section dimensions.

3.2.1 Thermal chip and the printed circuit board

A thermal chip was used to mimic the behavior of a CPU. Theses chips were manufactured by Delphi Corporation under the name PST1-02/5PU Thermal Test Die. Heaters were made on the back of a silicon wafer by locally doping silicon between two bus bars. Two temperature sensors were positioned at the center of each heater and solder balls were deposited on connection pads. Before shipping, the wafer's thickness was brought to 350μm.

As shown in Fig 3.5, each wafer contain many heaters. The wafers were diced into arrays of 7×9 heaters, of which the center 5×7 heaters were used for the experiments. For clarity, the following terminology will be used throughout the thesis:

- Heater: individual heater with its own thermal sensor.
- Chip or array heater: 5×7 individual heaters forming the unit generating the whole heat flux.
- Test section: Thermal package including the PCB, chip, TIM, evaporator and manifold.

The array heater was mounted in this study on a printed circuit board (PCB) using a flip-chip process. This process was developed in collaboration with the IBM Zurich Research Center and involves a lot of technical know-how, such that the following description is a simplified one. The PCB and the chip were placed in parallel and heated over the melting point of the solder balls. At this point, both surfaces were brought together, until the solder balls on the chip also wetted the corresponding pads on the PCB. The package was then cooled and the bond solidified. An underfill epoxy was flowed between the chip and the PCB in order to strengthen the bond.

For the silicon test section, the chip was directly mounted on a large PCB (300mm×200mm) used to make the external electrical connections. During the mounting process, a total of

Table 3.1: Test section dimensions.

Dimension	Silicon	Copper	Uncertainty
B: Evaporator width(mm)	17.78	17.78	±0.1
L_{ch}: Channel length(mm)	12.7	13.2	±0.1
l: Heater size(mm)	2.54	2.54	±0.02
H: Channel height(μm)	560	1560	±5
W: Channel width(μm)	85	163	±5
F: Fin thickness(μm)	47	178	±5
N: Number of channels	135	52	–
D_h: Hydraulic diameter(μm)	148	246	±10
e_{chip}: Thermal chip thickness(μm)	350	350	±5
e_{TIM}: TIM thickness(μm)	50	40	±15
e_{evap}: Evaporator base thickness(μm)	440	1800	±10
Wall roughness (nm)	90	460	±10/50
Inlet slit(mm)	0.5	0.5	±0.1
Outlet slit(mm)	1.5	2.0	±0.1
Slit height (mm)	1.66	6.67	±0.05
Inlet plenum(mm)	1.5	4.5	±0.05
Outlet plenum(mm)	3	4.5	±0.05
Pressure tap diameter(mm)	–	0.5	±0.05
L_{PTap1}: Pressure tap position 1(mm)	–	2.73	±0.01
L_{PTap2}: Pressure tap position 2(mm)	–	11.72	±0.01

420 connections needed to be made simultaneously. While cooling, the PCB, which contained copper, did not shrink uniformly nor at the same rate as the chip. This weakened the bonds and an operational base temperature limit of 65°C was respected to decrease thermal stresses. The temperature sensors were particularly at risk of failure, due to the small wire size used for their connections.

The package was improved for the copper test section by using an intermediate PCB. The chip was mounted on a PCB of 42.5mm×42.5mm, with a low coefficient of thermal expansion, which was designed to have uniform shrinking and with redundancies for the power and temperature lines. This assembly was then pressed on a cLGA (Land grid array socket) produced by Amphenol InterCon Systems. In this socket, 1052 metallic springs were found and once under sufficient pressure, physically connected the intermediate and the larger PCB(250mm×180mm).

The thermal chip itself was composed of 35 independent heaters arranged in a 5×7 array. Each heater was 2.54mm×2.54mm in size, and its electricalresistance was of about 25Ω. It was surrounded by a row of unactive heaters. The heater notation is given in Fig 3.6.

A switch box, connecting the PCB to the power supplies, was used to control the power to each heater independently. The individual electrical circuit allowed a current of up to 1.1A, thus the maximum design power per heater was 30W, so the total per chip was 1050W (465W/cm^2). For the experiments, the central temperature sensor of each heater was used. It was made of a series of temperature sensitive diodes, which once excited with a sufficient voltage, worked similarly to a 4-wire RTD.

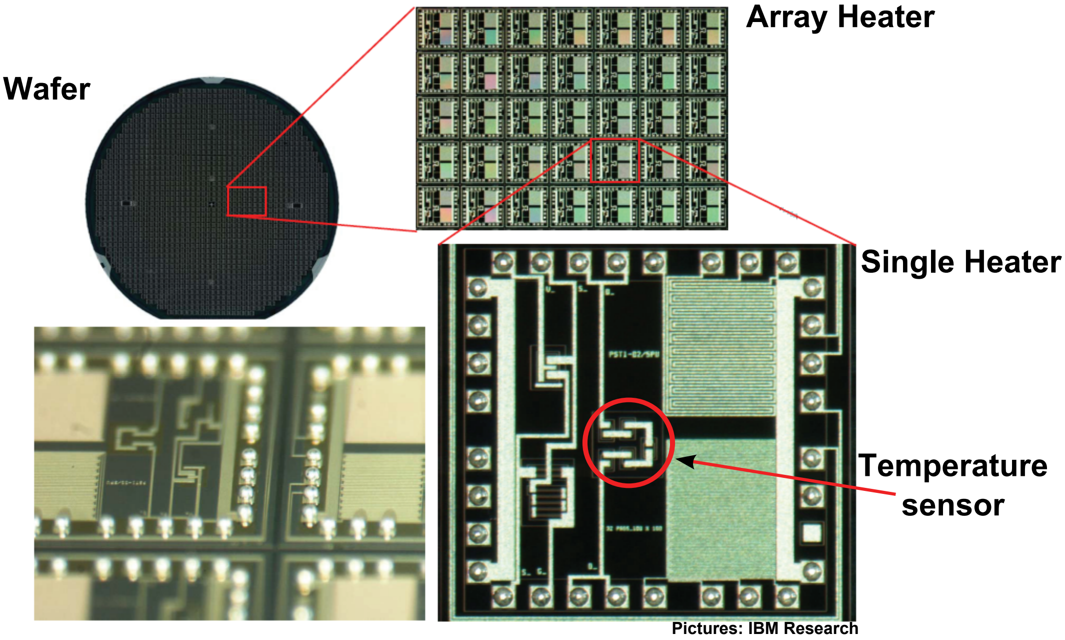
Wafer
Array Heater
Single Heater
Temperature sensor
Pictures: IBM Research

Figure 3.5: Heater subdividing process.

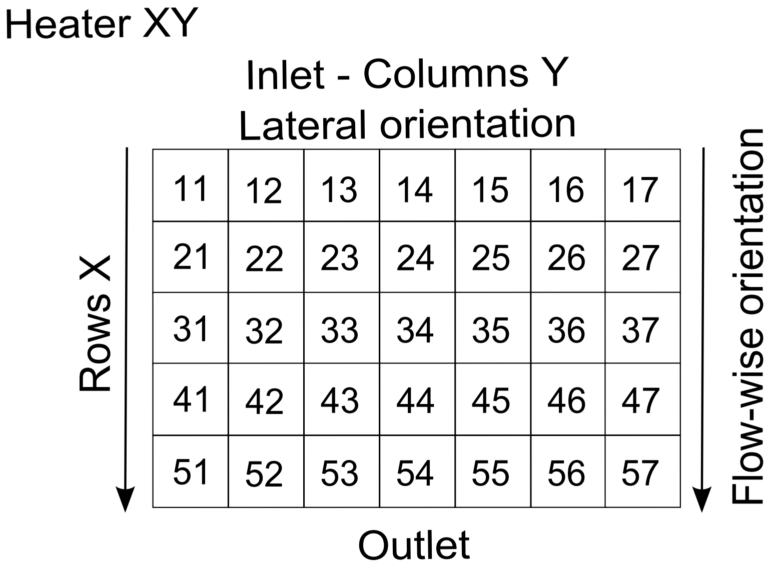
Heater XY
Inlet - Columns Y
Lateral orientation
Rows X
Flow-wise orientation
Outlet

11	12	13	14	15	16	17
21	22	23	24	25	26	27
31	32	33	34	35	36	37
41	42	43	44	45	46	47
51	52	53	54	55	56	57

Figure 3.6: Heater notation.

3.2.2 Thermal interface material

Between the thermal chip and the evaporator, a thermal interface material (TIM) was used. The TIM was a high thermal conductivity liquid metal alloy made of gallium, indium and tin (62.5Ga-21.5In-16.0Sn) and having a melting temperature of 10.7°C. The listed bulk thermal conductivity is 35 W/mK, but in order to include the influence of temperature and thickness across the TIM, tests were performed by André (2009) within the LTCM laboratory to determine the effective thermal conductivity across the thin layer, including the contact resistances, as shown in Fig 3.7(a).

A dimensional correlation was developed for determining the thermal conductance of the layer for the temperature range between 20 and 80°C, and is given as

$$\alpha = \frac{\lambda}{e_{TIM}} = 3.735 \times 10^6 \left(T \left(\frac{e_{TIM}}{100\mu m} \right)^2 \right)^{-0.9634} + 29080 \tag{3.1}$$

where T is the temperature in °C, e_{TIM} the thermal interface thickness in μm and the thermal conductance, α is in W/m^{2}K. The performance of the curve fit is shown in Fig 3.7(b), predicting 90% of the data to within 5%, finding values lower than that quoted by the manufacturer.

On the test section, the thickness of the thermal interface was indirectly determined by measuring the thickness of the assembled test section and substracting the evaporator, manifold and chip assembly thickness. For the silicon test section, the TIM layer was 50μm thick and for the copper test section, 40μm, resulting in a thermal conductivity at 40°C of respectively 22W/mK and 28W/mK, an order of magnitude higher than for commonly used polymer-based TIMs. The combination of the high thermal conductivity and the thin interface minimized the temperature drop across the interface, making the determination of heat transfer characteristics more accurate.

Hardy (1985) measured a surface tension of 700mN/m at 20°C for liquid gallium; the Ga–In–Sn alloy shares this high surface tension and is non-wetting. The chip surface was carefully covered by a thin layer of liquid metal (Fig 3.8(a)) and the evaporator was slowly placed on it. In this process, part of the liquid metal flowed out and partial dewetting of the surface was unavoidable. However, it was mostly contained to the unactive heaters on the chip, as it can be seen on Fig 3.8(b) taken when experiments with the copper test section were complete. Unfortunately, for the copper test section, dewetting extended to heater 15 and its results were not usable.

Liquid metal is corrosive and its reactivity with copper was uncertain, whereas it is chemically inert with silicon. After eight months of testing, the surface of the copper evaporator in contact with the liquid metal was inspected. A superficial footprint mark was visible, which disappeared after 5μm of the evaporator were grinded off.

3.2.3 Evaporators

The silicon and copper evaporators differed in many ways. The silicon evaporator's top view and its cross-section are shown in Fig 3.9. It was etched into the 1mm thick silicon

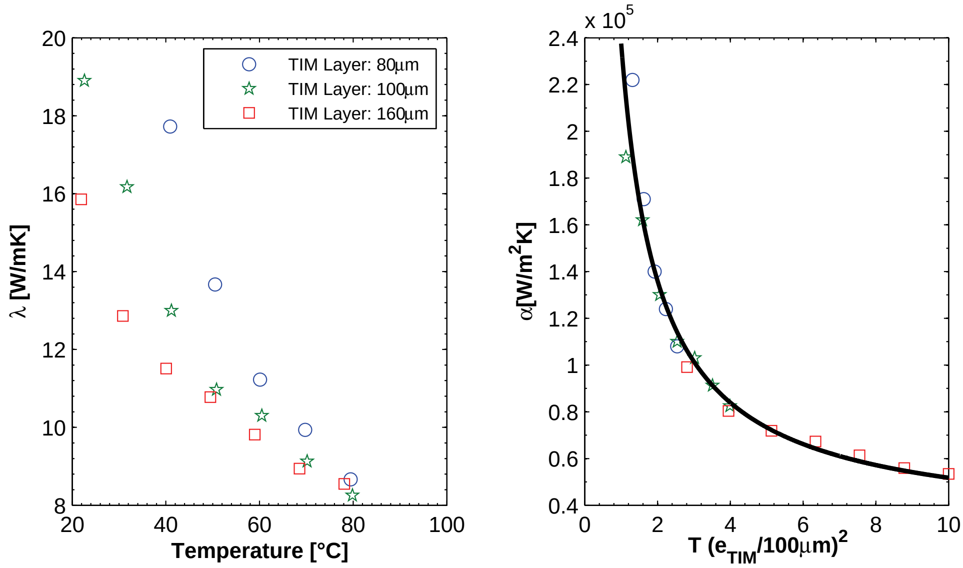

(a) λ for different thicknesses. (b) TIM layer heat transfer coefficient.

Figure 3.7: TIM thermal characteristics.

wafer using a DRIE process, described in Laermer & Urban (2003). It was then anodically bonded on top of a 1.1mm thick Pyrex glass, forming a hermetical bond. The evaporator was composed of 135 channels, each 85μm wide and 560μm high, with fins 47μm thick. The hydraulic diameter, measured by image processing, was 148μm. The same value can be computed from $D_h = \frac{2WH}{W+H}$. The total channel length was 14.7mm. At the channel extremities, two openings were made in the glass across the evaporator to create an inlet (0.5mm) and an outlet (1.5mm). The effective channel length, L$_{ch}$, was then 12.7mm. The inlet opening formed, with a 90° angle change of flow direction, a restriction at the inlet of each microchannel, in essence a micro-orifice.

Wolverine Tube Inc. manufactured the copper evaporator using a micro-deformation technology. The copper evaporator's top view and its cross-section are shown in Fig 3.10. The fins were first raised from a copper block. A copper surface was then milled around the fins to the desired thickness. Finally, the channels' extremities were closed by brazing a copper frame surrounding the fins on the copper surface. The frame was made higher than the fins for sealing and adjustment purposes.

The copper evaporator was composed of 52 channels, each 163μm wide and 1560μm high, with fins of 178μm thick. The hydraulic diameter was measured by image processing the channel cut view. Since the channels were not perfectly rectangular, the area to perimeter ratio was smaller and the hydraulic diameter was measured as 246μm. The value for $D_h = \frac{2WH}{W+H}$ was 294μm. The total channel length was 15.7mm and as in the silicon evaporator, restrictions were formed at the channel extremities. The inlet restriction was 0.5mm wide, the outlet restriction 2.0mm such that the effective channel length was 13.2mm. The copper channels were thus 0.5mm longer than the thermal chip (12.7mm). This extra length was positioned at the channel outlet and was accounted for in post-processing.

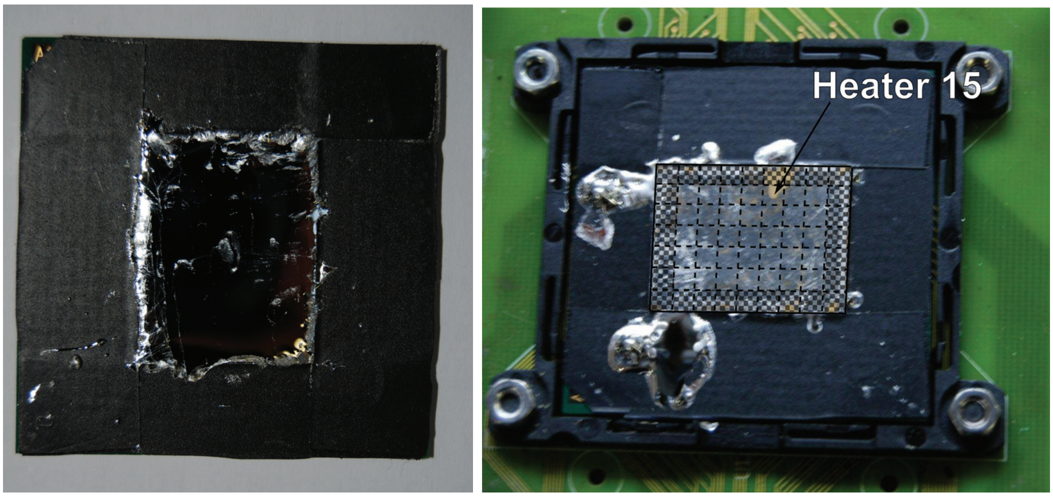

(a) Before (b) After

Figure 3.8: Thermal interface spreading on copper test section.

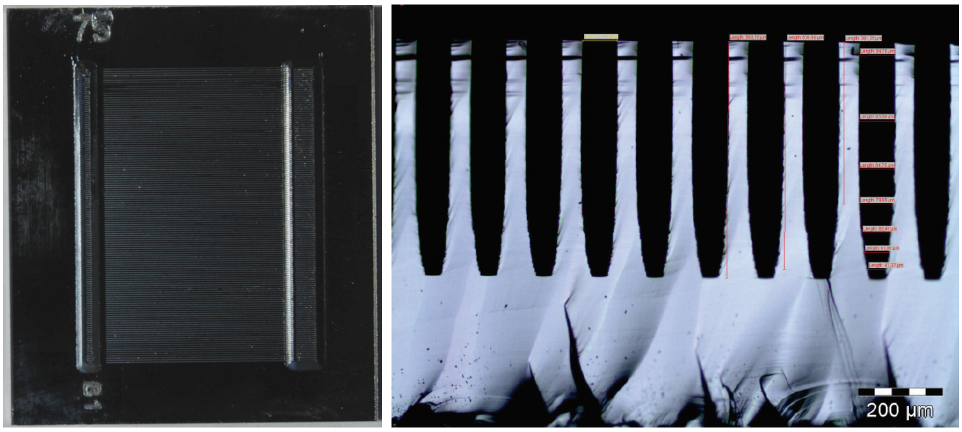

(a) Top view (b) Cut view of the evaporator

Figure 3.9: Silicon evaporator.

3.2.4 Manifolds

The manifolds were used to seal the test sections, to make pressure and temperature measurements and to connect the evaporator to the flow loop. The manifold in the silicon test section was made of polycarbonate. The inlet plenum was 1.5mm wide and the outlet one, 3mm. At plenum mid-height, two openings were made in each plenum. In one, a thermocouple was inserted. The other was used as a pressure tap. Each tap was connected to its own absolute pressure transducer and to a common inlet/outlet differential pressure transducer. Two O-rings were placed around the inlet and the outlet to seal them.

The copper test section's manifold was machined out of stainless steel. It was in contact with the evaporator on two planes. At the center, the manifold was pressed on the evaporator to close the top of the channels. On the edges, an O-ring sealed the test section. The inlet and outlet slits, respectively 0.5mm and 2mm wide, were machined

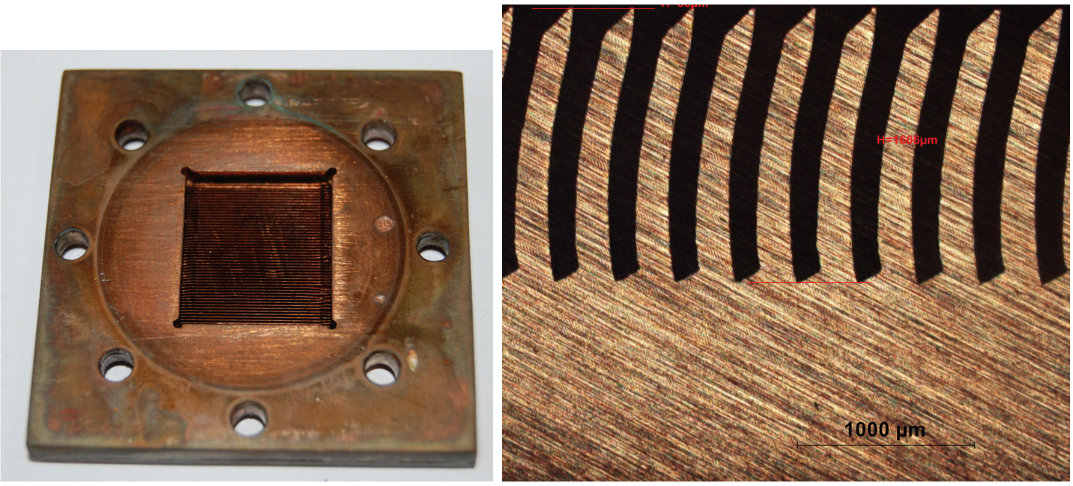

(a) Top view (b) Cut view of the evaporator

Figure 3.10: Copper evaporator.

in the manifold up to the plenums, both 4.5mm in diameter. As in the silicon test section, two openings were made in each plenum at mid-height for temperature and pressure measurements. In addition, two 0.5mm pressure tap holes were made on top of the evaporator at 2.73mm and 11.72mm from the inlet edge. They were positioned over column 2 and 6, 130μm away from their centerline (3.70mm and 13.82mm away for column 1 edge) and recorded pressure over two channels at most.

3.3 Test fluid

Four refrigerants were used for the tests, R-134a, R-1234ze(E), R-236fa and R-245fa. Table 3.2 compares some of their properties. The main differences are found in the liquid viscosity and liquid to vapor density ratio. In both cases, values for R-245fa and R-236fa are higher than those of R-134a and R-1234ze(E). R-1234ze(E) is produced by Honeywell International as a substitute for R-134a and was donated to the LTCM. It has a low greenhouse warming potential compared to the others and its properties are similar to R-134a.

After charging the refrigerant in the flow loop, pressures and temperatures were closely monitored to ensure that they corresponded to the listed values for saturation point, an indicator that the loop is free of contaminants. This was particularly important in the case of R-245fa, because its bottles contained nitrogen to maintain the pressure above the atmospheric pressure at low temperatures.

The silicon test section was limited to 4 bar and was only suitable for experiments with R-236fa and R-245fa. One inlet saturation temperature was tested in this test section, 30.5°C. It corresponded to an average saturation pressures of 3.26 bar for R-236fa and 1.81 bar for R-245fa. Higher pressures were achievable in the copper test section, which allowed tests at higher saturation temperatures, so that flow boiling at 30°C and 50°C was investigated with R-134a, R-1234ze(E) and R-245fa. In both test sections, the needle

Table 3.2: Refrigerant saturation properties at 30°C and 50°C.

	R-134a	R-1234ze(E)	R-236fa	R-245fa
30°C				
Pressure (bar)	7.70	5.78	3.21	1.78
Liquid density (kg/m^3)	1187.5	1146.3	1342.8	1324.9
Vapor density (kg/m^3)	37.54	30.56	21.57	10.17
Liquid to vapor density ratio	31.6	37.5	62.3	130.3
Latent heat (kJ/kg)	173.10	162.90	142.95	187.33
Liquid viscosity (μPas)	183	188	268	382
Vapor viscosity (μPas)	13	12.5	11	10.5
Liquid ther. cond. (mW/K)	79.0	72.68	71.4	86.5
Vapor ther. cond. (mW/K)	14.3	14.06	13.2	13.3
Surface tension (mN/m)	7.4	8.2	9.5	13.4
50°C				
Pressure (bar)	13.18	9.97	5.84	3.44
Liquid density (kg/m^3)	1102.3	1073.8	1270.3	1267.4
Vapor density (kg/m^3)	66.27	53.59	39.21	19.21
Liquid to vapor density ratio	16.6	20.0	32.4	66.0
Latent heat (kJ/kg)	151.81	145.55	129.96	174.64
Liquid viscosity (μPas)	142	148	209.5	300
Vapor viscosity (μPas)	13	13.5	12	11
Liquid ther. cond. (mW/K)	70.4	66.1	65.6	80.1
Vapor ther. cond. (mW/K)	16.7	16.0	15.1	14.8
Surface tension (mN/m)	4.89	5.74	7.13	10.8

valve placed before the test section was used to maintain a low subcooling into the inlet plenum. The inlet restriction (micro-orifices at the entrance of each channel) then partially flashed the fluid, providing vapor bubbles to start the boiling process.

3.4 Measurement and accuracy

In this section, the different measurement techniques, calibration methods and the experimental accuracy will be detailed. The measurement accuracy is composed of a systematic uncertainty (S$_\chi$) and a random one (R$_\chi$). For steady-state experiments, the random uncertainty was measured during the experiment by taking the standard deviation of 100 individual measurements, where:

$$\delta\chi_i = \sqrt{S_{\chi_i}^2 + 2R_{\chi_i}^2} \tag{3.2}$$

$$R_{\chi_i} = \sqrt{\frac{1}{N}\sum_{i=1}^{i=N}\left(\chi_i - \overline{\chi}\right)^2} \tag{3.3}$$

The systematic component was determined through a calibration or taken from the instrumentation documentation. Table 3.3 lists the systematic experimental error for each type of measurement. In transient experiments, power spectrum analysis was used to determine the cut-off frequency, where the background noise equals the strength of the significant signal.

Table 3.3: Systematic measurement errors.

	Silicon test section	Copper test section
Voltage	±0.045%	±0.045%
Flow rate	±0.05%	±0.05%
Thermocouple	±0.1°C	±0.1°C
Temperature diodes	±0.15°C	±0.15°C
Heater resistance	±0.003Ω	±0.003Ω
Absolute pressure	±750Pa	±1500Pa
Differential pressure SP	±37.5Pa	±17.5–37.5Pa
Differential pressure TP	±37.5Pa	±500Pa

3.4.1 Dimension

The evaporator length and width, the slit and plenum dimensions were measured using a vernier caliber, with an accuracy of 20μm. The values listed in Table 3.1 are larger, since they take into of account the variation of the dimension due to machining. For example, the copper test section inlet slit, machined by electro-erosion, went from 0.43mm to 0.6mm.

The channel height and width and the fin thickness were measured from the microscope pictures shown in Figs 3.9(b) and 3.10(b). The accuracy also took in account the variation along the height and between the channels. Finally, the pressure taps' positions and dimensions were measured on an optical table.

The picture of the wall roughnesses for both test sections are shown in Fig 3.11. The wall surface roughness of the silicon microchannels were evaluated using a Veeco Wyko NT1100 optical profiler. For the copper evaporator, a scanning electron microscope was used to obtain eight wall profiles at different positions and the wall roughness was calculated from the pictures. The root-mean square surface roughness R_q values are listed in Table 3.1.

3.4.2 Signal acquisition

The data acquisition was made using National Instruments cards. A SCXI-1102 module with a 2Hz filter was used for thermocouple and pressure measurements, a SCXI-1102c with a 10kHz filter was used for the temperature diode measurements and a SCXI-1104c with a 10kHz filter for heat flux and mass flow measurements. All modules were mounted in the same SCXI-1000 chassis and connected to the computer by a PCI-6251 card. The combined accuracy for the input modules and the PCI card were:

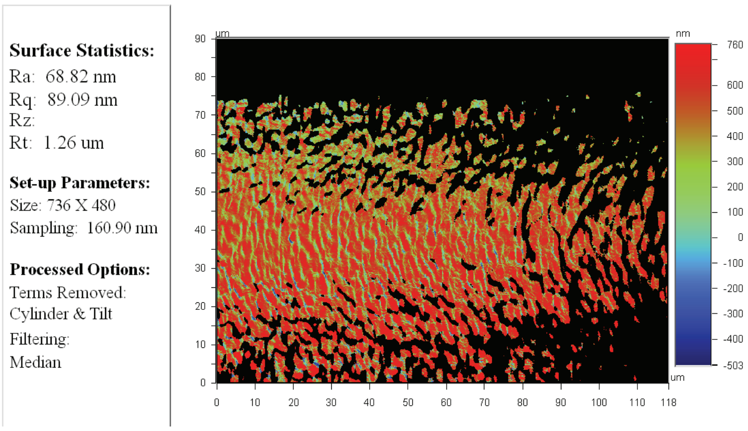

Surface Statistics:
Ra: 68.82 nm
Rq: 89.09 nm
Rz:
Rt: 1.26 um

Set-up Parameters:
Size: 736 X 480
Sampling: 160.90 nm

Processed Options:
Terms Removed:
Cylinder & Tilt
Filtering:
Median

um
90
80
70
60
50
40
30
20
10
0
0
10
20
30
40
50
60
70
80
90
100
110
118
um
nm
760
600
500
400
300
200
100
0
-100
-200
-300
-400
-503

(a) Silicon evaporator

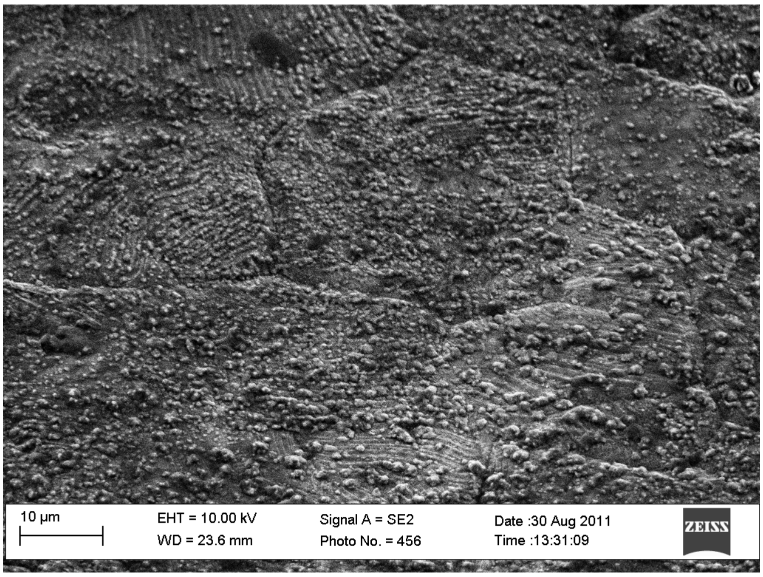

10 µm
EHT = 10.00 kV
WD = 23.6 mm
Signal A = SE2
Photo No. = 456
Date :30 Aug 2011
Time :13:31:09

(b) Copper evaporator

Figure 3.11: Surface roughness measurements.

- For 100mV: ±0.0485 mV or 0.0485%
- For 5V: ±2.0824 mV or 0.0416%
- For 10V: ±3.6231 mV or 0.0362%
- For 30V: ±14.2404 mV or 0.0475%

Thus, for all voltage measurement, an accuracy value of 0.045% was used.

3.4.3 Flow rate

The mass flow rate passing through the test section was measured using a Coriolis flowmeter made by MicroMotion. The maximum allowable flow rate was 108kg/h. Its accuracy is 0.05% of the rate down to 5% of the full scale. The experimental mass flows were always above the lower accuracy limit of 5.4kg/h, which corresponded in the silicon test section to a mass flux of 233kg/m^{2}s and in the copper test section to 115kg/m^{2}s.

3.4.4 Temperature

K-Type thermocouples, made by Thermocoax, were used in the experimental facility. Thermally compensated connection blocks of National Instruments, specially made for thermocouple measurements, were used to ensure a stable reference temperature. For these blocks, National Instruments acquisition software provided built-in calibration curves for thermocouples. In-house thermocouple calibration was used to determine the actual deviation from these built-in functions by a linear fit. For this, the thermocouples were placed in a thermal bath next to high-precision RTD probes and the bath's temperature varied from 20°C to 70°C and back to 20°C in increments of 4°C. There was no notable hysteresis in the measurements and the thermocouple systematic error was ±0.1°C.

The calibration of the diode sensors and the heater resistances were made with the flow loop, by varying the circulating single-phase fluid temperature by means of the pre-heater while maintaining adiabatic conditions in the test section. To ensure uniform temperature along the channels, the flow rate was set as high as possible. The temperature diodes were calibrated by taking the average of the inlet and the outlet temperatures. The systematic measurement error was ±0.15°C. The same average temperature was used for the calibration of the heater resistances. The diode sensor voltages decreased linearly against temperature, as shown in Fig 3.12(a), while the heater resistances rose slowly with temperature, Fig 3.12(b), depicting the results for heater 11 of the silicon test section.

It was not possible to directly assess the temperature diodes' time response. Based on their nanometer-sized thickness, the sensor's Biot number was very small $\left(Bi = \frac{h\delta}{\lambda}\right)$ and a lumped capacitance analysis shows that the response time was less than 1μs.

3.4.5 Absolute pressure

Absolute pressure measurements were made using Endress Hauser PMP75 transducers with adjustable measuring range. The transducers were placed at the same level as the inlet and outlet plenum and, starting at the connection point with the manifold, the capillary tubes were horizontal for more than 10cm (vertical bending was required to make the connection with the transducer), ensuring that there was no liquid height difference between the measurement point and the transducer. The absolute pressure calibration was done using a pressure balance. The resulting calibration accuracy was less than 500Pa. However, in order to take into account all parameters influencing the measurement, the accuracy guaranteed by the manufacturer was used: 750Pa for the 0–10bar range used in the silicon test section and 1500Pa for the 0–20bar range used in the copper test section.

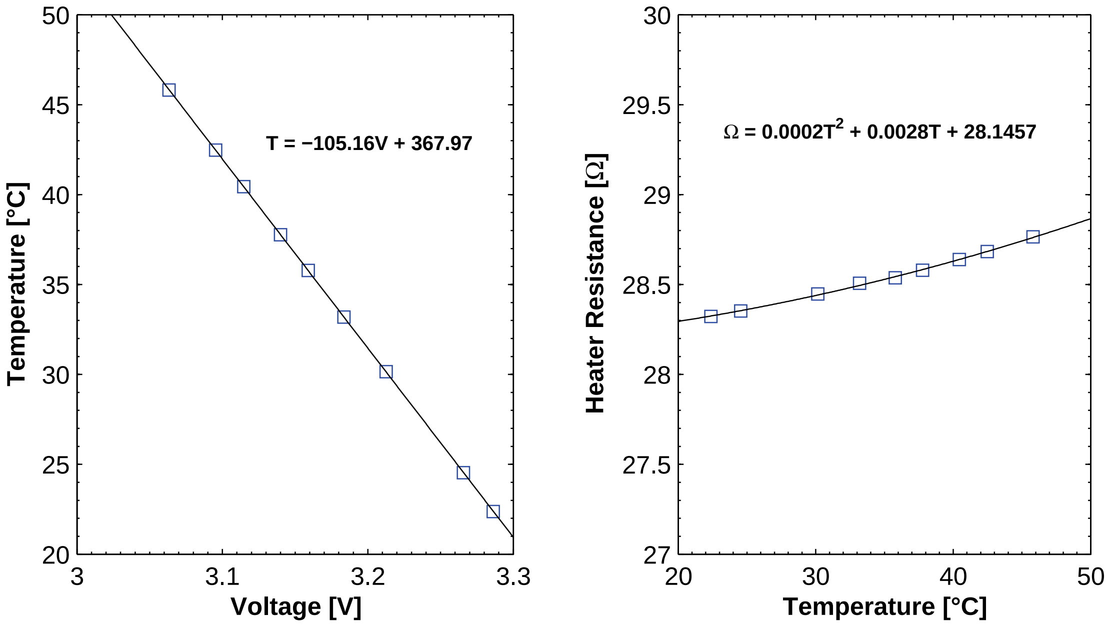

(a) Temperature sensor calibration. (b) Resistance calibration.

Figure 3.12: Silicon test section, heater 11 calibration.

3.4.6 Differential pressure

All differential pressure transducers were made by Endress Hauser. They were calibrated using a U-tube manometer filled with isopropyl-alcohol (786kg/m^3 at 20°C). The calibration curves were all linear and the calibration accuracy was below 15Pa. However, as in the case of the absolute pressure transducers, the manufacturer's accuracy was used. In the silicon test section, a 50'000Pa differential pressure transducer with an uncertainty of ±37.5Pa was placed between both absolute pressure transducers.

In the copper test section four differential pressure transducers were used. A 4000Pa transducer was placed between the inlet plenum and the pressure tap 1. Two transducers were placed in parallel between tap 1 and 2, one 50'000Pa and one 25'000Pa. Finally a ±5000Pa was placed between pressure tap 2 and the outlet plenum. The manufacturer's accuracy was 0.075% of the full-scale, however due to the vertical orientation of the pressure tap, shown in Fig 3.2(b), the fluid in the tube was not single-phase near the manifold. As there was 4.5cm before the capillary was completely exposed to the ambient air, this liquid height was used as absolute error. It corresponds to an error of around 500Pa depending on the fluid and its temperature. It was not possible to heat the capillary tubes to only have vapor, because of the high saturation temperature used in some experiments.

For single-phase measurements, the liquid column height was not a problem and the accuracies were much better. Except for the 50'000Pa transducer, the manufacturer's accuracy was smaller than the calibration one. In this case, the single-phase differential pressure systematic accuracy was the euclidian norm of the U-tube accuracy (±15Pa) and the random measurement error (±4Pa).

3.4.7 Heat flux losses

Part of the base heat flux did not go to the evaporator. These losses were due to natural convection to the ambient air and conduction in the inlet and outlet tubes. In single-phase, heat flux losses are typically measured by tracking the difference between enthalpy gain from inlet to outlet and the input heat flux. It is more difficult in two-phase to track these losses, as it is not possible to calculate the fluid properties in the outlet plenum conditions without knowing what was the heat flux absorbed by the fluid.

Most losses were due to conduction through the inlet and outlet pipes, as the test section and the flow loop were well insulated. Since the inlet pipe was subcooled, it was possible to track the change in enthalpy between the outlet of the preheater outlet and the inlet of the test section and evaluate the losses.

$$q_{loss} = mc_p \left(T_{in} - T_{preh}\right) \tag{3.4}$$

This idea was validated for single-phase against $q_{loss} = q_{input} - mc_p \left(T_{out} - T_{in}\right)$ and the results are shown in Fig 3.13.

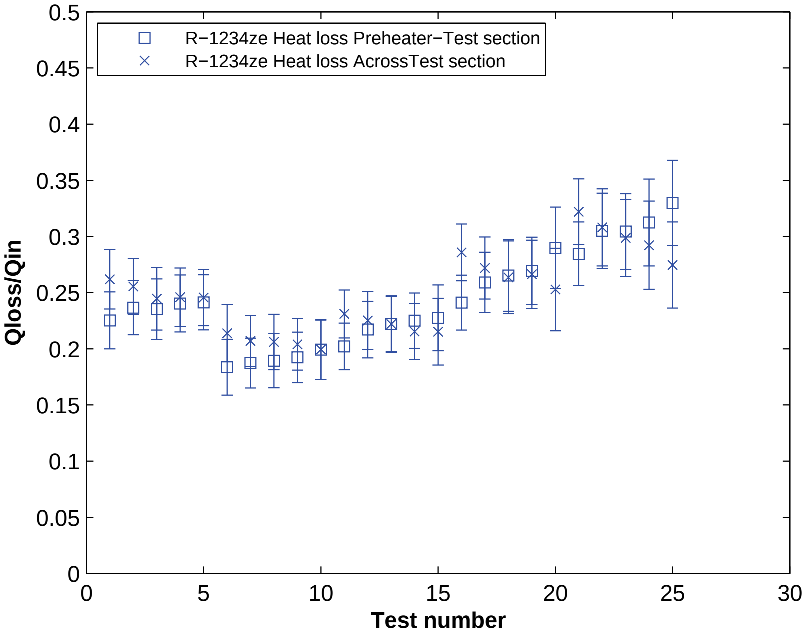

Figure 3.13: Comparison between heat losses based on measurement across the copper test section and between the preheater and the test section.

The agreement between both heat loss measurement techniques is good and applicable to two-phase experiments. Most losses were toward the inlet in single-phase, since it was where the lowest temperature was.

In two-phase, the conduction losses will also be toward the inlet, because the outlet pipe temperature is almost at the saturation temperature of the outlet plenum. Moreover, the outlet connection pipe was lined with PTFE (λ=0.25W/mK), which reduced the conduction losses. In comparison, the inlet pipe was made of stainless steel (λ=14.4W/mK).

The heat flux losses were applied uniformly to all heaters and to take into account that convection losses and conduction losses through the outlet were neglected, a relative uncertainty was added to equation 3.4. Typical two-phase heat flux losses measured in the copper test section were 3±1% and less than 1±0.3% for the silicon test section. The polycarbonate manifold (λ=0.7W/mK) in the silicon test section reduced losses.

3.4.8 Fluid and material properties

Fluid properties and the vapor pressure curve were obtained with REFPROP, the NIST Standard Reference Database 23, Version 8.0 using temperature and pressure measurements. In the plenums, pressure measurements were used to calculate the saturation point, since the curves P_{sat}–T_{sat} are less sensitive to pressure. Pressure and temperature measurements in the outlet plenum were in close agreement with respect to the saturation pressure curve as shown in Fig 3.14. Only a few points for R-1234ze(E) were distant by more than 1500Pa (max 1800Pa) at its saturation pressure of 600'000Pa.

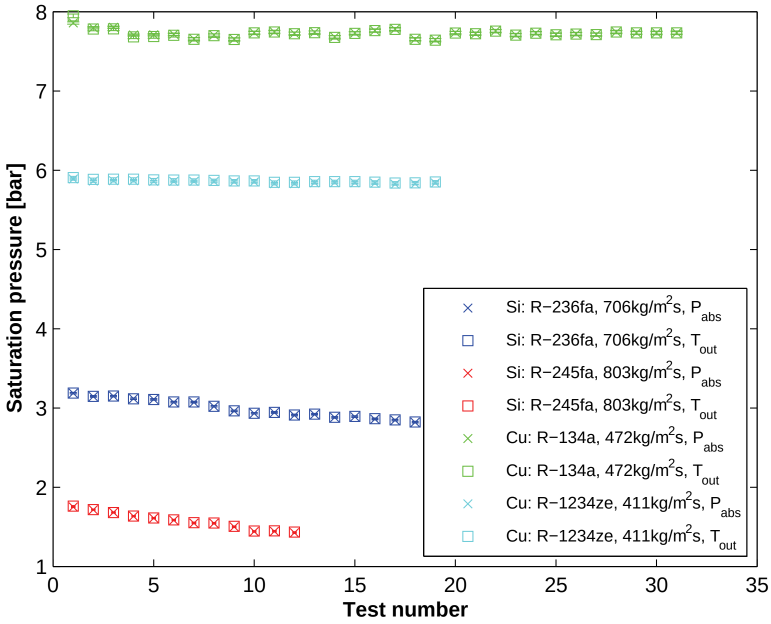

Figure 3.14: Saturation pressure from temperature and pressure measurements for uniform heat flux at T_{sat}=30°C.

The silicon thermal conductivity was calculated using a curve fit of the data of Shanks *et al.* (1963):

$$\lambda_{si} = 7 \times 10^{-4}(T)^2 - 0.5416T + 157.39 \tag{3.5}$$

where T is the local temperature in °C.

The copper evaporator were machined in ETP copper. Wolverine Tube provided a thermal conductivity value of 388W/mK at 20°C. To take into account the change in thermal conductivity with temperature, the equation of Abu-Eishah (2001) for pure copper was modified to match the listed thermal conductivity:

$$\lambda_{cu} = 82.56648T^{0.262301}e^{-4.06701\times10^{-4}T}e^{59.72934/T} - 10; \tag{3.6}$$

where T is the local temperature in Kelvin.

3.5 Data reduction and error propagation

The local pressure evolution in the test section and the local heat transfer coefficients must be derived from the measurements. In this data reduction, it is important to propagate the measurement absolute and random errors to the calculated quantities. This was done following the method of Kline & McClintock (1953):

$$\Gamma = f(\chi_1, \chi_2, \chi_3, ..., \chi_n) \tag{3.7}$$

$$\delta\Gamma = \sqrt{\left(\frac{d\Gamma}{d\chi_1}\delta\chi_1\right)^2 + \left(\frac{d\Gamma}{d\chi_2}\delta\chi_2\right)^2 + \left(\frac{d\Gamma}{d\chi_3}\delta\chi_3\right)^2 + ... + \left(\frac{d\Gamma}{d\chi_n}\delta\chi_n\right)^2} \tag{3.8}$$

where $\delta\chi_i$ is the norm of the absolute measurement error (S_χ), listed in Table 3.3, and the random measurement error (R_χ).

Differentiating Γ with respect to χ_i was always not possible, for example with REFPROP data, so the error was alternatively calculated as:

$$\delta\Gamma = f(\chi_1+\delta\chi_1, \chi_2+\delta\chi_2, \chi_3+\delta\chi_3, ..., \chi_n+\delta\chi_n) - f(\chi_1, \chi_2, \chi_3, ..., \chi_n) \tag{3.9}$$

The equations used to propagate errors are found in the Appendix A.

3.5.1 Heat conduction

The heat flux dissipated by each heater was calculated as:

$$q_{b-xy} = \frac{\frac{V_{xy}^2}{R_{xy}} - q_{loss}}{l^2} \tag{3.10}$$

To obtain the wall heat fluxes and temperatures, different thermal conduction schemes were used according to the situation. For a one-dimensional thermal conduction model, $q_w = q_b$ and the wall temperatures were determined as:

$$T_{w-xy} = T_{b-xy} - q_{b-xy}\left(\frac{e_{chip}}{\lambda_{chip}} + \frac{e_{TIM}}{\lambda_{TIM}} + \frac{e_{evap}}{\lambda_{evap}}\right) \tag{3.11}$$

The computation was sub-divided into 5μm layers in order to include the variation of the thermal conductivity with temperature.

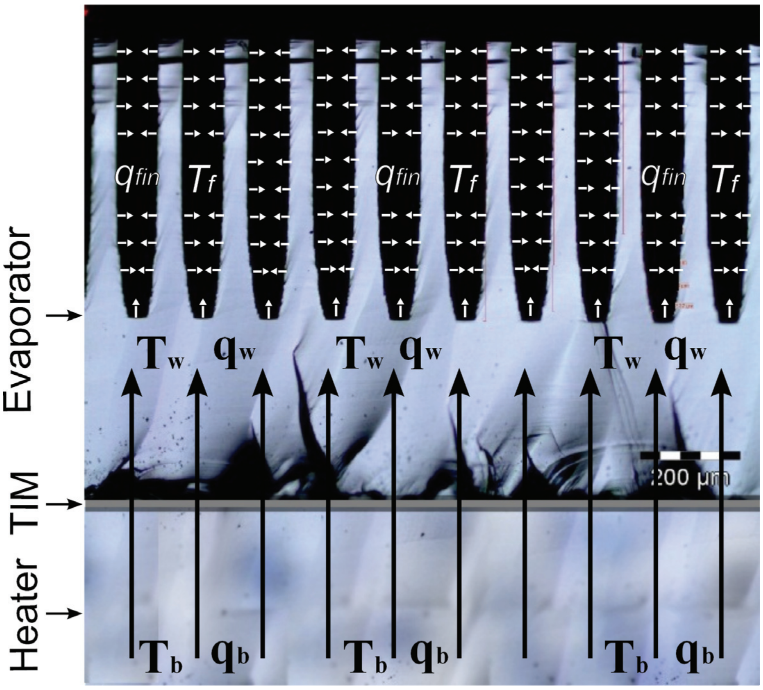

Figure 3.15: Schematic of the temperaturees and heat fluxes.

In some cases, the heat flux found at the evaporator (q_w) differed importantly from what was found at the base of the package (q_b), due to thermal conduction effects inside the package, in other words due to "heat spreading". Fig 3.15 helps to visualize the different heat flux definitions.

To solve this problem using the experimental measurements, there is no information regarding the fluid boundary, but both the local heat fluxes and temperatures are known at the base. Instead of relying on an iterative solution, the problem was solved as presented in Fig 3.16. In the experiment, T1, T2, T3 and qS are measured. After computing qW and qE from the temperature measurements by linear thermal conduction and qN is known from an energy balance on node 2. T4 can be then calculated using linear thermal conduction. By repeating this process for all nodes on the second layer and then layer by layer up to the top of the composite wall, including the effects of the thermal interface material (TIM) and the change in thermal conductivity due to temperature, the wall heat flux and temperature are obtained at the top layer.

Each layer was set to 5μm thickness and adiabatic conditions were used for external walls. The surface mesh was fixed by the heater size (2.54mm×2.54mm), so this way no assumptions were needed for the base temperature distribution between the sensors. This calculation was extended, when needed, into a three-dimensional thermal conduction scheme by linking the column nodes (front and back). Some temperature sensors failed during the experimental campaign and in order to proceed with the calculations, their values were set to the average temperature of all sensors on the same row.

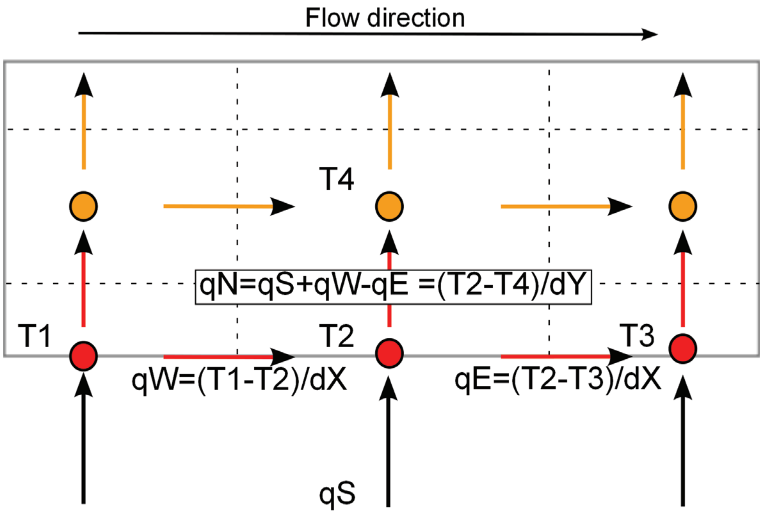

Figure 3.16: Two-dimensional heat conduction data reduction scheme.

3.5.2 Fluid-side parameters

The first quantity needed on the fluid side is the mass flux:

$$G = \frac{m}{NWH} \tag{3.12}$$

where m is the mass flow, N is the number of channels, W is the channel width and H is the channel height.

Δp_{total} was measured directly in the silicon test section, whereas in the copper test section it was calculated by adding the measurements of the three local differential pressure transducers: Δp_1 from the inlet plenum to tap 1, Δp_2 from tap 1 to tap 2 and Δp_3 from tap 2 to the outlet plenum. The total pressure drop can be divided into three components, the inlet restriction, the channel and the outlet restriction.

$$\begin{aligned} \Delta p_{total} &= \Delta p_{restr-in} + \Delta p_{ch} + \Delta p_{restr-out} \qquad (3.13)\\ &= \Delta p_1 + \Delta p_2 + \Delta p_3 \qquad (3.14) \end{aligned}$$

Silicon test section: inlet and outlet restriction losses

In the silicon test section, the single-phase channel pressure drop must first be calculated before the restriction losses can be determined. The single-phase liquid frictional channel pressure drop is:

$$\Delta p_{fr} = 4f\frac{G^2}{2\rho_l}\frac{L_{ch}}{D_h} \tag{3.15}$$

In order to evaluate f in the silicon test section, FLUENT (version 12.1.2) was used to perform a 3D numerical simulation of one channel with the plenums. The pressure drop measured across the test section was used for the inlet and the pressure outlet boundary conditions. The fluid used was R-236fa, with the physical properties evaluated at 20°C. The grid independence was ensured by comparing results obtained with two different grid sizes (103000 and 824000 elements).

For the same total pressure drop, the experimental mass fluxes were 10 to 15% lower than that of the simulation. This difference was probably caused by the geometrical simplification in the plenums and prevented using the CFD results to describe the single-phase behavior in the whole test section. On the other hand, the simulated frictional pressure drop in the channel was used, since both the CFD and experimental geometries were very similar. Thus, based on the CFD results, the single-phase frictional factor f for the silicon channel was expressed as:

$$f = \frac{25.18}{Re} \tag{3.16}$$

The single-phase inlet and outlet restriction losses were determined by subtracting Δp_{fr} from the total measured pressure drop. Based on the CFD simulation, the inlet losses were the most important, representing between 75 and 95% of the single-phase restriction and plenum losses. The inlet restriction pressure drop values are presented in Chapter 4.

For two-phase tests, the inlet restriction was used to flash the incoming fluid, which effectively increased the inlet restriction pressure drop. It was not possible to evaluate this parameter, but compared to the two-phase pressure drop in microchannels, it was certainly small. Therefore the single-phase inlet restriction pressure drops were used in the two-phase calculations.

To evaluate the two-phase channel pressure drop, $\Delta p_{restr-out}$ is needed. It is a complex quantity which includes an area expansion, thus pressure recovery, and several changes in flow direction, leading to frictional pressure drop. Instead of relying on imprecise prediction methods, the outlet restriction pressure drop was measured experimentally. This was done by heating and evaporating in the first part of the test section(Rows 1 & 2) and keeping a two-phase adiabatic flow of known vapor quality at the end of the channels (Rows 4 & 5).

In the adiabatic zone, there was negligible heat flux and the local base temperature measurements equaled the wall temperature. This temperature was assumed to be the same as the local saturation temperature, T_{4Y-5Y}=T_{sat}, such that the local saturation pressure could be determined using the fluid's vapor pressure curve. A linear drop was assumed between the local saturation pressures, p_{4Y} and p_{5Y}, and extrapolated to the channel end to obtain p_{ch-end}. To take into account the small variation of pressures in rows 4 & 5, the value used was an average of all columns. Since the outlet plenum pressure was already measured, the two-phase outlet restriction and plenum pressure losses could be evaluated. This was given as follows:

$$p_{ch-end} = p_{5-sat} - \frac{l}{2}\frac{p_{4-sat} - p_{5-sat}}{l} \tag{3.17}$$

where l is the length of a single heater (2.54mm) and the distance between two temperature sensors.

$$\Delta p_{restr-out} = p_{ch-end} - p_{out} \tag{3.18}$$

Due to the possibility of encountering conjugated effects within the channels, care was taken to ensure that the temperature sensors at the end of channels were still in an adiabatic zone. This was proven by heating Row 1 alone. Once a base temperature of around 60°C was recorded in Row 1, similar increases were done by heating of Row 2. As the heat source came closer to the end of the channels, the temperature sensors should have recorded a change if they were affected by heat spreading.

Fig 3.17 shows that when Row 2 was heated, there was a strong change in trend for the sensors of Row 3, but none for Rows 4 and 5. Their temperatures kept on dropping at the same rate, following the fall in saturation pressure in the channels. This shows that the temperature sensors of Row 5 remained in an adiabatic zone throughout the experiment and thus recorded the local saturation temperature of the two-phase refrigerant flowing in the channel.

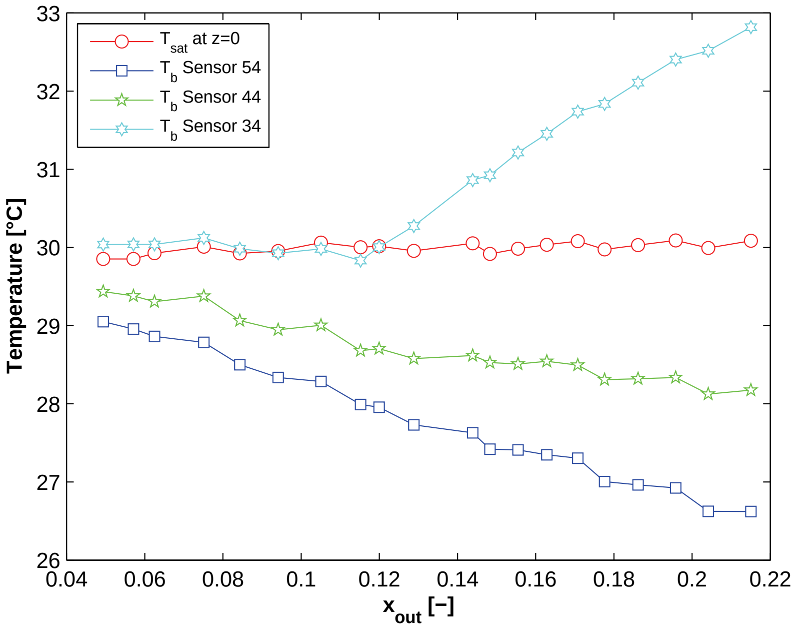

Figure 3.17: Base temperature evolutions for R-236fa at G=963kg/m^{2}s in silicon test section.

Copper test section: inlet and outlet restriction losses

In the copper test section, each component of the total pressure was measured, but due to geometrical constraints, it was not possible to directly place the pressure tap at z=0 and z=L$_{ch}$. The single-phase channel pressure drop (dP2) was then extrapolated linearly to determine the inlet restriction pressure drop, as shown in Fig 3.18. The resulting equation was:

$$\Delta p_{restr-in} = \Delta p_1 - \frac{\Delta p_2}{L_{PTap2} - L_{PTap1}} \times L_{PTap1}; \tag{3.19}$$

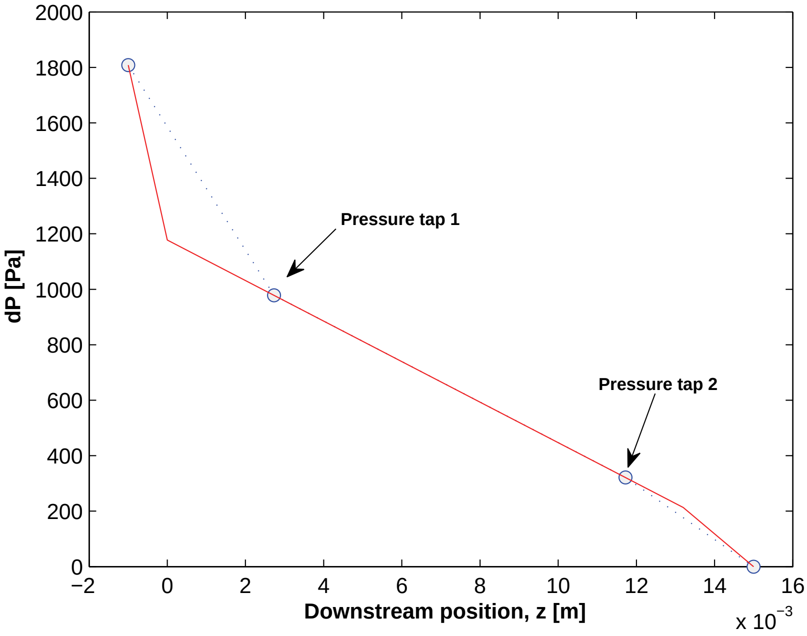

Figure 3.18: Single-phase pressure profile for R-134a at 502kg/m^{2}s in copper test section.

The two-phase outlet restriction pressure drop was calculated by the same technique:

$$\Delta p_{restr-out} = \Delta p_3 - \frac{\Delta p_2}{L_{PTap2} - L_{PTap1}} \times (L_{ch} - L_{PTap2})\,; \tag{3.20}$$

Channel pressure

For both test sections, a two-phase linear pressure drop was assumed to describe the local channel pressures. The channel length was discretized into 100 increments i. The first channel pressure, $\mathrm{p}_{1,y}$, was calculated by substracting the inlet restriction pressure drop from the inlet plenum absolute pressure:

$$p_{1,y} = p_{inlet} - \Delta p_{restr-in} \tag{3.21}$$

If the liquid entering the channel was sub-cooled, the local pressure drop was computed using:

$$p_{i,y} = p_{i-1,y} - 4f\frac{G^2}{2\rho_l}\frac{dz}{D_h} \tag{3.22}$$

where f was evaluated using equation 3.16 for the silicon test section and for the copper test section, using Biber & Belady (1997)'s correlation.

Once the fluid's saturation temperature was reached, the position was denoted as *onset* and the local pressure as $p_{onset,y}$. A linear pressure drop rate was assumed between $p_{onset,y}$ and a reference pressure, $p_{ref,y}$.

$$p_{i,y} = p_{onset,y} - dz(i - onset)\frac{p_{onset,y} - p_{ref,y}}{z_{ref,y} - z_{onset}} \tag{3.23}$$

For the silicon test section, the reference was the channel end:

$$p_{ref,y} = p_{ch-end} \tag{3.24}$$

and for the copper test section, pressure tap 2:

$$p_{ref,y} = p_{outlet} - \Delta p_3 \tag{3.25}$$

In some instances, pressure drop prediction methods were also used to determine the local channel pressure and a linear correction was sometimes applied to the prediction. It consisted in comparing the predicted pressure at the reference point with p_{ref}. The difference was then linearly corrected from the channels inlet to its outlet. The influence of this correction will be highlighted when it is used.

The local fluid enthalpy was calculated from an energy balance. The inlet restriction was assumed to be adiabatic.

$$h_{1,y} = h_{in} \tag{3.26}$$

$$h_{i,y} = h_{i-1,y} + q_{w,xy}\frac{dB}{GHW}dz \tag{3.27}$$

where dB=W+F and, using local pressure and temperature in REFPROP to determine the reference enthalphy h_l and h_v, the local vapor quality was:

$$x_{iy} = \frac{h_{iy} - h_{l,iy}}{h_{v,iy} - h_{l,iy}}. \tag{3.28}$$

Finally, the local fluid temperature was determined in REFPROP using the local pressure (and enthalpy for single-phase).

3.5.3 Heat transfer coefficient

With the local wall heat flux and the fluid and wall temperatures, the base heat transfer coefficient can be calculated:

$$\alpha_{b,xy} = \frac{q_{w,xy}}{T_{w,xy} - T_{f,xy}}. \tag{3.29}$$

As previously noted, the calculation of the fluid temperature was divided into 100 increments, whereas there were 5 base temperature measurements in each column. Thus for the calculation of the heat transfer coefficient, the average of the 20 local fluid temperatures found over each heater was used.

The base heat transfer coefficient (α_b) is useful for thermal resistance analysis in thermal packaging. However, to compare results to prediction methods and design an evaporator, information about the wall heat transfer coefficient, which includes the influence of the fins, is needed. The fin heat flux and local wall heat transfer coefficient were calculated by iteratively solving equations 3.30 – 3.32, adapted from Kreith & Bohn (2001) for N+1 fins:

$$q_{fin,xy} = q_{w,xy} \frac{(N+1)(F+W)-W}{NW+2(N+1)H\eta_{fin,xy}} \tag{3.30}$$

with

$$\eta_{fin,xy} = \frac{\tanh\sqrt{2\alpha_{fin,xy}\frac{(H)^2}{\lambda_{evap}F}}}{\sqrt{2\alpha_{w,xy}\frac{(H)^2}{\lambda_{evap}F}}} \tag{3.31}$$

and

$$\alpha_{w,xy} = \frac{q_{fin,xy}}{T_{w,xy}-T_{f,xy}}. \tag{3.32}$$

The results of the error propagation analysis are shown in Table 3.4.

Table 3.4: Results of the error propagation analysis.

	Silicon test section	Copper test section
Base heat flux	±1%	±2%
Wall heat flux	±1%	±2%
Fin heat flux	±1%	±2%
Wall temperature	±0.2–0.35°C	±0.18–0.25°C
Mass flux	±5–6%	±3%
Inlet restriction pressure drop	±10%	±6%
Outlet restriction pressure drop	±900Pa	±510Pa
Channel pressure drop TP	±901Pa	±512Pa
Fluid temperature SP	±0.1°C	±0.1°C
Fluid temperature TP	±0.15%	±0.02–0.09°C
Vapor quality	±0.02%	±0.01–0.05%
Base heat transfer coefficient	±3–15%	±3–15%
Wall heat transfer coefficient	±3–15%	±3–15%

Chapter 4

Pressure drop

Pressure measurements were taken at different locations in the test sections in order to evaluate the following pressure drop components: the inlet restriction pressure drop, the microchannel pressure drop and the outlet restriction pressure drop. Added together, they formed the total pressure drop across the test section. The measurement and calculation procedures were detailed in Chapter 3.

4.1 Inlet restriction pressure drop

The pressure drop found in the inlet restriction was evaluated for each refrigerant in single-phase adiabatic conditions. It covers pressure drop from 50 to 30'000Pa. It was then used for two-phase experiments, although the restriction, by flashing the incoming liquid as it exits the restriction, increased the pressure drop. This added pressure component was assumed to be negligible when compared to the two-phase channel pressure drop.

The measurements were repeated for several mass fluxes and using a standard formulation for singularity pressure losses (Idelcik (1999)), the inlet restriction losses were modeled as:

$$\Delta p_{restr-in} = \frac{G^2}{2\rho_l}\xi \tag{4.1}$$

where ξ is the pressure loss coefficient.

Fig 4.1 shows all five curves for the different test conditions. In the silicon test section the coefficient ξ was found to be a function of G. Comparing with equation 3.15 for single-phase frictional pressure drops, ξ is in fact equivalent to $4f\frac{L}{D_h}$. Since the friction factor f is a function of the Reynolds number, thus of the mass flux, it can be expected that over a large range of mass flux, $\xi = f(G)$.

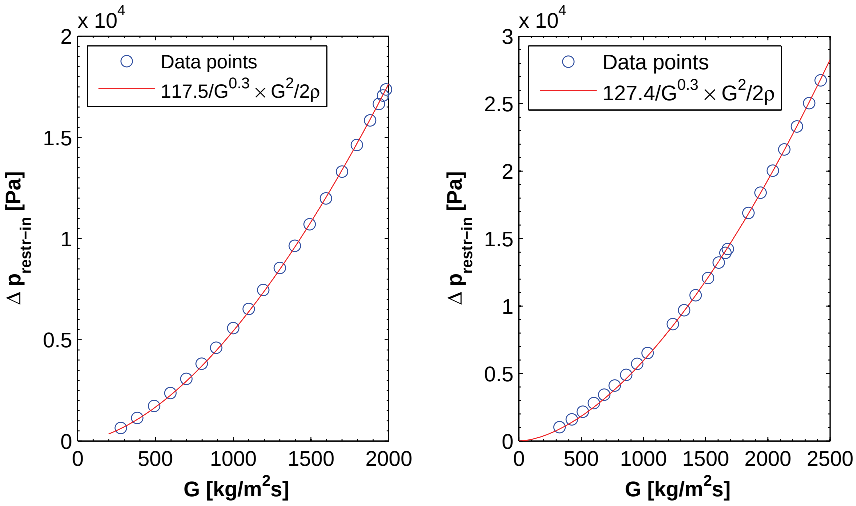

(a) Silicon test section: R-236fa (b) Silicon test section: R-245fa

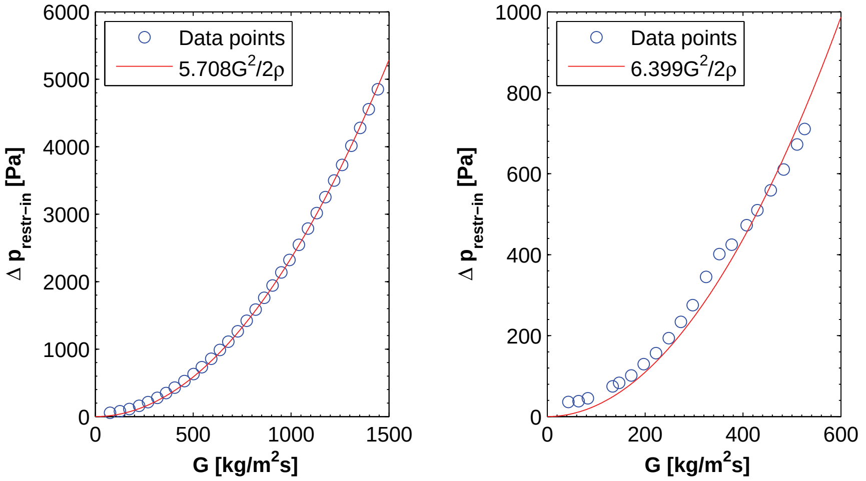

(c) Copper test section: R-134a (d) Copper test section: R-1234ze(E)

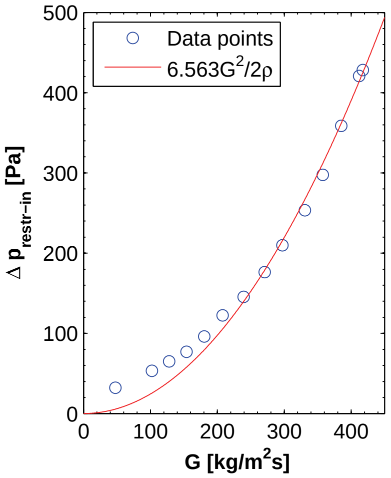

(e) Copper test section: R-245fa

Figure 4.1: Inlet restriction pressure drops in the silicon and the copper test sections.

In the copper test section it is possible to assess if the increase in pressure drop in the inlet restriction due to flashing is indeed negligible using its local pressure taps near the entrance of the microchannels, as shown in Fig 3.4,. This was done by comparing the pressure drop measured by the first differential pressure transducer, Δp_1, to the one calculated through equation 4.1. The results for R-134a are shown in Fig 4.2. The values for Δp_1 are less than two times that calculated for the inlet restriction alone. Taking into consideration that part of the pressure drop measured by Δp_1 is due to the channel (pressure tap 1 is positioned 2.73mm away from the restriction), once removing that influence, the single phase inlet restriction correlation for a flow flashing in the restriction appears still to be precise, as long as vapor qualities remain low.

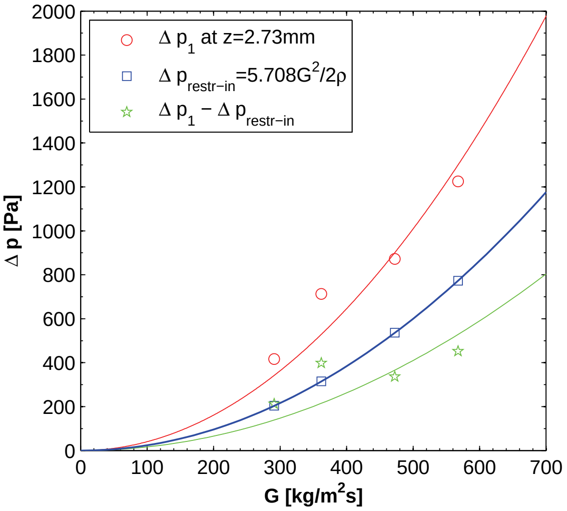

Figure 4.2: Comparison between Δp_1 and equation 4.1 for R-134a at T$_{sat}$=30°C for the copper test section.

To obtain an estimate of ξ without experimentation, Idelcik (1999) lists pressure loss coefficients for simplified geometries (sudden expansion, round to square pipe, etc...). The inlet restrictions of the test sections must be divided into three sections to fit the description of Idelcik (1999). The flow first enters a sudden contraction, when it goes from the plenum to the slit. Then it flows through a second area reduction, when entering the channels from top, and finally it makes a right angle turn into the channels.

The pressure loss coefficient for each section was calculated for a channel-based mass flux of 500kg/m^{2}s and the results are tabulated in Table 4.1. The sum of the three components is close to the values shown in Fig 4.1 for the copper test section (5.708, 6.399 and 6.563), but its predictions are not accurate compared the losses calculated for the silicon test section.

4.2 Outlet restriction pressure drop

The outlet restriction pressure drop was measured in two different manners. In the silicon test section it was possible to obtain adiabatic temperature measurement corresponding

Table 4.1: Pressure loss coefficients ξ from Idelcik (1999).

	Silicon test section	Copper test section
Section 1	0.5	1.7
Section 2	0.5	0.4
Section 3	4.5	6.5
Sum	5.5	8.6

to the local saturation pressure at Row 5 using the mean temperature of the row. The difference between this pressure and the outlet plenum pressure corresponds to the restriction pressure drop. As Fig 4.3 shows, the losses can be up to 7kPa for R-245fa. It is also important to note that the uncertainty on these measurements is relatively high, ±1.8kPa, compared to the measured values.

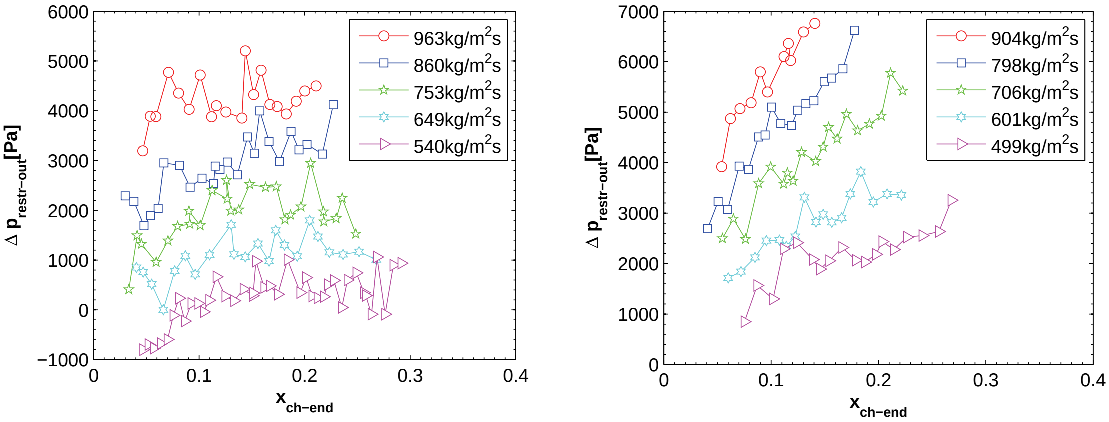

(a) R-236fa

(b) R-245fa

Figure 4.3: Outlet restriction pressure drop in silicon test section, T_{sat}=30°C.

In the copper test section, the restriction pressure drop was measured directly by a differential pressure transducer, Δp_3. This technique is more precise than the one used in the silicon test section. However, since copper is about four times more conductive than silicon, conduction effects in the thermal package were more important and it was not possible to form a quasi-adiabatic zone in the copper test section. The tests were made with R-134a, R-1234ze(E) and R-245fa for mass fluxes between 205 and 562kg/m^{2}s at two saturation temperatures.

The pressure drops shown in Fig 4.4 are lower than those of the silicon test section, which means that the pressure drop in the restriction is a function of the channel width. In both test sections, R-245fa has the highest pressure drop level. As noted in Table 3.2, this fluid has the highest liquid to vapor density ratio, which increases the pressure drop. Finally, the pressure drop increases with mass flux and vapor quality.

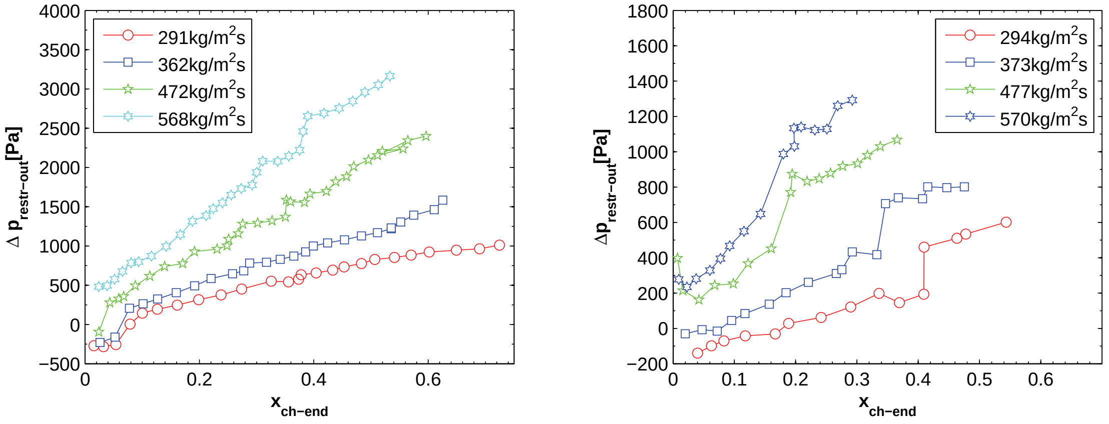

(a) R-134a, T$_{sat}$=30.5°C (b) R-134a, T$_{sat}$=50.8°C

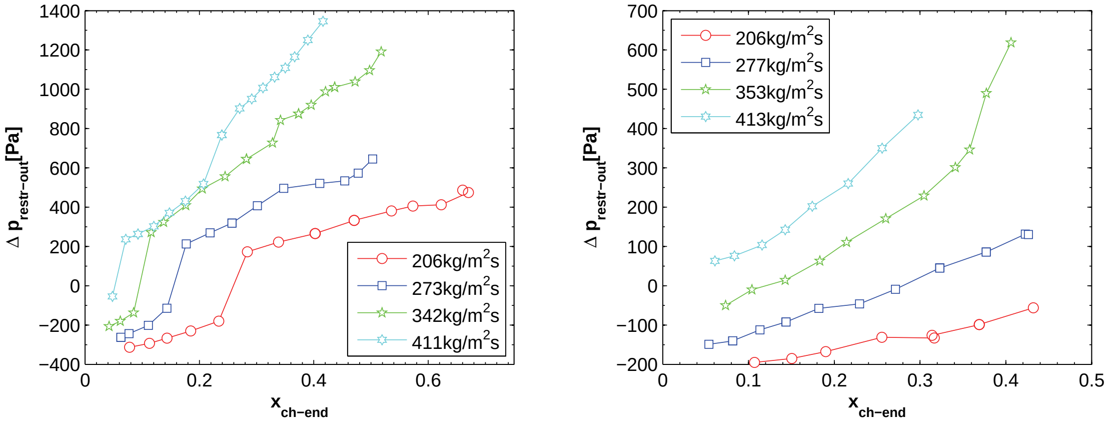

(c) R-1234ze(E), T$_{sat}$=30.7°C (d) R-1234ze(E), T$_{sat}$=50.1°C

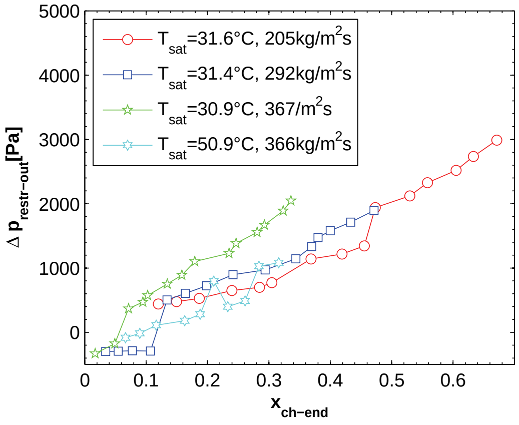

(e) R-245fa

Figure 4.4: Outlet restriction pressure drop in copper test section.

The density ratio, geometry, vapor quality and mass flux are all present in Collier & Thome (1994) equation for pressure drop in expansion flows. A simple enlargement will lead to a pressure recovery, which is predicted by equation 2.16, taken from their book. However, in the outlet restriction the complex geometry leads to a pressure drop from the channel end to the plenum in most cases.

All pressure measurements for the outlet restriction (585 datapoints) have been collected into a single database in order to develop a prediction method. Starting from, Collier & Thome (1994)'s equation, the term $1 + \frac{v_{lv}}{v_l}x$ was simplified into $\frac{\rho_l}{\rho_v}x$. The area ratio was replaced by the channel width (W_{ch}) to the slit width (W_{slit}) ratio to an exponent. This exponent value was found by numerical least-square fit iteration. The resulting equation is:

$$\Delta p_{restr-out} = \frac{G^2}{\rho_l}\frac{W_{ch}}{W_{slit}}^{0.2274} x_{ch-end}\frac{\rho_l}{\rho_v} \tag{4.2}$$

The predicted data are shown against the experimental ones in Fig 4.5. The mean average error for pressure drops larger than 500Pa is 28.5% and 65.1% of all data are predicted within 30%.

Based on equation 4.2, reducing $\Delta p_{restr-out}$ for a constant mass flow and heat flux without increasing the total pressure drop can be done two ways:

1. By increasing W_{slit} to reduce the ratio of W_{ch}/W_{slit} (decreasing W_{ch} would increase the channel pressure drop) .
2. By using a refrigerant with a low liquid to vapor density ratio. R-134a and R-1234ze(E) are then better choices than R-236fa and R-245fa.

4.3 Channel pressure drop

The experiments used to evaluate the microchannel pressure drops were made under a uniform heat flux, varying the mass flux and the saturation temperature. As described in Chapter 3, two methods were used to obtain the channel pressure drop. In the silicon test section, it was calculated by substracting the inlet and outlet restriction losses from the total pressure drop and in the copper test section, it was directly measured through Δp_2.

4.3.1 Single-phase validation

Single-phase microchannel pressure drops in the copper test section were used to validate the measurement and data reduction methods. Using the same measurement datasets as the one used to determine the inlet pressure loss coefficient, Fig 4.6 shows that the experimental frictional pressure drop factor in the channel is very well predicted by

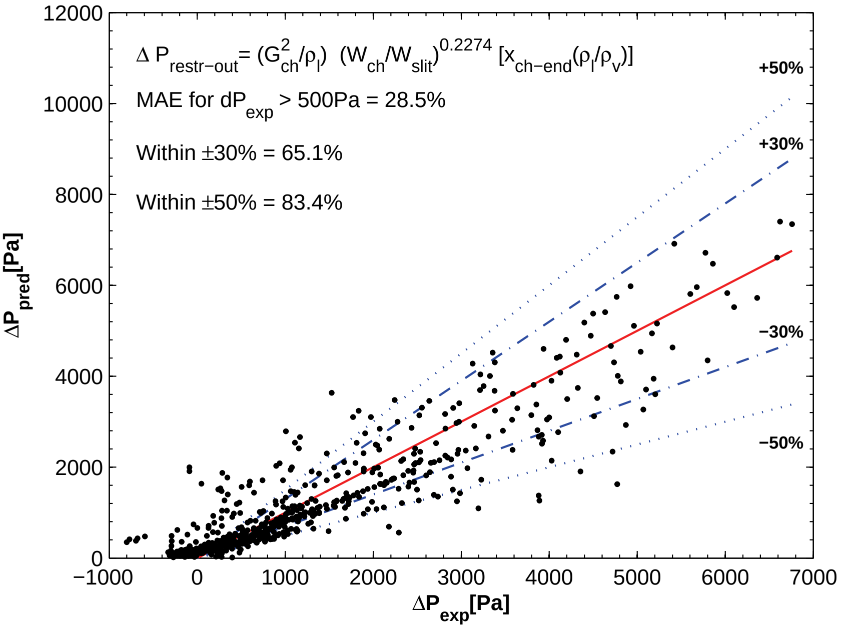

Figure 4.5: Prediction of outlet restriction pressure drop.

Biber & Belady (1997)'s method. Only a few measurement points below Re=100 are not accurate. At these Reynolds number, the mass fluxes are below 150kg/m^{2}s and the fixed systematic measurement error of the pressure drop leads to large uncertainties in the determination of the friction factor.

The channel pressure drop measurement technique is thus validated for the copper test section. The same validation was not possible with the silicon test section, but a numerical model was used to evaluate the single phase channel pressure drop. Furthermore, methods to predict the inlet and outlet pressure drops in microchannel test sections have been developed, which can be tentatively used as design equations for these types of cold plates.

4.3.2 Flow distribution

One of the central assumptions in multi-microchannels is that the flow is uniformly distributed. Assessing the lateral variation of mass flux in the evaporator is therefore important. As it is difficult to measure the mass flow in each channel, substitute methods were used. In the silicon test section, the results from experiments used to determine $\Delta p_{restr-out}$ also provided information about pressure drops over each column from each column's temperature. The lateral pressure drop variation from the inlet plenum to the exit at Row 5 for all tests was close to or less than 5%, as shown in Fig 4.7. Since the pressure drop is proportional to the square of the mass flux, 5% in lateral pressure drop variation corresponds to a mass flux variation of about 2.5%. Thus, the inlet restriction in the silicon test section was well designed to distribute the flow and the pressure drop in all channels was uniform.

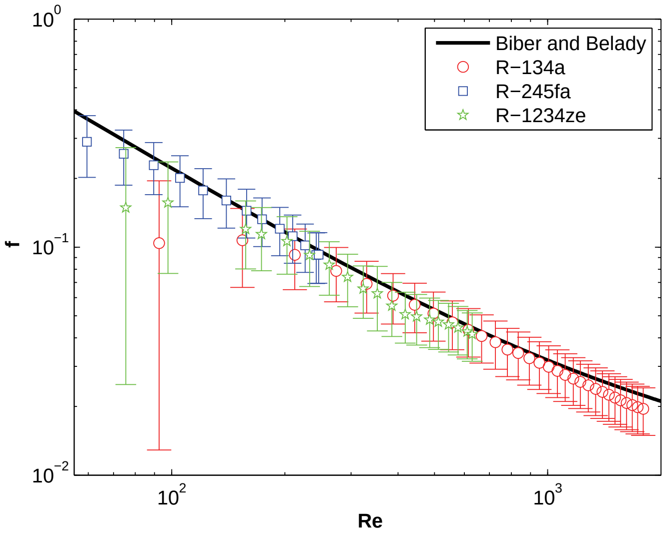

Figure 4.6: Frictional pressure drop factor for copper test section.

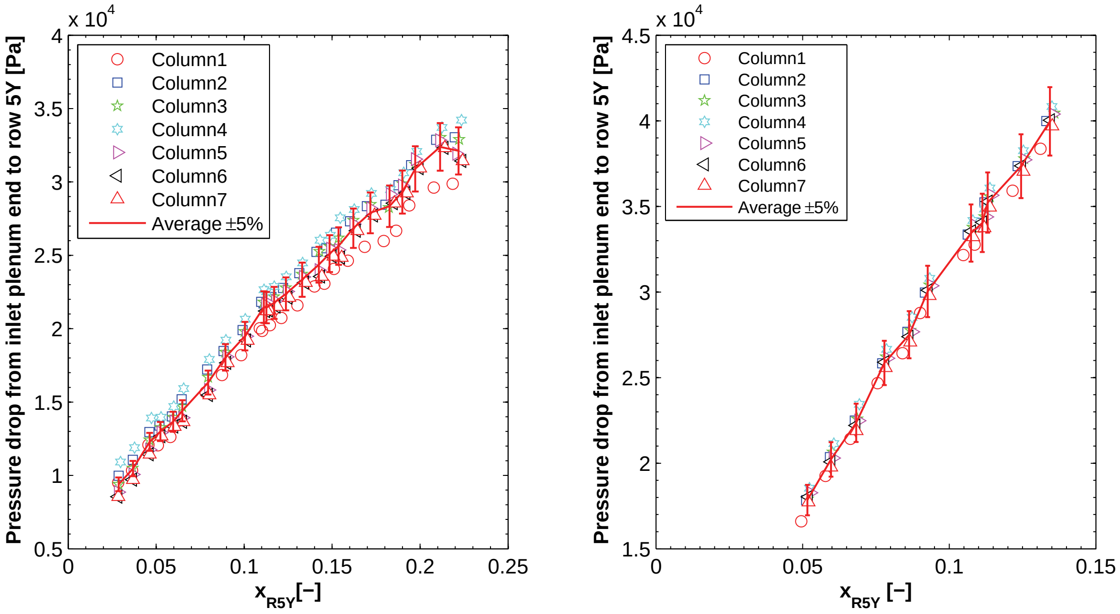

(a) R-236fa, 860kg/m^{2}s (b) R-245fa, 904kg/m^{2}s

Figure 4.7: Pressure drop from the inlet plenum to Row 5 for silicon test section.

In the copper test section, another proxy method was used to assess the flow distribution. As presented in Chapter 3, Δp_2 was measured along Column 2 and along Column 6. As shown in Fig 4.8, their pressure drop measurements for several different test conditions differ by less than 500Pa, the systematic measurement accuracy. Combined with the single-phase pressured drop validation, whose computation was based on the expected mass flux, Fig 4.8 shows, indirectly, that the mass flow across the evaporator was uniformly distributed.

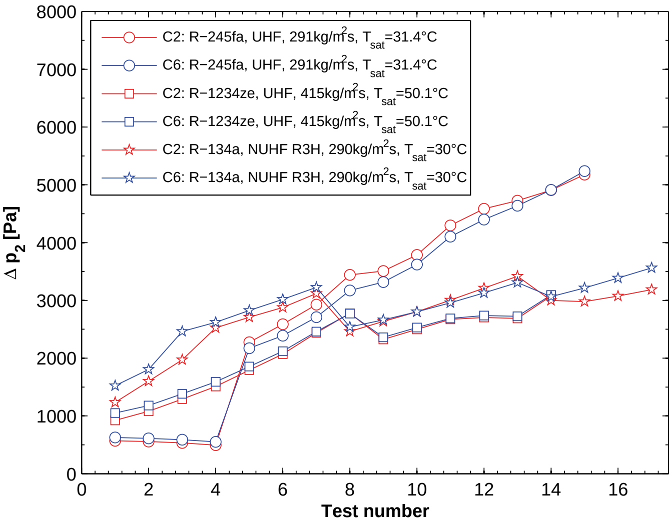

Figure 4.8: Comparison between Δp_2 measured along Columns 2 and 6 for copper test section.

4.3.3 Results

The results for the two-phase channel pressure drops for both test sections are shown in Figs 4.9 and 4.10. The pressure drop increases almost linearly with the quality and with mass flux. As the vapor quality nears zero, the total pressure drop tends toward the single phase pressure drop of each fluid.

The pressure drop levels are much higher in the silicon test section than in the copper test section. The pressure drop rate can be as high as 50bar/m in the first, compared to 9bar/m in the latter. This is mostly due to the difference in hydraulic diameter. Starting from equation 3.15 for the frictional pressure drop, this time using a two-phase frictional factor, the hydraulic diameter appears in the denominator and in the calculation of the friction factor, f. This coefficient is typically a function of $\frac{1}{Re}$, and thus a function of $\frac{1}{D_h}$. The two-phase channel pressure drop is therefore proportional to:

$$\Delta p_{ch} \propto \frac{1}{D_h^2} \tag{4.3}$$

For the present test sections, this proportion means that for the same fluid and mass flux, the channel pressure drop in the silicon evaporator should be 2.8 times larger than in the copper one. This result can be compared to the values obtained for R-245fa in

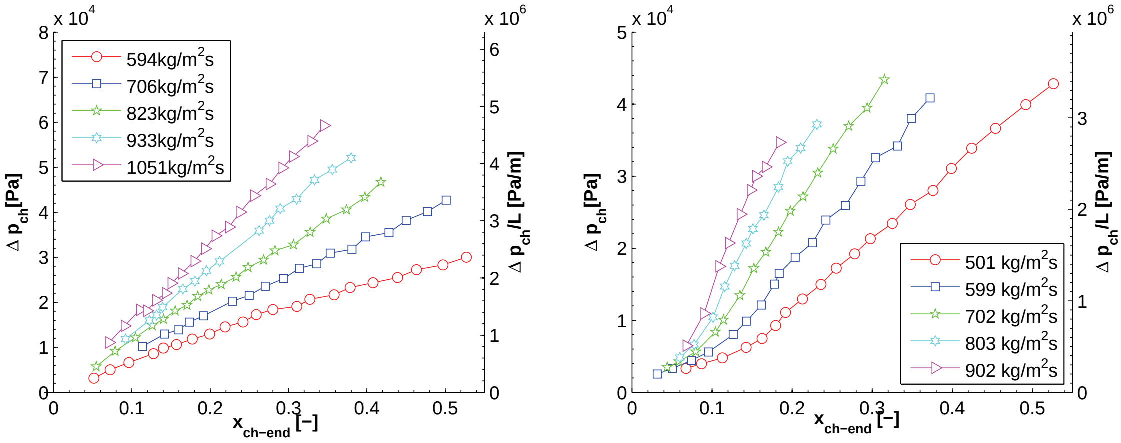

(a) R-236fa (b) R-245fa

Figure 4.9: Channel pressure drops in silicon test section.

Figs 4.9(b) and 4.10(e). In the first graph, at 501kg/m^{2}s and for x=0.325, the pressure drop is 23’440Pa. For the copper test section, at 367kg/m^{2}s, for the same vapor quality, the pressure drop is 6682Pa, a ratio of 3.5 between the two. This is larger than the 2.8 factor previously found, but quite close considering that the experimental mass fluxes were different.

Comparing the fluids, Figs 4.9 and 4.10 show that the pressure drops for R-245fa are the highest. This is once again explained by the high liquid to vapor density ratio of R-245fa, provided in Table 3.2, which is twice that of R-236fa and four times that of R-134a. For a given vapor quality, the vapor portion of R-245fa needs to move faster to respect the conservation of mass and in doing so, produces more shear.

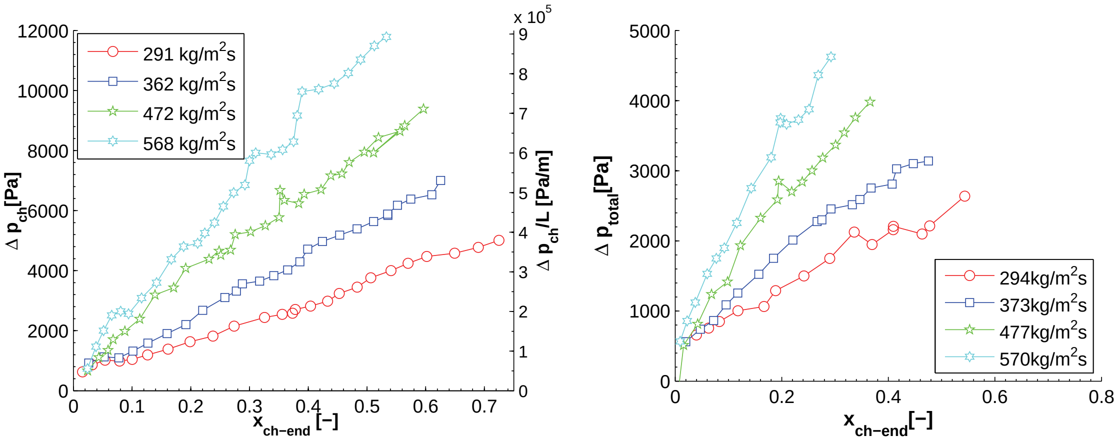

(a) R-134a, T$_{sat}$=30.5°C (b) R-134a, T$_{sat}$=50.8°C

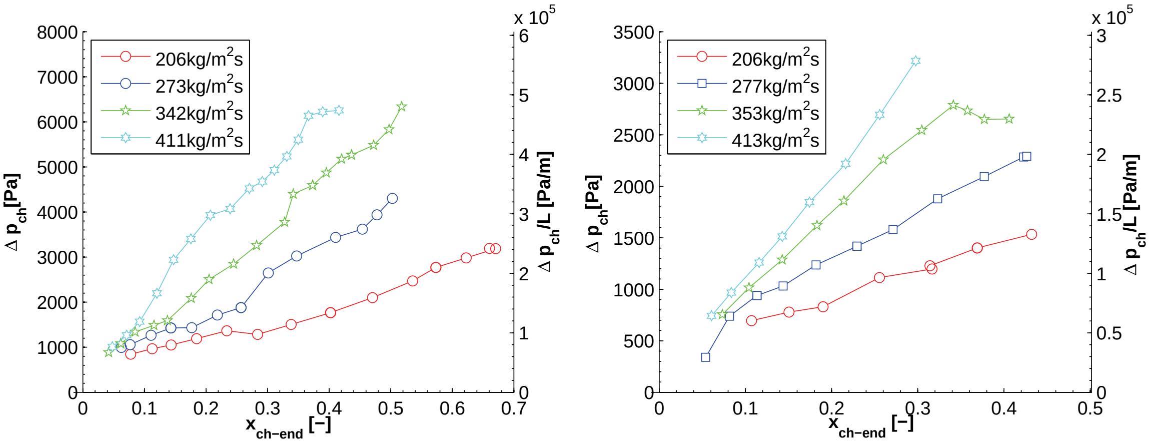

(c) R-1234ze(E), T$_{sat}$=30.7°C (d) R-1234ze(E), T$_{sat}$=50.1°C

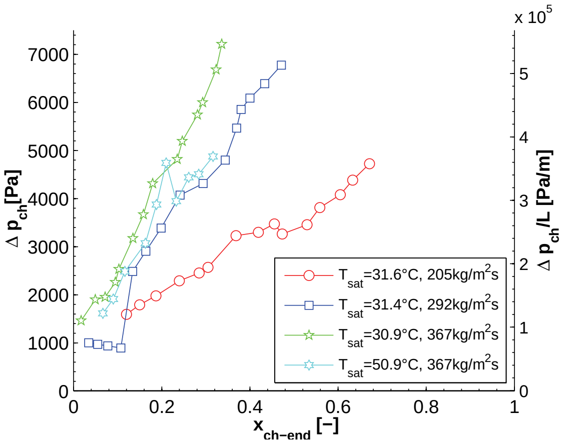

(e) R-245fa

Figure 4.10: Channel pressure drops in copper test section.

4.3.4 Temperature

The channel pressure drop is used to determine the local fluid saturation temperature and subsequently the local heat transfer coefficients. Thus the pressure drop values given in Figs 4.9 and 4.10 also tell what is the fluid temperature drop from one end of the channel to the other. If the pressure drop is small, the fluid temperature is almost constant. In such case, the evaporator thermal performance is independent from hydraulic considerations, which simplifies the design process.

In Fig 4.11, the drop in saturation temperature associated with the pressure drop are shown for both test sections using the respective vapor pressure curves. The temperature changes in the copper test section are much lower than in the silicon test section. In the case of R-134a and R-1234ze(E) below Δp_{ch}=6000Pa, the temperature drops are less than three times the measurement accuracy. For these two fluids, a constant fluid temperature boundary condition can certainly be used for numerical simulations, although the actual values were used for reducing the heat transfer coefficient.

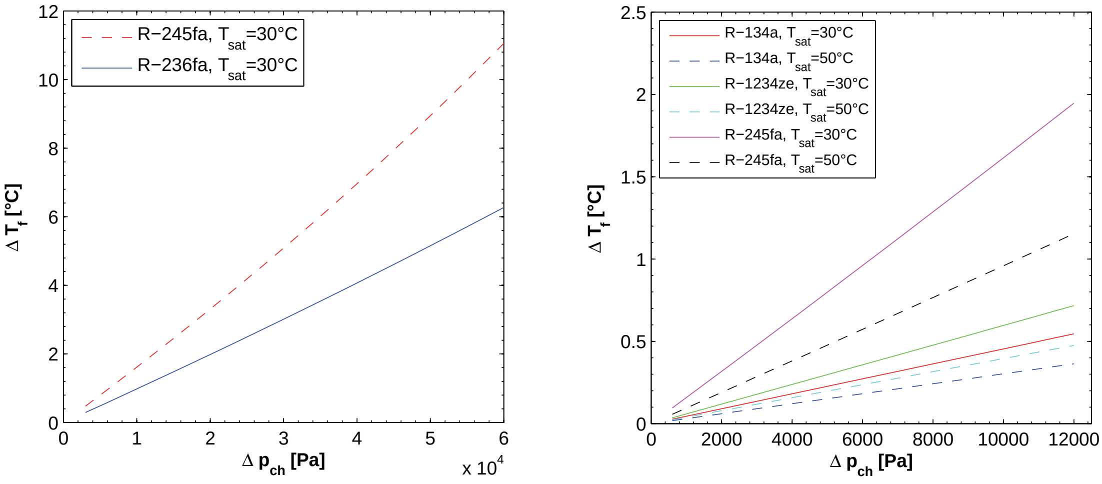

(a) Silicon test section (b) Copper test section

Figure 4.11: Fluid temperature drop versus pressure drop.

4.3.5 Comparison with prediction methods

Most pressure drop prediction methods cited in the state of the art review were developed for circular tubes and applying them to high aspect ratio cross-sections can be problematic. Three methods were developed using data derived from rectangular microchannels, those of Tran *et al.* (1999), Lee & Garimella (2008) and Lee & Mudawar (2005b), although neither had aspect ratios over 3.6 while the present ratios were 6.6 (silicon test section) and 10 (copper test section). Along with these three correlations, the homogeneous model with Cicchitti *et al.* (1960)'s viscosity model, the separated flow model of Lockhart & Martinelli (1949) and the methods of Cioncolini *et al.* (2009), Friedel (1979), Mueller-Steinhagen & Heck (1986), Mishima & Hibiki (1996) and Baroczy (1965), adapted by Chisholm (1973) will be compared to the experimental results.

The method of Cioncolini *et al.* (2009) cannot handle low vapor qualities as it was derived for annular flows. Thus at low vapor qualities, the method of Lockhart & Martinelli (1949) will be used and after the IB–CB transition vapor quality predicted by the map of Ong & Thome (2011a) is reached, Cioncolini *et al.* (2009) will be applied. The momentum pressure drop component will be included in the comparisons. To calculate it, Zivi (1964)'s void fraction method was be used if the authors did not specify another one. Finally, each method will be evaluated using three different definitions for the hydraulic diameters:

$$D_h = \frac{4A}{P} \tag{4.4}$$

$$D_h = \frac{2WH}{W+H} \tag{4.5}$$

$$D_h = \sqrt{\frac{4WH}{\pi}} \tag{4.6}$$

The last one is also called the equivalent diameter, as it gives a circle of the same area as the rectangle. The actual mass flux is inputed into the calculation and it is only the value of the diameter that changes. For the silicon test section, the first two definitions give the same value of D_h=146 μm, and the last equation gives D_h=246μm. In the copper test section, the three hydraulic diameters are respectively: 246μm, 294μm and 567μm.

Tables 4.2 and 4.3 list the mean average error (MAE) obtained for each prediction method with each definition of hydraulic diameter. For each test section, the four best predictions, based on the mean value of MAE for all fluids, are highlighted. These are found for the two first definitions the hydraulic diameter. Thus the equivalent diameter version of D_h is not a good choice to extend circular pipe correlations to high aspect ratio channels.

Three prediction methods are in the top four for both test sections: Cioncolini *et al.* (2009), Lockhart & Martinelli (1949) and Lee & Mudawar (2005a). A visual comparison of these methods against all experimental channel pressure drops is shown in Fig 4.12. Cioncolini *et al.* (2009)'s method can be considered as the best method, as it centers the data well around the middle line, whereas the two other tend to underestimate the channel pressure drop. Notably, the larger pressure drops are more accurately predicted, i.e. those in the silicon test section.

Table 4.2: Mean average error for silicon test section.

$D_h = 146\mu m$	R-236fa	R-245fa	Mean
Baroczy (1965)	17.4	86.1	51.8
Cioncolini *et al.* (2009)	**5.3**	**32.5**	**18.9**
Friedel (1979)	37.0	305.6	171.3
Homogeneous model	19.0	271.7	145.4
Lee & Garimella (2008)	59.7	48.2	54.0
Lee & Mudawar (2005a)	**20.7**	**50.0**	**35.4**
Lockhart & Martinelli (1949)	**28.7**	**41.8**	**35.3**
Mishima & Hibiki (1996)	65.7	50.9	58.3
Mueller-Steinhagen & Heck (1986)	**27.0**	**43.3**	**35.2**
Tran *et al.* (1999)	6.5	119.6	63.1
$D_h = 246\mu m$	R-236fa	R-245fa	Mean
Baroczy (1965)	52.1	32.4	42.3
Cioncolini *et al.* (2009)	77.7	70.3	74.0
Friedel (1979)	46.3	41.0	43.7
Homogeneous model	42.4	41.7	42.1
Lee & Garimella (2008)	69.9	54.6	62.3
Lee & Mudawar (2005a)	47.1	42.5	47.1
Lockhart & Martinelli (1949)	59.7	44.7	52.2
Mishima & Hibiki (1996)	78.5	65.9	72.2
Mueller-Steinhagen & Heck (1986)	51.2	30.9	41.1
Tran *et al.* (1999)	57.8	31.3	44.6

Table 4.3: Mean average error for copper test section.

$D_h = 246\mu$m	R-134a	R-1234ze(E)	R-245fa	Mean
Baroczy (1965)	31.0	20.0	53.0	34.7
Cioncolini *et al.* (2009)	50.7	56.1	94.3	67.0
Friedel (1979)	29.5	24.6	192.1	82.1
Homogeneous model	41.0	26.3	149.3	72.2
Lee & Garimella (2008)	57.8	51.6	42.7	50.7
Lee & Mudawar (2005a)	**31.8**	**34.2**	**38.6**	**34.9**
Lockhart & Martinelli (1949)	**43.2**	**35.7**	**29.2**	**36.0**
Mishima & Hibiki (1996)	66.3	59.5	49.4	58.4
Mueller-Steinhagen & Heck (1986)	49.7	41.4	22.0	37.7
Tran *et al.* (1999)	42.2	27.7	43.6	37.8
$D_h = 294\mu$m	R-134a	R-1234ze(E)	R-245fa	Mean
Baroczy (1965)	**42.4**	**30.9**	**28.9**	**34.1**
Cioncolini *et al.* (2009)	**35.0**	**35.7**	**36.3**	**35.6**
Friedel (1979)	44.0	27.7	108.4	60.0
Homogeneous model	52.2	37.6	86.6	58.8
Lee & Garimella (2008)	61.8	56.5	45.9	54.7
Lee & Mudawar (2005a)	42.6	45.0	44.0	43.7
Lockhart & Martinelli (1949)	53.1	47.7	35.7	45.5
Mishima & Hibiki (1996)	71.5	66.3	54.4	64.1
Mueller-Steinhagen & Heck (1986)	56.6	49.5	24.3	43.5
Tran *et al.* (1999)	55.5	43.6	21.0	40.0
$D_h = 567\mu$m	R-134a	R-1234ze(E)	R-245fa	Mean
Baroczy (1965)	68.8	63.7	41.7	58.1
Cioncolini *et al.* (2009)	79.7	73.4	70.5	74.5
Friedel (1979)	75.5	69.5	39.0	61.3
Homogeneous model	70.7	66.1	26.6	54.5
Lee & Garimella (2008)	67.8	65.5	52.0	61.8
Lee & Mudawar (2005a)	67.6	68.7	62.2	66.3
Lockhart & Martinelli (1949)	74.1	72.6	59.8	68.8
Mishima & Hibiki (1996)	81.2	79.4	69.5	76.7
Mueller-Steinhagen & Heck (1986)	70.2	66.3	40.7	59.1
Tran *et al.* (1999)	78.3	75.2	58.1	70.5

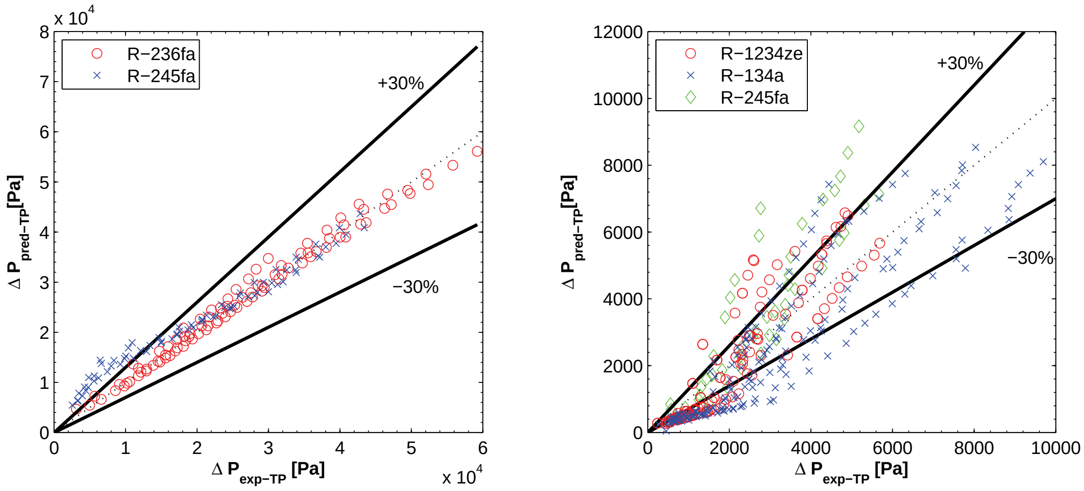

(a) Cioncolini *et al.* (2009), Silicon test section (b) Cioncolini *et al.* (2009), Copper test section

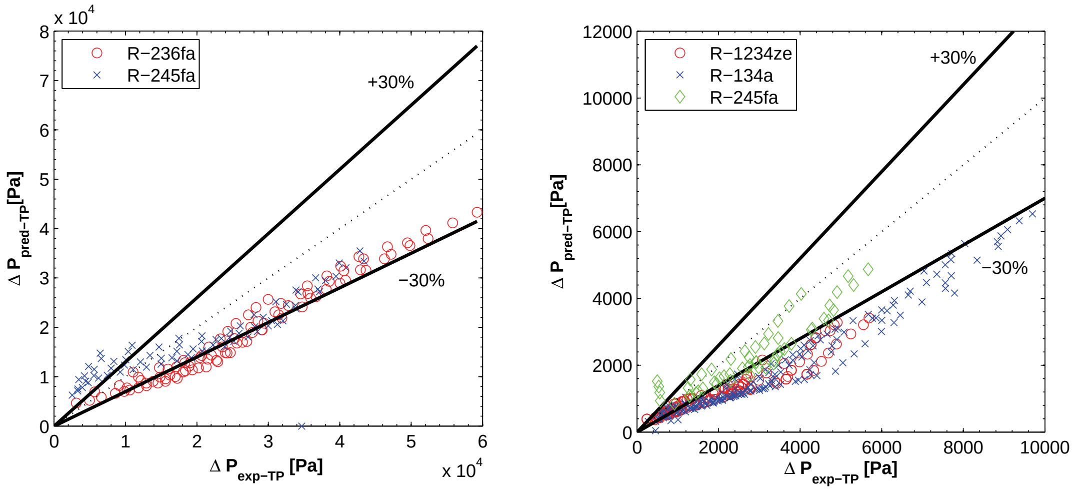

(c) Lockhart & Martinelli (1949), Silicon test section (d) Lockhart & Martinelli (1949), Copper test section

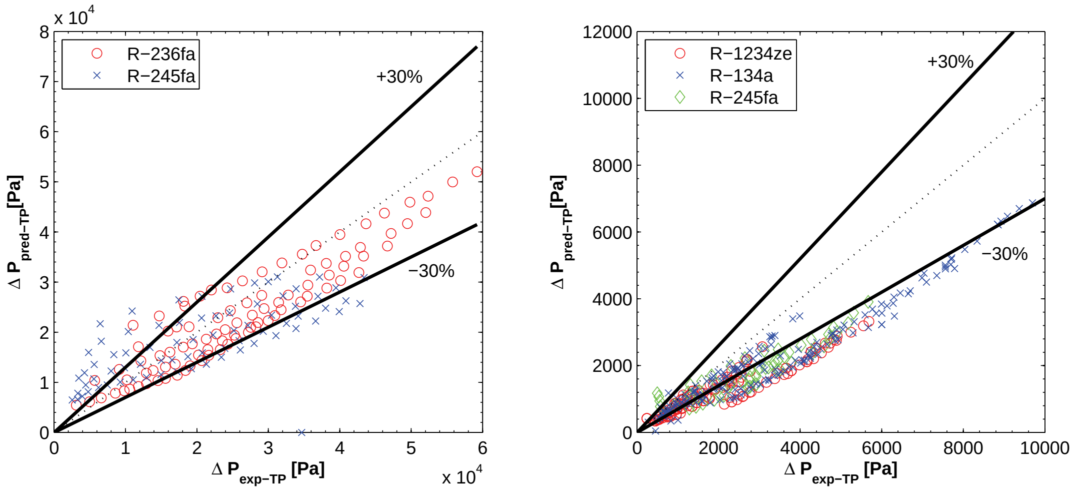

(e) Lee & Mudawar (2005a), Silicon test section (f) Lee & Mudawar (2005a), Copper test section

Figure 4.12: Comparison with best channel pressure drop prediction methods.

With mean average errors of 30%, the choice of the pressure drop model can then have consequences on the determination of the heat transfer coefficients, especially in the case of the silicon evaporator, where the change in fluid temperature can be important. In Fig 4.13, the different fluid temperature profiles computed using the best prediction methods are shown for R-236fa and R-134a in the silicon and copper test sections for high heat fluxes. In the copper test section, the largest temperature difference between the methods is 0.3°C, found at the end of channel. Since the wall to fluid temperature difference at q_w=334kW/m^2 is larger than 15°C, the pressure model chosen has little consequence in the calculation of the heat transfer coefficients. On the other hand, in the silicon test section, the largest temperature difference is about 2°C, found around z=8mm, for a wall to fluid temperature difference of 13°C for a linear pressure drop. Thus in the silicon test section, between the pressure models, there is a 15% difference in the calculation of the heat transfer coefficient due to the evaluation of the fluid temperature.

For evaluation of the heat transfer coefficient under uniform heat flux, the linear pressure drop model was used as is common in the literature (e.g. Lin *et al.* (2001), Karyiannis *et al.* (2010) and Ong & Thome (2011b)). Although the pressure drops are not in fact linear, it is the only model that insured that the measured channel inlet and end pressures were respected.

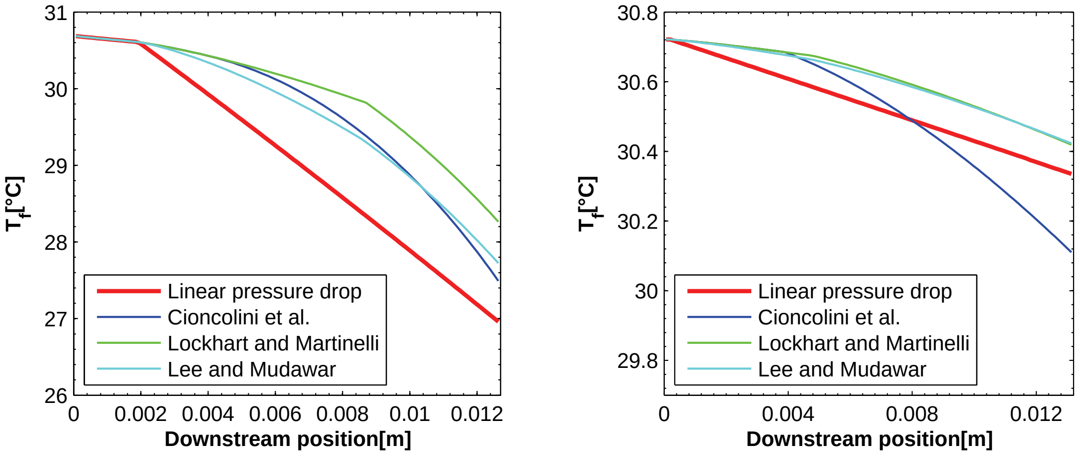

(a) Silicon test section, R-236fa at 933kg/m^{2}s, T_{sat}=31.1°C and q_w=160kW/m^2

(b) Copper test section, R-134a at 473kg/m^{2}s, T_{sat}=30.4°C and q_w=332kW/m^2

Figure 4.13: Comparison with best channel pressure drop prediction methods.

4.4 Total pressure drop

For the design of efficient cooling systems, knowing the total pressure drop over the test section is imperative. If the total pressure drop is very low, a pump-free system such as a thermosyphons could be used to drive the system. In this arrangement, the fluid circulation is induced by a column of liquid. Taking into consideration that in current datacenters, two meter high columns are possible, around 24kPa would be available to run a pump-free system.

In Figs 4.14 and 4.15 are plotted the total pressure drops for the silicon and copper test sections. The total pressure drop increases approximately linearly with the vapor quality. Extending these trends to x=0 gives an estimate of what would be the single-phase pressure drop over the test section. It is lower than the two-phase pressure drop, but as it was pointed out in the state of the art review, a flow of single-phase refrigerant is not able to meet the thermal requirement of chip cooling.

As it can be expected from the channel pressure drop results, the silicon test section has higher total pressure drops than the copper ones. In the latter case, the total pressure drop remains well below 20kPa for all cases, such that a pump-free cooling system could be possible. In fact, except with R-134a for 472kg/m^{2}s and 569kg/m^{2}s at T$_{sat}$=30°C, the values of total pressure drop in the copper test section remain below 10kPa. This corresponds to a liquid column height of less than one meter, well within what is achievable in a datacenter. Therefore, with a careful sizing of the other elements in the cooling systems, it could possible to bring the overal pressure drop of the system below the 20kPa.

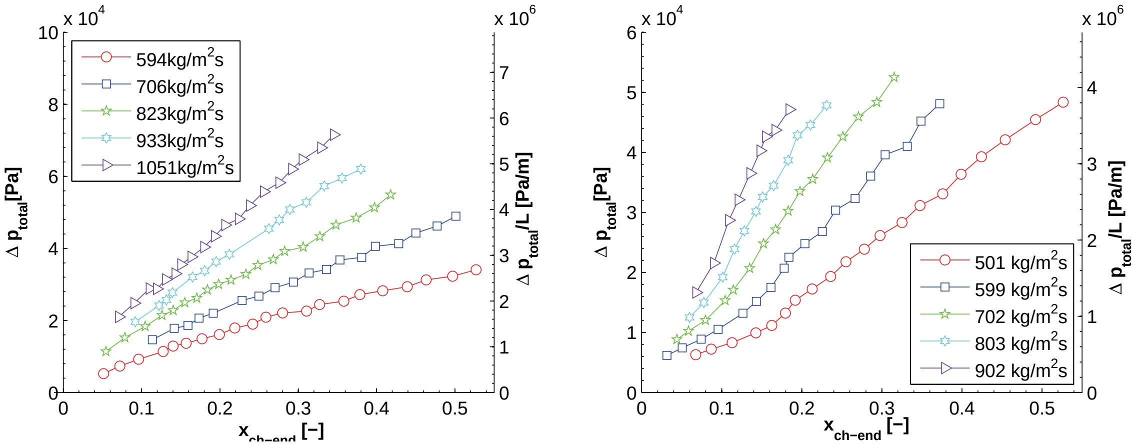

(a) R-236fa (b) R-245fa

Figure 4.14: Total pressure drop in silicon test section.

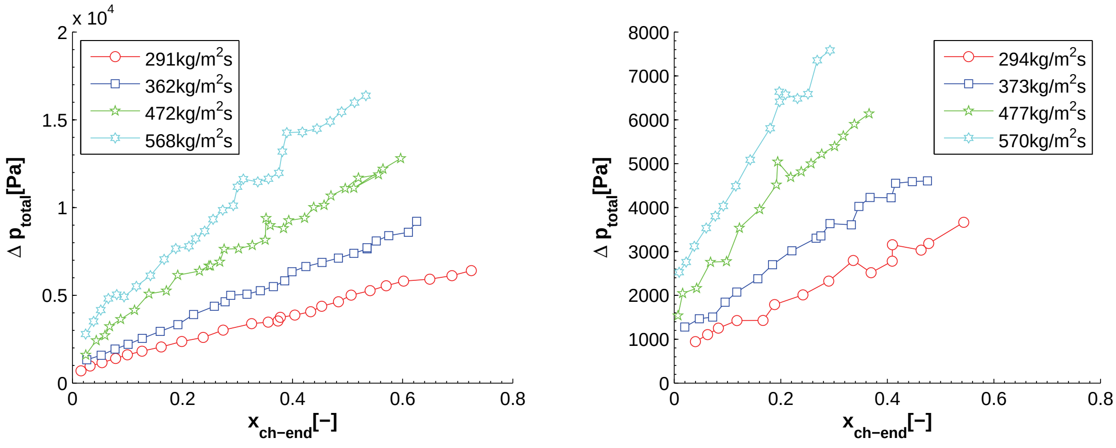

(a) R-134a, T$_{sat}$=30.5°C (b) R-134a, T$_{sat}$=50.8°C

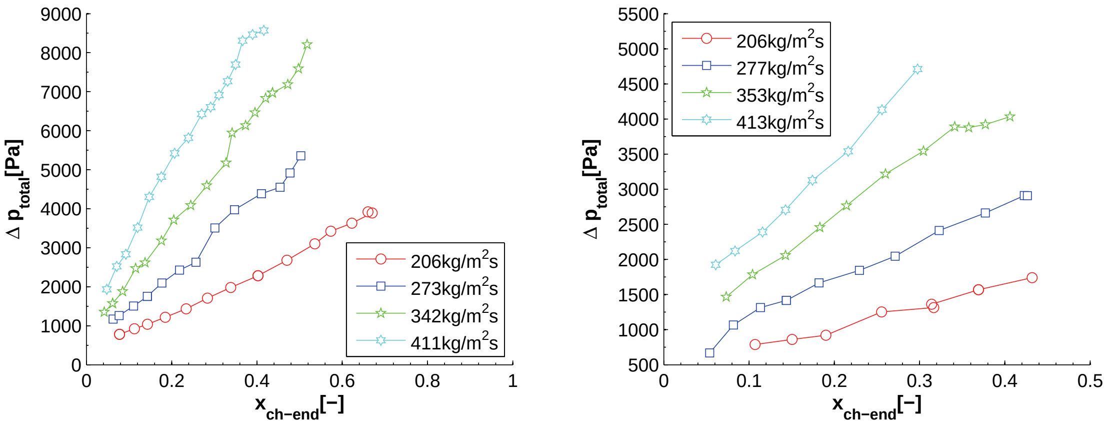

(c) R-1234ze(E), T$_{sat}$=30.7°C (d) R-1234ze(E), T$_{sat}$=50.1°C

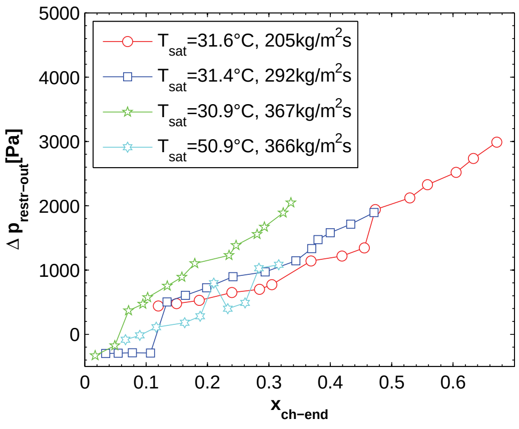

(e) R-245fa

Figure 4.15: Total pressure drop in copper test section.

4.4.1 Pressure drop ratios

Using the inlet and outlet restriction pressure losses and the channel pressure drop, it is possible to evaluate the relative importance of each component in the total pressure drop. With this information, it will be then be possible to assess which part of the test section should be improved to reduce the total pressure drop. The ratio of the channel, inlet and outlet pressure components divided by the total pressure drop are plotted in Figs 4.16 and 4.17. Note that some graphs were placed in Appendix B to lighten the text.

Since at the outlet, pressure recovery sometimes occured, the outlet pressure ratio are sometimes negative at low vapor qualities. When this happens, the ratio of the two other pressure component increases and it is possible that in the case of the channel pressure that the ratio goes over 1.

In the silicon test section, the channel pressure drop is by far the most important pressure drop component. For $x_{ch-end} > 0.2$ is represents more than 70% of the total pressure drop and it does not fall below 45%. At low vapor quality, the inlet and outlet restriction losses in the silicon test section can represent half the pressure drop, equally distributed between the inlet and the outlet. Pressure recovery is seen for R-236fa at low mass fluxes, Fig 4.16(e). In the case of R-245fa, the importance of the outlet losses falls for $x_{ch-end} < 0.1$.

The importance of the inlet restriction pressure drop decreases rapidly with vapor quality. For $x > 0.4$, it tends towards 5%. The outlet restriction represents about 10 to 15% of the total losses at high vapor qualities. In the case of R-236fa, the outlet losses become independent of the mass flux for $x_{ch-end} > 0.3$, whereas for R-245fa, this happens for $x_{ch-end} > 0.15$.

Similarly the importance of the inlet pressure restriction in the copper test section is small. The channel pressure drop remains the most pressure component in the copper test section, but it tends towards lower ratios. At high vapor qualities, the outlet restriction pressure drops are high, representing 10 to 20% of the total pressure drop and peaking at almost 40% in Fig 4.17(i).

This analysis of channel pressure drop stresses the importance of evaluating each pressure drop component (inlet, outlet, channel) individually. The outlet restriction pressure drop is an important factor, which has often been neglected, possibly leading to important error in pressure drop and heat transfer analysis. For example, in the silicon test section, if the outlet restriction losses were neglected and the outlet plenum pressure was used to calculate the fluid saturation temperature at the end of the channel, it would lead to a temperature of 0.8 °C lower for R-236fa, for a mass flux of 1051 kg/m^{2}s and $x_{ch-end} = 0.35$. The heat transfer coefficient would then be underestimated by 17% for a wall superheat of 4°C.

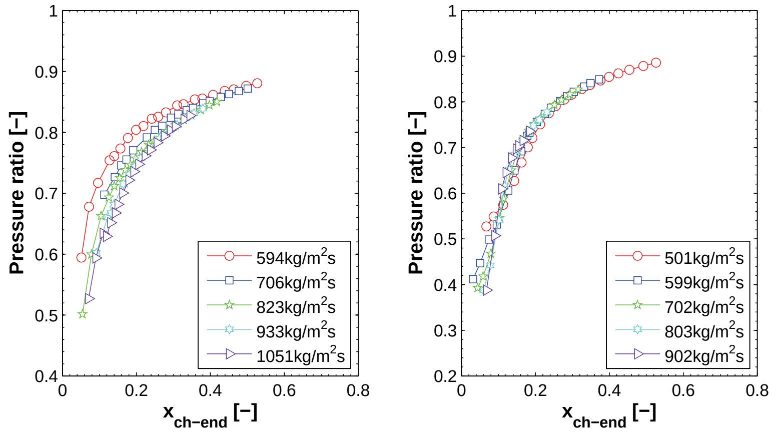

(a) R-236fa: Channel (b) R-245fa: Channel

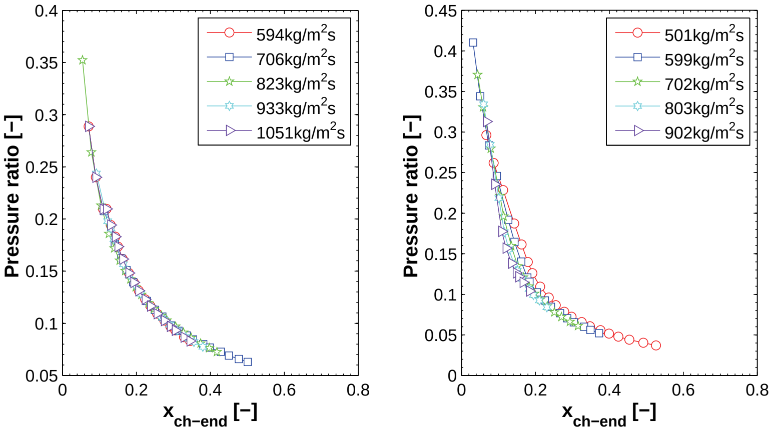

(c) R-236fa: Inlet restriction (d) R-245fa: Inlet restriction

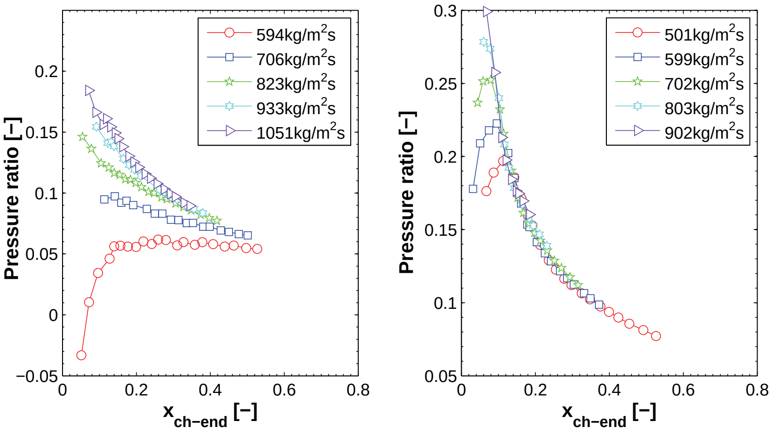

(e) R-236fa: Outlet restriction (f) R-245fa: Outlet restriction

Figure 4.16: Pressure drop ratios for silicon test section, T_{sat}=30°C.

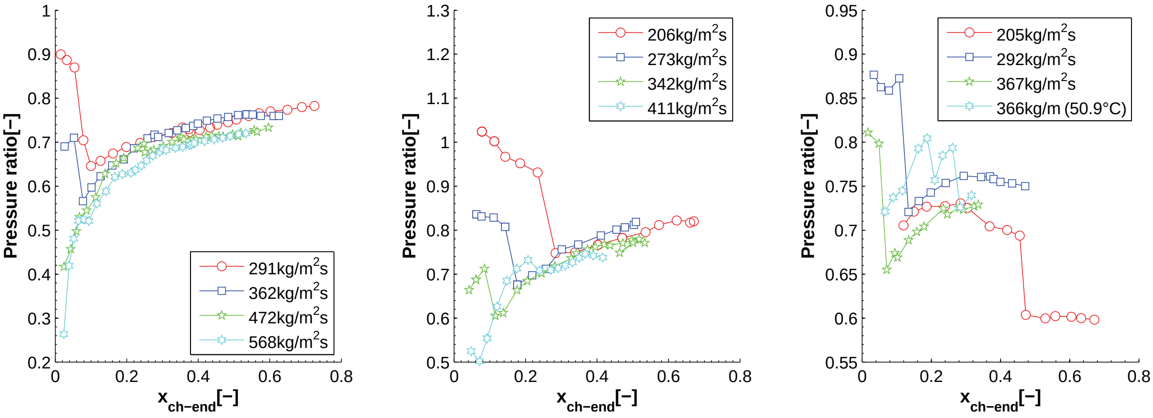

(a) R-134a: Channel (b) R-1234ze(E): Channel (c) R-245fa: Channel

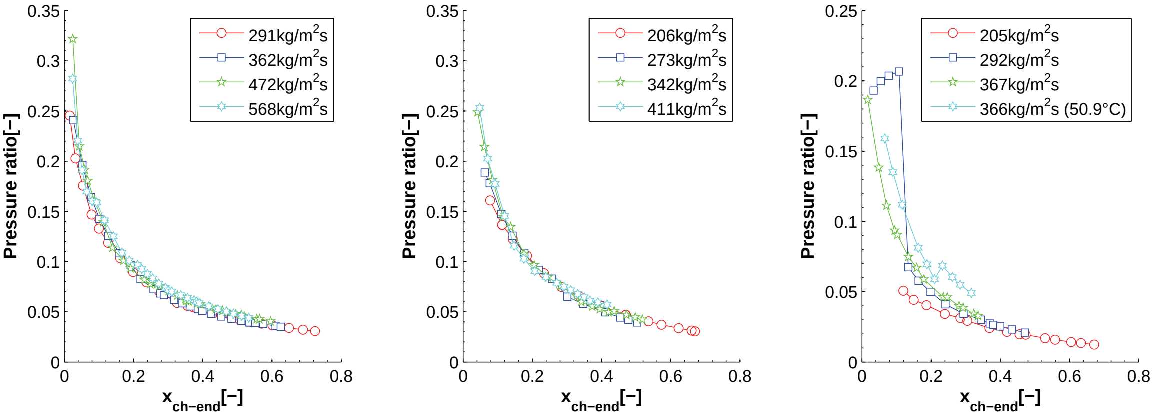

(d) R-134a: Inlet restriction (e) R-1234ze(E): Inlet restriction (f) R-245fa: Inlet restriction

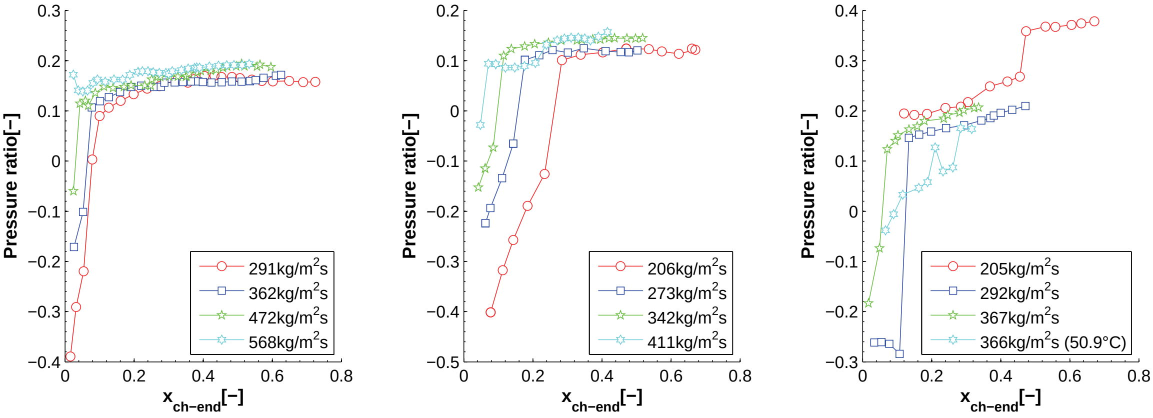

(g) R-134a: Outlet restriction (h) R-1234ze(E): Outlet restriction (i) R-245fa: Outlet restriction

Figure 4.17: Pressure drop ratios for copper test section, T$_{sat}$=30°C.

Chapter 5

Uniform heat flux: Heat transfer coefficients

The 35 temperature sensors provided simultaneous information about the heat transfer over the array heater. Therefore, the experimental database for heat transfer coefficients under uniform heat flux is very extensive. Experiments were performed at several mass fluxes, with four refrigerants, at two saturation temperatures and numerous heat fluxes.

5.1 Validation

Four different validations were done with respect to the local wall heat transfer coefficient results:

- Accuracy with respect to single-phase Nusselt predictions for subcooled liquid tests
- Exactness of the data reduction scheme
- Lateral uniformity of the results
- Repeatability of the results

5.1.1 Single-phase Nusselt number

As discussed in the state of the art review, the results tabulated by Shah & London (1978) for hydrodynamicaly and thermally developing laminar flows can be expressed in a Taylor series expansion as (Olivier (2008)):

$$Nu_x = 3.04 + \frac{0.0244}{z^*} + 0.448\gamma - \frac{2.69 \times 10^{-5}}{z^{*2}} - 0.02\gamma^2 - \frac{6.78 \times 10^{-4}}{z^*\gamma} \tag{5.1}$$

where

$$z^* = \frac{\pi}{4} \frac{z}{RePrD_h} \tag{5.2}$$

and γ is the aspect ratio W/H. This expression has been compared versus subcooled liquid heat transfer data taken in the test section. As z* increases, the value of Nusselt number tends toward is fully developped value, respectively 5.1 and 5.5 for the silicon and the copper test sections.

Silicon test section

In the silicon test section, single-phase experiments were performed with subcooled liquid flow of R-236fa and R-245fa. For this last fluid, the validation could only be made on a narrow range of Reynolds numbers. For the tests, the refrigerant entered the evaporator at 22°C and the fluid pressure was set high enough to avoid flow boiling. With R-236fa, the tests were performed at 12 mass fluxes from 275 to 1400kg/m^{2}s. The base heat fluxes were varied between 40kW/m^2 and 350kW/m^2. In the case of R-245fa, 4 mass fluxes from 1500 to 2080kg/m^{2}s were tested between 360kW/m^2 and 540kW/m^2. A one-dimensional thermal conduction scheme was used to reduce the data.

The local and average Nusselt numbers measured versus the Reynolds number are shown in Fig 5.1, and they are compared to the prediction method of Shah & London (1978) for hydrodynamically and thermally developing laminar flow. In the top graphs results for Nu$_x$ against z* are plotted. The lateral average of these local Nu$_x$ are plotted in the middle graphs, which shows that across the evaporator's columns the differences in heat transfer are small. In the bottom graphs, the evaporator mean Nusselt number is plotted against the Reynolds number of the microchannels.

The bottom Nu$_m$ graphs show that above Re$_{av}$ = 400 the experimental results are in good agreement with the predictions. The deviation at low Reynolds numbers is probably due to conjugate conduction effects in the evaporator and to the differences between the experiment and the simulations of Shah & London (1978): heating from three sides, two of which being fins, instead of four in their case and having a non-uniform channel inlet velocity. The perturbations are better seen on the local Nusselt number plot, Figs 5.1(a) and 5.1(b), showing that the best local agreement is obtained at high Reynolds numbers and toward the end of the channel. As shown in Table 5.1, the average results agree well with the prediction method. For R-236fa, 91% of Nu$_m$ (Fig 5.1(e)) datapoints are within ±20% of predicted values, while 82% of the local values (Fig 5.1(a)) are predicted to within ±20%. For R-245fa, all Nu$_m$ (Fig 5.1(f)) are within ±20% and, 85% of Nu$_x$ (Fig 5.1(b)) within ±20%. Note tha the test section was not designed for measuring single-phase heat transfer coefficients. especially not at low Reynolds number, Hence overall, the agreement with Shah & London (1978) is excellent, which validates the instrumentation and the data reduction for the silicon test section.

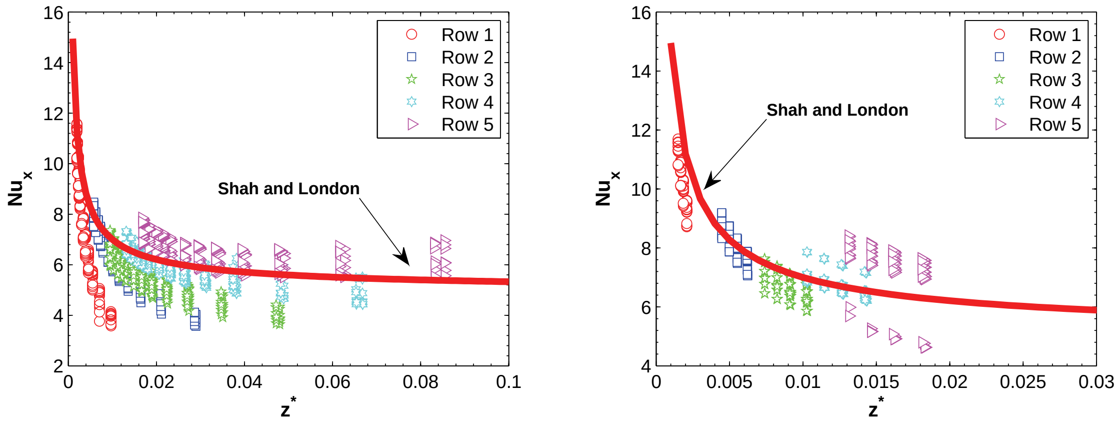

(a) R-236fa, All Nu$_x$ (b) R-245fa, All Nu$_x$

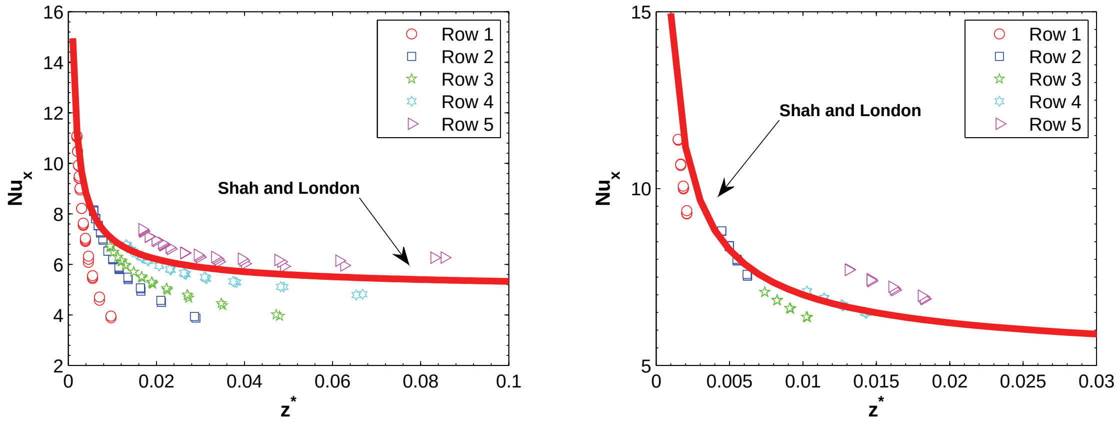

(c) R-236fa, Lateral average Nu$_x$ (d) R-245fa, Lateral average Nu$_x$

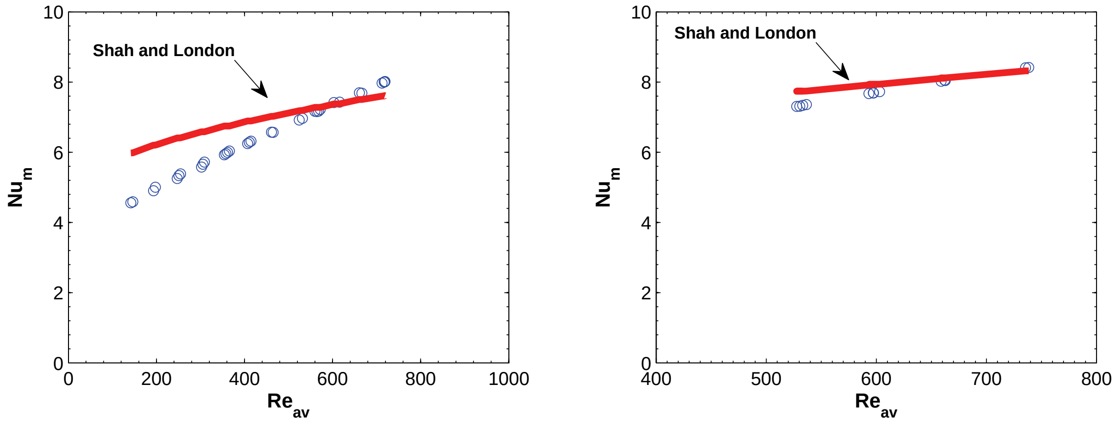

(e) R-236fa, Nu$_m$ (f) R-245fa, Nu$_m$

Figure 5.1: Single-phase validation of Nusselt number in the silicon test section.

Table 5.1: Mean average error and accuracy for single-phase Nusselt number

	Nu_x MAE – Within ±20%	Nu_m MAE – Within ±20%
Si: R-236fa	12% – 82%	9% – 91%
Si: R-245fa	9% – 91%	3% – 100%
Cu: R-134a	23% – 83%(with error band)	7% – 93%
Cu: R-1234ze	23% – 75%(with error band)	10% – 80%

Copper test section

The same validation tests were performed on the copper test section with R-134a and R-1234ze. It was not possible to reach more than Re=400 with R-245fa, such that the single-phase validation could not be made for this fluid. The data reduction in the copper test section presents other difficulties. Since copper is about four times more conductive than silicon, conduction effects are more important in the copper test section. The top view of the evaporator in Fig 3.3(b) shows that the copper frame surrounding the multi-microchannels is large and in single-phase flow, this mass will redistribute the heat flux towards the colder inlet. Two measures were then taken to counter heat spreading in the copper test section. First, a two-dimensional conduction scheme was used for the data reduction to include the flow-wise heat spreading. Second, the results from Columns 1 and 7 were not used, because the copper frame also pulled heat flux through the side of the evaporator area and measurement zones most affected by this effect were Columns 1 and 7. Both of these measures will be also applied to the data reduction for two-phase flow.

The local and average Nusselt numbers obtained in the copper test section in Fig 5.2 are compared to Shah & London (1978)'s method. The values obtained for Nu_m are well predicted; the mean average error for R-134a was 7% and for R-1234ze, 10%. It was possible to reach transitional flow regime ($\mathrm{Re}\geq1200$) with R-134a and the correlations of Pethukov (1970) for turbulent flow and Olivier (2009) for transitional flow in smooth pipe were used for the comparison. The results for laminar Nu_x are scattered around Shah & London (1978)'s prediction, but once the error bars are taken into account, most datapoint uncertainties cover the predicted values. For R-134a 83% of the data, including the error bars, falls within ±20%. For R-1234ze, the number of data within ±20% is 75%. Taking the lateral average of Nu_x centers the data on the prediction line.

The test sections were designed and instrumented for two-phase flow boiling experiments and for low Reynolds number single-phase heat transfer tests, the instrumentation was not appropriate to measure heat spreading. Thus some single-phase test results will lie outside the predicted values and the validations cannot be performed for all conditions. The importance of heat spreading is greatly reduced in flow boiling as the heat transfer coefficients are ten to thirty-fold higher. Thus, based on the results shown in Fig 5.2, the single-phase validations show that the instrumentation and the data reduction used for the copper test section are adequate for two-phase heat transfer coefficients experiments.

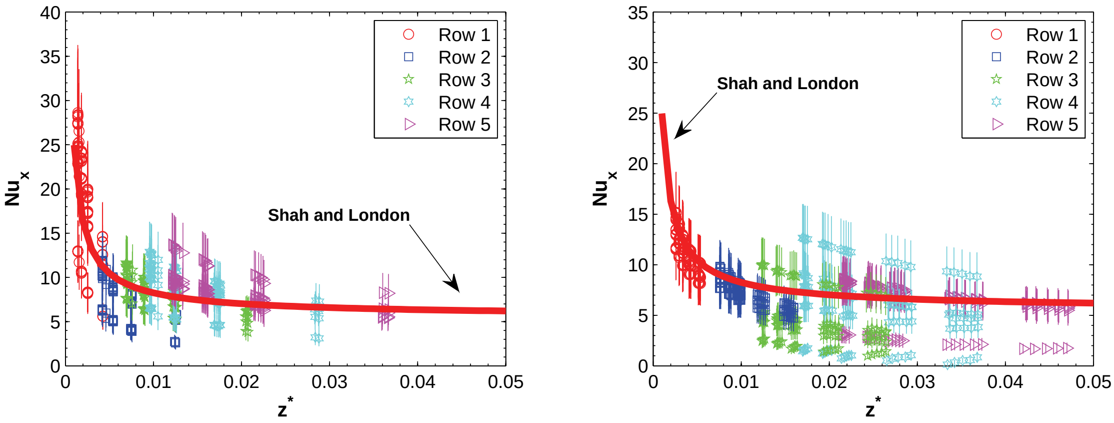

(a) R-134a, All Nu$_x$ (b) R-1234ze, All Nu$_x$

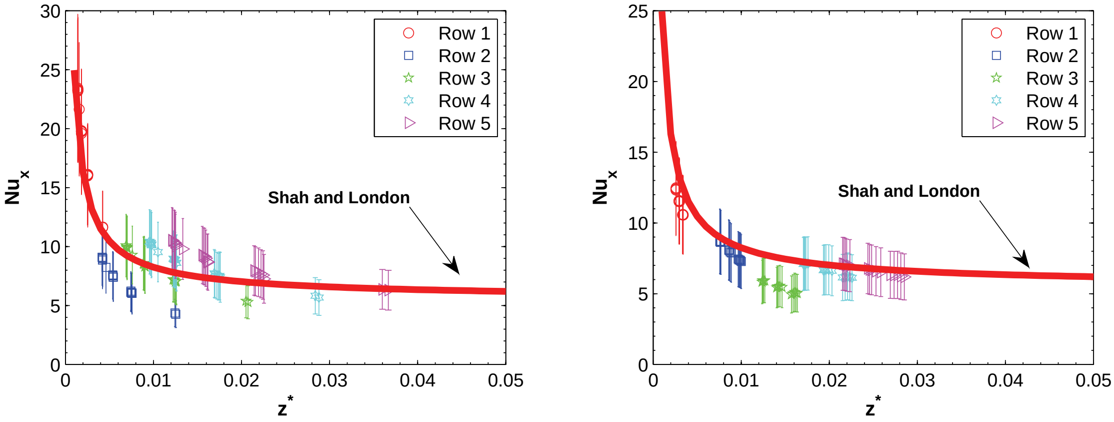

(c) R-134a, Lateral average Nu$_x$ (d) R-1234ze, Lateral average Nu$_x$

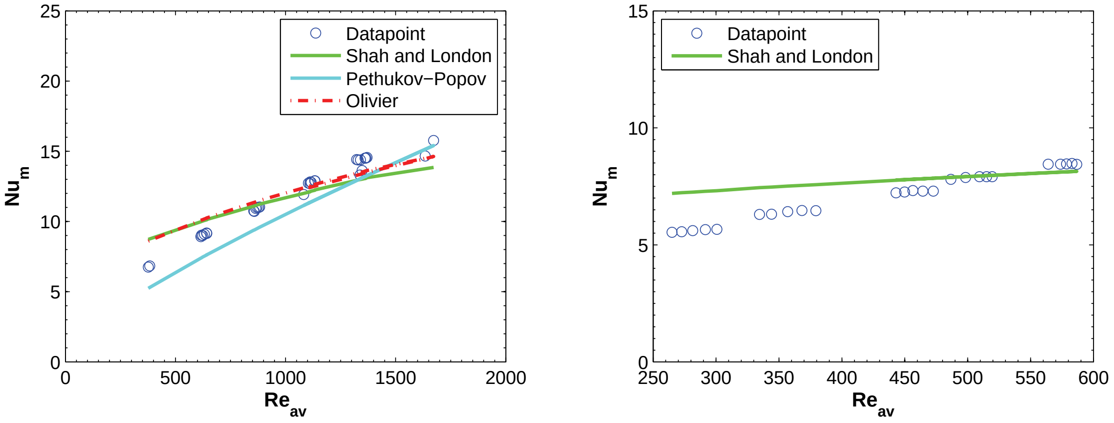

(e) R-134a, Nu$_m$ (f) R-1234ze(E), Nu$_m$

Figure 5.2: Single-phase validation of Nusselt number in the copper test section.

5.1.2 Thermal conduction data reduction scheme

For the data reduction of two-phase flow results, the thermal conduction schemes used in single-phase validations were applied to the experimental measurements. It is important to show that the thermal conduction was well computed and for this, validations were performed with a numerical simulation program, COMSOL Multiphysics 4.0. This validation is actually a reverse calculation: the results of data reduction are used in the program to set the heat transfer coefficients and then the base temperatures are recalculated. If the results for base temperature agree with the measurements, then the exactness of the data reduction scheme is validated.

In simulations with COMSOL, all boundary conditions must be specified since the program used a different solving strategy than the data reduction scheme. The local heat transfer coefficients calculated through the data reduction were used to create a continuous function from z=0 to L to be input in COMSOL. Comparisons were then made between the measured base temperatures and those calculated by COMSOL using a one-dimensional conduction scheme for the silicon test section and a two-dimensional for the copper test section.

The results of these validations are shown in Fig 5.3(a) with R-236fa and in Fig 5.4(a) with R-1234ze(E) along with the input base ("footprint") heat transfer coefficient curve in Figs 5.3(b) and 5.4(b). The simulated base temperatures fall very close to the measured values, except for one point with R-236fa where the base temperature gradient is steep. The one-dimensional scheme used for the silicon test section does not capture the heat spreading due to this gradient and the calculated local wall heat flux is greater than the real one. Evenso, agreement is still good. The heat spreading is well captured by the two-dimensional conduction model used for the copper test section, which means that using a three-dimensional scheme is not needed for uniform heat flux tests. Thus, the thermal conduction models used for both test sections are accurate and can be used for the calculation of local heat transfer coefficients.

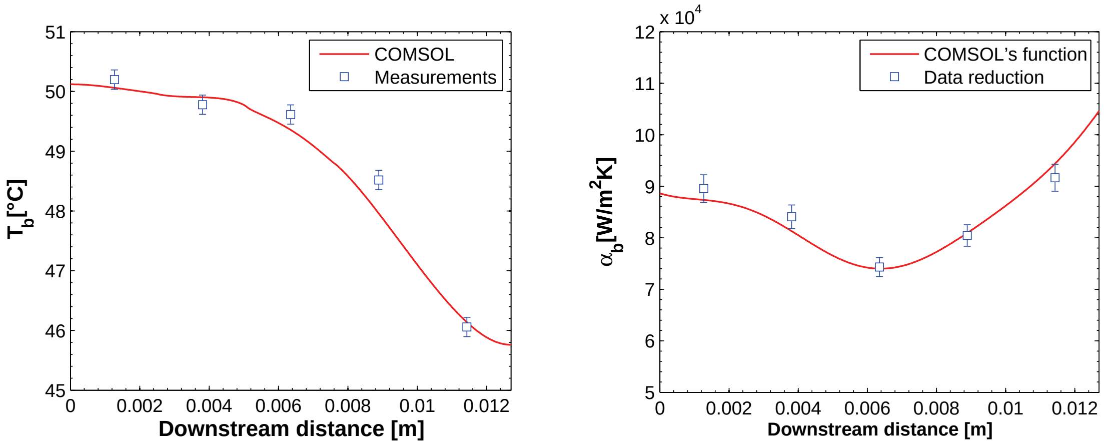

(a) Base temperature (b) Base heat transfer coefficients

Figure 5.3: Comparison between the one-dimensional thermal conduction data reduction and COMSOL Multiphysics' results for the silicon test section: R-236fa, 933kg/m^{2}s, Column 4, q_b=96.4W/cm^2.

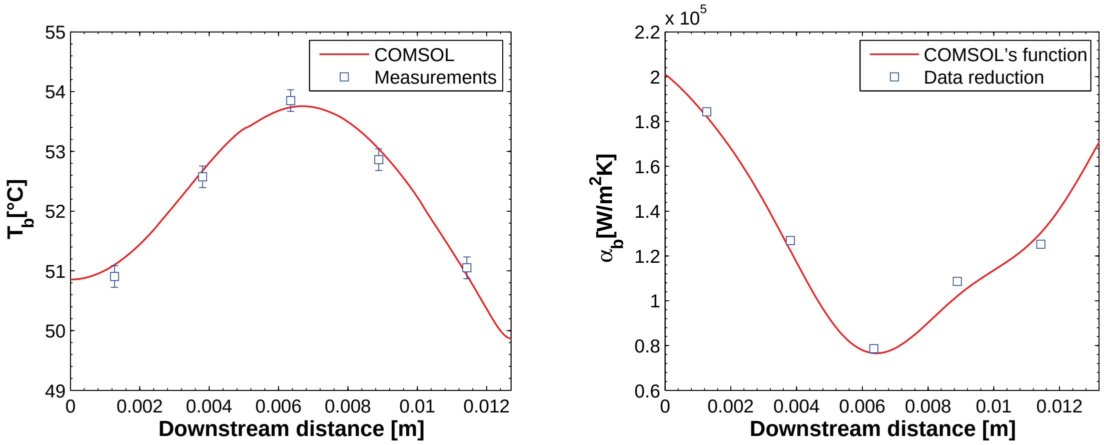

(a) Base temperature (b) Base heat transfer coefficients

Figure 5.4: Comparison between the two-dimensional thermal conduction data reduction and COMSOL Multiphysics' results for the copper test section: R-1234ze(E), 411kg/m^{2}s, Column 6, q_b=136.3W/cm^2.

5.1.3 Lateral heat transfer coefficients uniformity

In order to lighten the presentation of the results, the downstream evolution of the local heat transfer coefficients will be presented as a lateral average of the values in all columns. This is possible because the heat flux and mass flux in each channel are the same, such that in theory the local heat transfer coefficients at any lateral position will also be the same. However in practice, due to small geometrical variations between the channels, there will be differences in heat transfer. These will be more important when the local flow regime is sensitive to the wall geometry, for example for bubble generations and cyclical dry-outs.

In Fig 5.5, the profiles of heat transfer coefficients are plotted for two cases. In the silicon test section, the trends in each column are similar and the main difference is found at Row 3, where the minimum value of heat transfer is lower in Column 1 and 2. In the copper test section, the position of the minimum heat transfer coeffcient moves. In Columns 2 and 4 it is positioned over Row 3 and in the other columns over Row 4. The differences in trends are probably due to a delay in the flow regime transitions.

Since the heat transfer coefficients are not perfectly uniform laterally, the standard deviation will be reported on each graph and noted as the RMS value. A typical example is provided in Table 5.2. For all heat fluxes tested with R-236fa at 933kg/m^{2}s in the silicon test section, the mean standard deviation is 9.9% and for R-134a at 473kg/m^{2}s in the copper test section it is 15%. In comparison, the mean uncertainty in the calculation of the local wall heat transfer coefficients in the first case is 5.9% and in the second case is 6.1%. Later, however for the comparison of the heat transfer coefficients with different prediction methods, all measurements will be used.

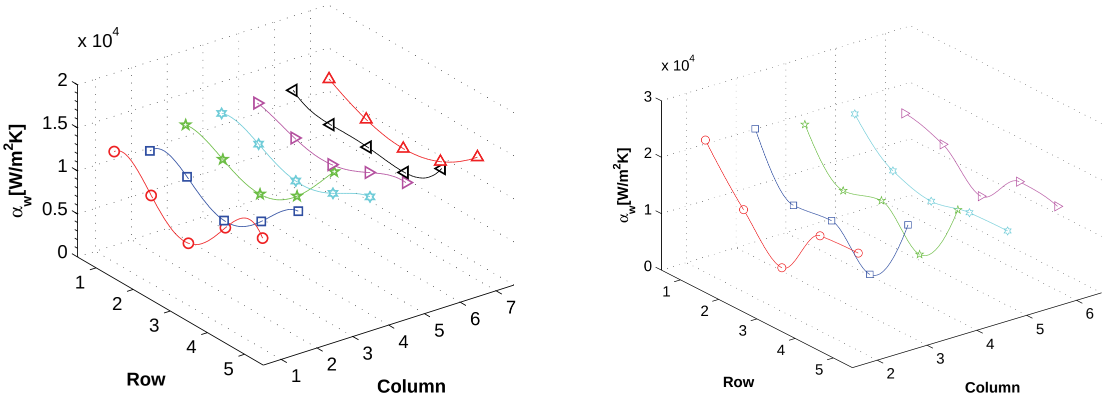

(a) Silicon test section: R-236fa, 933kg/m^{2}s, q$_b$=964kW/m^2, T$_{sat}$=31.1°C

(b) Copper test section: R-134a, 477kg/m^{2}s, q$_b$=1290kW/m^2, T$_{sat}$=50.7°C

Figure 5.5: Heat transfer coefficients in all columns.

Table 5.2: Ratio of lateral standard deviation over lateral mean value of the local heat transfer coefficient.

	Silicon test section R-236fa 933kg/m^{2}s,T$_{sat}$=31.1°C	Copper test section R-1234ze(E)(E) 412kg/m^{2}s, T$_{sat}$=50.6°C
Column 1	5.5%	10.0%
Column 2	8.0%	6.4%
Column 3	17.2%	17.6%
Column 4	7.1%	26.5%
Column 5	11.5%	14.6%
Mean	9.9%	15.0 %

5.1.4 Repeatability of the results

An important issue in flow boiling is the repeatability of the tests. The reproductibility of the heat transfer coefficient results are presented in Fig 5.6 for both test sections with R-245fa and R-134a using the lateral mean of the heat transfer coefficients. The different sets of data were recorded with about month interval between them referred to as Test 1 and Test 2. In each case, the results for both tests fall on the same trend curve for all heat fluxes. On the graphs, the spread around the trend lines for the Test 1 and 2 pairs are smaller than the heat transfer coefficient uncertainty and small offsets in vapor quality are observed due to experimentally setting the inlet subcooling. The results were therefore found to be very reproducible both over time and location on the test sections.

5.2 Uniform heat flux heat transfer coefficients

An experimental database for local heat transfer coefficients under uniform heat flux conditions was obtained for both test sections. The refrigerants were tested at two saturation

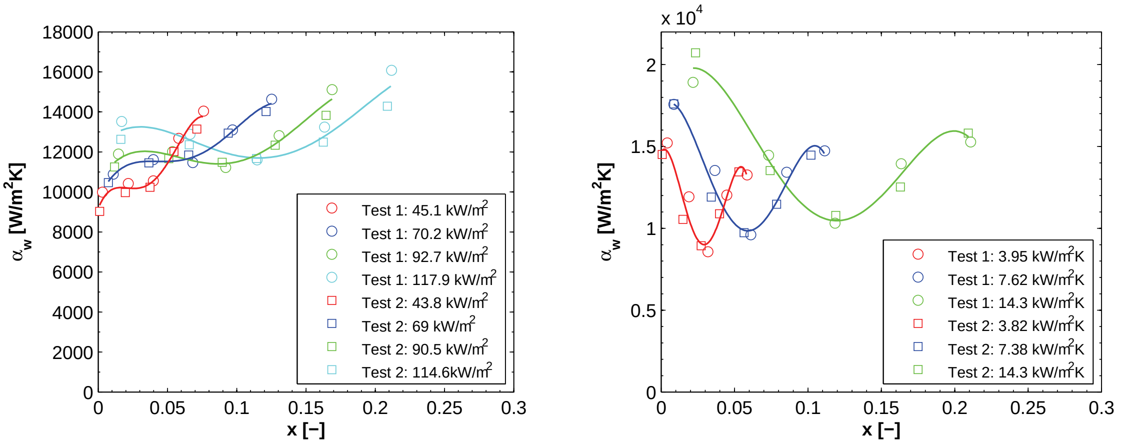

(a) Silicon test section: R-245fa, 702kg/m^{2}s (b) Copper test section: R-134a, 411kg/m^{2}s

Figure 5.6: Reproductibility of α_w at different wall heat fluxes.

temperatures, 31°C and 50°C and at mass fluxes from 205 to 569kg/m^{2}s. The heat flux was incrementally raised until the base temperature reached 85°C. Base heat fluxes varied from 130 to 2950kW/m^2 (13 to 295W/cm^2). No attempt was made to reach the critical heat flux, which was avoided to prolong the life of the test sections.

In order to report the results in a consistent fashion, the wall heat transfer coefficients are analyzed only with respect to the wall heat flux, accounting of course for the fin efficiency of the walls. For quick comparisons, multiplying the wall heat flux and heat transfer coefficients by 7 for the silicon test section and by 8 or the copper test section yields a value close to the equivalent "base area" heat transfer coefficient. Seven and eight are the rounded value of the right hand side coefficient multiplying $q_{b,xy}$ in equation 3.30.

Some temperature sensors were not used, seven in for the silicon test section and three for the copper test section, mostly because the connections of their temperature sensor failed during the flip-chip mounting process and the sensors did not work. In some instances, the sensors were working, but reported inconsistent results and were probably damaged. Lastly, in the copper test section, heater 15 was not properly wetted by the liquid metal and its readings were not used. For the multi-dimensional thermal conduction calculations, the temperature of a non-functioning sensor was replaced by the lateral average of the temperatures in the same row. Since the temperatures in one row were almost uniform, as shown in Fig 5.7 for the same cases as in Fig 5.5, this replacement will not affect the heat transfer calculations. Note that all power connections were working and thus all heaters were functioning for the experiments.

A representative sample to the results for average wall heat transfer coefficients versus vapor quality are shown in Figs 5.8 to 5.9 and 5.13 to 5.15. The remaining part of the database is shown in Appendix B in Figs B.2 to B.12. On the graphs, each curve is composed of five measurement points, corresponding to each row position. The points are linked by a spline to help the visualization of trends. This curve fit should not be used to infer the local heat transfer coefficients between the measurement points. The wall heat transfer coefficients were calculated using the local wall heat flux values. However each curve is described by the average value of wall heat flux for that test condition. Due to

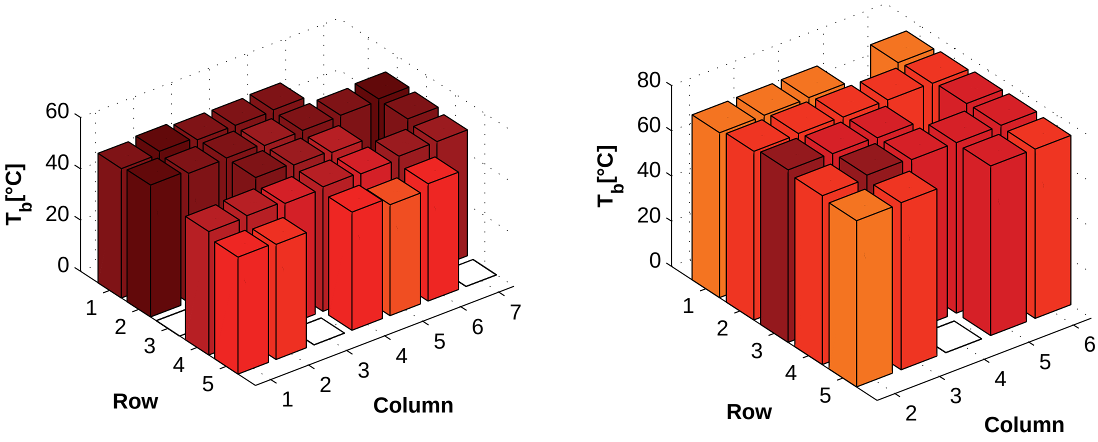

(a) Silicon test section: R-236fa, 933kg/m^{2}s, q$_b$=964kW/m^2, T$_{sat}$=31.1°C

(b) Copper test section: R-134a, 473kg/m^{2}s, q$_b$=1290kW/m^2, T$_{sat}$=50.7°C

Figure 5.7: Base temperatures.

the local change in fin efficiency, there are differences between this average value and the local ones. These can represent up to ± 20% of the mean value, but is usually closer to ± 10%. Error bars are not shown in order to make the graphs readible.

Figs 5.8 and 5.9 show that in the silicon test section the average level of heat transfer coefficients increases with heat flux, although this relation becomes less dependent for wall heat fluxes over 100kW/m^2. At low wall heat fluxes, the heat transfer coefficients increase from Row 1 to Row 5, at a faster rate after Row 3. For wall heat fluxes over 45kW/m^2, the heat transfer coefficients follow a V-shape, centered on the heaters of Row 3. They decrease from Row 1 to 3 and then increased in Row 3 to 5. The maximum values, found at Row 1 and 5, are almost of of the same level at both ends, between 15'000 and 18'000W/m^{2}K. On the right hand branch, the rate of increase is less dependent on the heat flux. The increasing branches are separated, but keep a common rate of increase. The minimum value initially increases with heat flux and after 100kW/m^2, this value stabilizes around 12'000W/m^{2}K for both fluids.

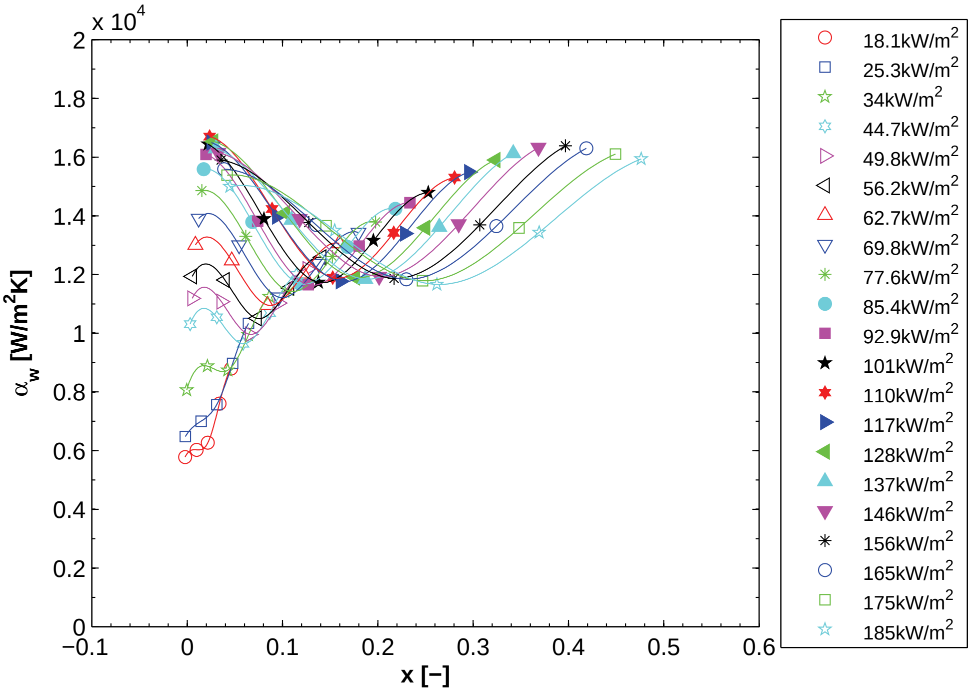

(a) T$_{sat}$: 31.4°C, 594kg/m^{2}s, Error: 7.7%, RMS: 12.2%

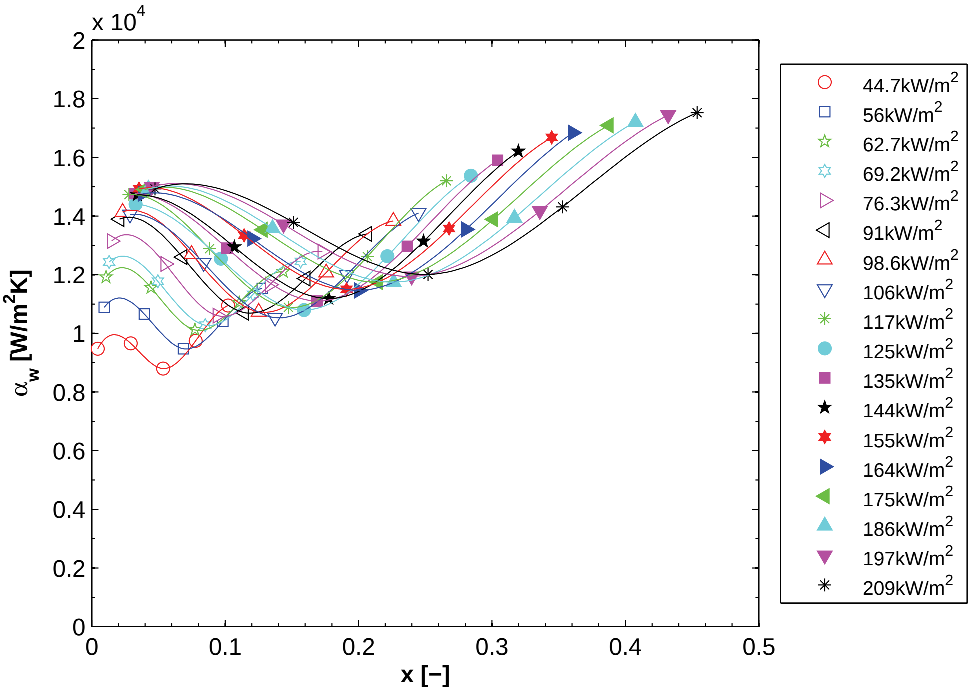

(b) T$_{sat}$: 30.9°C, 706kg/m^{2}s, Error: 6.4%, RMS: 10.4%

Figure 5.8: α_w for different q$_w$. Silicon test section R-236fa.

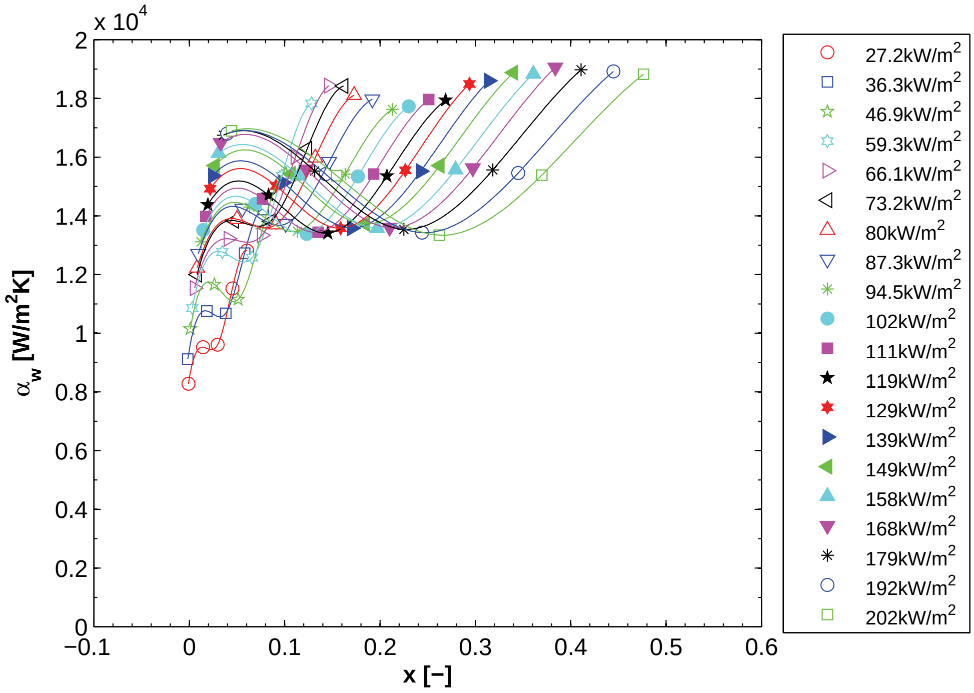

(a) T$_{sat}$: 31.4°C, 501kg/m^{2}s, Error: 8.4%, RMS: 11.5%

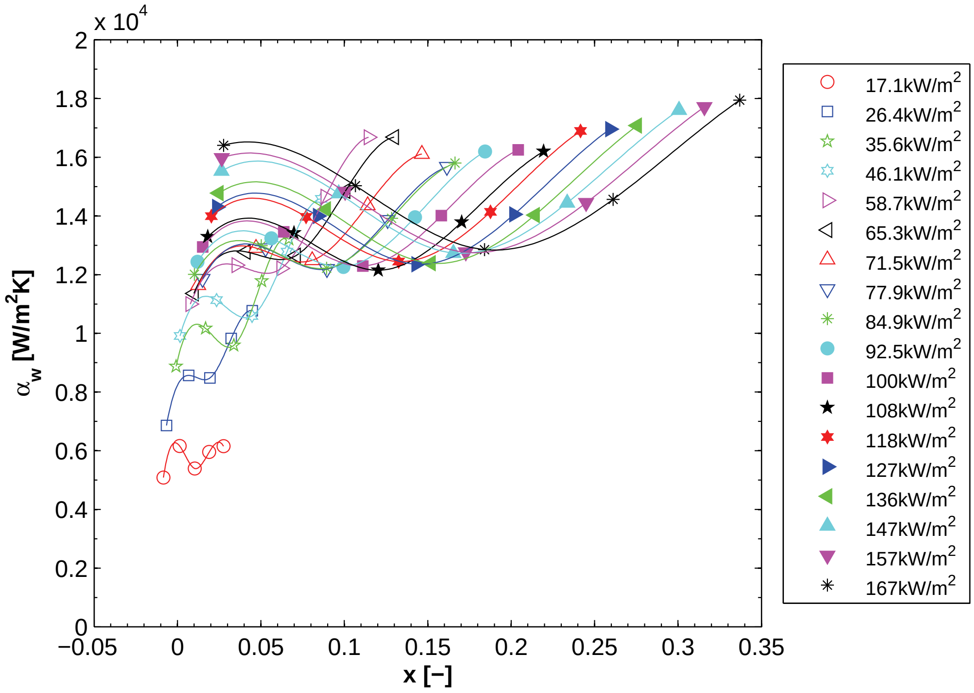

(b) T$_{sat}$: 31.2°C, 599kg/m^{2}s, Error: 8.6%, RMS: 11.9%

Figure 5.9: α_w for different q$_w$. Silicon test section R-245fa.

As it can be seen in Fig 5.10, the heat transfer for R-245fa is higher than for R-236fa. This difference increases with vapor quality and it probably due to the vapor-to-liquid density ratio. Due to this factor, the local void fraction for R-245fa is higher than that of R-236fa, such that thermal resistance due to the liquid film is reduced. Figs 5.11 and 5.12 show the local heat transfer coefficient at various mass fluxes for different wall heat fluxes. The curves on the decreasing branch are almost parallel, but once the minimum is reached, the heat transfer coefficients fall on a common line, for example in Figs 5.11(a) and 5.12(b), or increase faster for higher mass fluxes, as in Fig 5.11(b). Notably, the heat transfer coefficient decreases with increasing mass flux at lower vapor qualities.

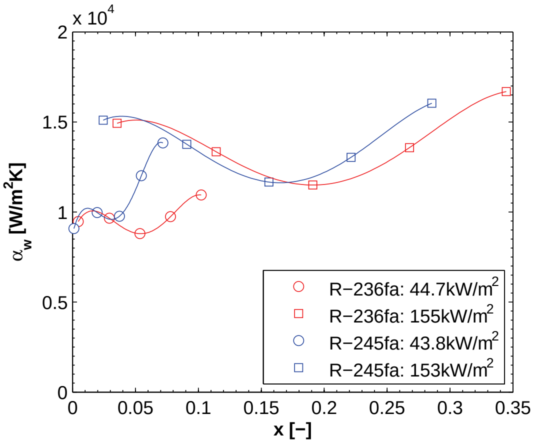

Figure 5.10: Comparison between R-236fa and R-245fa at 703kg/m^{2}s in the silicon test section.

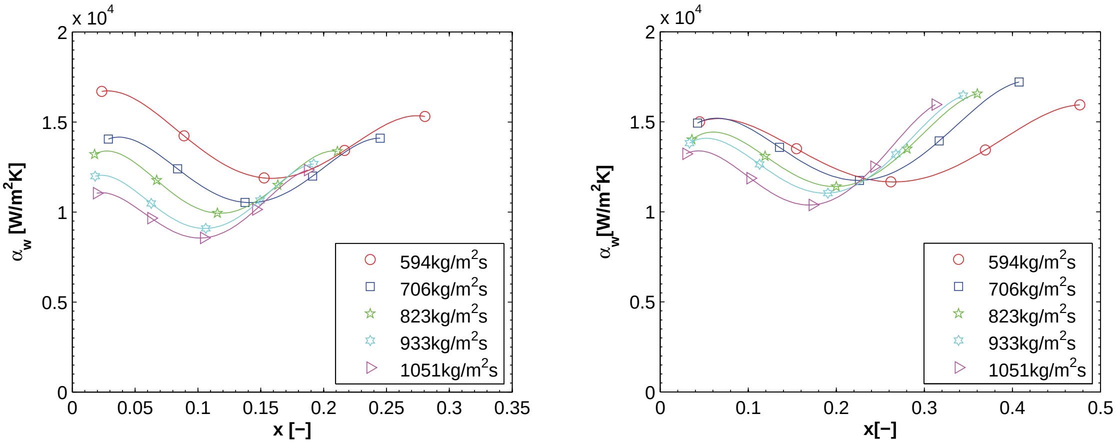

(a) q$_w$=109kW/m^2 (b) q$_w$=190kW/m^2

Figure 5.11: α_w for R-236fa for increasing mass fluxes in the silicon test section.

In Figs 5.13 to 5.15 the local heat transfer coefficients are plotted for R-134a, R-1234ze(E) and R-245fa in the copper test section. The peak heat transfer is positioned at Row 1 and increases with heat flux. The highest heat transfer coefficient measured is 27'000W/m^{2}K with R-134a at 387kW/m^2 (as a "footprint" heat transfer coefficient this is a value of about 216'000W/m^{2}K). In most cases, the heat transfer increases at the end of the curve and the minimum is positioned over Row 3 or 4. As the vapor quality increases, the influence

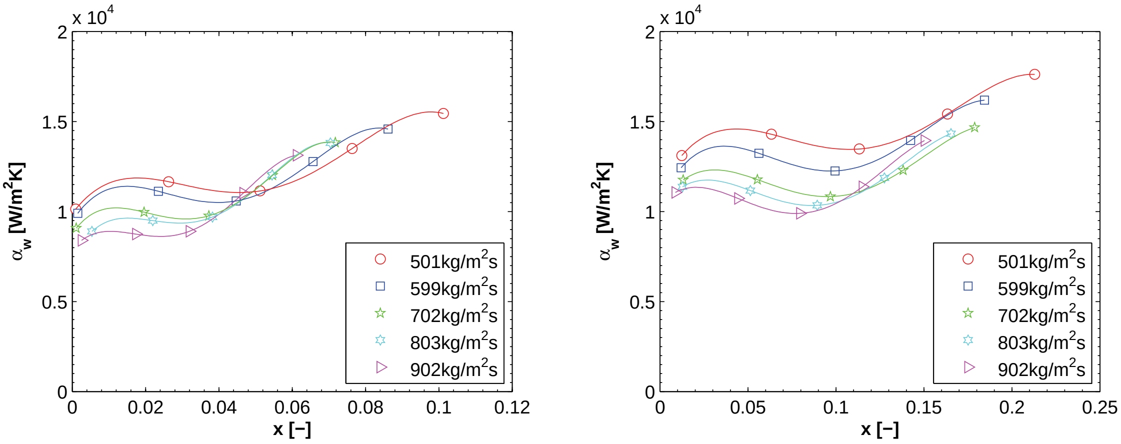

(a) q_w=45kW/m^2 (b) q_w=95kW/m^2

Figure 5.12: α_w for R-245fa for increasing heat fluxes in the silicon test section.

of heat flux decreases and the heat transfer coefficients tend toward a common curve, as it was seen in the silicon test section and by Ong & Thome (2011b) in single channel tests. In Fig 5.15(a), for 159kW/m^2, the heat transfer coefficients always decreases with heat flux. This is a possible sign that cyclical dry-outs are occurring on the channel perimeter. The higher saturation temperature does not significantly change the heat transfer trends, although the heat transfer levels are slightly higher at higher temperature. For example, in Figs 5.14(a) and 5.14(b), the heat transfer values at 100kW/m^2 are on average 1260W/m^{2}K higher at 50.9°C than at 30.2°C.

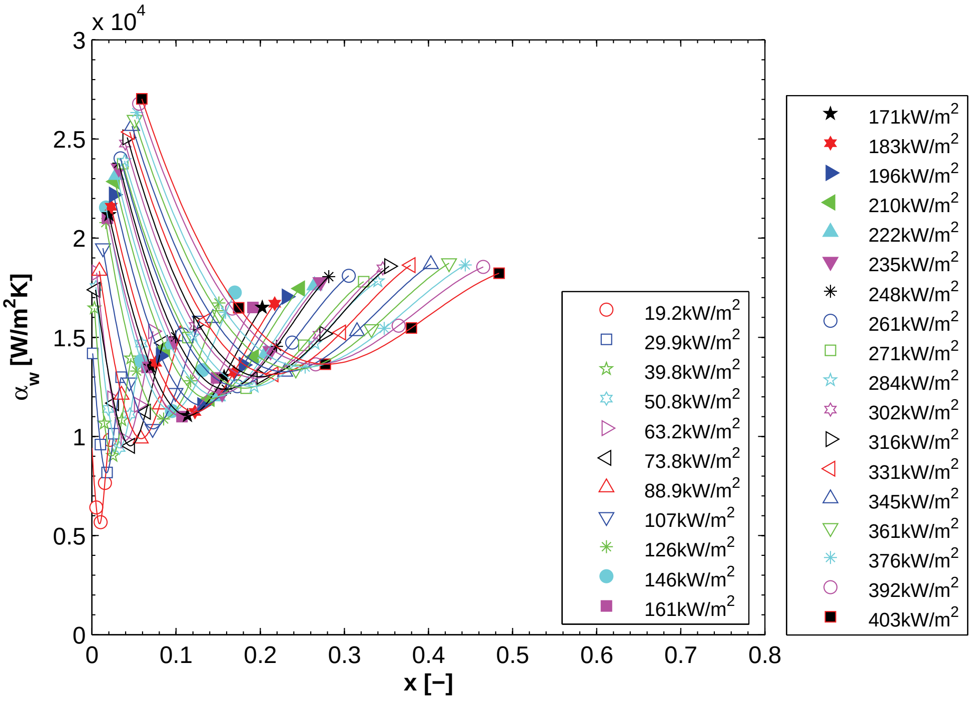

(a) T$_{sat}$: 29.9°C, Error: 5.4%, RMS: 15.8%

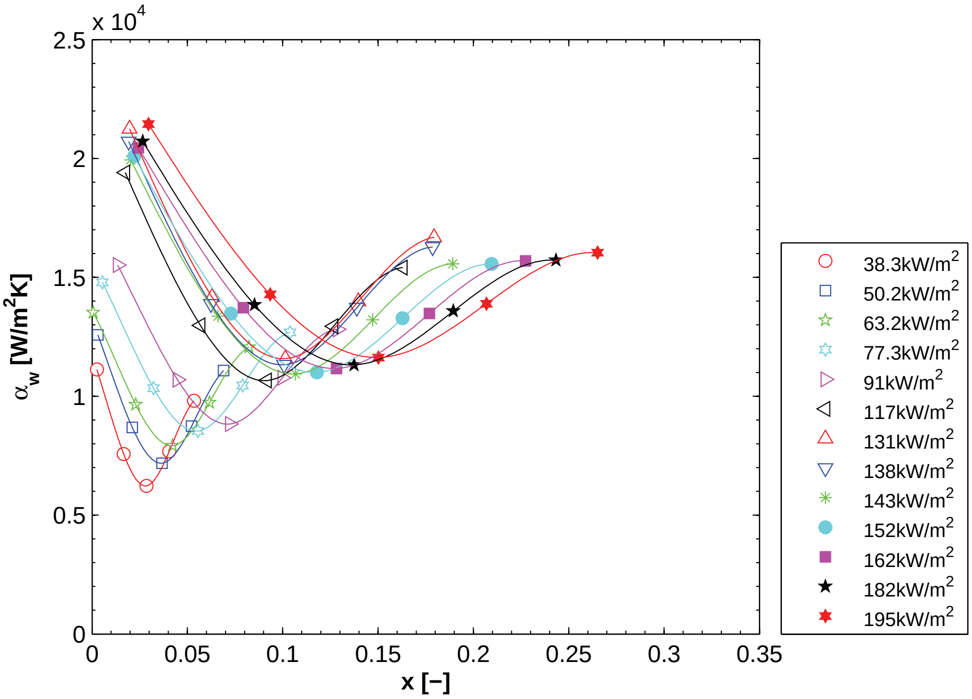

(b) T$_{sat}$: 50.7°C, Error: 7.9%, RMS: 17.8%

Figure 5.13: α_w for different q$_w$. Copper test section R-134a, 569kg/m^{2}s.

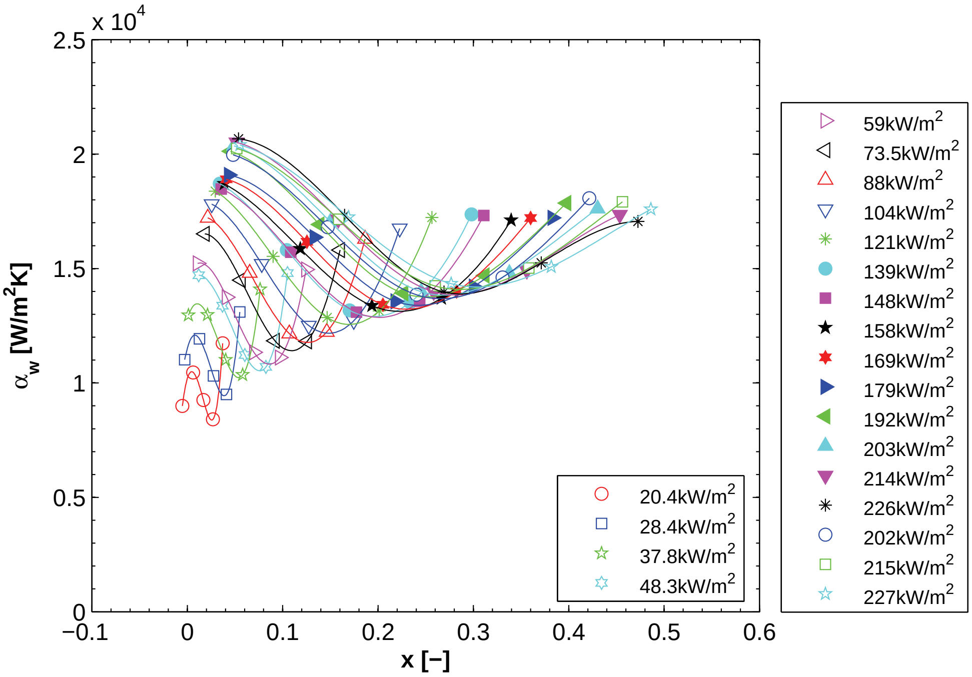

(a) T_{sat}: 30.2°C, Error: 7.1%, RMS: 16.7%

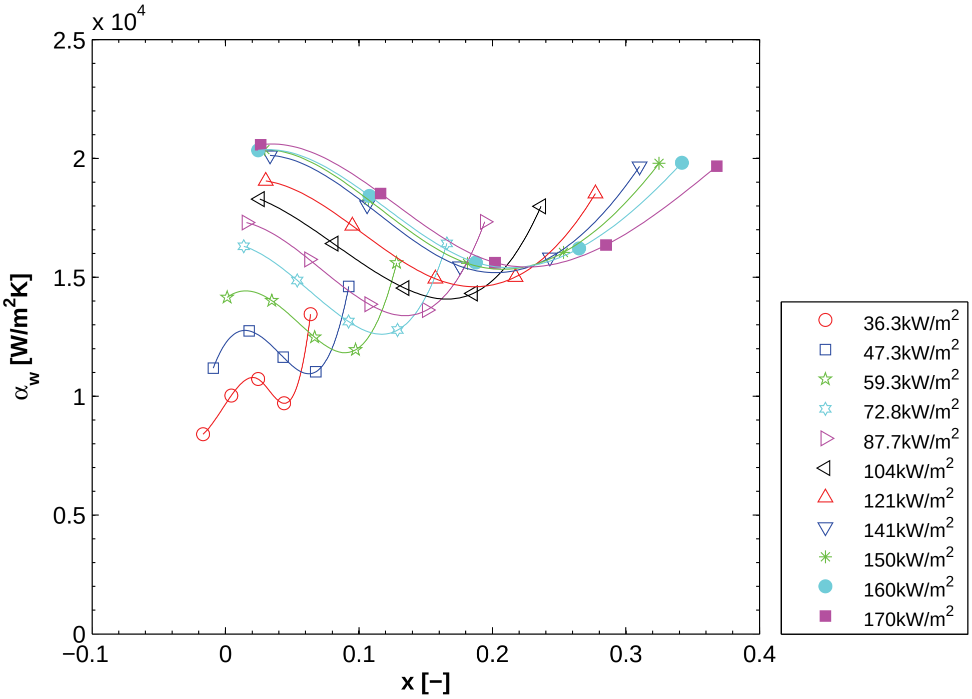

(b) T_{sat}: 50.9°C, Error: 7.2%, RMS: 14.3%

Figure 5.14: α_w for different q_w. Copper test section R-1234ze(E), 346kg/m^{2}s.

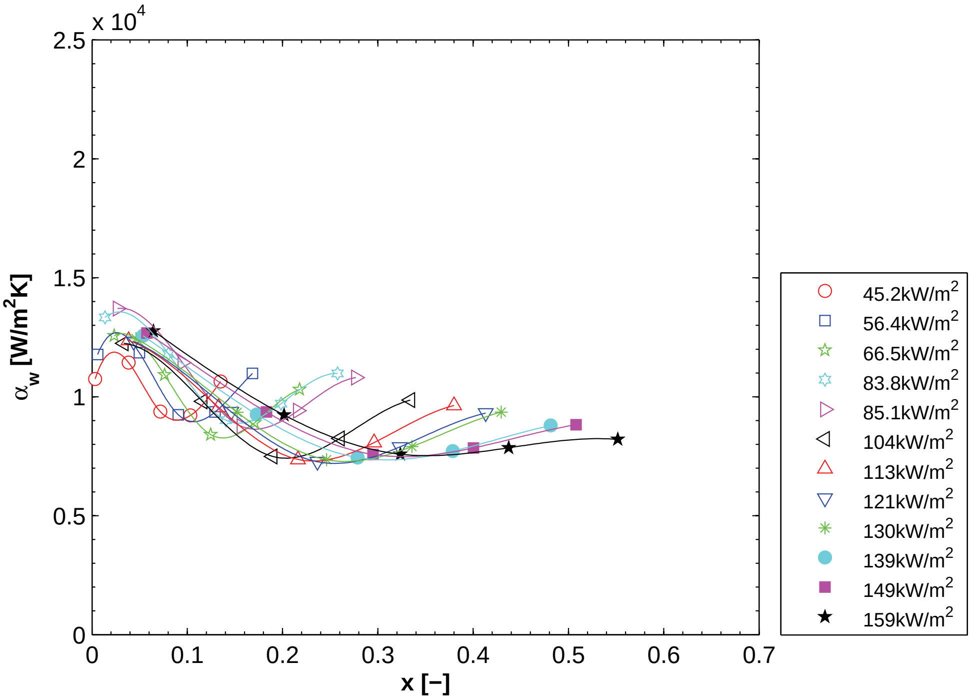

(a) T_{sat}: 31.7°C, 205kg/m^{2}s, Error: 7.0%, RMS: 17.2%

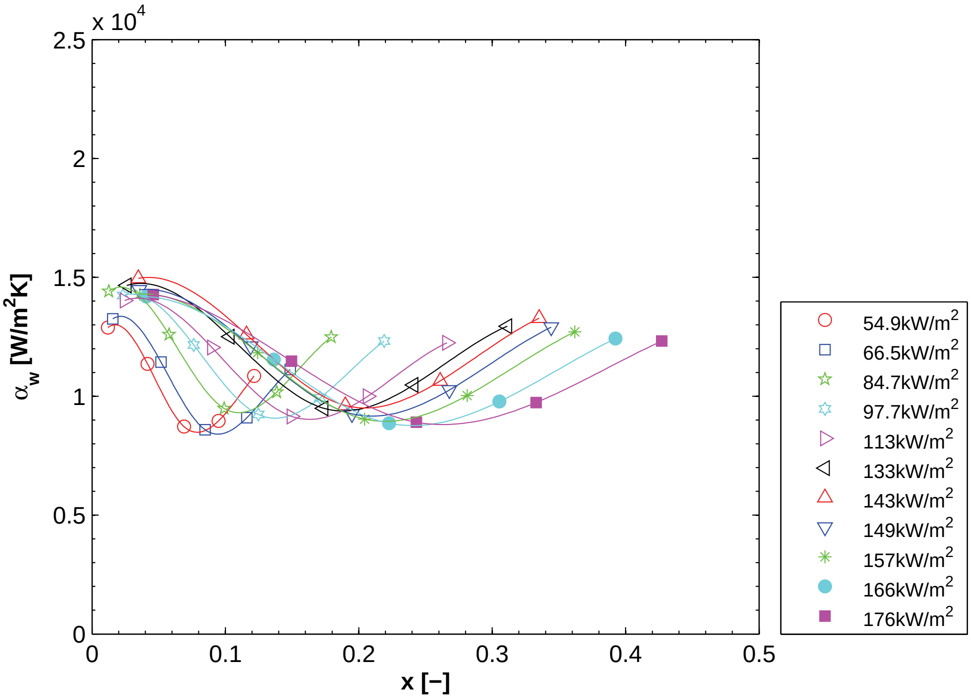

(b) T_{sat}: 31.4°C, 290kg/m^{2}s, Error: 7.3%, RMS: 13.5%

Figure 5.15: α_w for different q_w. Copper test section R-245fa.

At 160kW/m^2 and at about 350kg/m^{2}s, Fig 5.16 shows that the highest heat transfer coefficients are obtained with R-1234ze(E) and that all three fluids follow the same general trend. The wall heat transfer coefficients were replotted for R-134a and R-1234ze(E) at constant heat flux and varying mass fluxes in Figs 5.17 and 5.18. As it was seen in the silicon test section, at low vapor quality, the heat transfer coefficient is higher for low mass fluxes. Otherwise in Fig 5.17(b), the mass flux has no influence on the increasing branch. When the heat flux is higher, as in Figs 5.17(a), 5.18(a) and 5.18(b), the curves are separated at high vapor quality with lower heat transfer at low mass fluxes. This again supports the possibility that cyclical dry-outs are occurring, as observed by Borhani *et al.* (2010). Since those dry-outs are not permanent, they do not lead to critical heat flux, but once time-averaged, they decrease the local heat transfer coefficient.

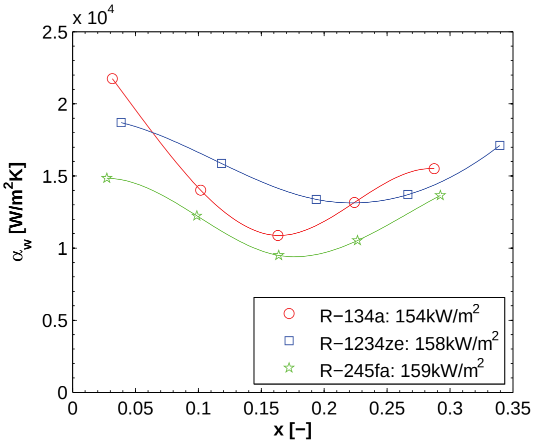

Figure 5.16: Comparison between R-134a, R-1234ze(E) and R-245fa around 350kg/m^{2}s and T$_{sat}$=31°C, in the copper test section.

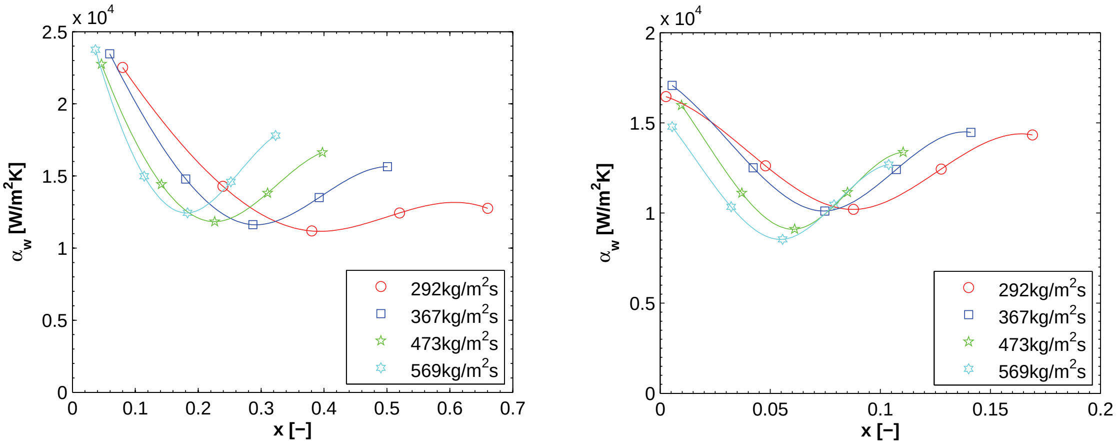

(a) T$_{sat}$: 31°C, q$_w$=270kW/m^2

(b) T$_{sat}$: 51°C, q$_w$=72kW/m^2

Figure 5.17: α_w for R-134a for increasing mass fluxes in the copper test section.

The heat transfer coefficients can also be plotted against the wall heat flux in a pseudo-boiling curve. Agostini *et al.* (2008a) found that once plotted this way, the heat transfer coefficients for vapor qualities between 2 and 8% fell on an exponential curve with an

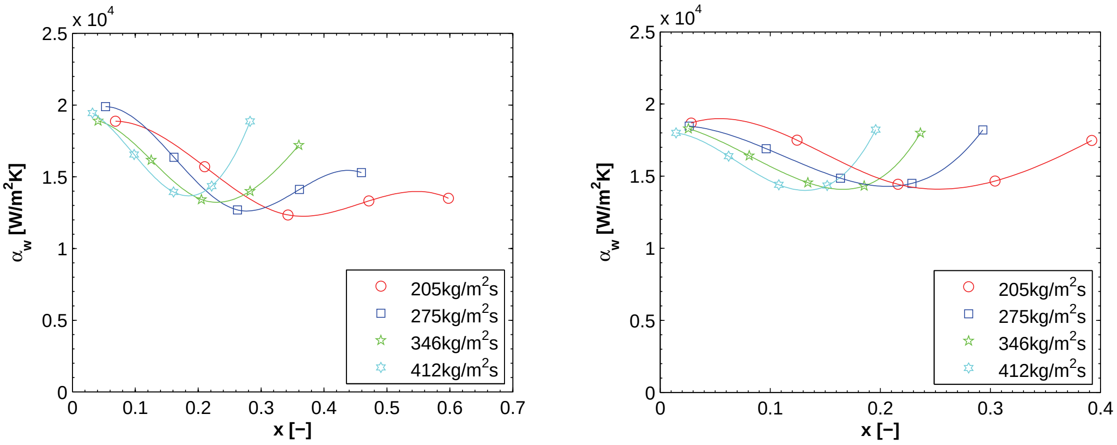

(a) T$_{sat}$: 31°C, q$_w$=165kW/m^2 (b) T$_{sat}$: 51°C, q$_w$=100kW/m^2

Figure 5.18: α_w for R-1234ze(E) for increasing mass fluxes in the copper test section.

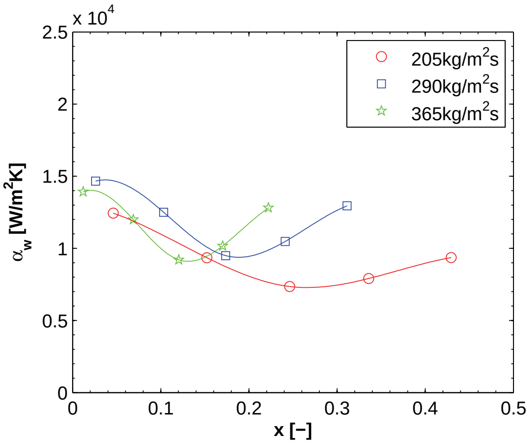

Figure 5.19: α_w for R-245fa for increasing mass fluxes and q$_w$=130kW/m^2 in the copper test section at T$_{sat}$=31.0°C.

exponent of 0.67. Harirchian & Garimella (2008) reported that heat transfer coefficients taken at the exit of their microchannel (at the same position as heater 54) were independent of the mass flux and of the channel width. This type of plot was done in Figs 5.20 and 5.21. The heat transfer coefficients in the copper test section at Row 1 follow a power curve, although the exponents are relatively low, around 0.2 for R-134a and R-1234ze(E). The other rows are rather insensitive to heat flux. In the silicon test section, the heat transfer coefficients for R-236fa in all rows can be fitted with a power curve, but the curves remain separated. Thus heat transfer in the test section are certainly a combined function of the heat flux, mass flux and vapor quality.

Comparing wall heat transfer coefficient results with flow pattern maps, Ong & Thome (2011a) predicts a IB–CB transition at around x=0.05 and a CB–AF transition at around x=0.15 for both test sections. The influence of the IB–CB transition is not seen in the heat transfer results, although the cubic spline can give this impression in some graphs. On the other hand, the CB–AF transition vapor quality is sometimes close the position of the minimum heat transfer coefficients, although the predicted transition vapor quality

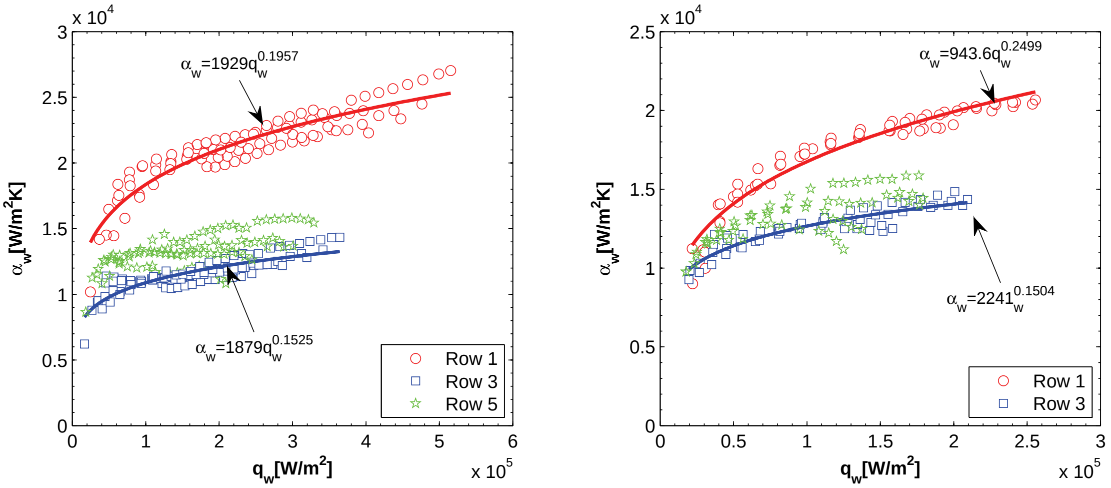

(a) R-134a for T_{sat}=31°C (b) R-1234ze(E) for T_{sat}=31°C

Figure 5.20: α_w versus q_w at all mass fluxes in the copper test section.

does not change with heat flux.

The CB–AF transition should influence the heat transfer level. In the coalescing bubble flow regime, the heat transfer should drop, because depending on the theory, the importance of dry-out increases (Thome *et al.* (2004)) or the importance of nucleate boiling, which has an higher rate of heat removal, decreases (Bertsch *et al.* (2009) and Kandlikar & Balasubramanian (2004)). In the annular flow regime, heat transfer is a function of the liquid film thickness. When the vapor quality increases, the film becomes thinner and the heat transfer coefficient increases.

In this case, the inflection point in the heat transfer coefficient curves should denote a change in flow pattern and could be used to track the diabatic CB–AF transition. This was done in Fig 5.22 for R-134a in the copper test section. The vapor quality where the minimum heat transfer occurs increases with increasing heat flux and to a lesser degree with a decreasing mass flux. Tracking the minimum on the wall heat transfer coefficients graphs, a new transition criteria can be defined to include the effect of heat flux and was also plotted in Fig 5.22.

The vapor quality at which the minimum heat transfer coefficients was found to be well predicted by

$$x_{CB-AF} = 132.77 \left(\frac{\rho_l}{\rho_v}\right)^{0.0707} Bl^{1.105} \tag{5.3}$$

where Bl is the boiling number. The constants were found by a least fit square iteration. Equation 5.3 says that the transition is a function of the liquid to vapor density ratio, the heat flux and the mass flux, both contained in the boiling number. In the database, the minima found at Row 1 and Row 5 were excluded, because in the first case, they were due to a subcooling effect and in the second case, it is not possible to say if the minimum has been reached.

The results of the statistical analysis for each fluid are given in Table 5.3. Points falling within the experimental resolution were counted as accurate. The resolution is defined as

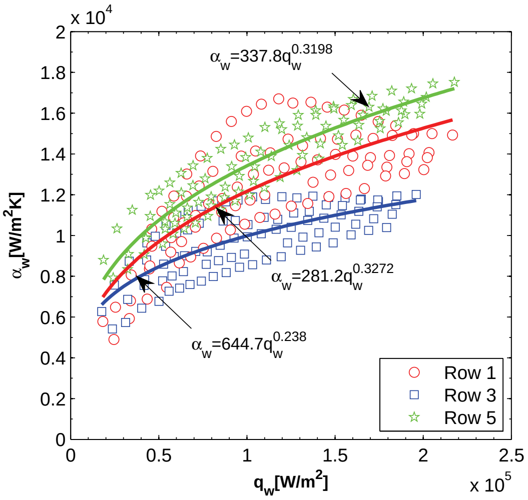

Figure 5.21: α_w versus q_w for R-236fa at all mass fluxes in the silicon test section.

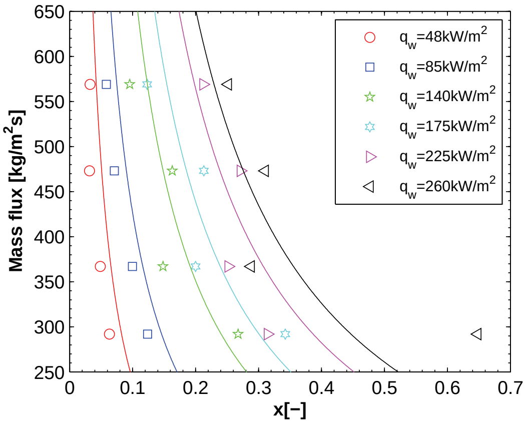

Figure 5.22: Vapor quality at the minimum heat transfer coefficients for R-134a in copper test section

the difference in vapor quality between two measurement points. For example, if at Row 3 is x=0.3 and at Row 4, x=0.4, the resolution is x=0.1. In Table 5.3, more than 90% of the data fall within the experimental resolution.

Although the number of mass fluxes tested is small, the shape of the transition curves in Fig 5.22 is reminiscent of those of Revellin *et al.* (2006) and Ong & Thome (2011a). However the boiling number is absent from their correlations. Their observations were made in a adiabatic glass tube placed after an heated section of stainless steel tube. Differences in the test setup could explain that they did not find an effect of the heat flux on the CB–AF transition. Thus, it is recommended here to use the Ong & Thome (2011a) map with the new CB–AF transition proposed here.

Table 5.3: Prediction of the vapor quality at minimum heat transfer coefficient using three-zone model.

	Within experimental resolution
Si: R-236fa	81%
Si: R-245fa	98%
Cu: R-134a	99%
Cu: R-1234ze(E)	75%
Cu: R-245fa	94%

5.3 Comparison with prediction methods

The heat transfer coefficient results for uniform heat flux will be compared with six prediction methods, namely:

1. Bertsch *et al.* (2009)
2. Kandlikar & Balasubramanian (2004)
3. Thome *et al.* (2004) (Three-zone model)
4. Lee & Mudawar (2005b)
5. Tran *et al.* (1996)
6. Cioncolini & Thome (2011)(Annular flow model)

As discussed previously, all local measurements were be used for the comparison, which amounts to more than 15'000 indivual datapoints. In the five first prediction methods, the hydraulic diameters used were respectively 146μm and 246μm for the silicon and copper test sections. Applying the method of Cioncolini & Thome (2011) to non-circular shapes is more complicated. It balances forces in the channel to calculate a radial film thickness in a circular channel. This film must be redistributed to the rectangular perimeter keeping the same area proportion between the shapes and to conserve the liquid cross-sectional area proportions, so it make sense to use the equivalent diameter, D$_h$=$\sqrt{\frac{4WH}{\pi}}$ for this method. Note that in the copper test, the true value of the perimeter was used and not 2(W+H). As a consequence of this adaptation, the average rectangular film thickness was about half the circular one.

The three-zone model used for the comparison differed from the original publication. First, as shown by several authors (e.g. Agostini *et al.* (2008a) and Ong & Thome (2011b)), the three-zone model works better when the minimum film thickness was set to the wall roughness. Second, the correlations used in the Nusselt number calculations for the liquid and vapor slugs were changed, based on the recommendations of Olivier & Costa-Patry (2010). The developing flow equations, which could lead to non-sensical results in small channels, were replaced by fully-developed ones as follows:

$$Nu_{lam} = 4.36 \tag{5.4}$$

$$N_{turb} = \frac{Pr\frac{f}{8}\left(Re - 1000\right)}{1 + 12.7\left(\frac{f}{8}\right)^{0.5}\left(Pr^{2/3} - 1\right)} \tag{5.5}$$

for Re≥1500.

Finally, the original definition of the liquid film heat transfer was used to prevent the computational problems observed by Dupont *et al.* (2004) when $\delta_0 \approx \delta_{end}$, the denominator was stabilized by adding one nanometer in the substraction such that:

$$h_{film} = \frac{\lambda_l}{\delta_o - \delta_{end} + 1 \times 10^{-9}} ln \frac{\delta_o}{\delta_{end}} \tag{5.6}$$

The results of the comparison between the experimental data and the prediction methods are shown in Figs 5.23 and 5.24, each fluid being shown in a different color. The methods of Thome *et al.* (2004) and Bertsch *et al.* (2009) are the best at centering the data within the ±30% accuracy range. The mean average errors are listed in Tables 5.4 and 5.5 by flow pattern, using Equation 5.3 as transition criteria. As it can be expected, the three-zone model has a better accuracy for isolated and coaslescing bubble flow and the annular flow method of Cioncolini & Thome (2011) is more precise for annular flows.

The two methods were here combined to form the first flow-pattern based prediction method for flow boiling in microchannels. The three-zone model was used until the CB–AF transition (equation 5.3) found on the heat transfer coefficient graphs was reached. For the measurement point with a vapor quality the closest the transition, the heat transfer was set to be a combination of the three-zone and the annular flow models:

$$\alpha_{CB-AF} = \alpha_{3Z} + \frac{\alpha_{AF}}{\alpha_{3Z} + \alpha_{AF}}\left(\alpha_{AF} - \alpha_{3Z}\right) \tag{5.7}$$

such that if α_{3Z} is small, α_{AF} dominates and vice versa. This equation than creates a smooth transition from intermittent flow to annular flow. The vapor quality transition region to which it should be applied can be based on the experimental resolution: $x_{CB-AF} \pm x_{ch-end}/5$. For measurements at higher quality, the annular flow model was used.

As given in Tables 5.4 and 5.5 and shown in Fig 5.25, the method centers all fluids around the ±30% range and its accuracy is very good. For the copper test section, the mean average error for all fluids is 27.8% and the same accuracy is obtained in the IB/CB and annular flow regions. For the silicon test section, the mean average error decreases to 19.4%.

Fig 5.26 shows some simulations of the new model at conditions similar to Fig 5.8(b) for R-236fa in the silicon test section and Fig 5.13(a) for R-134a in the copper test section. The minimum in the test data are seen to be reproduced by the new flow pattern based model. This aspect is particularly important for modelling the microprocess temperature map for two-phase cooling of computer chips.

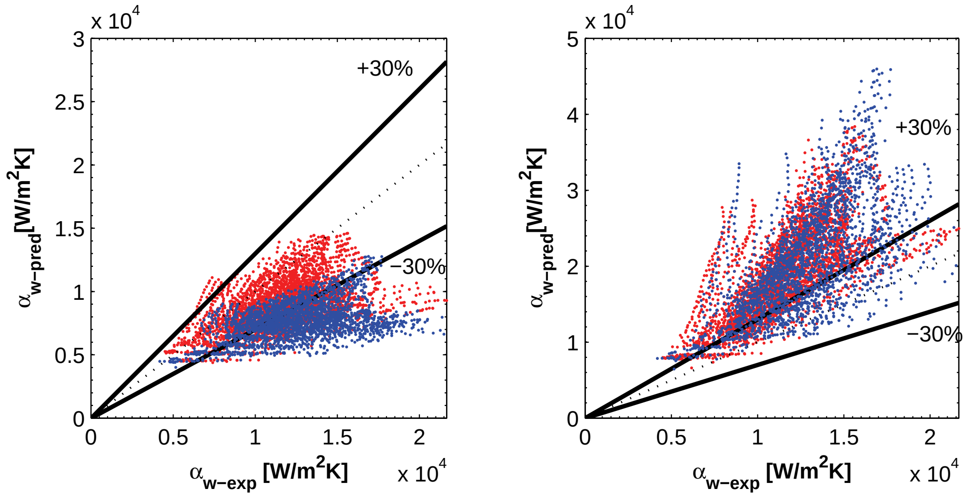

(a) Bertsch *et al.* (2009) (b) Kandlikar & Balasubramanian (2004)

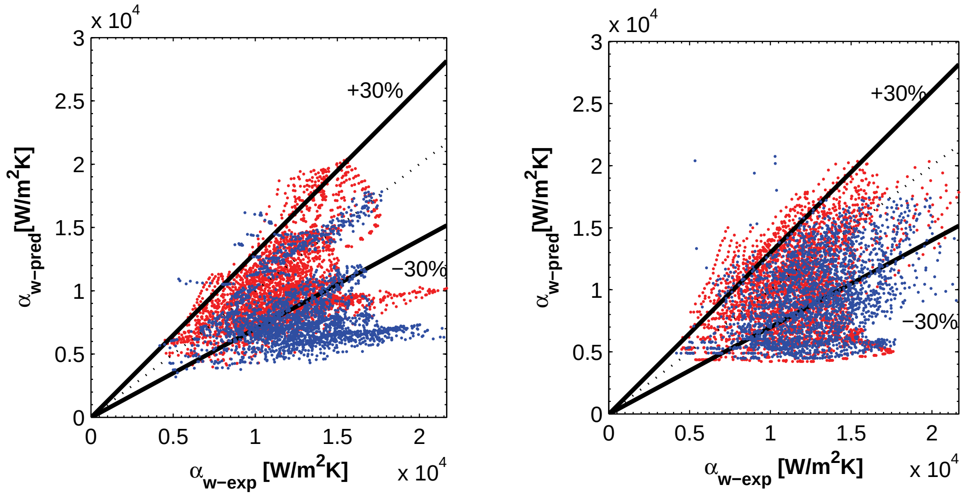

(c) Thome *et al.* (2004) (d) Cioncolini *et al.* (2009)

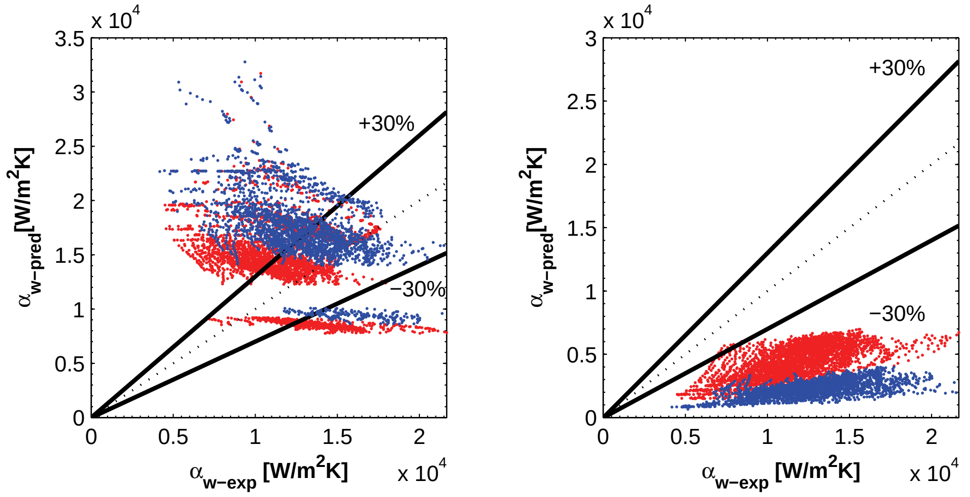

(e) Lee & Mudawar (2005b) (f) Tran *et al.* (1996)

Figure 5.23: Comparison with heat transfer prediction methods for silicon test section. Red:R-236fa, Blue:R-245fa.

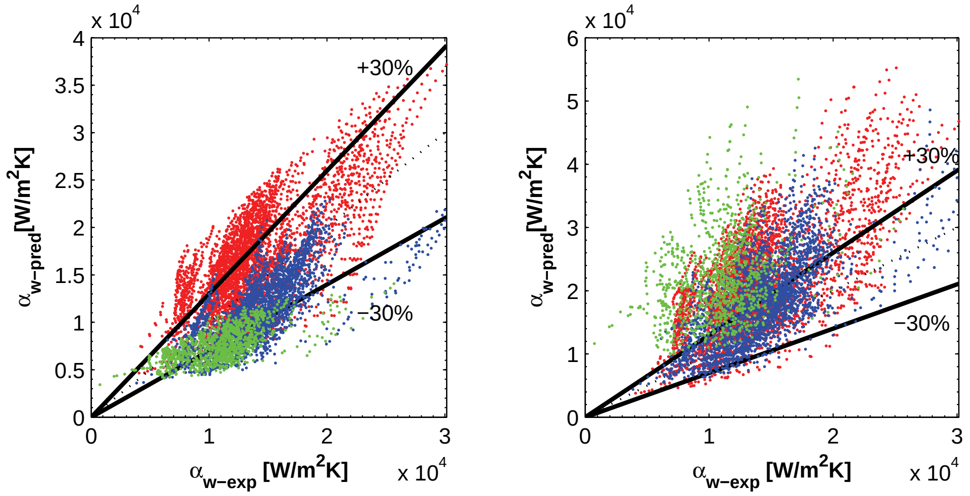

(a) Bertsch *et al.* (2009) (b) Kandlikar & Balasubramanian (2004)

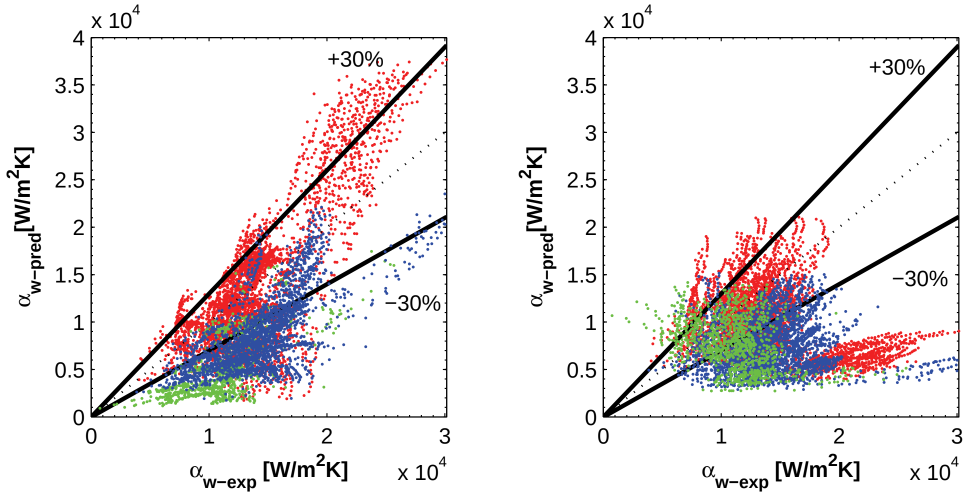

(c) Thome *et al.* (2004) (d) Cioncolini *et al.* (2009)

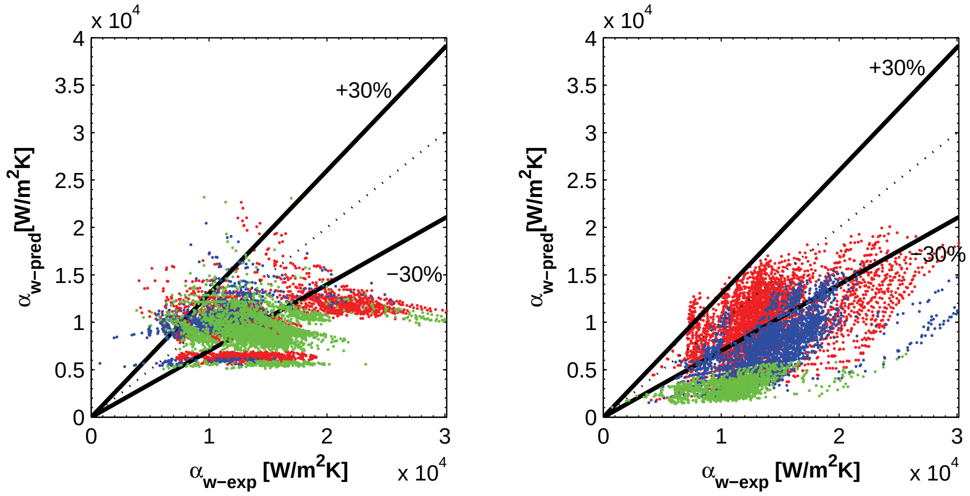

(e) Lee & Mudawar (2005b) (f) Tran *et al.* (1996)

Figure 5.24: Comparison with heat transfer prediction methods for copper test section. Red:R-134a, Blue:R-1234ze(E), Green:R-245fa.

Table 5.4: Mean average error for local heat tranfer coefficients in the silicon test section.

Silicon test section	R-236fa	R-245fa
Bertsch *et al.* (2009)	IB/CB:18.1% AF:24.8%	IB/CB:29.5% AF:39.6%
Kandlikar & Balasubramanian (2004)	IB/CB:70.6% AF:63.4%	IB/CB:80.2% AF:59.6%
Thome *et al.* (2004)	**IB/CB:17%** AF:22.5%	**IB/CB:14.3%** AF:42%
Cioncolini & Thome (2011)	IB/CB:49.1% **AF:20.8%**	IB/CB:78.1% **AF:23.5%**
Lee & Mudawar (2005b)	IB/CB:60.8% AF:43.1%	IB/CB:99.6% AF:47.8%
Tran *et al.* (1996)	IB/CB:63.6% AF:62.3%	IB/CB:81.1% AF:82.4%
New method	**IB/CB:17.3%** **AF:16.6%**	**IB/CB:15.1%** **AF:24.1%**

Table 5.5: Mean average error for the local heat tranfer coefficients in the copper test section.

Copper test section	R-134a	R-1234ze(E)	R-245fa
Bertsch *et al.* (2009)	IB/CB:27.1% AF:30.5%	IB/CB:19.9% AF:26.4%	IB/CB:31.1% AF:30.7%
Kandlikar & Balasub. (2004)	IB/CB:50.1% AF:59.1%	IB/CB:37% AF:33.2%	IB/CB:104% AF:122%
Thome *et al.* (2004)	**IB/CB:23.1%** AF:26.2%	**IB/CB:27.8%** AF:48.8%	**IB/CB:49%** AF:69.2%
Cioncolini & Thome (2011)	IB/CB:46.5% **AF:23.8%**	IB/CB:62.1% **AF:34.4%**	IB/CB:43.4% **AF:37.7%**
Lee & Mudawar (2005b)	IB/CB:35.2% AF:36.7%	IB/CB:36.6% AF:41.0%	IB/CB:16.1% AF:30.5%
Tran *et al.* (1996)	IB/CB:34.6% AF:28.2%	IB/CB:48.8% AF:48.8%	IB/CB:72.0% AF:67.7%
New method	**IB/CB:22.5%** **AF:20.5%**	**IB/CB:28.9%** **AF:36.4%**	**IB/CB:35.4%** **AF:32.6%**

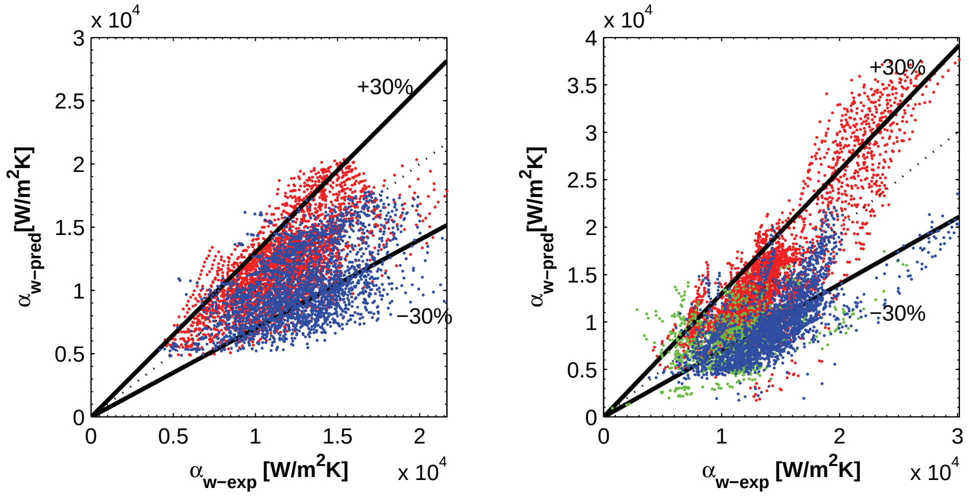

(a) Silicon Red:R-236fa, Blue:R-245fa (b) Copper Red:R-134a, Blue:R-1234ze(E), Green:R-245fa

Figure 5.25: Comparison with the new flow pattern based heat transfer model.

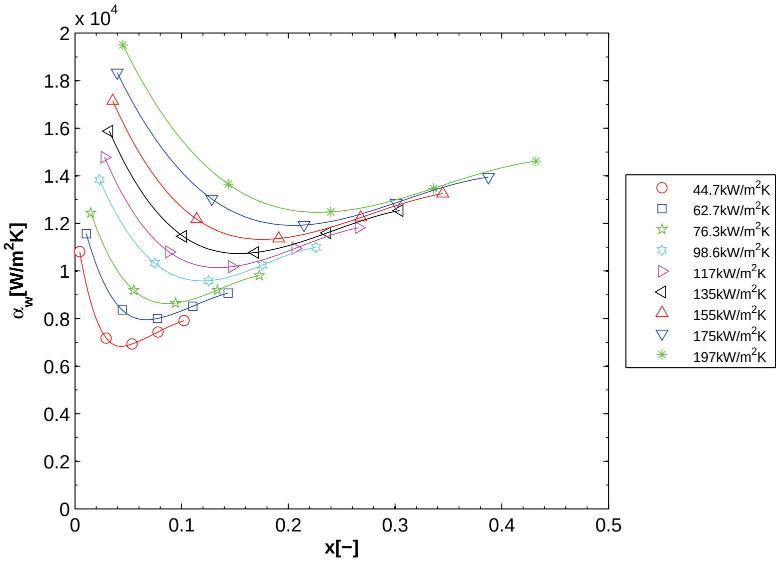

(a) Silicon test section: R-236fa, 706kg/m^{2}s

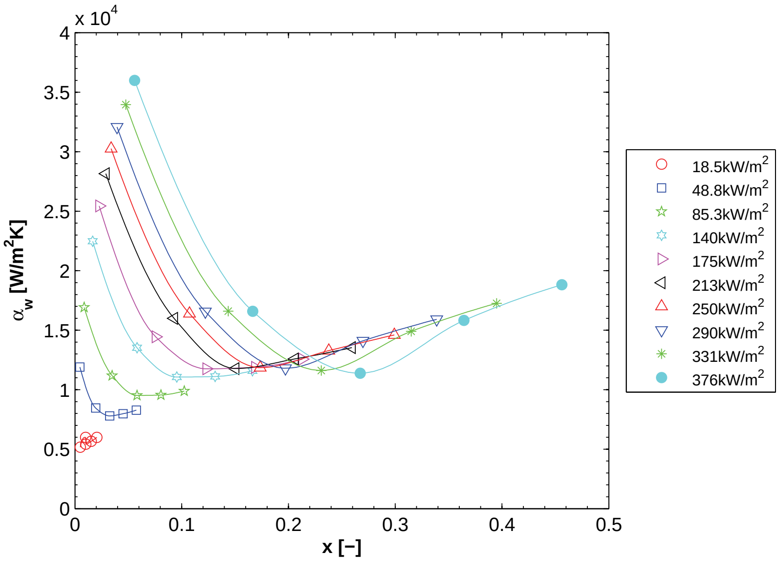

(b) Copper test section: R-134a, 569kg/m^{2}s, T$_{sat}$=29.9°C

Figure 5.26: Predicted α_w by the new flow pattern based heat transfer model.

Chapter 6

Non-uniform heat flux

Microprocessors typically generate a non-uniform heat-flux over their footprint (or base) area. To decrease the overall thermal resistance of the package, micro-coolers need to be mounted as close as possible to the heat source. In such cases, micro-evaporators will operate also under a non-uniform heat flux. The objectives in this chapter are to assess the response of two-phase multi-microchannel evaporators to non-uniform heat fluxes and to analyze the interactions between different power maps and the two-phase cooling system.

6.1 Power and temperature maps

The present array heater is well adapted to study micro-cooling under non-uniform heat flux conditions. The power map can be divided into zones where the heat flux is high, called "hot-spot" and zones where the heat flux is lower, called "background". Tests were performed by varying both the background and the hot-spot heat fluxes for different mass fluxes. With the silicon microchannel test section, seven different power map configurations were tested with R-245fa at a saturation temperature of 30°C:

- "Point" hot-spots as individual heater subjected to the high heat flux using heaters 14, 34 and 54. Notation: 14H, 34H and 54H
- Row hot-spots as a whole row subjected to the same high heat flux using Rows 1, 3 and 5. Notation: R1H, R3H and R5H.
- Column hot-spot as a whole column subjected to the same high heat flux using Column 4. Notation: C4H.

These are shown in Fig 6.1(a) overlayed over the heater notation. Similar power maps were tested with the copper microchannel test section for R-134a, R-1234ze(E) and R-245fa at two saturation temperatures, 30°C and 50°C. The point and column hot-spots were placed over Column 2, as seen in Fig 6.1(b), to compare the pressure drops using two differential pressure transducers, Δp_2, placed over Column 2 and Column 6. To describe the heat flux conditions, the power map configuration will be first given, then the hot-spot and background base heat fluxes. For example the notation for a hot-spot at Row 3 with a footprint heat flux of 1000kW/m^2 against a background footprint heat flux of 100kW/m^2 is R3H, q_b [kW/m^2] 1000:100.

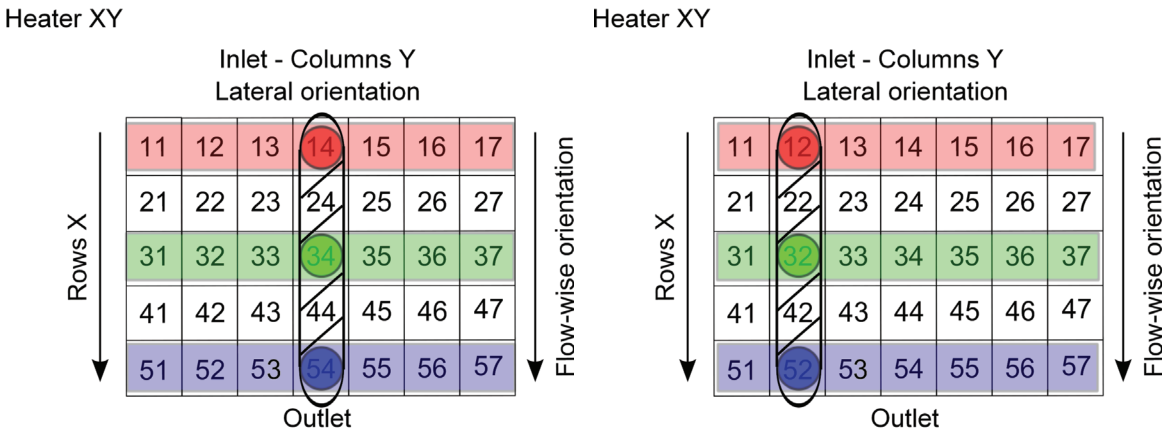
Heater XY
Inlet - Columns Y
Lateral orientation
Rows X
Flow-wise orientation
Outlet
11 12 13 14 15 16 17
21 22 23 24 25 26 27
31 32 33 34 35 36 37
41 42 43 44 45 46 47
51 52 53 54 55 56 57
Heater XY
Inlet - Columns Y
Lateral orientation
Rows X
Flow-wise orientation
Outlet
11 12 13 14 15 16 17
21 22 23 24 25 26 27
31 32 33 34 35 36 37
41 42 43 44 45 46 47
51 52 53 54 55 56 57

(a) Silicon test section (b) Copper test section

Figure 6.1: Power maps configuration.

6.2 Base heat flux and package thermal resistance without heat spreading

A first order analysis of non-uniform heat flux can be done by using the measured base temperatures, base heat flux and the mean fluid temperature, $(T_{inlet}+T_{outlet})/2$. This type of evaluation is interesting when one is concerned solely about the impact on the chip itself. Heat spreading in the thermal package occurs mostly outside of the heater chip, such that a one-dimensional approach answers most chip-level concerns. Hence, first in this section a one-dimensional approach is applied to illustrate the results. The detailed multi-dimensional analysis of the data is then presented in section 6.3.

A typical example of the impact of a non-uniform heat flux on the base of the chip is given for each power map configuration in Figs 6.2 to 6.4 for the copper test section. The lower values are drawn in dark blue and the higher in red. Similar graphs for the silicon test section were placed in Appendix B. As seen in the left graphs, in the copper test section hot-spots over 3MW/m^2 were cooled without problems for all configurations, maintaining a maximum base temperature below 85°C. For hot-spot to background heat flux ratios over 8, the base temperature gradients are high, sometimes greater than 15°C between two neighbouring sensors. This difference was stable: the deviation of all base temperature sensors was lower than 0.1°C for 100 measurements sampled at about 2Hz.

The effect of heat spreading can be seen in the base temperature maps shown in the middle graphs. The base temperature of the area surrounding the hot-spot increase slightly with respect to the remaining part of the background region and the thermal conductance around the hot-spot decreases. This effect is mostly contained within the length of one heater.

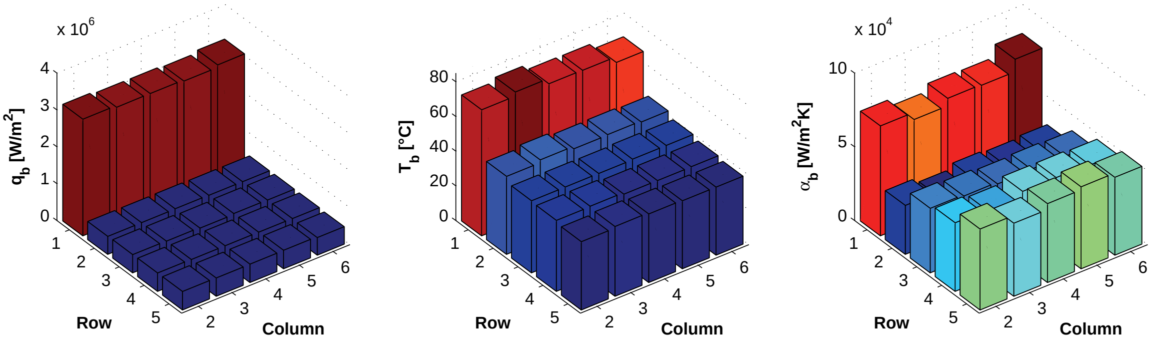

(a) q_b R1H (b) T_b R1H (c) α_b R1H

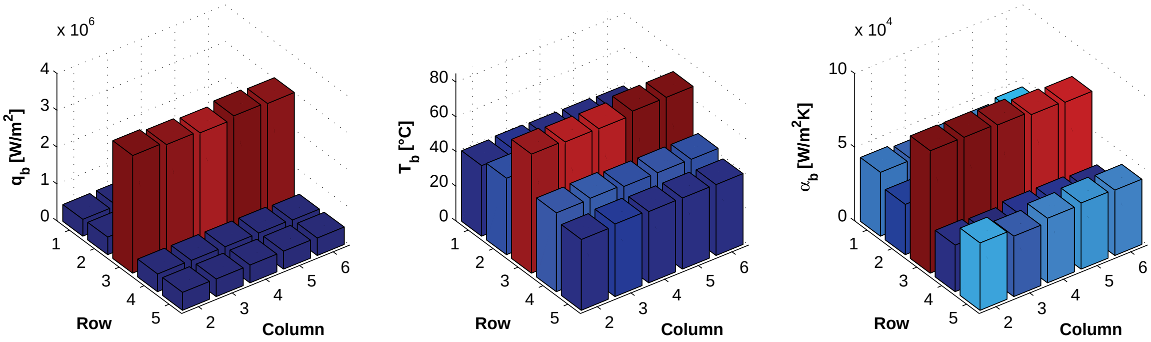

(d) q_b R3H (e) T_b R3H (f) α_b R3H

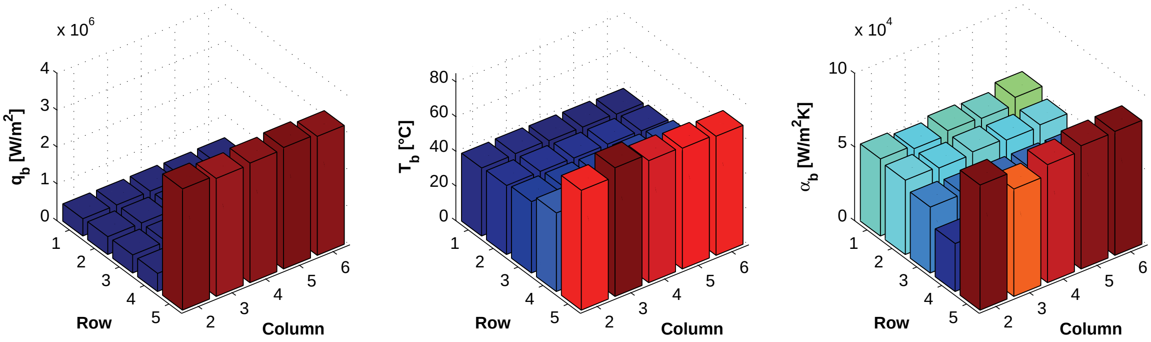

(g) q_b R5H (h) T_b R5H (i) α_b R5H

Figure 6.2: Copper test section: Thermal conductance for row hot-spots in the package R-1234ze(E), T_{sat}=30°C, 350kg/m^{2}s, assuming one-dimensional conduction.

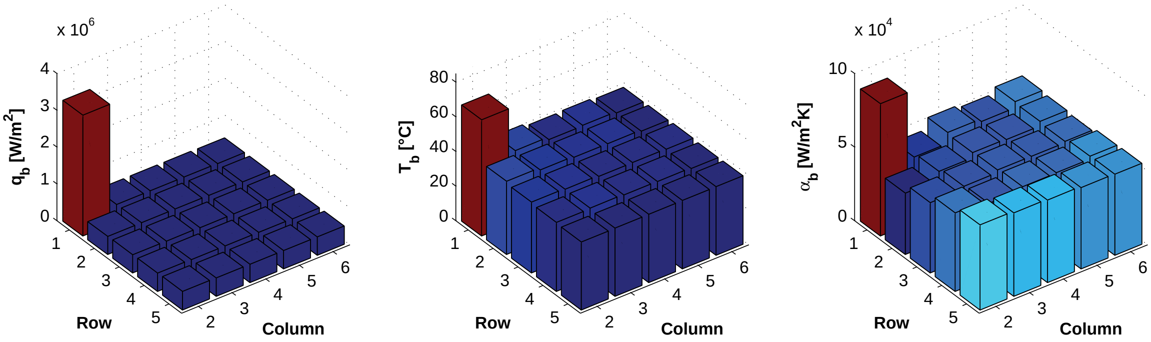

(a) q_b R1H (b) T_b 12H (c) α_b 12H

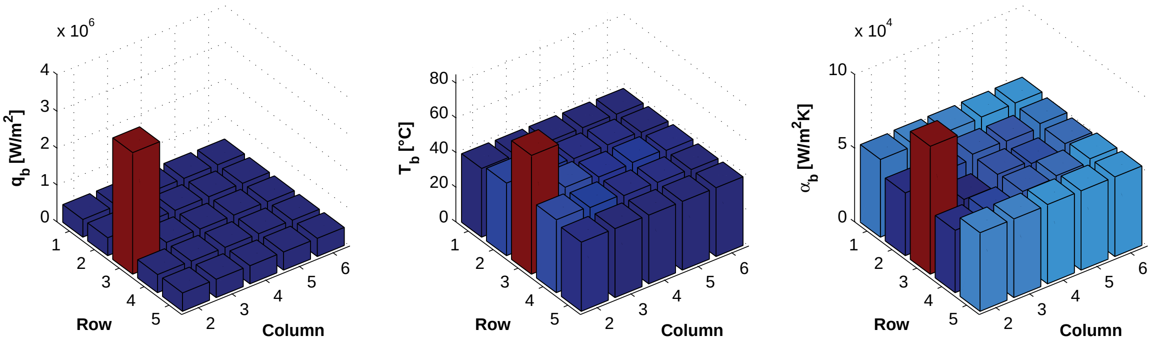

(d) q_b 32H (e) T_b 32H (f) α_b 32H

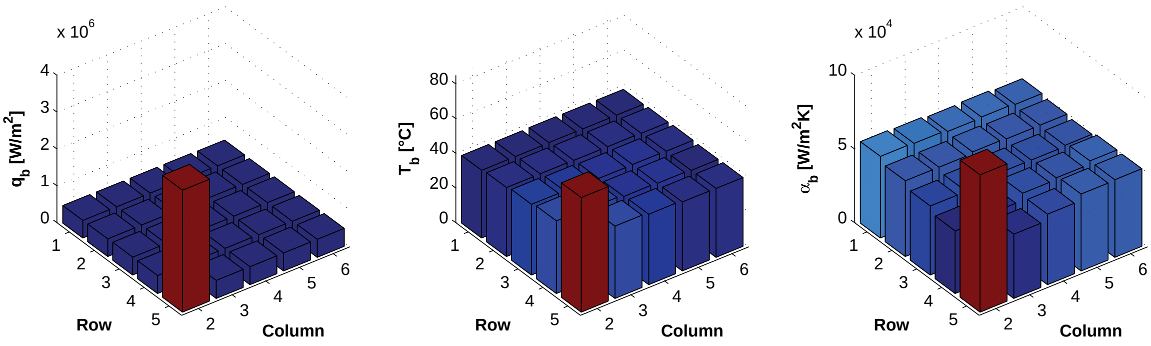

(g) q_b 52H (h) T_b 52H (i) α_b 52H

Figure 6.3: Copper test section: Thermal conductance for point hot-spots in the package for R-134a, T_{sat}=30°C, 364kg/m^{2}s, assuming one-dimensional conduction.

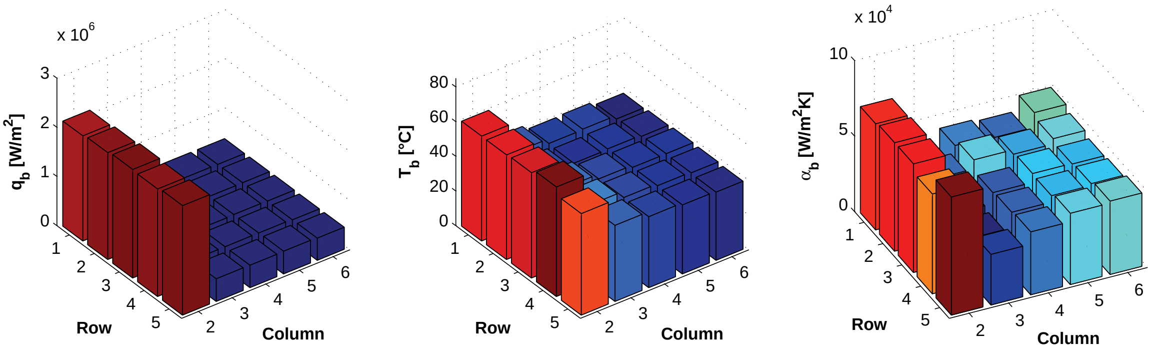

(a) q_b 12H (b) T_b C2H (c) α_b C2H

Figure 6.4: Copper test section: Thermal conductance for column hot-spot in the package for R-245fa, T_{sat}=30°C, 280kg/m^2s, assuming one-dimensional conduction.

In all cases, the local thermal conductance, shown in the right graphs, is the highest were the hot-spot is placed. Since the thermal conductivity through the composite wall is not a function of the heat flux, this self-compensating mechanism is due to two-phase flow cooling. Using the whole non-uniform heat flux database, in total 1120 test conditions, the thermal conductance over the hot-spot was plotted against the local heat flux and fitted with power law curves in Figs 6.5 and 6.6. These values are higher for the copper test section, between 50'000W/m^2K and 90'000W/m^2K, than for the silicon test section (40'000W/m^2K to 70'000W/m^2K). The thermal conductance and exponent changes slightly with the power map configuration, but at the base no clear influence of the mass flux and fluid can be seen.

Notably, the exponent values, which vary from 0.08 to 0.24, are lower than those found in Figs 5.21 and 5.20 for uniform heat flux. In both test sections, the composite wall has a thermal resistance of around 9×10^{-6}m^{2}K/W, whereas the total thermal resistance ($1/\alpha_b$) over the hot-spot varies from 11×10^{-6}m^{2}K/W to 20×10^{-6}m^{2}K/W. The self-cooling property of two-phase flow, which increases the fluid-side heat transfer with heat flux, is thus dampened by the thermal resistance of the composite wall, which is not a function of the heat flux. At q_b=3MW/m^2, the composite wall represents sometimes more than 70% of the total thermal resistance and to reduce the total thermal resistance, the composite wall would need to be thinned.

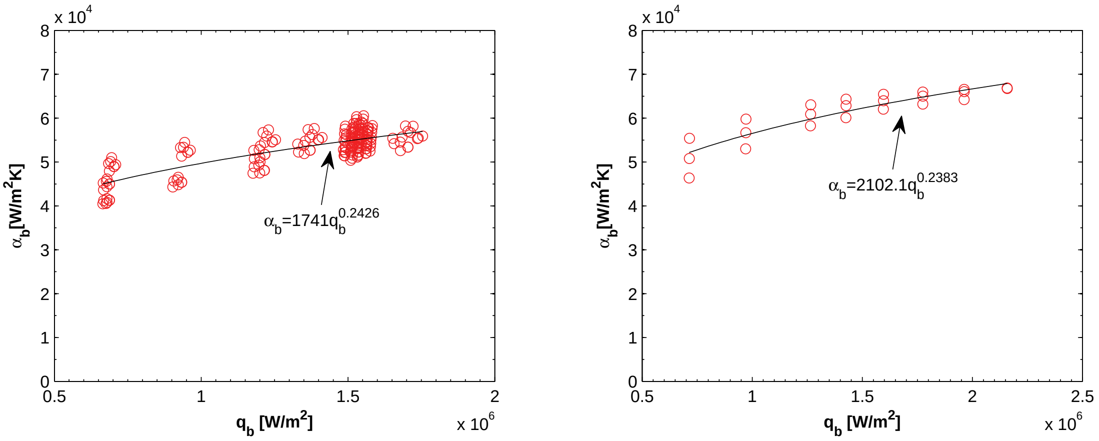

(a) R1H (b) 14H

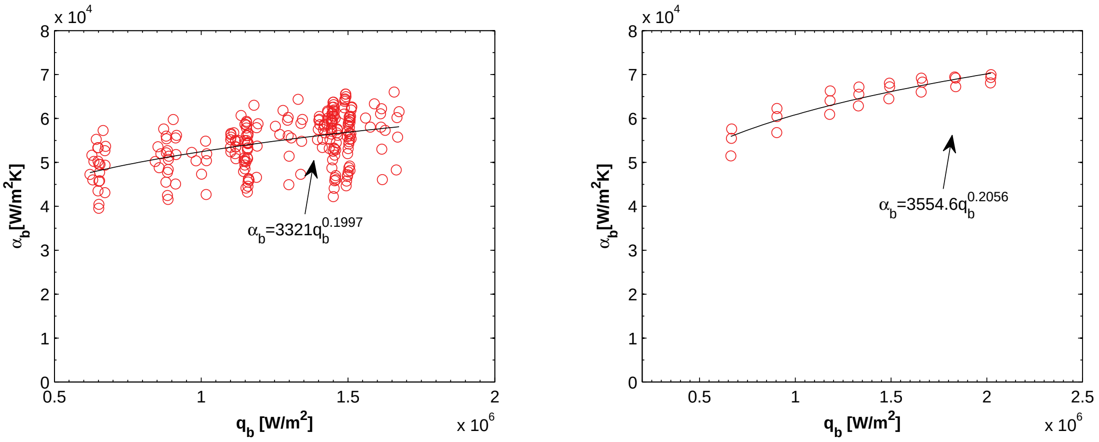

(c) R3H (d) 34H

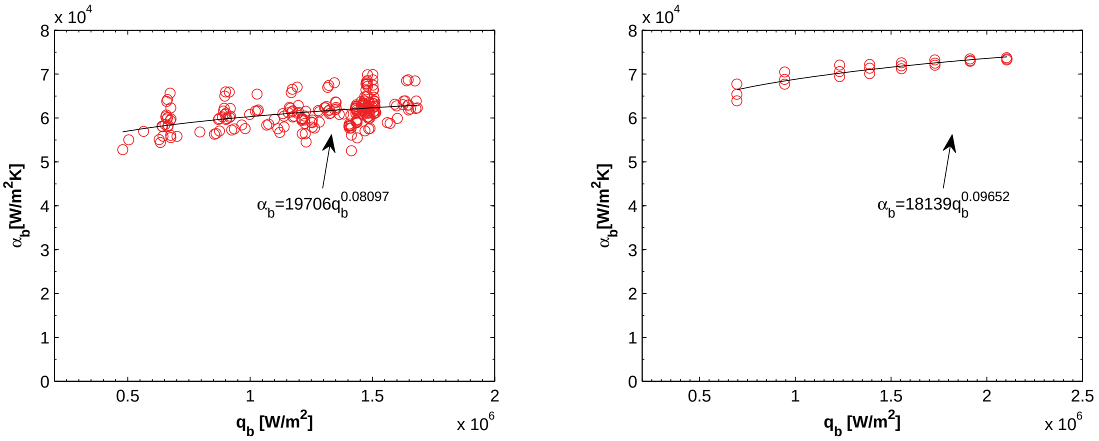

(e) R5H (f) 54H

Figure 6.5: Thermal conductance over the hot-spot versus local heat flux for R-245fa in the silicon test section.

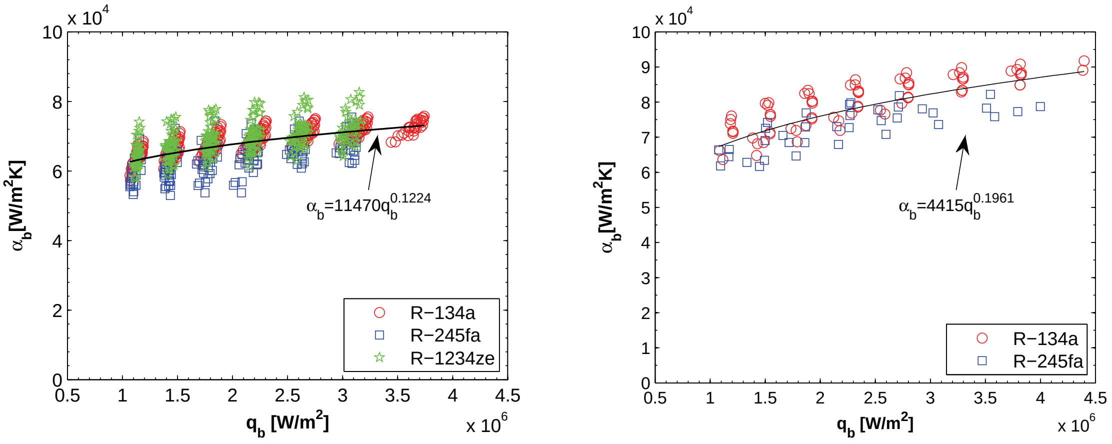

(a) R1H (b) 12H

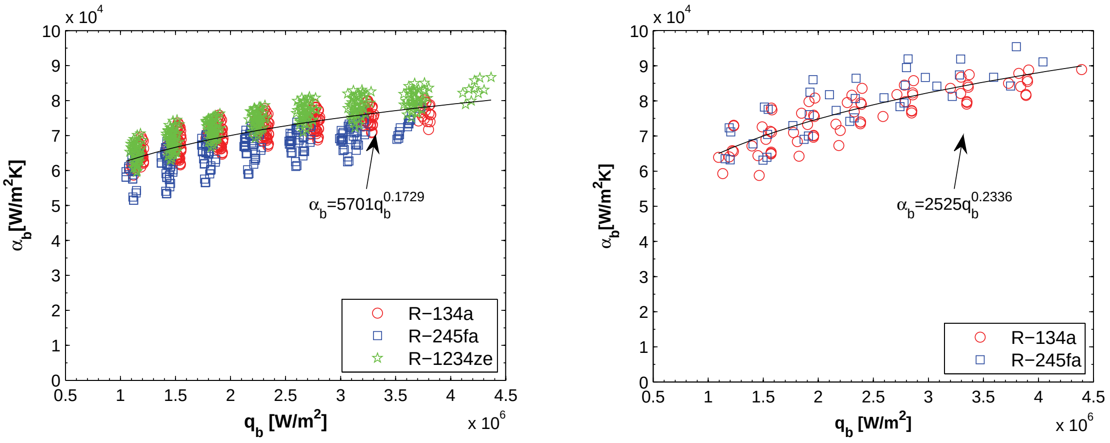

(c) R3H (d) 32H

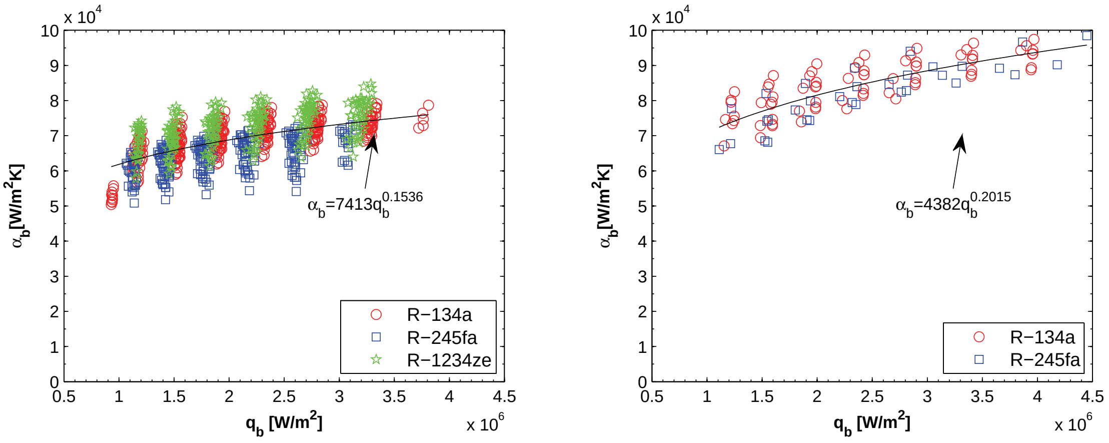

(e) R5H (f) 52H

Figure 6.6: Thermal conductance over the hot-spot versus local heat flux in the copper test section.

6.3 Footprint heat flux and wall temperatures with heat spreading

To study the reaction of two-phase flow to non-uniform heat flux, the conditions found at the wall are needed. The multi-dimensional thermal conduction scheme presented in Chapter 3 will be used now to calculate the wall heat flux and temperatures. For row hot-spots, the two-dimensional scheme will be used and for point and column hot-spots, the three-dimensional one is required to take into account the lateral temperature gradients. Capturing precisely heat spreading is central to be able to evaluate the local fluid-side performance, where local here refers to that over an individual heater. It will now be shown how the thermal conductance over the hot-spot, previously calculated using a one-dimensional distribution, will be distributed at the fluid-side surface of the evaporator.

As noted in Chapter 5, some temperatures sensors were not working and their readings were replaced by the row-averaged temperature, excluding where relevant the hot-spot temperature. In row hot-spots, this replacement will have little effect on the calculation of heat transfer coefficients, since heat spreading occurs in the flow direction.

For point and column hot-spots, the situation is different. In the silicon test section, all inactive sensors, except one, are separated from Column 4 by one or more heater. Only when the hot-spot covers heater 54 could this replacement lead to imprecision, since the temperature sensor at heater 53 was inactive. However, as seen in Fig B.14(h), the thermal conductance calculated in this situation for heater 53 is close to the value at heater 55, such that this error is assumed to remain small.

In the copper test section, reducing the data accurately to obtain heat transfer coefficient values for the point hot-spots was not possible. Heat spreading was very important and the wall heat flux over the hot-spot was on average 40% of its base value. In the thermal conduction scheme, the temperature difference between two heaters is assumed to be evenly distributed. However, when heat spreading is very important, the mesh size of the array heater is too coarse to compute reliably the heat transfer and thus a linear temperature drop profile cannot be assumed over 2.54mm. The results for point hot-spots could however be used to evaluate quantities less dependent on the local heat flux, such as the total pressure drop and the total vapor quality, both of which are more a function of the total heat flux than the local one.

6.3.1 Thermal conduction data reduction scheme

As it was done for uniform heat flux, the exactness of the two- and three-dimensional schemes can be assessed using Comsol Multiphysics 4.0. The results of these validations for row hot-spots are shown in Figs 6.7(a) and 6.8(a) with R-245fa and R-1234ze(E) along with the inputed "footprint" heat transfer coefficient curves in Figs 6.7(b) and 6.8(b). The same work was done for point hot-spots and is shown in Fig 6.9 for R-245fa in the silicon test section. More validations for point hot-spots in the silicon test section are shown in Appendix B. The simplified two- and three dimensional data reduction schemes agree well with the numerical simulations for all power map configurations. The difference in base temperature over the hot-spot is at most 1°C. Therefore, although the data reduction described in Fig 3.16 uses a coarse mesh, it is sufficiently precise for row hot-spots in both test sections and for point hot-spots in the silicon test section and ensures that the heat transfer coefficient solutions are realistic and stable.

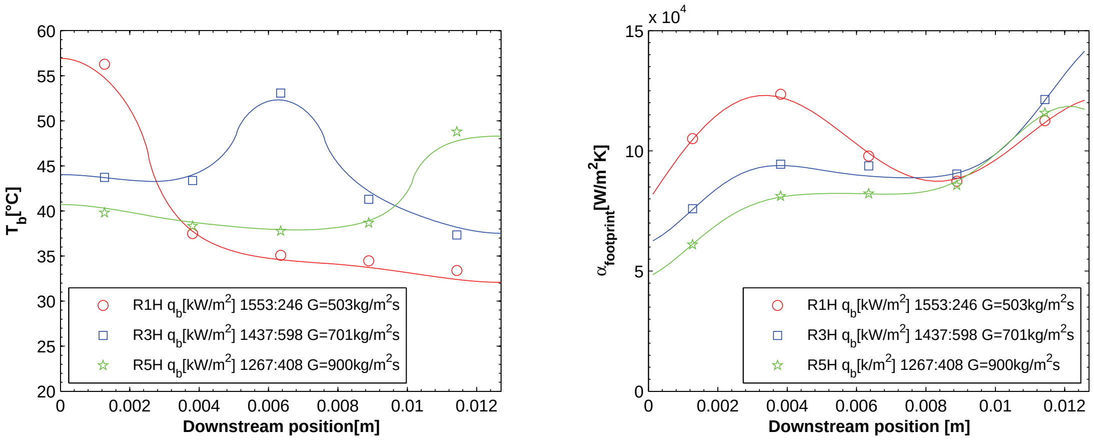

(a) Base temperature (b) Footprint heat transfer coefficient

Figure 6.7: Comparison between the two-dimensional thermal conduction data reduction and COMSOL Multiphysics numerical results for the silicon test section with R-245fa along Column 4.

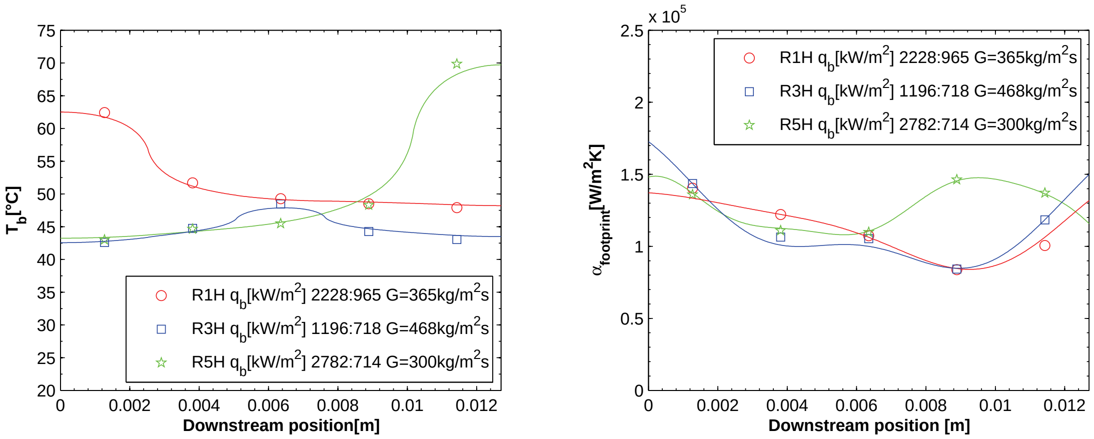

(a) Base temperature (b) Footprint heat transfer coefficient

Figure 6.8: Comparison between the two-dimensional thermal conduction data reduction and COMSOL Multiphysics numerical results for the copper test section with R-134a along Column 4 for T_{sat}=30°C.

6.3.2 Footprint heat flux and wall temperature maps

Typical examples of the footprint heat flux and temperature maps are shown in Figs 6.10 and 6.11. Heat spreading is contained within one heater around the hot-spot and is more important in the copper test section. As it is highlighted in Fig 6.12, half the of the hot-spot heat flux is redistributed inside the package, mostly to Row 2. The footprint

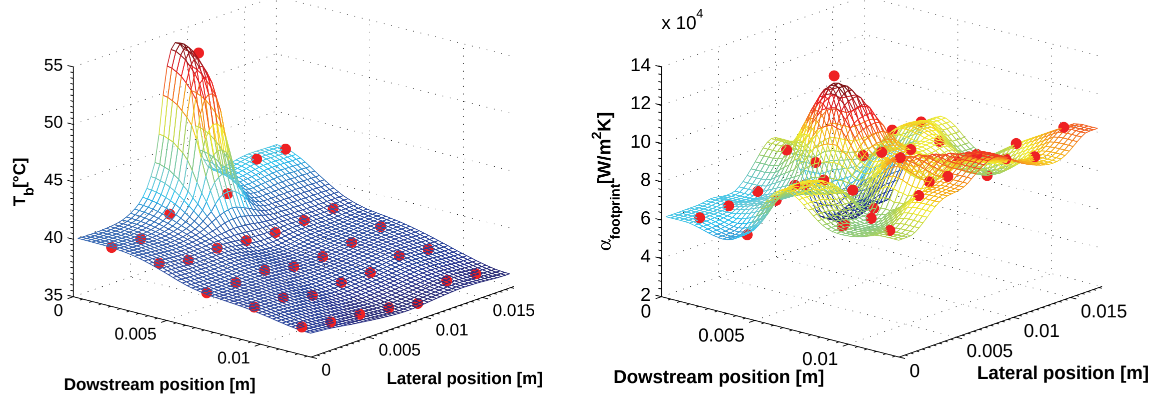

(a) Base temperature (b) Footprint heat transfer coefficient

Figure 6.9: Comparison between the three-dimensional thermal conduction data reduction and COMSOL Multiphysics numerical results for the silicon test section with R-245fa for hot-spot at 14H, q$_b$[kW/m^2] 2100:400, 507kg/m^{2}s.

heat flux in that row can be 3 times larger than the base heat flux. In the silicon test section heat spreading in more moderate, as shown in Fig 6.13, the background heat flux increases at most by 1.5 times.

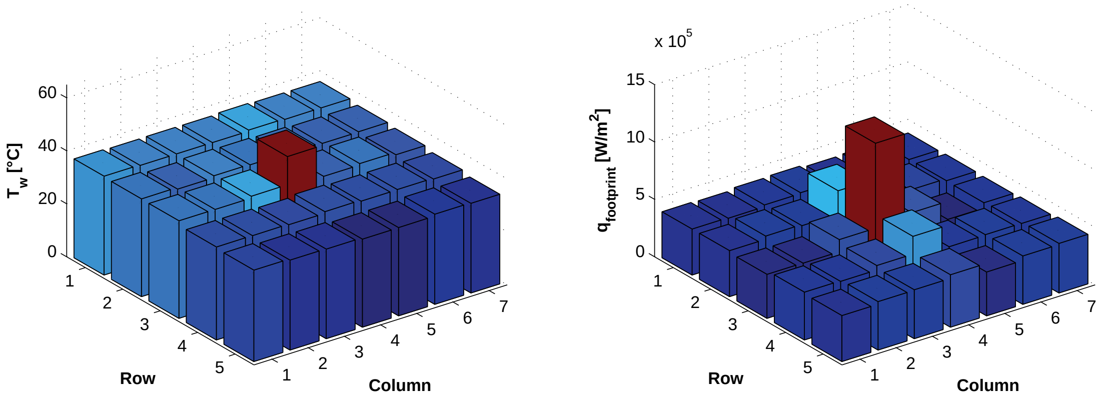

(a) Wall temperature (b) Footprint heat flux

Figure 6.10: Wall temperature and footprint heat flux for R-245fa with hot-spot at heater 34 in the silicon test section using a three-dimensional thermal conduction reduction method, q$_b$[kW/m^2] 2020:400, T$_{sat}$=30°C, 713kg/m^{2}s.

For cooling purposes, heat spreading of hot-spots in the evaporator is positive. Heat spreading activates a larger part of the evaporator and exposes the backgroud zones to higher heat flux. Since the heat transfer coefficient is a function of the wall heat flux, this decreases the overall base temperature. It is interesting to note that for the same heat flux ratios, the heat spreading in both examples is relatively close. For example for q$_b$[kW/m^2] 1332:407 and 1394:466, respectively for the silicon and copper test section, Figs 6.13(b) and 6.12(b) show that the footprint heat flux over the hot-spot are 66% and

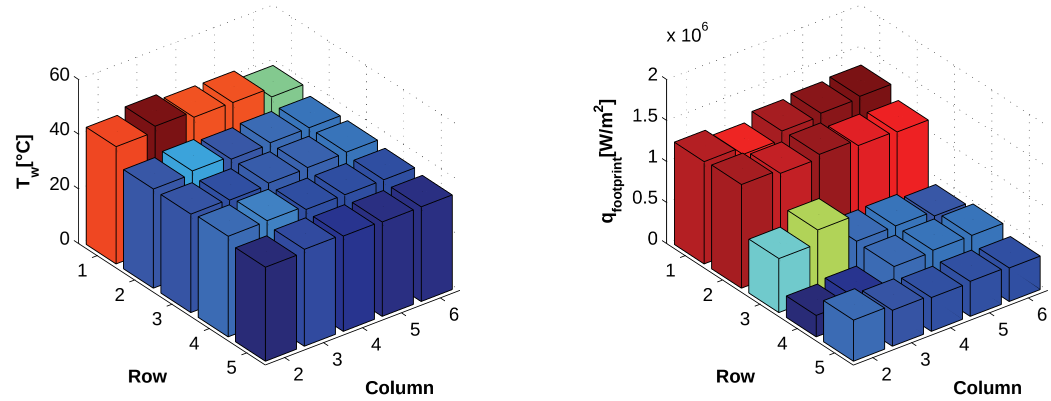

(a) Wall temperature (b) Footprint heat flux

Figure 6.11: Wall temperature and footprint heat flux for R-1234ze(E) with hot-spot at Row 1 in the copper test section using a three-dimensional thermal conduction reduction method, q_b[kW/m^2] 2100:400, T_{sat}=30°C, 350kg/m^{2}s.

55% of their base value. The amount of heat spreading is due to the combined effect of the evaporator's thermal conductivity and the local two-phase heat transfer coefficients, such that the footprint heat flux and the local heat transfer coefficient maps are intertwined. The next section deals with this aspect fir determining the local heat transfer coefficients.

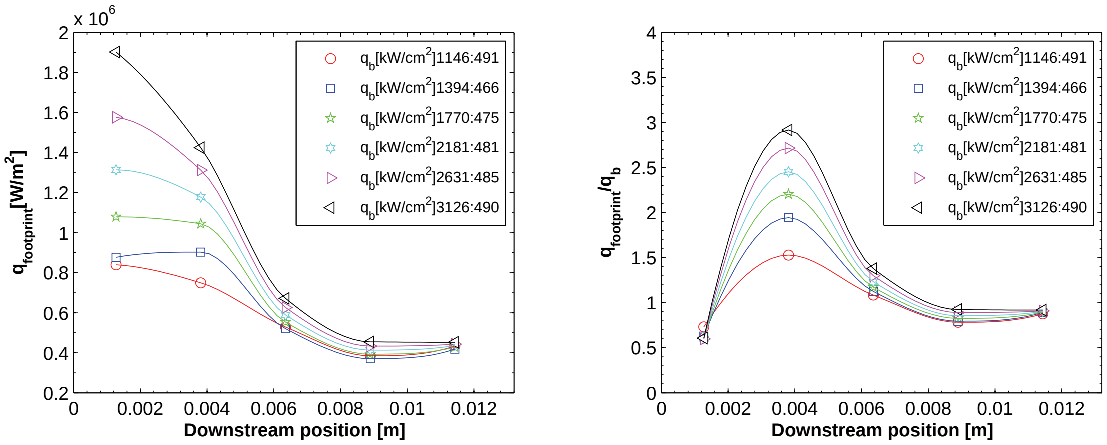

(a) Footprint heat flux (b) Ratio of footprint to base heat flux

Figure 6.12: Mean lateral heat spreading for R-1234ze(E) with hot-spot at Row 1 in the copper test section using a three-dimensional thermal conduction reduction method, T_{sat}=30°C, 350kg/m^{2}s.

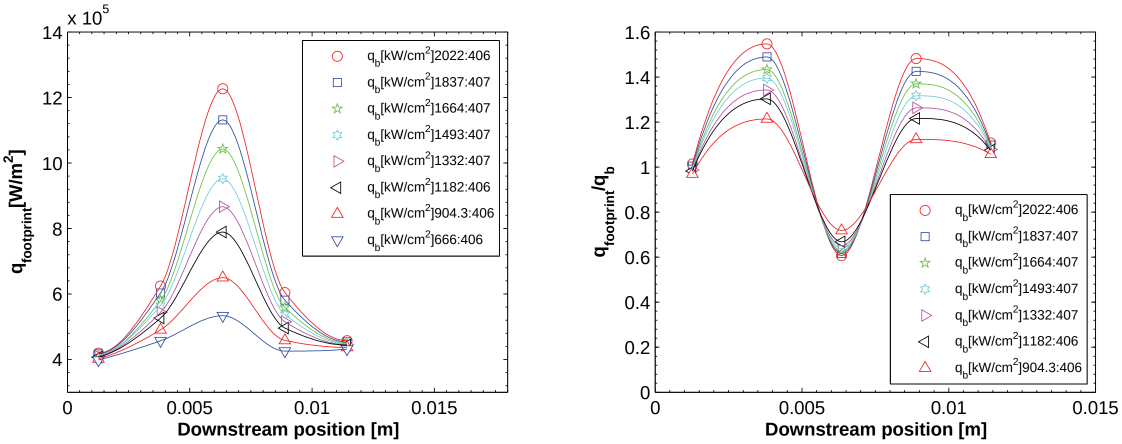

(a) Footprint heat flux (b) Ratio of footprint to base heat flux

Figure 6.13: Heat spreading for R-245fa with hot-spot at heater 34 in the silicon test section along Column 4 using a three-dimensional thermal conduction reduction method, T$_{sat}$=30°C, 713kg/m^{2}s.

6.4 Heat transfer coefficient under non-uniform heat flux

6.4.1 Pressure drop model

In non-uniform heat flux situations, the evaporation rate changes over the hot-spot and the linear pressure drop assumption in the microchannels cannot be used. A modified version of the annular flow model of Cioncolini *et al.* (2009), combined to that of Lockhart & Martinelli (1949), was used instead, since it was found to be the most accurate in Chapter 4, especially for the silicon test section where channel pressure drops are more important. This model can react to the change in local heat flux and momentum pressure drop arising from the influence of the vapor quality. The modification consisted in adding a linear correction to the pressure drop model to meet the channel inlet and outlet pressure level.

In hot-spot situations, the combination of the annular flow model of Cioncolini *et al.* (2009) and Lockhart & Martinelli (1949) pressure drop models will have a more realistic shape than a linear approximation. Since the pressures at the channel extremities are known and the pressure drop model is forced to meet these values, the largest uncertainty in fluid temperature will be at the center row. Examples of the pressure drop correction are given in Fig 6.14. In the silicon test section, the pressure correction increases the saturation temperature at the end of the channels by about 0.6°C, which in turn increase the local heat transfer by decreasing the wall to fluid temperature difference. The change in temperature in the copper test section are smaller than 0.1°C, and will not affect the local heat transfer measurably.

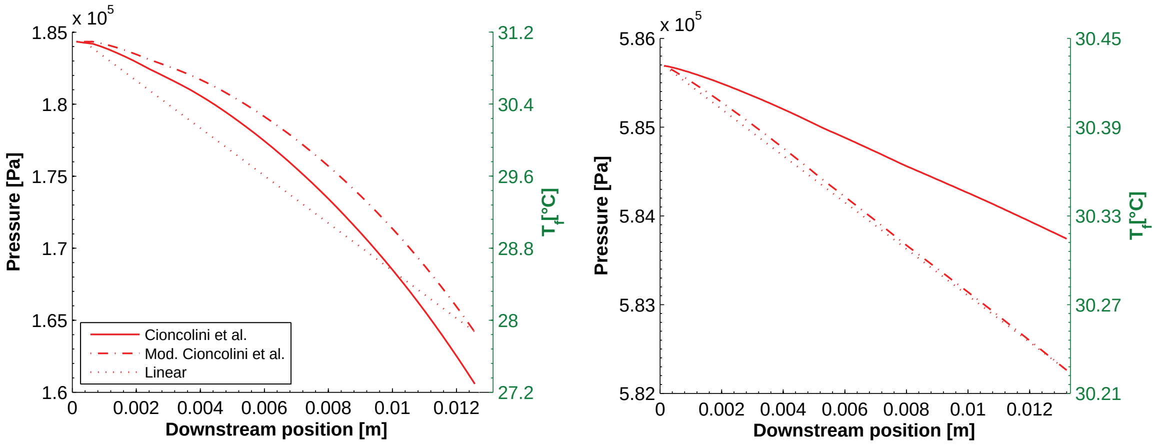

(a) Silicon test section: Along Column 4 for 14H, q_b 1600:400 kW/m^2, 713kg/m^{2}s

(b) Copper test section: R-1234ze(E) along Column 4 for R1H, q_b 2181:481 kW/m^2, 350kg/m^{2}s

Figure 6.14: Pressure drop model correction.

6.4.2 Mass flux variation due to non-uniform heat flux

In the case of a row hot-spot, the increase in pressure drop due to the hot-spot will be uniform in all channels and the mass flux will be uniform across all channels since the flow path is normal to the row hot-spot. Note that the mass flux distribution validation for the silicon test section presented in Chapter 4, used this characteristic of row hot-spots.

In the other power configurations, the different evaporation rates and vapor quality profiles will force the mass flux to vary in the parallel channels in order maintain the same differential pressure drop over the test section. Thus in channels running over column and point hot-spot conditions, the mass flux will be lower due to the higher resistance to flow. This effect was taken into account in the data reduction process. The fluid-side calculations were repeated over each column by changing the local mass flux until the total pressure drop over all columns varied by less than 2.5%.

The variation of the mass flux across the two evaporators is shown in Fig 6.15. The mass flux over the hot-spot decreases as its heat flux increases. In the copper test section, the mass flux also decreases slightly in the neighbouring columns. For q_b[kW/m^2]2020:410, the local mass flux in the silicon test section was calculated to be 68% of the nominal value. In the copper test section, the changes are less important: the pressure drops are lower, since the channels are bigger and there is more heat spreading. For a hot-spot at 12H, q_b[kW/m^2]4300:500, the local mass flux represents 78% of the nominal value.

This situation could runaway and reach dry-out in the channels where the hot-spot is situated. Such cases were encountered in the column hot-spot configuration, as shown in Fig 6.16, where the calculated exit qualities in the center channels were close 1, but a temperature run-off, denoting critical heat flux, was not recorded. This means that the heat spreading within the evaporators delayed the onset of the critical heat flux.

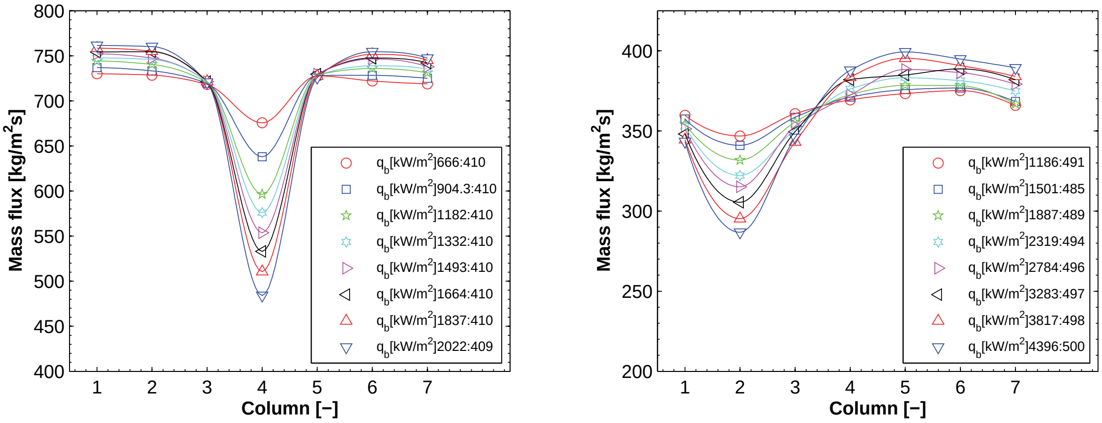

(a) Silicon test section: 34H, R-245fa, T_{sat}=30°C, 713kg/m^{2}s

(b) Copper test section: 12H, R-134a, T_{sat}=30°C, 367kg/m^{2}s

Figure 6.15: Mass flux variation due to hot-spot.

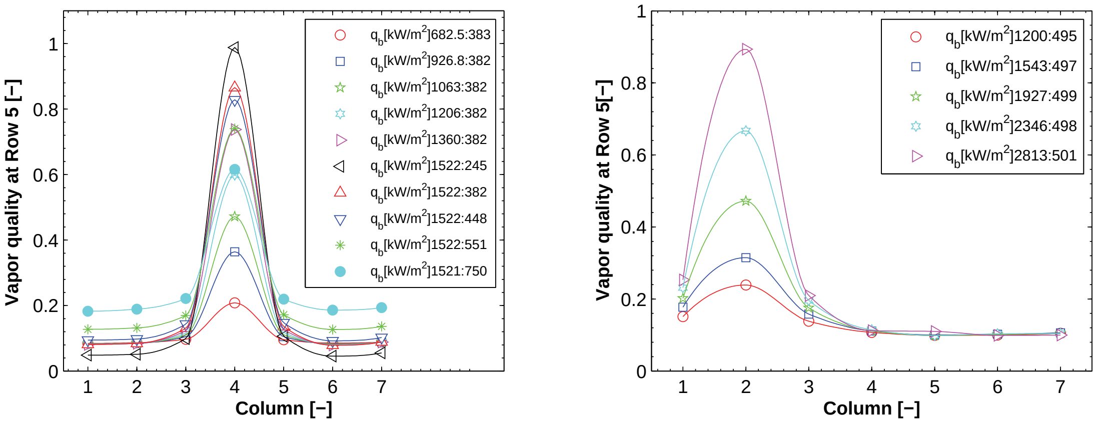

(a) Silicon test section: C4H, R-245fa, T_{sat}=30°C, G=702kg/m^{2}s

(b) Copper test section: C2H, R-134a, T_{sat}=30°C, G=373kg/m^{2}s

Figure 6.16: Vapor quality variation at Row 5 due to hot-spot.

6.4.3 Wall heat transfer coefficients

In this section, wall heat transfer coefficients will be described in the manner in which they will be needed to define the boundary condition in a numerical simulation of the present thermal packages, i.e. α_w will be plotted for different T_f and q_b. Since two-phase flow heat transfer coefficients are a function of the local heat flux, information about the average heat spreading over the hot-spot, $q_{footprint}/q_b$, will be listed along with, as it was done for uniform heat flux results, the lateral standard deviation (for row hot-spots), the uncertainty obtained through the error propagation and for point and column hot-spot, the mass flux variation over the hot-spot at the maximum heat flux difference.

The increase in local heat flux in the area surrounding the hot-spot, due to heat spreading, is sometimes quite important. Since the background base temperature were much colder than the hot-spot temperature, this led in a few cases to larger uncertainty in the calculation of such wall heat transfer coefficients. When this uncertainty was larger than 30% of the calculated heat transfer coefficient, the curves were considered too uncertain for use and were discarded.

Silicon test section

The heat transfer coefficients for row hot-spots at 701kg/m^{2}s are plotted in Fig 6.17 and point hot-spots at 712kg/m^{2}s in Fig 6.18. Due to the large amount of results obtained with the silicon test section, results for 503kg/m^{2}s and 900kg/m^{2}s were placed in Appendix B. The row and point hot-spots lose respectively 10 to 20% and 20 to 35% of their strength to heat spreading and it is more important in Row 3 than in Row 1 and 5.

In row hot-spot situations, wall heat transfer coefficients are ranged from 8000–22'000 W/m^{2}K, similar to what was found for uniform heat flux conditions. The strength of the hot-spot is more important the closer it is positioned to the inlet. Row 1 hot-spot had a V-shape trend as seen earlier for uniform heat fluxes when $q_b \geq 500 \mathrm{kW/m^2}$. For R3H and R5H, this shape is not seen, since in most tests, the background heat flux was below this level of $500 \mathrm{kW/m^2}$. As seen in Fig 6.17(a), doubling the hot-spot base heat flux over Row 1, results in a 30% increase in heat transfer. On the other hand, in Fig 6.17(c) for Row 5, the difference in heat transfer coefficients over the hot-spot are not significant. This is consistent with what was observed in uniform heat flux tests. The situation for Row 3 is more complex. There is an effect of heat flux, but more importantly Row 3 lies over the CB–A flow pattern transition line, discussed in Chapter 5, where minimum local heat transfer coefficient is often found.

In the case of varying background heat flux, the heat transfer evolution depends on the hot-spot position. For an hot-spot at Row 5, it increases with heat flux until it reaches the hot-spot. On the other hand, if the hot-spot is at Row 1, the heat transfer coefficients stay around 15'000$\mathrm{W/m^2K}$ for all vapor qualities. For uniform heat fluxes, relatively constant heat transfer coefficients were observed for base heat fluxes over $700 \mathrm{kW/m^2}$.

For point hot-spot experiments, the background heat flux was fixed at $400 \mathrm{kW/m^2}$ and the heat flux at the hot-spot was varied from 650 to $2200 \mathrm{kW/m^2}$. In Fig 6.18, the heat transfer coefficient over the hot-spot is in line with what was observed in Fig 5.9 for uniform heat flux: between 12'000 and 17'000$\mathrm{W/m^2K}$ for 14H, 14'000$\mathrm{W/m^2K}$ for 34H and around 20'000$\mathrm{W/m^2K}$ for 54H, which in this case is slightly over the uniform heat flux values. The heat transfer coefficients for 14H increase with increasing hot-spot heat flux. This increase is in part due to the relation between the heat flux and the heat transfer but it is also due to the mass flux reduction expected on Column 4. The mass flux variation can be important, down to 59% for 14H, $q_b[\mathrm{kW/m^2}]$ 2158:398. This reduction in mass flux can be used positively: for uniform heat flux, in Fig 5.12, it was observed that lower mass flux led to higher heat flux dependent heat transfer coefficients in the IB and CB flow regimes (this was not the case in the annular flow regime). However, the mass flux reduction also decreases the critical heat flux level, such that this effect should be carefully used.

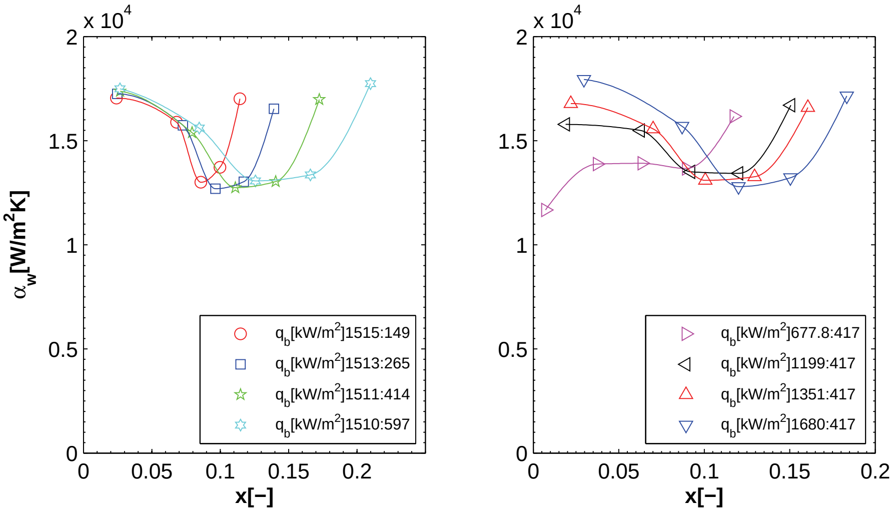

(a) R1H: Error: 6.9%, RMS: 13.6%, $q_{footprint}/q_b$: 88%

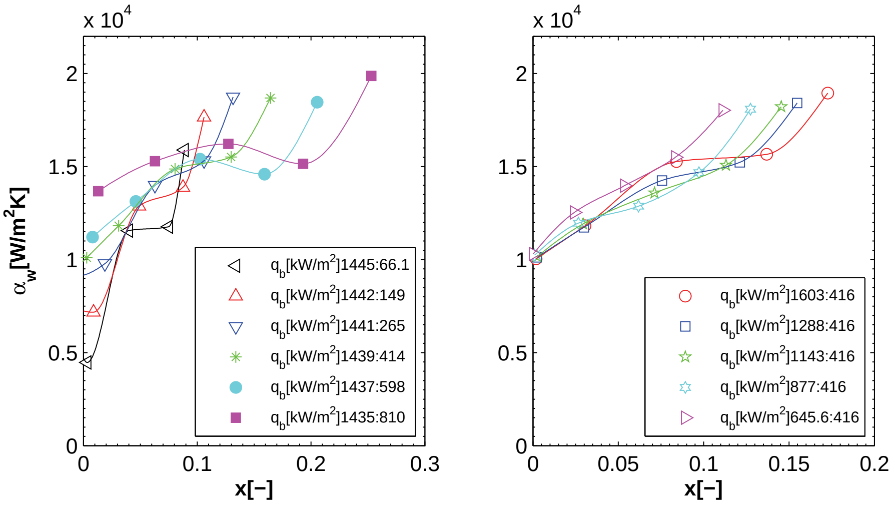

(b) R3H: Error: 5.1%, RMS: 11.1%, $q_{footprint}/q_b$: 80%

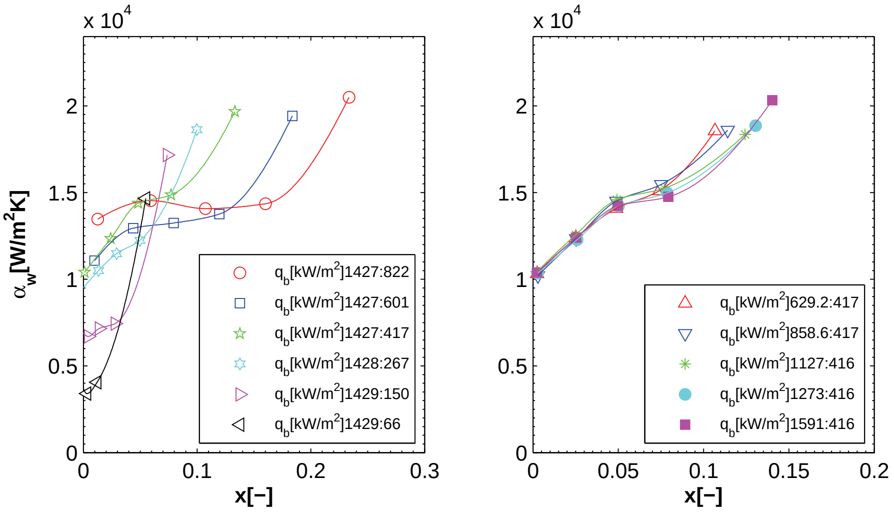

(c) R5H: Error: 5.1%, RMS: 10.7%, $q_{footprint}/q_b$: 91%

Figure 6.17: α_w for row hot-spot in the silicon test section at 701kg/m²s, T_{sat}=30°C.

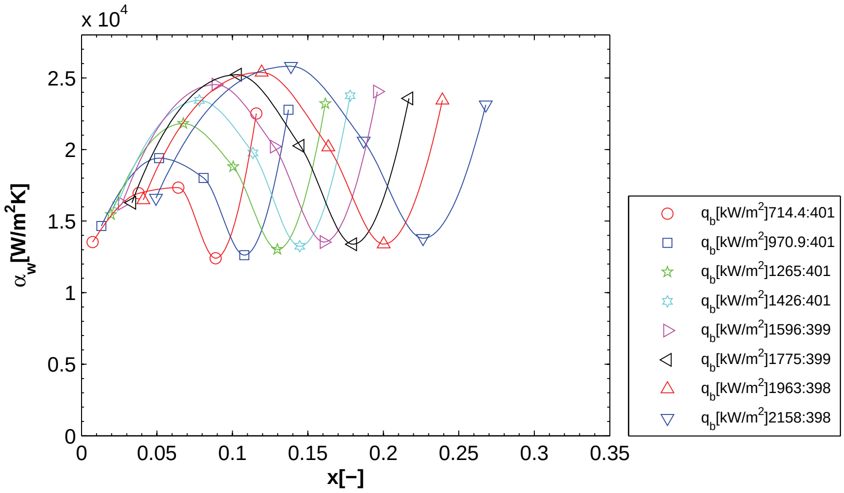

(a) 14H: Error: 11.1%, $q_{footprint}/q_b$: 72%, G_{min}/G_{nom}: 59%

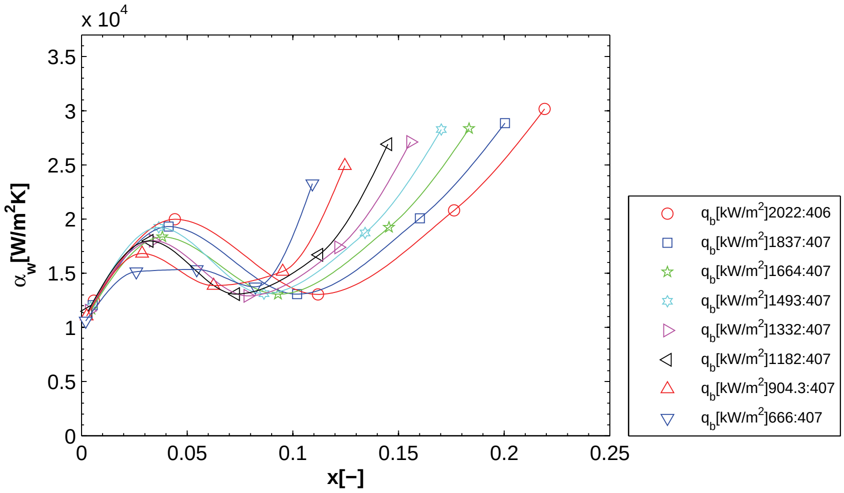

(b) 34H: Error: 10.8%, $q_{footprint}/q_b$: 64%, G_{min}/G_{nom}: 72%

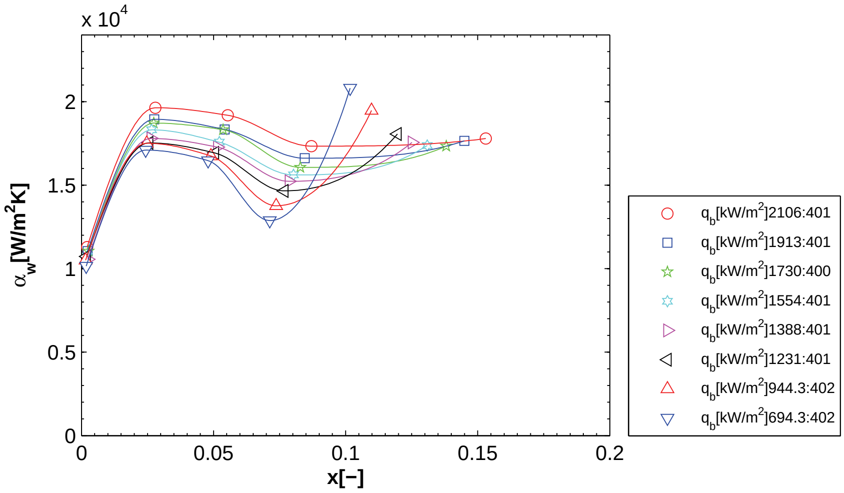

(c) 54H: Error: 11.3%, $q_{footprint}/q_b$: 72%, G_{min}/G_{nom}: 86%

Figure 6.18: α_w along Column 4 in the silicon test section for point hot-spot at 712kg/m^{2}s, T_{sat}=30°C.

In Fig 6.18(a), the 14H hot-spot seems to have a beneficial effect on the cooling of the surrounding heaters. This effect was not clearly seen for the row hot-spots, although in Fig B.18(a) at 503kg/m^{2}s, the heat transfer coefficients at Row 2 are larger than those of Row 1. To ensure that this was not a deviation induced by differences between the two- and three-dimensional conduction scheme, the data in Fig 6.17(a) were also reprocessed with the three-dimensional scheme and, shown in Fig 6.19, the results are the same as the one obtained with the two-dimensional scheme in Fig 6.17(a).

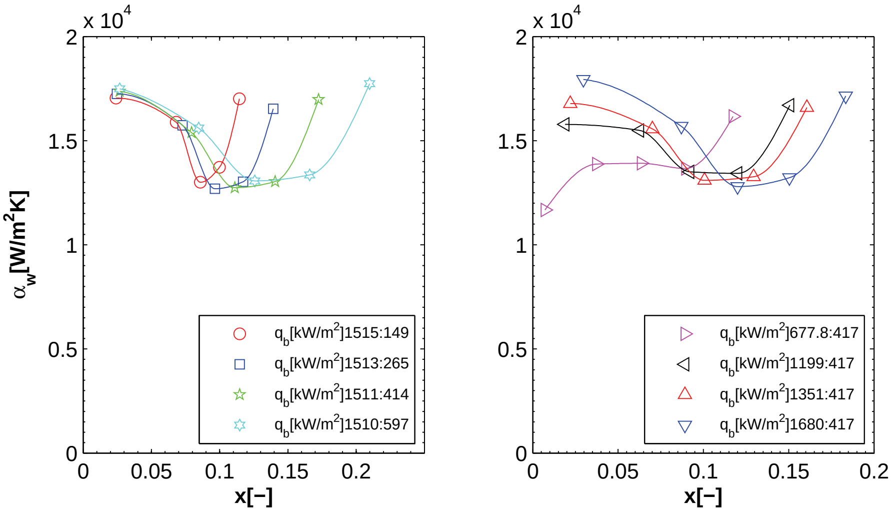

Figure 6.19: α_w for R1H at 701kg/m^{2}s, T$_{sat}$=30°C, calculated using the three-dimensional conduction scheme.

Since several parameters come into play when comparing row and point hot-spots, two similar situations have been compared in Fig 6.20 for results along Column 4. In the first case, the hot-spot is at R1H, 502kg/m^{2}s and q$_b$[kW/m^2] 1724:384 and for the other, the hot-spot is at 14H, the nominal mass flux is 714kg/m^{2}s, but the calculated one flowing over Column 4 is 499kg/m^{2}s and q$_b$[kW/m^2] 1596:399.

The wall heat transfer coefficients over Rows 1 and 2 for 14H are 16'200 and 22'500W/m^{2}K and for R1H, they are 17'400 and 20'250W/m^{2}K. Since the difference is within the margin of error, heat spreading in the point hot-spot is more important, but the wall heat fluxes for Rows 2 to 5 along Column 4 for both cases are almost the same, which means that the refrigerant extracted the same amount of heat flux. It is important to remember that the calculation of the mass flux variation is an estimate. Still, Fig 6.20 shows that for similar conditions the refrigerant reacts the same way to a row or to a point hot-spot.

Plotting uniform heat flux and hot-spot heat flux results in Fig 6.21, similarities and differences between them are highlighted. When heat transfer coefficients are plotted versus vapor quality, Row 5 hot-spots follow uniform heat flux results until they reach the hot-spot. Row 1 hot-spots start from the corresponding uniform heat flux value, but then tend toward the lower heat flux value. This is clearer when plotted against the downstream position in the right graph: the hot-spot heat transfer coefficients fall on the same point and can be deduced from the uniform heat flux one. Over the hot-spot, the heat transfer coefficients are as high as their uniform value and then tend toward the heat transfer coefficient of a uniform background heat flux.

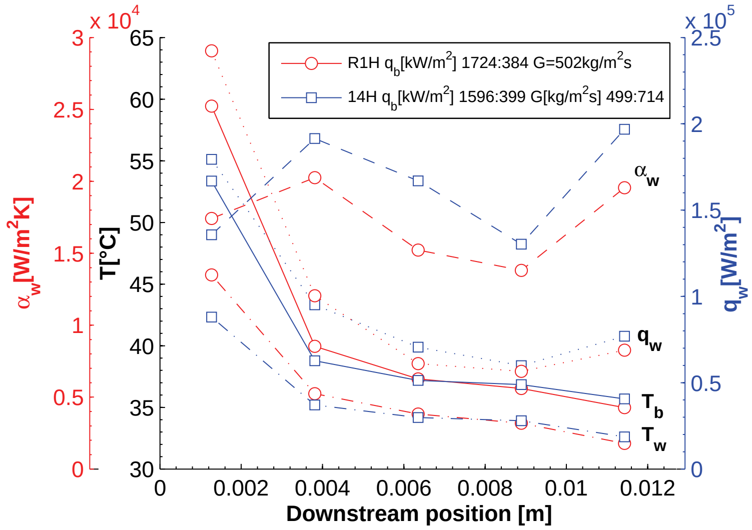

Figure 6.20: Comparison between the cooling for R1H and 14H at similar heat fluxes and mass flux along Column 4.

Vapor quality does not describe completely the fluid state and behavior. For the case of a uniform heat flux, the CB–A transition can be inferred from the heat transfer coefficient graphs. In the Row 1 hot-spot heat transfer curves, the same observations can be made, but the method cannot be extended to determine the flow pattern for hot-spots placed further downstream, because the heat transfer coefficient increases continuously. The effect of the hot-spot on the transition is difficult to assess, but it could generate the local flow pattern found in uniform heat flux conditions, even though the vapor qualities are different.

Hot-spots certainly modify the local flow regime compared to what would happen if it were formed only by background heat flux, an effect that could be used to raise the overall heat transfer coefficient. Close to the inlet, the hot-spot will be cooled by a slug flow flow, which reacts positively to an increase in heat flux. The increase in heat transfer over Row 2 can be tentatively explained by looking at the mechanism described by the three-zone model of Thome *et al.* (2004). The bubbles are generated at the inlet, where the hot spot is, at a frequency higher than if it was generated by the background heat flux. By the time the liquid film has reached the minimum film thickness, the heat flux is lower and the dry-out zone does not grow as fast. Thus on average, the local heat transfer coefficient is augmented.

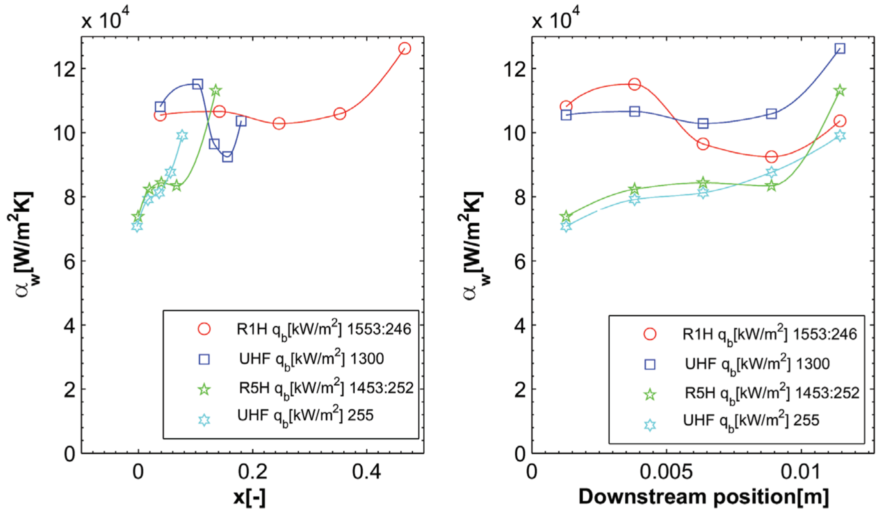

Figure 6.21: Comparison between the cooling for uniform heat flux and row hot-spots for R-245fa around 500kg/m^{2}s, in the silicon test section for similar heat fluxes.

Copper test section

The heat transfer coefficients for row hot-spots in the copper test section are plotted for R-134a, R-1234ze(E) and R-245fa in Figs 6.22 to 6.24, for different combinations of hot-spot and background heat fluxes. These graphs are representative of the trends observed for row hot-spots and the other results are presented in Appendix B. The heat transfer coefficients vary between 5000 and 27'000W/m^{2}K, within the range of what was seen in the copper test section for uniform heat flux. However direct comparisons are difficult because the wall heat fluxes are different from the base heat flux due to heat spreading.

Compared to the silicon test section, the background heat fluxes tested were higher and sufficiently high to have a V-shape, based on the uniform heat flux results. The peak heat transfer coefficients have about the same level as those of the silicon test section and results for R-245fa are lower than for R-134a and R-1234ze(E). In Row 1 hot-spots, i.e. the top graphs in the figures, heat spreading is moderate and the hot-spot losses about 20% of its strength. The heat transfer level over Row 1 appears to be lower than what was measured at uniform heat flux (15'000 instead of 20'000W/m^{2}K). For this configuration, the boosting effect observed in the silicon test section over Row 2 is also present. Its importance increases with the hot-spot heat flux and decreases with increasing background heat flux. In Fig 6.22(a), for q$_b$[kW/m^2]3125:494, the heat transfer coefficient at Row 2 is about 25'000W/m^{2}K, whereas for q$_b$[kW/m^2]3147:975, it is below 20'000W/m^{2}K.

In Row 5 hot-spots, the bottom graphs in the figures, the heat spreading is more moderate. For R-1234ze(E), the heat transfer coefficient is continously increasing reaching over 25'000W/m^{2}K for q$_b$[kW/m^2]3249:478. On the other hand, the heat transfer coefficient forms sometimes a plateau for R-245fa or drops over Row 5 for R-134a. The plateau can be explained for the annular flow regime, which is expected to occur towards the end of the channel. As it was discussed in Chapter 5, heat transfer in the annular flow regime is a predominantly a function of the liquid film and not of the heat flux. For R5H, q$_b$[kW/m^2] 1176:699, the wall heat flux goes from 120kW/m^2 at Row 4 to 145kW/m^2 at Row 5 and the wall heat transfer changes from 17'900W/m^{2}K to 18'800W/m^{2}K, which is comparable to the increase seen for a uniform heat flux in Fig B.7 for a similar situation. As for the drop in heat transfer coefficient, it could signal partial dry-out at the channel outlet, although the heat transfer level remains above 15'000W/m^{2}K.

Compared to non-uniform heat flux results observed in the silicon test section, the minimum heat transfer coefficient at Row 3 for hot-spots at the same position is a new trend. In many cases, the curves for Row 3 hot-spots dip over the hot-spot, some taking the V-shape seen for uniform heat flux conditions. In Fig 6.22(b), this effect increases with increasing hot-spot heat flux, but in Fig 6.23(b), it stays constant around 10'000W/m^{2}K. In Row 3 hot-spots, heat spreading is important and the hot-spots lose on average 40% of their strength.

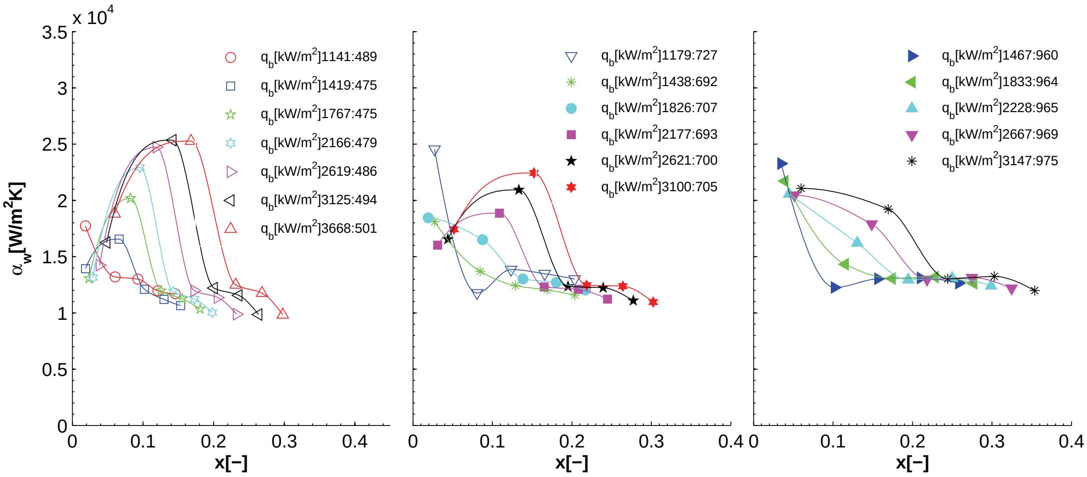

(a) R1H: G=364kg/m^{2}s, Error: 11.2%, RMS: 18.3%, q$_{footprint}$/q$_b$: 81%

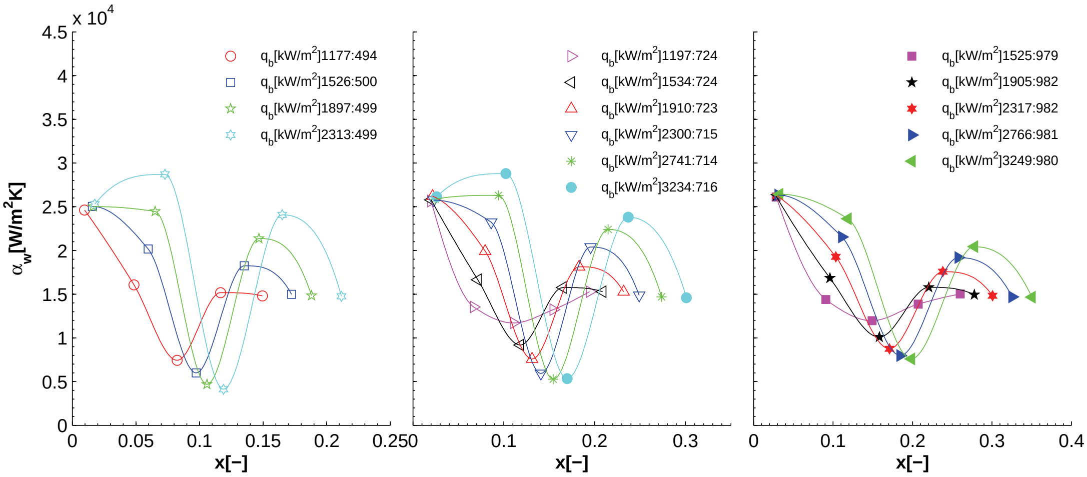

(b) R3H: G=366kg/m^{2}s, Error: 11.3%, RMS: 20.1%, q$_{footprint}$/q$_b$: 56%

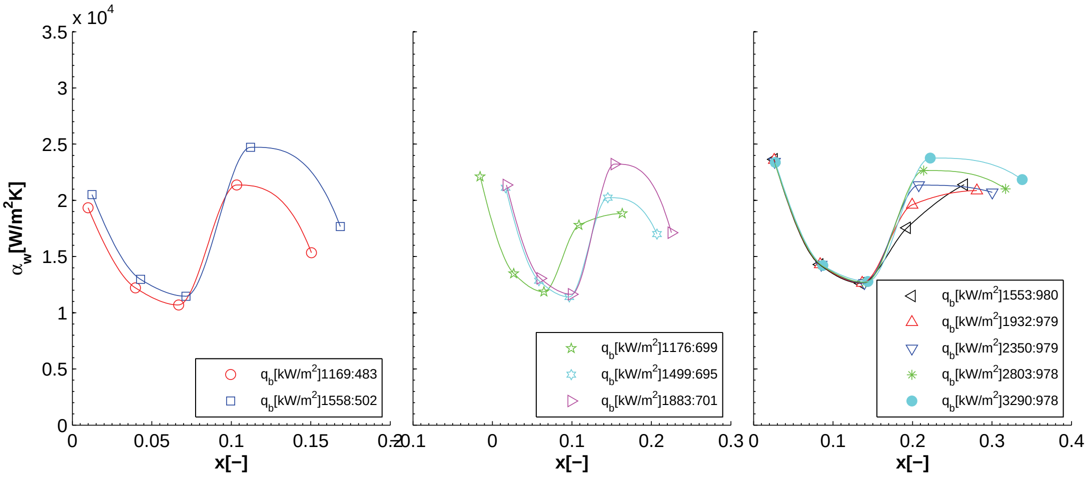

(c) R5H: G=365kg/m^{2}s, Error: 10.8%, RMS: 19.7%, q$_{footprint}$/q$_b$: 80%

Figure 6.22: α_w for row hot-spots with R-134a in the copper test section, T$_{sat}$=30°C.

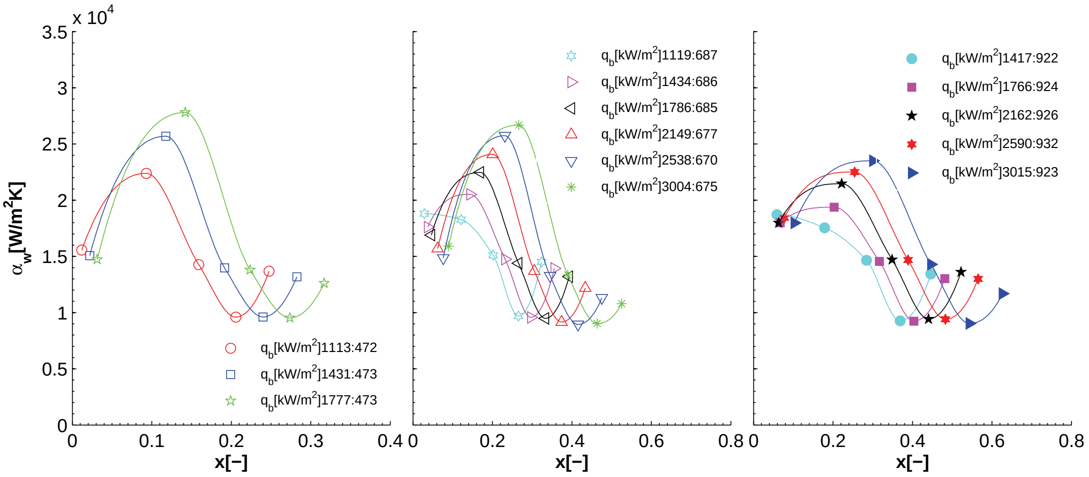

(a) R1H: G=212kg/m^{2}s, Error: 11.7%, RMS: 23.6%, q$_{footprint}$/q$_b$: 78%

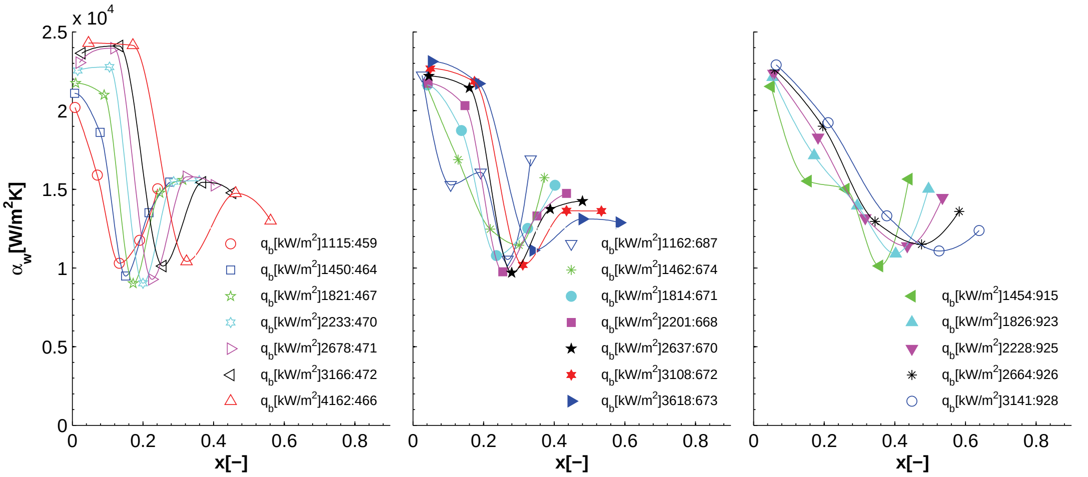

(b) R3H: G=210kg/m^{2}s, Error: 11.4%, RMS: 21.6%, q$_{footprint}$/q$_b$: 63%

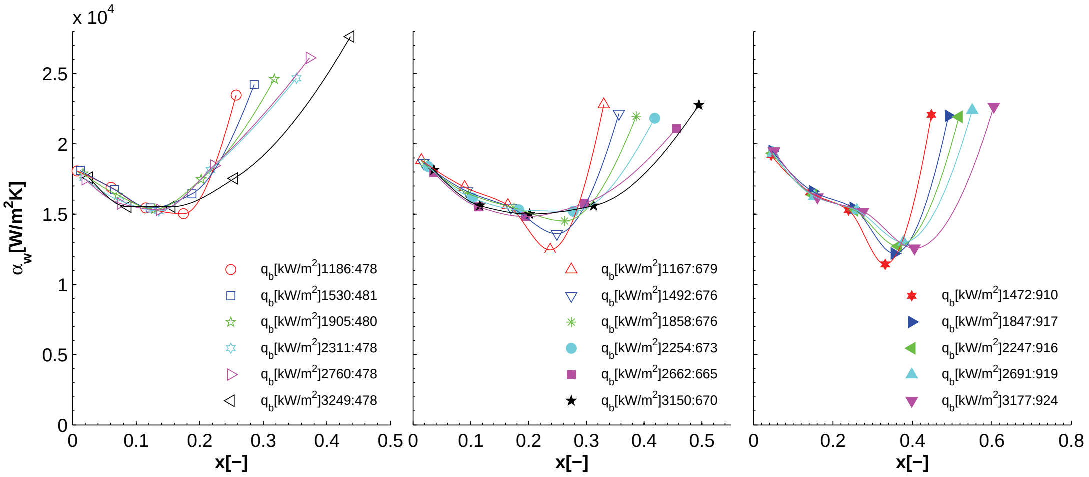

(c) R5H: G=211kg/m^{2}s, Error: 11.4%, RMS: 21.7%, q$_{footprint}$/q$_b$: 84%

Figure 6.23: α_w for row hot-spots with R-1234ze(E) in the copper test section, T$_{sat}$=30°C.

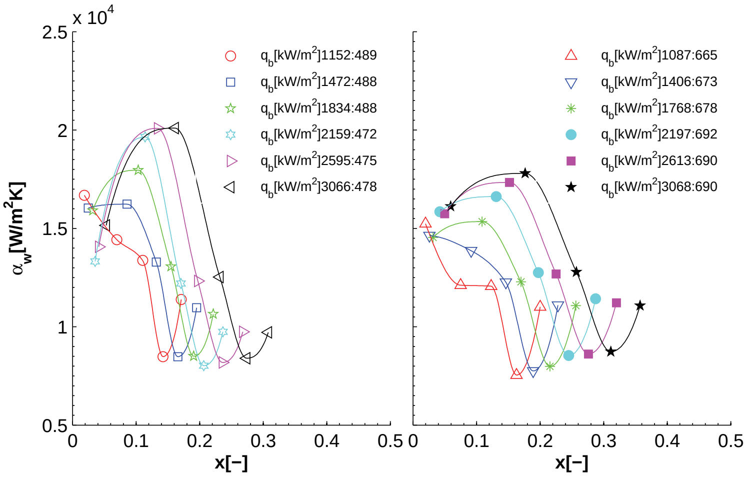

(a) R1H: G=286kg/m^{2}s, Error: 11.8%, RMS: 27.1%, q$_{footprint}$/q$_b$: 78%

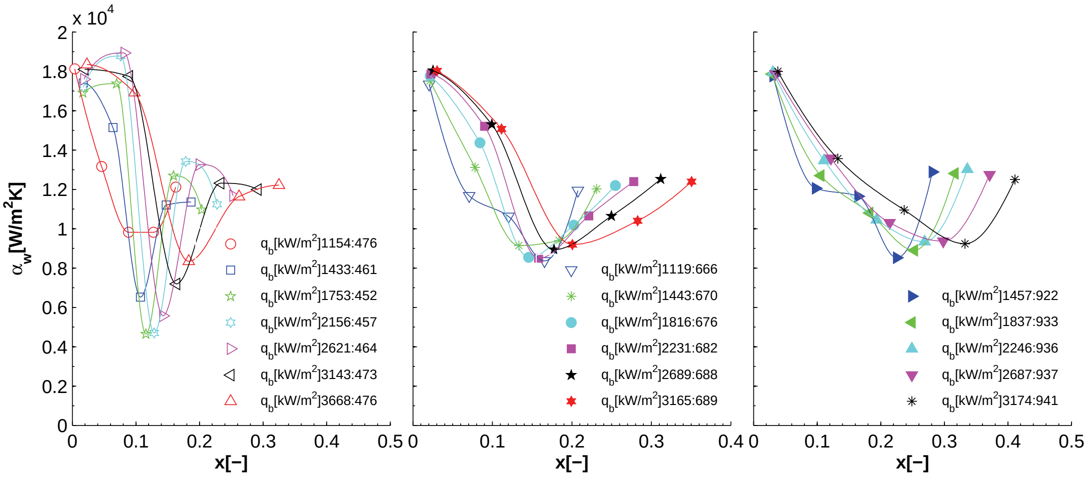

(b) R3H: G=286kg/m^{2}s, Error: 11.3%, RMS: 19.2%, q$_{footprint}$/q$_b$: 61%

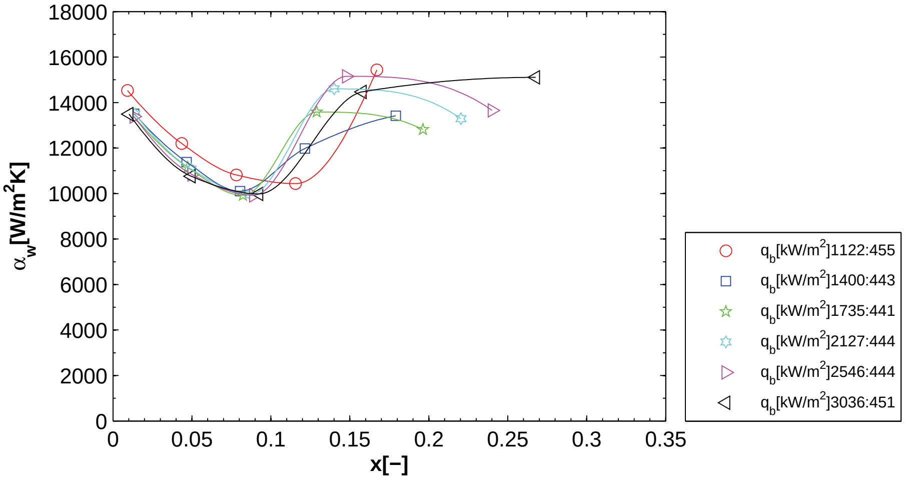

(c) R5H: G=284kg/m^{2}s, Error: 15.6%, RMS: 18.8%, q$_{footprint}$/q$_b$: 77%

Figure 6.24: α_w for row hot-spots with R-245fa in the copper test section, T$_{sat}$=30°C.

The minimum over Row 3 could thus be mostly due to heat spreading. Fig 6.25 helps to explain this trend. The heat spreads to the surrounding rows and the wall heat flux is the smallest at Row 3 and so is the heat transfer. The minimum observed over Row 3 is thus indeed due to heat spreading. This means that for Row 3 hot-spots, the path of least thermal resistance in the composite wall passes through Rows 2 and 4. In Fig 6.25, the difference in base temperature between Row 2 and 3 is 17.2°C, a strong driver for heat spreading. The heat transfer coefficient also contributes to heat spreading towards Rows 2 and 4, albeit to a lesser extend than the high thermal conductivity.

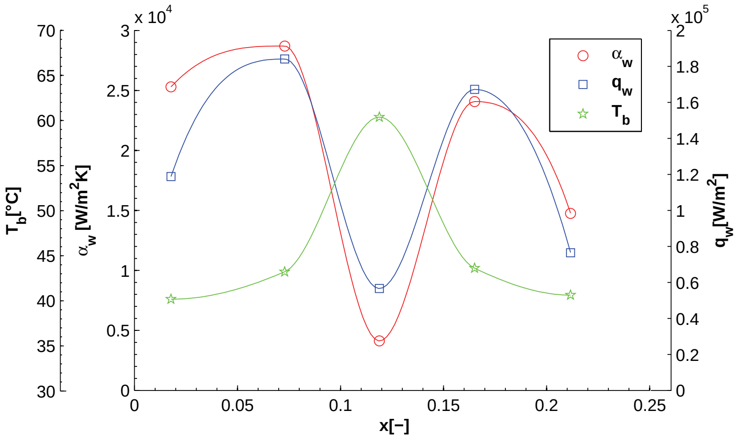

Figure 6.25: Base temperature, wall heat transfer coefficients and heat flux for R3H, q_b[kW/m^2]2212:499, 366kg/m^{2}s.

In some cases, heat spreading from the R3H hot-spots creates an almost uniform wall heat flux condition. It is then possible to make a comparison with results from Chapter 5, as it was done in Fig 6.26. For each fluid, the heat transfer coefficients for the hot-spot and uniform heat flux situation are close together, often within the margin of uncertainty (about 10%). The largest difference in heat transfer is found for R-134a at the inlet (R3H: 25'500W/m^{2}K, UHF: 19'000W/m^{2}K), but the wall heat fluxes also differ: 186kW/m^2 for the hot-spot and 165kW/m^2 for the uniform heat flux case.

A similar comparison is shown in Fig 6.27 for R1H and R5H, although in this case heat spreading does not form a uniform wall heat flux. The results are the same as what was observed for the silicon test section, shown in Fig 6.21: when plotted against the downstream position, the non-uniform heat transfer coefficients can be deduced from the uniform heat flux one. Over the hot-spot, the heat transfer coefficients are as high as their uniform value and then tend toward the heat transfer coefficient of a uniform background heat flux.

More generally, no important distinction was observed for flow boiling in microchannels between uniform and non-uniform heat flux. In both situations, the pressure drop and the local heat transfer coefficient are a combined function of the local mass flux, wall heat flux, vapor quality and flow pattern. Figs 6.21, 6.26 and 6.27 show that when the conditions at the wall are the same, the heat transfer coefficients for uniform and non-uniform base heat flux are similar. This is an important conclusion since it means that uniform heat flux heat transfer methods should extrapolate well to non-uniform conditions.

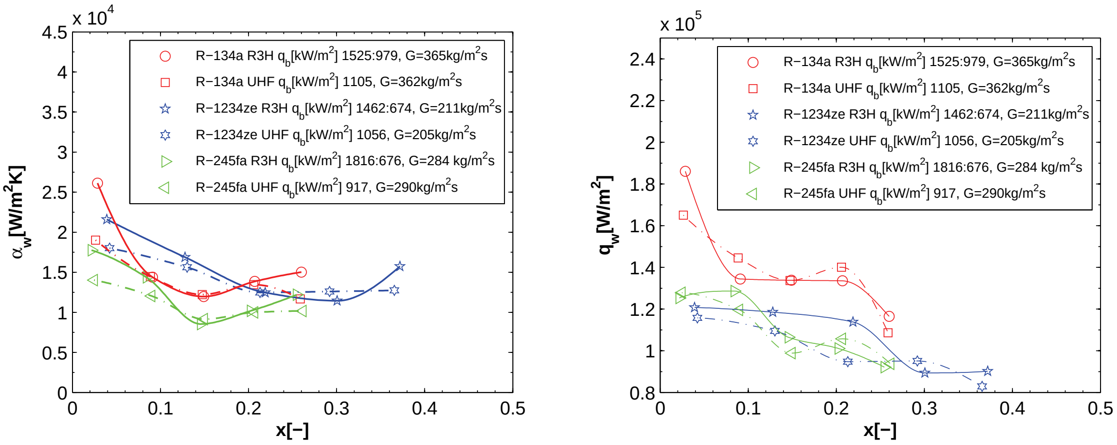

(a) Wall heat transfer coefficient (b) Wall heat flux

Figure 6.26: Comparison between some results obtained with the copper test section for R3H hot-spots and uniform heat flux results at T$_{sat}$=30°C.

The difficulty with non-uniform heat flux lies in calculating the local wall conditions. In the case of uniform heat flux, the computations are relatively simple because the mass flux can be assumed to be uniform across the evaporator and the wall heat flux to be equal to the base heat flux (for a one-dimensional thermal conduction approach). The vapor quality is easily determined from an energy balance and the equations for flow pattern transition are often based on the vapor quality. For non-uniform heat flux conditions, a few assumptions need to be made, since in most cases neither the local mass flux nor the wall heat flux can be directly known (but only backed out by appropriate calculations). In the present experimental setup, iterative calculations could be avoided to determine the wall heat flux by using the direct multi-dimensional thermal conduction scheme presented in Chapter 3, which greatly speeds up the iterative calculation process with respect to a fully numerical analysis.

If the thickness of the composite wall was smaller, it would first result overall in a lower base temperature. Then the effect of heat spreading would be less important such that the wall heat flux would be closer to the base heat flux values. This could simplify the calculation of the thermal conduction if the heat spreading was low enough to use a one-dimensional approach. For the fluid-side calculations, the situation would remain the same; once the local conditions at wall are determined, it is possible to obtain the local heat transfer coefficient.

Although the wall heat transfer coefficients can be derived from uniform heat flux results, the hot-spot position and orientation remain important factors. It is clearly better to orient "long" hot-spots perpendicular to the flow direction to diminish the mass flux non-uniformity. Placing the hot-spot near the inlet or the outlet brings different advantages. Positioned near the inlet, the average heat transfer coefficient will be higher along the entire channel and, as it was discussed by Revellin *et al.* (2008), the critical heat flux value will be higher, but for point hot-spots, the mass flux in the channels running over the hot-spot will be smaller. On the other hand, when the hot-spot is placed near the outlet, the pressure drop will be lower, especially for the silicon test section, and the mass

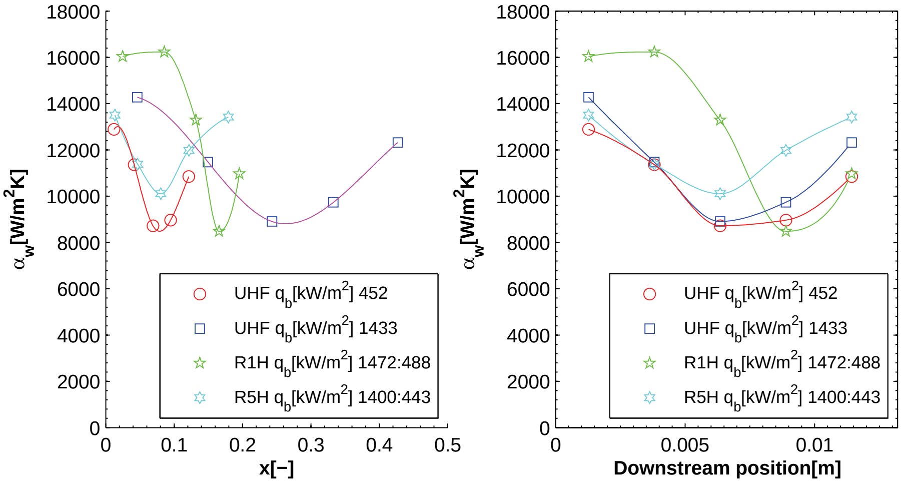

Figure 6.27: Comparison between the cooling for uniform heat flux and row hot-spots for R-245fa in the copper test section for 290kg/m^{2}s and T$_{sat}$=30°C, at similar heat fluxes.

flux will be more uniform.

6.5 Comparison with prediction methods

Since the characteristics of flow boiling in microchannels do not change locally between uniform and non-uniform heat flux conditions, uniform heat flux prediction methods can extended to non-uniform heat flux situations, although the computation must imperatively be done will the local mass flux and wall heat flux accounting for the influence of heat spreading. For uniform heat flux, two methods were reasonably precise for all fluids and both test sections: the new flow pattern-based method and the one of Bertsch *et al.* (2009) (see Tables 5.4 and 5.5).

Two modifications were made here to the flow pattern-based method. Firstly, since a clear link between the vapor quality and the CB–A flow pattern transition could not be seen for non-uniform heat flux results, equation 5.3 cannot be used, and the criteria for changing from the three-zone to annular flow model was to use the greater of the two values, i.e.:

$$\alpha_w = max\left(\alpha_{3Z}, \alpha_{AF}\right) \tag{6.1}$$

Second, to bring in the increase in heat transfer coefficient over Row 2 when the hot-spot is placed at Row 1 or 14H, the bubble frequency calculated for Row 1 was used for these power configurations in the downstream calculation for Row 2:

$$f_{R2} = (1-c)\left(\frac{q_w}{q_{ref}}\right)^{1.74} + cf_{R1} \tag{6.2}$$

The effect of the multiplier c is shown in Fig 6.28. As c increases, the heat transfer over the whole evaporator increases. In the silicon test section, n=0.25 was found to improve the prediction accuracy, whereas in the copper test section, it was better to set n=0, because for high wall heat fluxes, the three-zone model overpredicted the heat transfer coefficients.

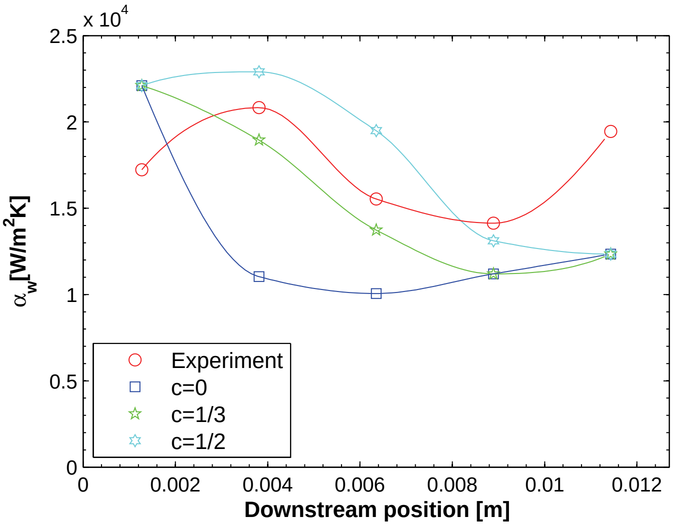

Figure 6.28: Impact of the multiplier for the bubble frequency in the silicon test section for R1H, q_b[kW/m^2] 1550:553, 503kg/m^{2}s.

In Figs 6.29 and 6.30, all the test conditions that were processed are compared against the prediction methods. Both methods centered the result for the copper test section well, although, as it is listed in Table 6.1, the flow pattern-based method has a smaller mean average error and places more data within ±30%. In the case of the silicon test section, the method of Bertsch *et al.* (2009) is not precise. The flow pattern-based method is more precise, although it has a problem with the point hot-spots. Overall, this method predicts all the data with a mean average error of less than 30%, which is quite good when taking into account the relatively large experimental uncertainty found in non-uniform heat flux situations.

Table 6.1: Mean average error and percentage of data within ±30% for the local heat tranfer coefficients for non-uniform heat flux.

	Silicon test section	Copper test section
Bertsch *et al.* (2009)	MAE 46%	MAE 27.9%
	Within ±30%: 18.2%	Within ±30%: 55.6%
New method	MAE 31%	MAE 28.8%
	Within ±30% 49.7%	Within ±30%: 59.8%

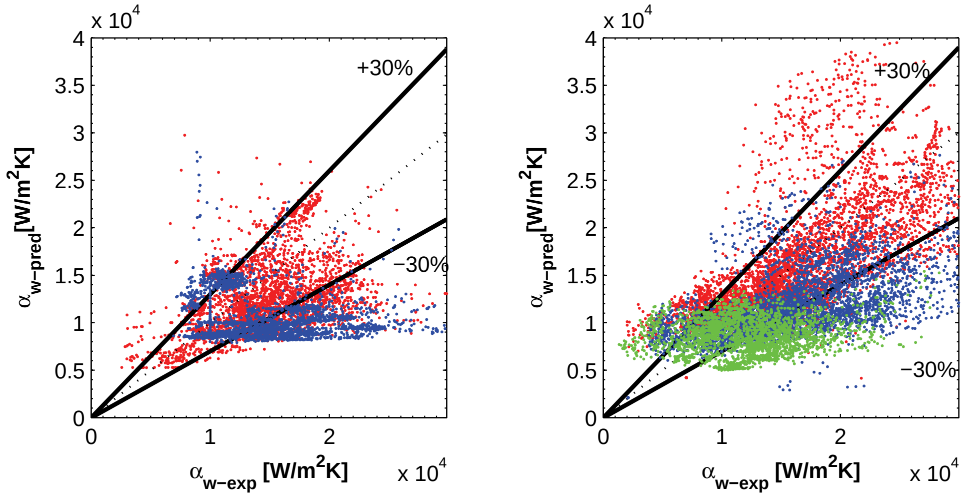

(a) Silicon Red: Row hot-spot Blue: Point hot-spot

(b) Copper Red: R-134a, Blue: R-1234ze(E), Green: R-245fa

Figure 6.29: Comparison of non-uniform heat flux results with the new flow pattern based heat transfer model.

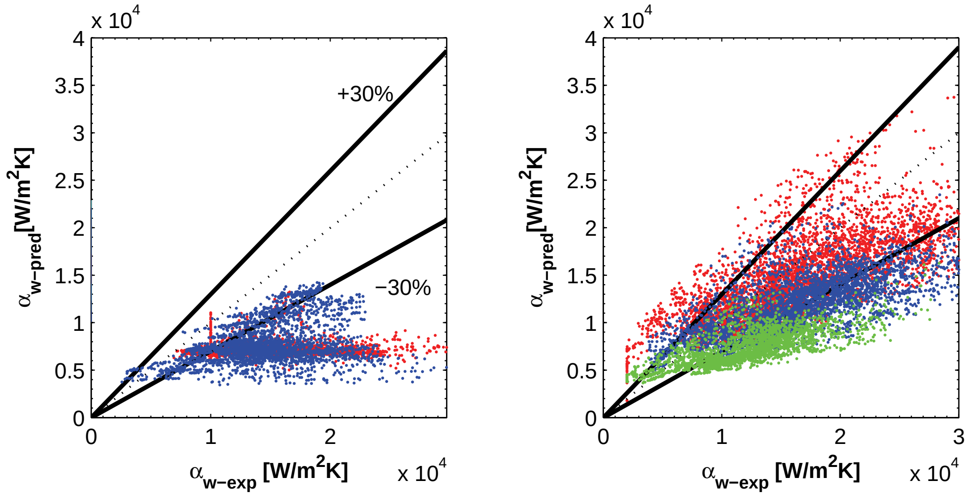

(a) Silicon Red: Row hot-spot Blue: Point hot-spot

(b) Copper Red: R-134a, Blue: R-1234ze(E), Green: R-245fa

Figure 6.30: Comparison of non-uniform heat flux results with the method of Bertsch *et al.* (2009).

Chapter 7

Transient response

In two-phase cooling system for microelectronics, there are two important transient thermal processes. First, the heat flux generated by the chip changes with the CPU usage and second, the instantaneous heat removal by the fluid is time-dependent, since liquid slugs are followed by vapor ones. The instrumentation on the test sections was designed to be able to track the changes in the base temperature, the base heat flux and the mass flux at rates over 1000Hz and provide insight on the physical reaction of the whole thermal package.

7.1 Constant base heat flux

The first series of transient tests consisted of studying the instanteneous response measured for constant base heat flux cases, under conditions similar to those presented in Chapter 5. The objective was to obtain information about the frequencies at which the local base temperatures vary. These tests were done with the copper test section. The procedure and results are presented below.

The first step is to determine what are the relevant frequencies found at the base. Fig 7.1 presents the signal to noise ratio of the base temperature signal for heater 34 for R-245fa. Both signals were sampled at 1000Hz in 10 blocks of 2048 samples. The noise was defined as the signal measured when all electrical equipment on the test facility were turned on, the refrigerant was at the desired saturation temperature and the mass flux and heat flux were set to zero. The power spectral density (PSD) of the two-phase signals has the same strength as the noise signal for frequencies over 20Hz. The strong peak at 50Hz is the noise created by the alternating current frequency. Based on these results, the sampling frequency was reduced to 200Hz and anything occuring above 30Hz will be ignored.

The power spectral densities of various local base temperatures for a two-phase flow of R-134a flowing at 290 and 460kg/m^{2}sover Column 4 are shown in Fig 7.2. Similar graphs for R-1234ze(E) and R-245fa are shown in Appendix B and the PSD for the other columns were similar to those for Column 4. A peak is present at 8Hz for 290kg/m^{2}s and at 13Hz for 460kg/m^{2}s. At Row 5 in Fig 7.2(f), the peak almost disappears.

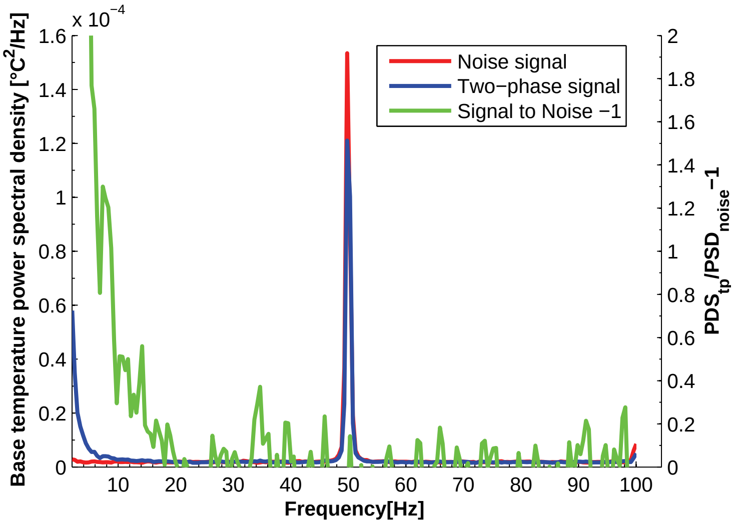

Figure 7.1: Signal to noise ratio for the copper test section with R-245fa.

These frequencies are the result of the combined effects of the thermal diffusivity in the composite wall and the variation in instantaneous heat removed by the fluid. It is difficult to separate these factors, but it is possible to evaluate a characteristic time (or frequency) for heat conduction inside the composite wall and estimate its importance.

The copper base is the main component in the thermal package. It has a thermal diffusivity of $116.6\times10^{-6}\mathrm{m}^2/\mathrm{s}$ at 20°C (Kreith & Bohn (2001)). Taking the copper base thickness as the characteristic length (1800μm), the characteristic frequency of the copper base is 36Hz, much smaller than the peak frequencies. Even adding the characteristic frequencies of the silicon chip and the TIM (using data for pure gallium), the characteristic frequency does not become smaller than 30Hz.

Consequently, the frequency peaks in Fig 7.2 could be linked to the fluid-side response. Dupont *et al.* (2004) showed in a graph, reproduced in Fig 7.3, that for a wall heat flux between 10 and $60\mathrm{kW/m}^2$, the bubbles frequencies were around 10Hz. In such case, the peak can be potentially explained by the bubble frequency. However if it was the only factor, the peak would change with heat flux, which is not observed. Since the peak changes with mass flux, the inlet restriction could be playing a role. It is used to flash the incoming fluid and it is possible that the faster the flow is, the higher the bubble frequency. Finally, the disappperance of the peak at Row 5 would then be expected if the flow was annular, since the instantaneous heat transfer mechanism in annular flow region is more constant, as the intermittency dissappears.

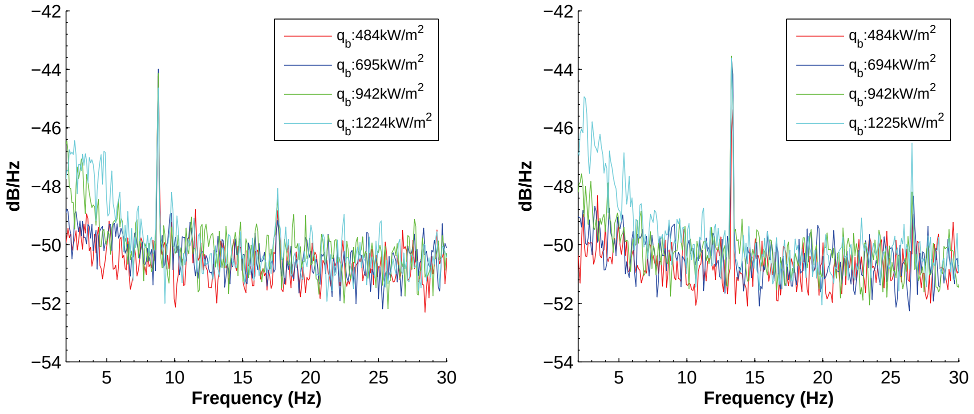

(a) Heater 14, 290kg/m^{2}s (b) Heater 14, 460kg/m^{2}s

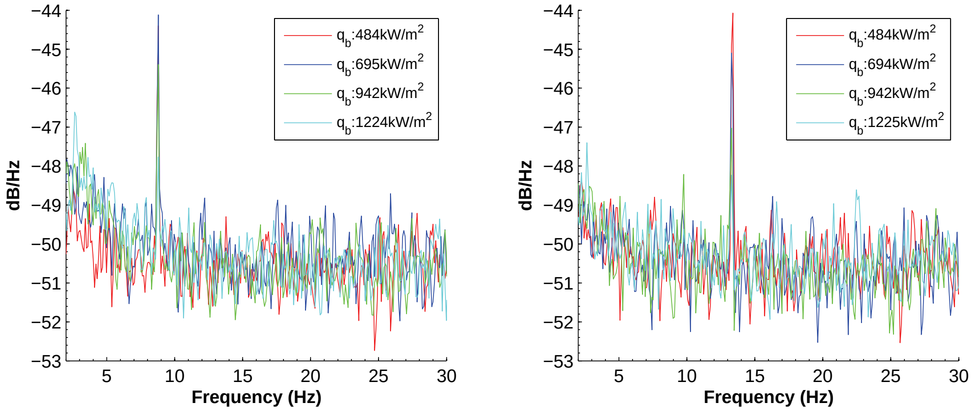

(c) Heater 34, 290kg/m^{2}s (d) Heater 34, 460kg/m^{2}s

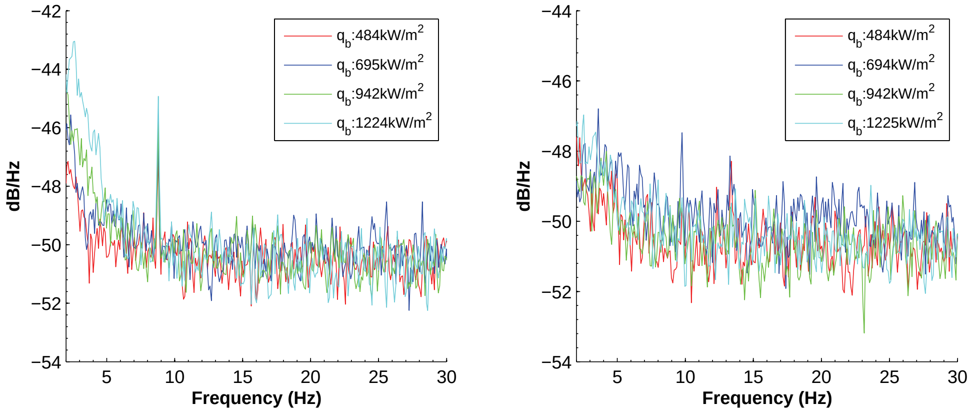

(e) Heater 54, 290kg/m^{2}s (f) Heater 54, 460kg/m^{2}s

Figure 7.2: Power spectral density for R-134a in the copper test section at T$_{sat}$=30°C

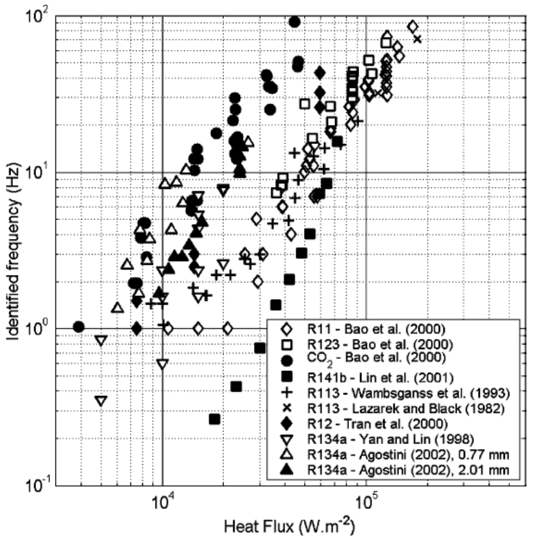

Figure 7.3: Evolution of the optimum frequency identified for each series of test versus heat flux for different fluid and tube diameter. From Dupont *et al.* (2004).

7.2 Varying base heat flux

In situations where the base heat flux varies, it is important to see if there is a time response lag between an increase in heat flux and the rate of heat transfer. As it was seen in Chapter 5 and 6, the steady-state base temperature increases as the heat flux increases. However, if the fluid-side does not react fast enough, an undesirable temperature overshoot could occur.

In Fig 7.4 the results for the base temperature response are shown at heater 34 to a step change of the uniform heat flux for different mass fluxes. The signals for the other heaters were very similar to those of heater 34. In these tests, the increase in heat flux is denoted in a similar fashion to a non-uniform heat flux. To described a condition where the initial base uniform heat flux is 300kW/m^2 that then jumps to 600kW/m^2, the notation is q$_{h-l}$[kW/m^2]600:300. The change in heat flux was almost instanteneous, as shown in Fig 7.5. Each signal was sampled for 10 seconds at 1000Hz, during which the heat flux jumped. The moment when the heat flux was changed corresponds to the time when temperature started increasing.

The base temperature changes rapidly and reaches an almost constant value within one second. In Fig 7.4(a), the fourth curve for 800kg/m^{2}s, q$_{h-l}$[kW/m^2] 889:396 presents a small temperature overshoot of about 0.3°C just after the heat flux increased. From the transient signal, the characteristic reaction time of the thermal response can be calculated. The response curve to a step input (Ogata (1998)) is:

$$\theta(t) = \left(1 - e^{\frac{-t}{\tau}}\right)\theta_0 \tag{7.1}$$

where τ is the characteristic time, θ_0 is the difference in temperature at the start of the step (T$_0$) and that measured one second later. θ is then the difference between the instantaneous temperature and T_0.

For the three graphs in Fig 7.4, the average characteristic times were respectively from top to bottom: 61ms, 83ms and 50ms. The corresponding frequencies are: 16Hz, 12Hz and 20Hz. These are relatively close to the peak frequencies seen in Fig 7.2, such that both could be linked.

The copper test section was also tested for square wave change in heat flux in Fig 7.5 and for sudden change in heat flux starting from a single-phase flow in Fig 7.6. The test section reacted very well to the square signal. Over the six cycles, the upper and lower temperatures are stable and change by less than 0.5°Cfrom the start to the end of the sampled data. The temperature response follows the change in heat flux and its reaction is instantaneous. Unfortunately, it was not possible to increase the frequency for the signal and bring it closer to the characteristic response time, due to limitation in the speed of the communication protocol used by the power sources.

In the case of a sudden change in heat flux starting from a single-phase flow condition, the copper test section has no problem to handle thermally an increase from 0 to 582kW/m^2, as shown in Fig 7.6(a). The temperature overshoot is more important, about 2°C, and is probably due to the level of superheat needed to trigger the onset of boiling. On the other hand, the evolution of the mass flux is more problematic. From an initial value of 455kg/m^2s, it decreases in 10 seconds to 150kg/m^2s. If this trend was allowed to continue, the mass flux would become small enough to come close to a critical heat flux situation. It is thus important for start-up situation to have a control mechanism which insures a minimum mass flux. For example, on the present test loop, a quick reaction valve could be installed right before the test section to increase the flow rate in the test section by reducing the pressure drop up-front of the test section. In summary, the transient tests showed that the two-phase cooling process responds rapidly and adequately to cool microelectronics.

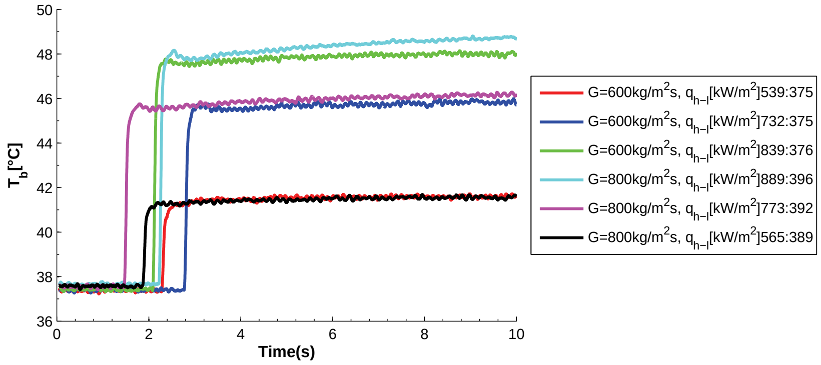

(a) Silicon test section: R-245fa

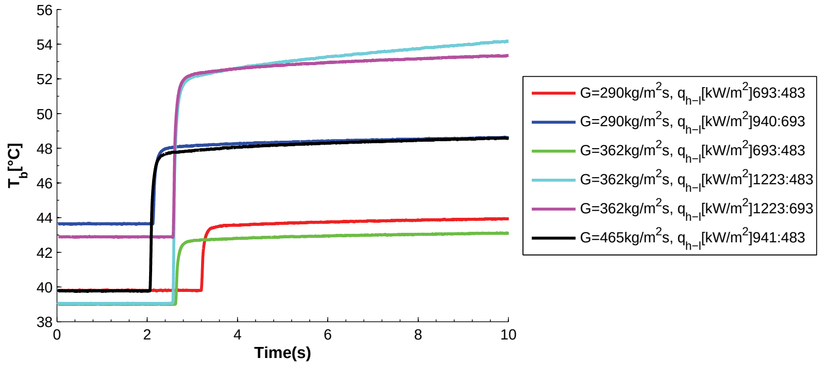

(b) Copper test section: R-134a

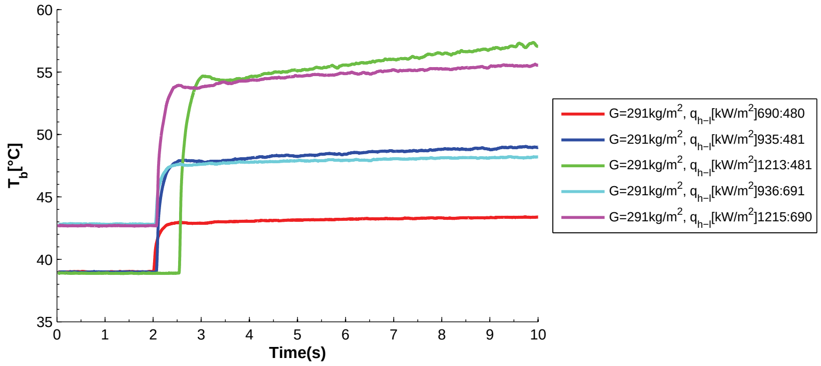

(c) Copper test section: R-245fa

Figure 7.4: Base temperature signal at heater 34 for sudden change in base uniform heat flux.

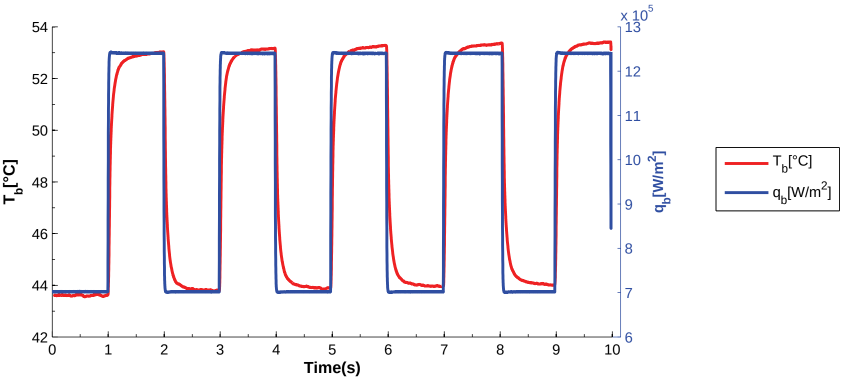

Figure 7.5: Thermal response at heater 34 of the copper test section to a square change in base uniform heat flux for R-134a, 453kg/m^{2}s, T$_{sat}$=30°C.

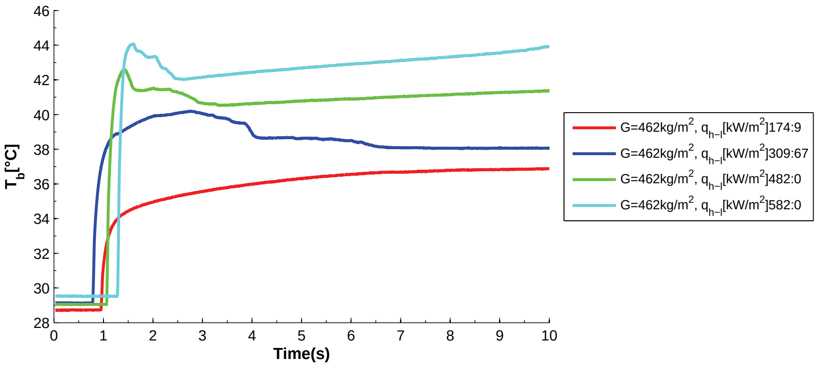

(a) Base temperature of heater 34

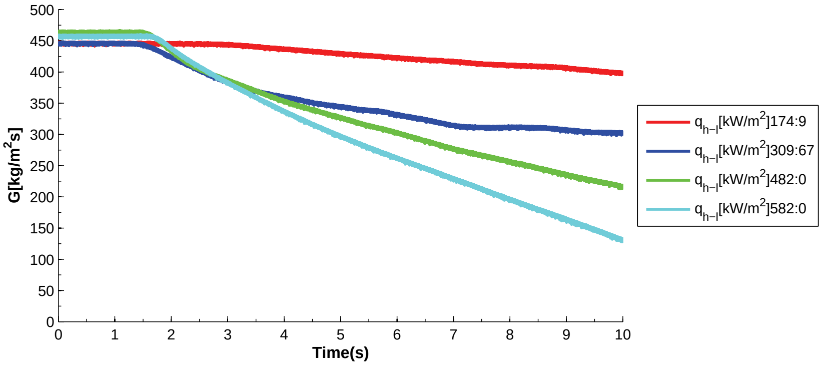

(b) Mass flux

Figure 7.6: Response of the copper test section to a sudden change in base uniform heat flux from single-phase condition for R-134a, 453kg/m^{2}s, T$_{sat}$=30°C.

Chapter 8

Conclusions

In the introduction to this work, open points concerning the thermal response of multi-microchannels evaporators under uniform, non-uniform and transient heat flux situations were listed. To answer them, an extensive experimental campaign was performed with four refrigerants and two test sections at different mass fluxes. In order to extract the most information from these measurements, a new method was implemented to measure the pressure drop across the outlet restriction of a micro-evaporator and a robust multi-dimensional thermal conduction scheme was developed to include in the data reduction the effect of heat spreading inside the thermal package.

The analysis of the results was divided into four categories: pressure drop, heat transfer under uniform heat flux, physical reaction to non-uniform heat flux conditions and the thermal response to transient heat flux conditions. For each aspect, the following conclusions can be highlighted:

- Each pressure drop component was evaluated, such that their relative importance could be evaluated. The inlet restriction pressure drop had the smallest influence on the total pressure drop, but was critical to ensure stable flow boiling conditions in the microchannels. The channel pressure drop was the most important component. It was found to be inversely proportional to the square of the hydraulic diameter, such that it was much more important in the silicon test section (D_h=146μm - up to 50kPa) than in the copper test section (D_h=246μm - up to 15kPa). A combination of the prediction methods of Lockhart & Martinelli (1949) and Cioncolini *et al.* (2009) was found to be very precise for both test sections and is recommended for design purposes.

  The experimental instrumentation was designed to be able to measure outlet restriction pressure drop. This component is not negligible as it can represent in some situations more than 30% of the total pressure drop. Using the results from both test sections, a prediction method for the outlet restriction pressure drop was developed starting from the equation from Collier & Thome (1994) for a two-phase pressure drop across a sudden expansion. The total pressure drop in the copper test section was found to be low enough to allow it in practice to be driven by a pump-free system, such as a thermosyphon.

- Heat transfer coefficients for uniform heat flux conditions were obtained for wall heat fluxes varying from 15 to 400kW/m^2 and were found to be as high as 27'000W/m^{2}K. For a given heat flux, the data typically depicted a V-shape as the vapor quality increased. Each branch associated to a flow pattern: slug flow and annular flow. In the slug flow region, the heat transfer was found to increase with increasing heat flux and decreasing mass flux. In the annular flow region, the heat transfer coefficients were less a function of the heat flux and the mass flux: the dominant factor was the annular liquid film thickness.

  The minimum point in the V-shape was used to develop an heat flux dependent transition criteria between slug and annular flow. Using this criteria, it was then possible to develop the first flow pattern-based prediction method for heat transfer coefficients in microchannels. For the intermittent flow, the three-zone model of Thome *et al.* (2004) was used and for the annular flow region, the model of Cioncolini & Thome (2011). At the transition a combination of the prediction of both model was used. The resulting method was found to give the most precise predictions and to follow very well the experimental trends.

- The influence of non-uniform heat flux on several aspects of the cooling process was studied. First of all, the overall cooling was found to be the highest where the hot-spot was positioned. The composite wall represented up to 70% of total thermal resistance and a simple thermal improvement would be to thin the wall. For a non-uniform heat flux, the heat spreading inside the evaporator was found to be important. Its influence was included in the data reduction procedure using a multi-dimensional thermal conduction scheme. Using the local conditions found at the wall, it was possible to show that two-phase flow of refrigerant reacted in the same way to uniform and non-uniform heat fluxes.

  The biggest difficult with a non-uniform heat flux operating condition is that several assumptions have to be made for the flow distribution, such that the local mass flux, wall heat flux and vapor qualities must all be iteratively determined. Once the wall conditions were defined, the flow pattern-based method predicted well the heat transfer coefficients calculated for non-uniform heat flux conditions and is suitable for design of micro-evaporator under uniform and non-uniform heat fluxes.

- At constant heat flux situations, the power spectral density analysis of the base temperature of the copper test section showed that frequencies between 8 and 13Hz are important and that these could be linked to the bubble frequencies in the channel. When the heat flux is varied following a step or a square function, the base temperatures reached their steady state values in less than one second and the characteristic times where around 60ms. Thermally sudden start-up from single-phase conditions were easily handle, but the reduction the mass flux can be problematic if a compensation system is not included in the system.

Together, these results answered most concerns related to the use of two-phase flow cooling for micro-electronic applications. Well-designed micro-evaporators are capable of handling a wide range of conditions safely and without a complex control system. The heat transfer levels are high enough to respect the 85°C upper operating limit of CPU while cooling at saturation temperatures over 50°C, such that the heat can be reused for other applications. Future steps include integrating two-phase cooling systems into datacenters and evaluating how much energy can be saved and reused. The saving could be increased if micro-evaporators were integrated into pump-free systems and further investigation should be made in this direction.

The evolution of flow patterns in microchannels smaller than 500μm is not well understood and further studies in this direction are recommended. These results could then be used to improve the definition of the transition criteria in the flow pattern-based prediction method and to include the effect of cyclical dry-outs in the model.

Appendix A

Error propagation

The error propagation was calculated following the Kline & McClintock (1953) method. The equations to implement this are shown below.

A.1 Heat flux

$$\delta q_{b-xy} = \sqrt{\left(\frac{2V_{xy}}{R_{xy}}\delta V_{xy}\right)^2 + \left(\frac{V_{xy}^2}{R_{xy}^2}\delta R_{xy}\right)^2 + \delta q_{loss}^2} \tag{A.1}$$

A.2 Thermal conductivity

$$\delta\lambda_{si} = 1.4\times 10^{-3} T\delta T - 0.5416\delta T \tag{A.2}$$

$$C = 3.598\times 10^6 \tag{A.3}$$

$$\Gamma = \lambda_{TIM}(e+\delta e) - \lambda_{TIM}(e) \tag{A.4}$$

$$\delta\lambda_{TIM} = \sqrt{\left(Ce_{TIM}\left(T\left(\frac{e_{TIM}}{100\mu m}\right)^2\right)^{-1.9634}\delta T\right)^2 + \Gamma^2} \tag{A.5}$$

$$\delta\lambda_{cu} = \lambda_{cu}(T+\delta T) - \lambda_{cu}(T) \tag{A.6}$$

A.3 Wall temperature

A.3.1 1-D thermal conduction

$$\Gamma = \left(\frac{e_{chip}}{\lambda_{chip}} + \frac{e_{TIM}}{\lambda_{TIM}} + \frac{e_{evap}}{\lambda_{evap}} \right) \tag{A.7}$$

$$\delta\Gamma = \sqrt{\sum \left(\left(\frac{\delta e_i}{\lambda_i} \right)^2 + \left(\frac{e_i \delta\lambda_i}{\lambda_i^2} \right)^2 \right)} \tag{A.8}$$

$$\delta T_{w-xy} = \sqrt{\delta T_{b-xy}^2 + (\delta q_{b-xy}\Gamma)^2 + (q_{b_{xy}}\delta\Gamma)^2} \tag{A.9}$$

A.3.2 Multi-dimensional thermal conduction

Based on Fig 3.16. The process is repeated at each node.

$$\delta qW = \sqrt{\left(\frac{\delta T1}{dX} \right)^2 + \left(\frac{\delta T2}{dX} \right)^2} \tag{A.10}$$

$$\delta qE = \sqrt{\left(\frac{\delta T2}{dX} \right)^2 + \left(\frac{\delta T3}{dX} \right)^2} \tag{A.11}$$

$$\delta qN = \sqrt{\delta qS^2 + \delta qW^2 + \delta qE^2} \tag{A.12}$$

$$\delta q_w = \delta qN_{top} \tag{A.13}$$

$$\delta T4 = \sqrt{(\delta qNdY)^2 + \delta T2^2} \tag{A.14}$$

$$\delta T_w = \delta T4_{top} \tag{A.15}$$

A.4 Fluid

A.4.1 Fluid properties

The fluid properties were determined using REFPROP, the NIST Standard Reference Database 23, Version 8.0.

For single-phase quantities:

$$\delta\rho_l = \rho_l(T_f + \delta T_f, P + \delta P) - \rho_l(T, P) \tag{A.16}$$

$$\delta\mu_l = \mu_l(T_f + \delta T_f, P + \delta P) - \mu_l(T, P) \tag{A.17}$$

$$\delta T_f = T_f(h_l + \delta h_l, P + \delta P) - T_f(h, P) \tag{A.18}$$

$$\delta h_l = h_l(T_f + \delta T_f, P + \delta P) - h_l(T, P) \tag{A.19}$$

For two-phase quantities:

$$\delta\rho_l = \rho_l(P_{sat} + \delta P_{sat}) - \rho_l(P_{sat}) \tag{A.20}$$

$$\delta\mu_l = \mu_l(P_{sat} + \delta P_{sat}) - \mu_l(P_{sat}) \tag{A.21}$$

$$\delta T_f = T_f(P_{sat} + \delta P_{sat}) - T_f(P_{sat}) \tag{A.22}$$

$$\delta P_{sat} = P_{sat}(T_{sat} + \delta T_{sat}) - P_{sat}(T_{sat}) \tag{A.23}$$

$$\delta h_l = h_l(P_{sat} + \delta P_{sat}) - h_l(P_{sat}) \tag{A.24}$$

$$\delta h_v = h_v(P_{sat} + \delta P_{sat}) - h_v(P_{sat}) \tag{A.25}$$

A.4.2 Mass flux

$$\delta A = \sqrt{(W\delta H)^2 + (H\delta W)^2} \tag{A.26}$$

$$\delta Per = \sqrt{(2\delta W)^2 + (2\delta H)^2} \tag{A.27}$$

$$\delta D_h = \sqrt{\left(4\frac{\delta A}{Per}\right)^2 + \left(4\frac{A}{Per^2}\delta Per\right)^2} \tag{A.28}$$

$$\delta G = \sqrt{\left(\frac{\delta m}{NA}\right)^2 + \left(\frac{m\delta A}{NA^2}\right)^2} \tag{A.29}$$

A.4.3 Pressure

$$
\begin{aligned}
\delta\Delta p_{fr}^2 = \left(4\delta f\frac{G^2}{2\rho_l}\frac{L}{D_h}\right)^2 + \left(8f\frac{G}{2\rho_l}\frac{L}{D_h}\delta G\right)^2 + \\
\left(4f\frac{G^2}{2\rho_l^2}\frac{L}{D_h}\delta\rho_l\right)^2 + \left(4f\frac{G^2}{2\rho_l}\frac{\delta L}{D_h}\right)^2 + \\
\left(4f\frac{G^2}{2\rho_l}\frac{L}{D_h^2}\delta D_h\right)^2
\end{aligned}
\tag{A.30}
$$

$$\delta\Delta p_{restr-in} = \sqrt{\left(2\frac{G\delta G}{2\rho_l}\xi\right)^2 + \left(\frac{G^2}{2\rho_l^2}\xi\delta\rho_l\right)^2} \tag{A.31}$$

$$\delta\Delta p_{ch} = \sqrt{\delta\Delta p_{total}^2 + \delta\Delta p_{restr-in}^2 + \delta\Delta p_{restr-out}^2} \tag{A.32}$$

$$\delta p_{1,y} = \sqrt{\delta p_{inlet}^2 + \delta\Delta p_{restr-in}^2} \tag{A.33}$$

Single-phase channel pressure:

$$\delta p_{i,y} = \sqrt{\delta p_{i-1,y}^2 + \delta\Delta p_{fr}^2} \tag{A.34}$$

Two-phase channel pressure:

$$\delta L_{tp} = \delta L\frac{100 - onset}{100} \tag{A.35}$$

$$\Gamma = dz(i - onset) \tag{A.36}$$

$$\delta p_{i,y} = \sqrt{\delta p_{onset,y}^2 + \left(\Gamma\frac{\delta p_{onset,y}}{L_{tp}}\right)^2 + \left(\Gamma\frac{\delta p_{ref,y}}{L_{tp}}\right)^2 + \left(\Gamma\frac{p_{onset,y} - p_{ref,y}}{L_{tp}^2}\delta L_{tp}\right)^2} \tag{A.37}$$

Specific to the silicon test section:

$$\delta\Delta p_{ch-end} = \sqrt{\delta p_{5-ave}^2 + (0.5\delta p_{4-ave})^2 + (0.5\delta p_{5-ave})^2} \tag{A.38}$$

$$\delta\Delta p_{restr-out} = \sqrt{p_{ch-end}^2 + p_{out}^2} \tag{A.39}$$

Specific to the copper test section:

$$\delta\Delta p_{total} = \sqrt{\delta\Delta p_1^2 + \delta\Delta p_2^2 + \delta\Delta p_3^2} \tag{A.40}$$

$$\delta\Delta p_{restr-out} = \sqrt{\delta\Delta p_2^2 + (0.1646\delta\Delta p_2)^2}; \tag{A.41}$$

$$\delta p_{ref,y} = \sqrt{\delta p_{outlet}^2 + \delta\Delta p^2} \tag{A.42}$$

A.4.4 Enthalpy and vapor quality

$$\delta dB = \sqrt{\delta W^2 + \delta F^2} \tag{A.43}$$

$$\delta h_{i,y}^2 = \delta h_{i-1,y}^2 + \left(\delta q_{w,xy}\frac{B}{GHW}dz\right)^2 + \left(q_{w,xy}\frac{\delta B}{GHW}dz\right)^2 + \left(q_{w,xy}\frac{B\delta G}{G^2HW}dz\right)^2 + \left(q_{w,xy}\frac{B\delta H}{GH^2W}dz\right)^2 + \left(q_{w,xy}\frac{B\delta W}{GHW^2}dz\right)^2 \tag{A.44}$$

$$\delta h_{lv,iy} = \sqrt{\delta h_{l,iy}^2 + \delta h_{v,iy}^2} \tag{A.45}$$

$$\delta x_{iy} = \sqrt{\left(\frac{\delta h_{iy}}{h_{lv,iy}}\right)^2 + \left(\frac{\delta h_{l,iy}}{h_{lv,iy}}\right)^2 + \left(\frac{h_{iy} - h_{l,iy}}{h_{lv,iy}^2}\delta h_{lv,iy}\right)^2} \tag{A.46}$$

A.5 Heat transfer coefficient

$$\Delta T = T_{w,xy} - T_{f,xy} \tag{A.47}$$

$$\delta\Delta T = \sqrt{\delta T_{w,xy}^2 + \delta T_{f,xy}^2} \tag{A.48}$$

$$\delta\alpha_{b,xy} = \sqrt{\left(\frac{\delta q_{w,xy}}{\Delta T}\right)^2 + \left(\frac{q_{w,xy}}{\Delta T^2}\delta\Delta T\right)^2} \tag{A.49}$$

For the fin heat flux, q_{fin}, the error was assumed to be proportional to that of the wall heat flux.

$$\delta q_{fin} = q_{fin}\frac{\delta q_w}{q_w} \tag{A.50}$$

$$\delta\alpha_{w,xy} = \sqrt{\left(\frac{\delta q_{fin,xy}}{\Delta T}\right)^2 + \left(\frac{q_{fin,xy}}{\Delta T^2}\delta\Delta T\right)^2} \tag{A.51}$$

Appendix B

Further results

B.1 Pressure drop ratios

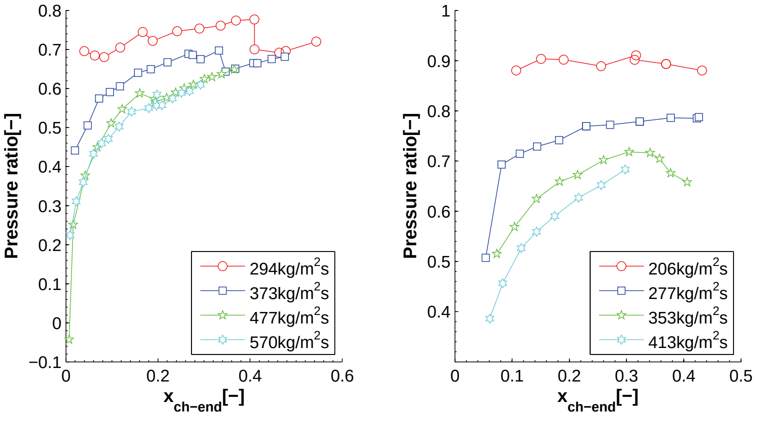

(a) R-134a: Channel (b) R-1234ze(E): Channel

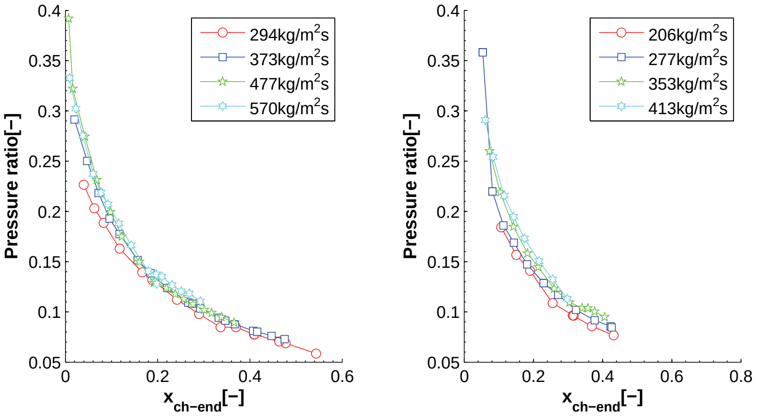

(c) R-134a: Inlet restriction (d) R-1234ze(E): Inlet restriction

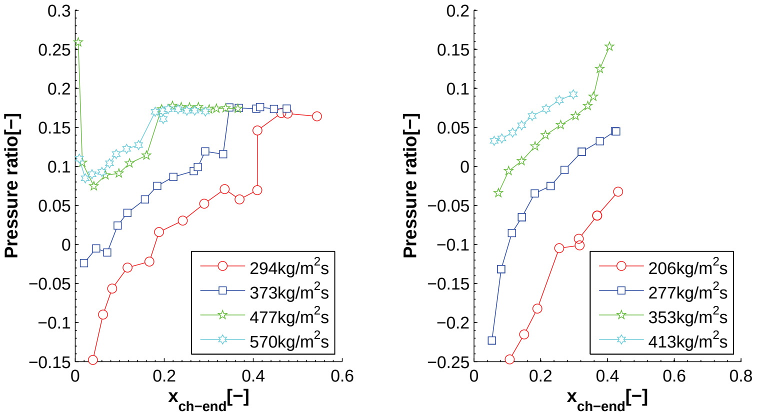

(e) R-134a: Outlet restriction (f) R-1234ze(E): Outlet restriction

Figure B.1: Pressure drop ratios for copper test section, T_{sat}=50°C.

B.2 Uniform heat flux heat transfer coefficients

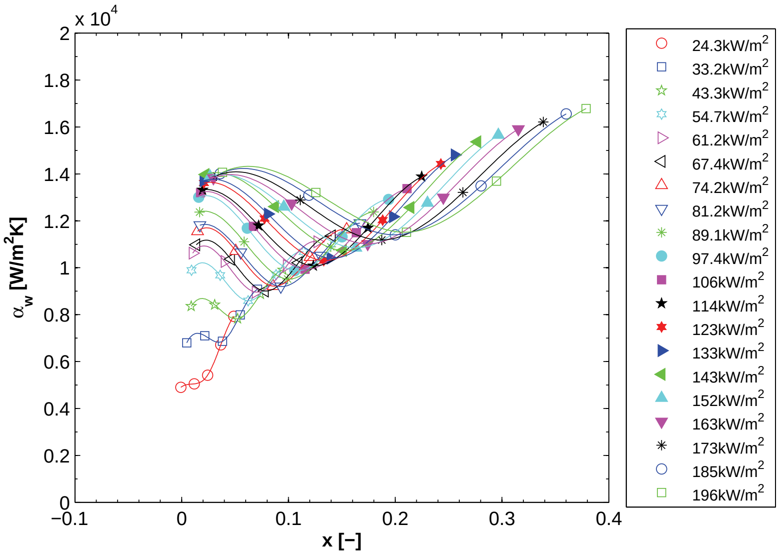

(a) T$_{sat}$: 31.1°C, 823kg/m^{2}s, Error in α_w: 6.4%, RMS: 9.7%

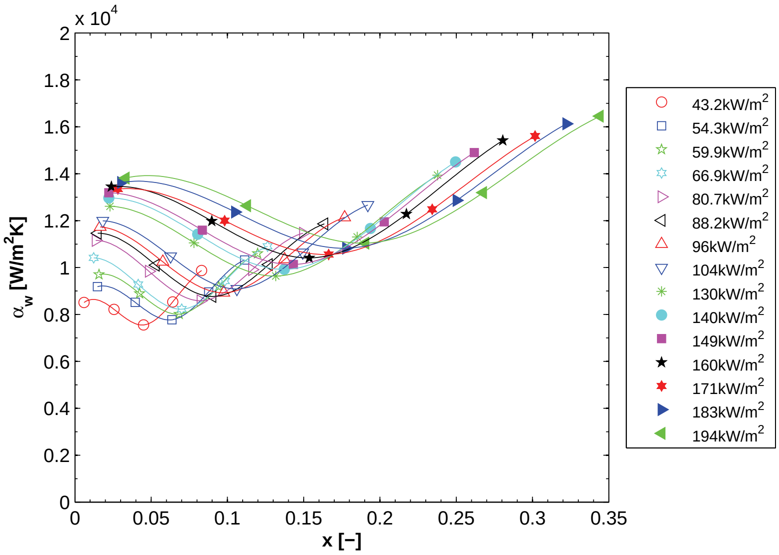

(b) T$_{sat}$: 31.1°C, 933kg/m^{2}s, Error in α_w: 5.9%, RMS: 9.8%

Figure B.2: α_w for different q$_w$. Silicon test section R-236fa.

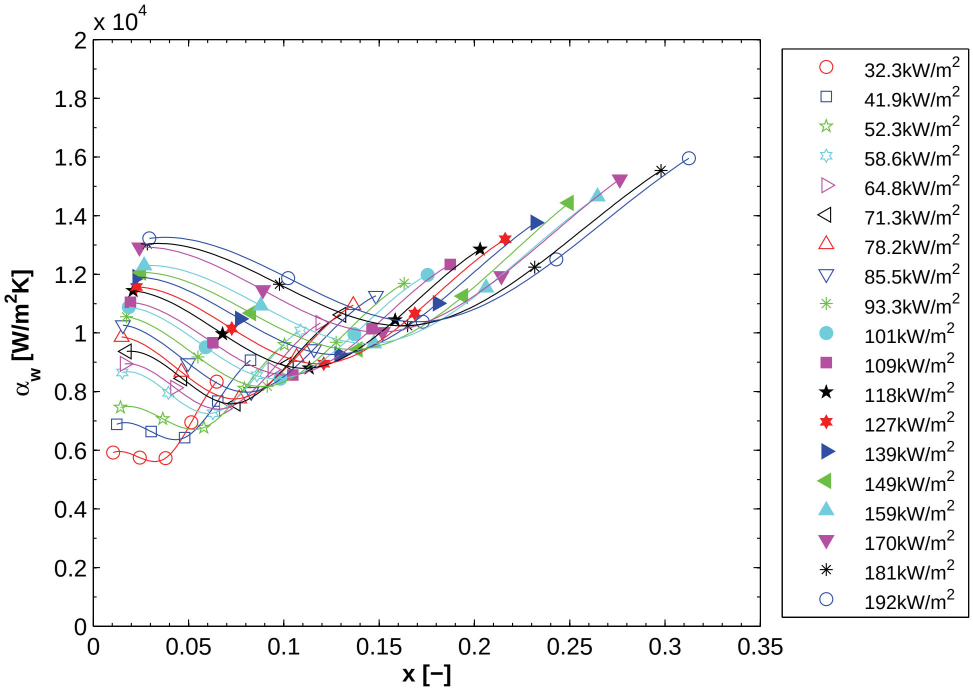

Figure B.3: α_w for different q_w. Silicon test section R-236fa, T_{sat}: 31.0°C, 1051kg/m^{2}s, Error in α_w: 5.7%, RMS: 8.5%.

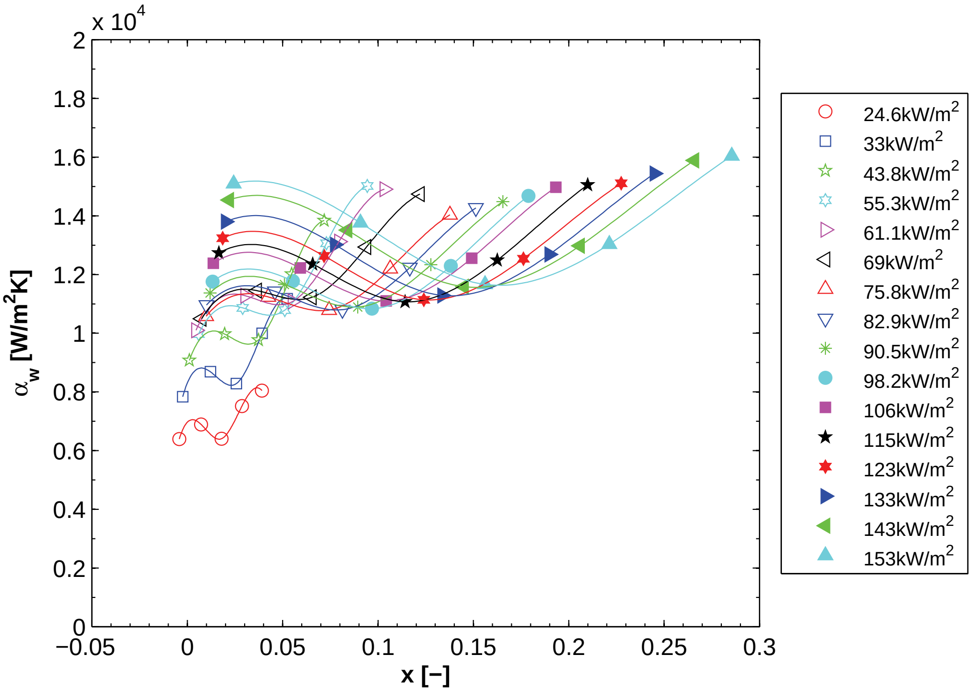

(a) T$_{sat}$: 31.3°C, 703kg/m^{2}s, Error in α_w: 7.7%, RMS: 10.4%

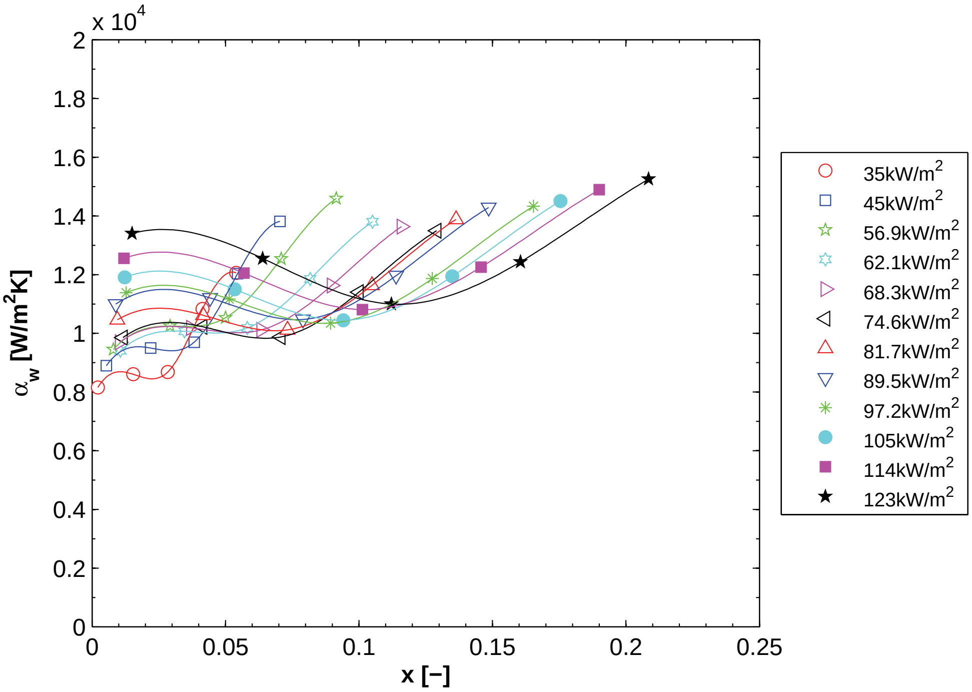

(b) T$_{sat}$: 31.2°C, 803kg/m^{2}s, Error in α_w: 7.7%, RMS: 9.5%

Figure B.4: α_w for different q$_w$. Silicon test section R-245fa.

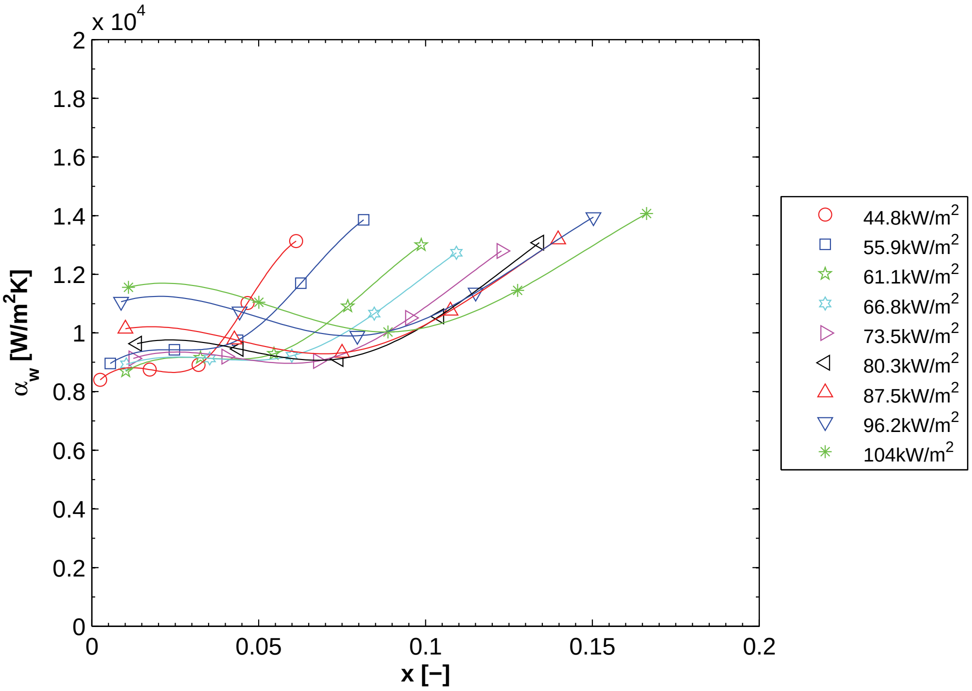

Figure B.5: α_w for different q$_w$. Silicon test section R-245fa, T$_{sat}$: 31.1°C, 902kg/m^{2}s, Error in α_w: 7.2%, RMS: 8.6%.

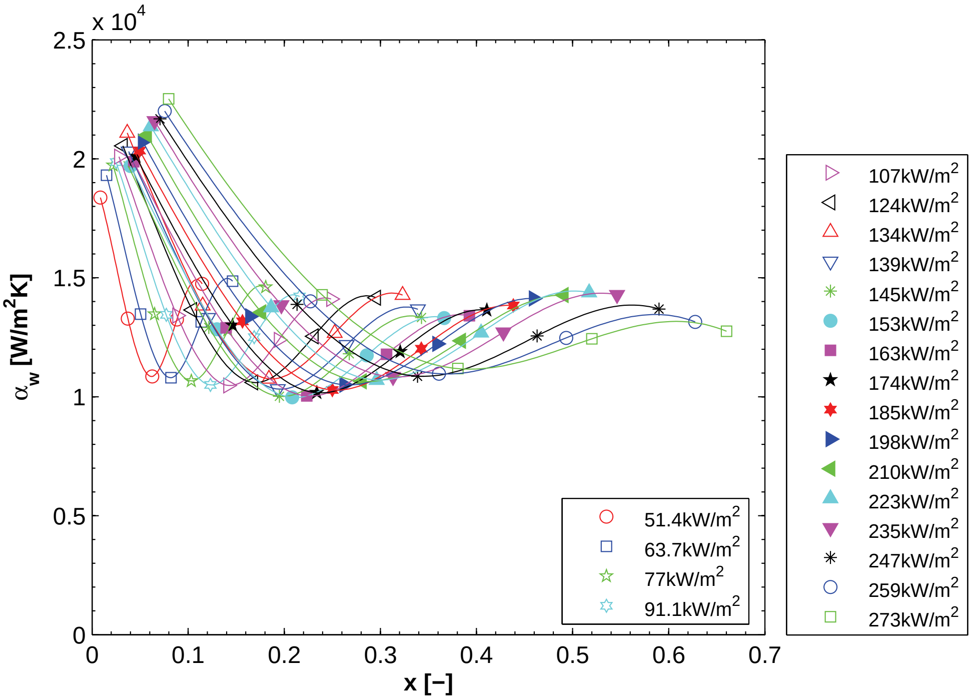

(a) T$_{sat}$: 31.2°C, Error in α_w: 4.9%, RMS: 13%

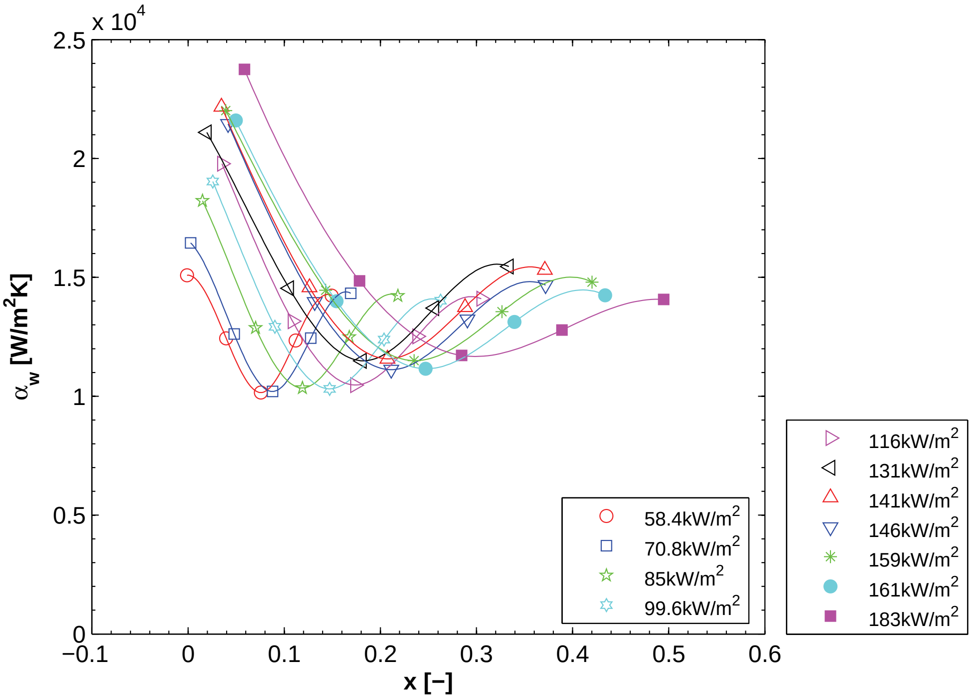

(b) T$_{sat}$: 51.3°C, Error in α_w: 6.0%, RMS: 13.9%

Figure B.6: α_w for different q$_w$. Copper test section R-134a, 292kg/m^{2}s.

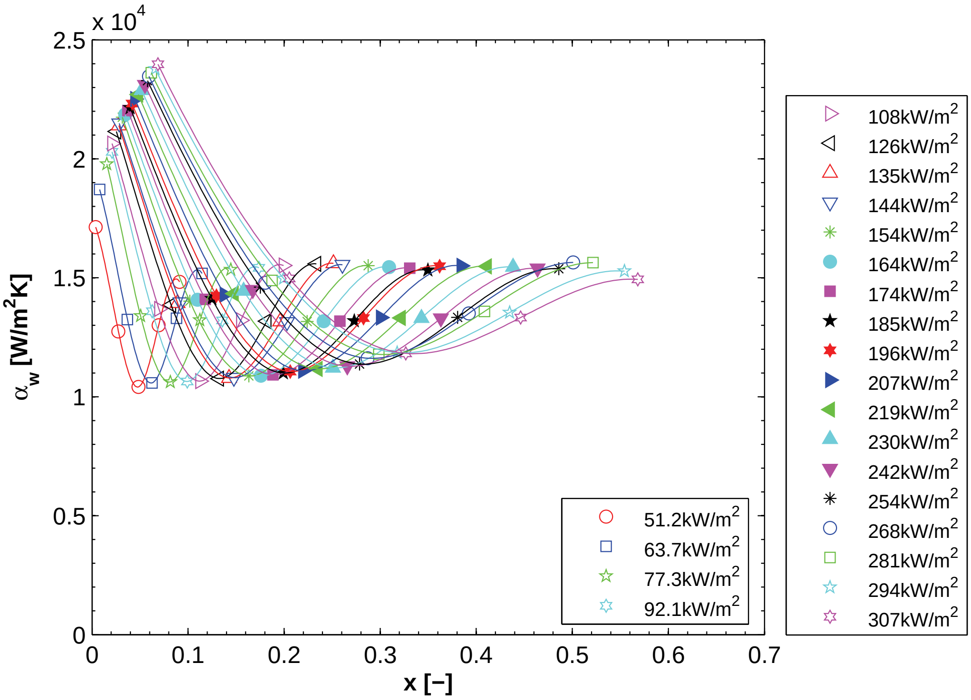

(a) T$_{sat}$: 30.6°C, Error in α_w: 4.8%, RMS: 13.3%

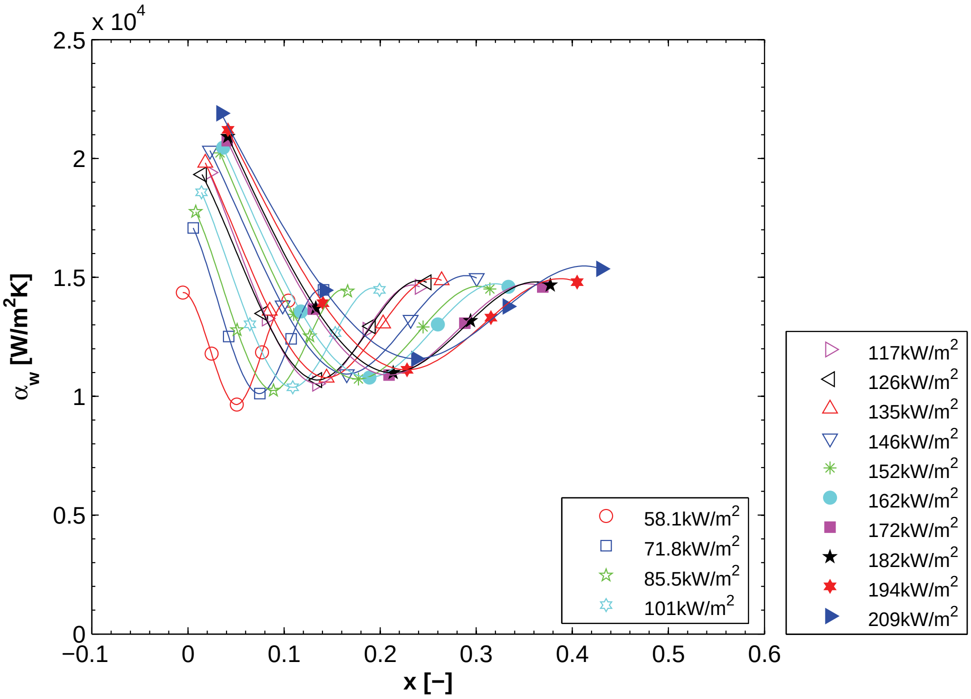

(b) T$_{sat}$: 50.7°C, Error in α_w: 5.8%, RMS: 14.5%

Figure B.7: α_w for different q$_w$. Copper test section R-134a, 367kg/m^{2}s.

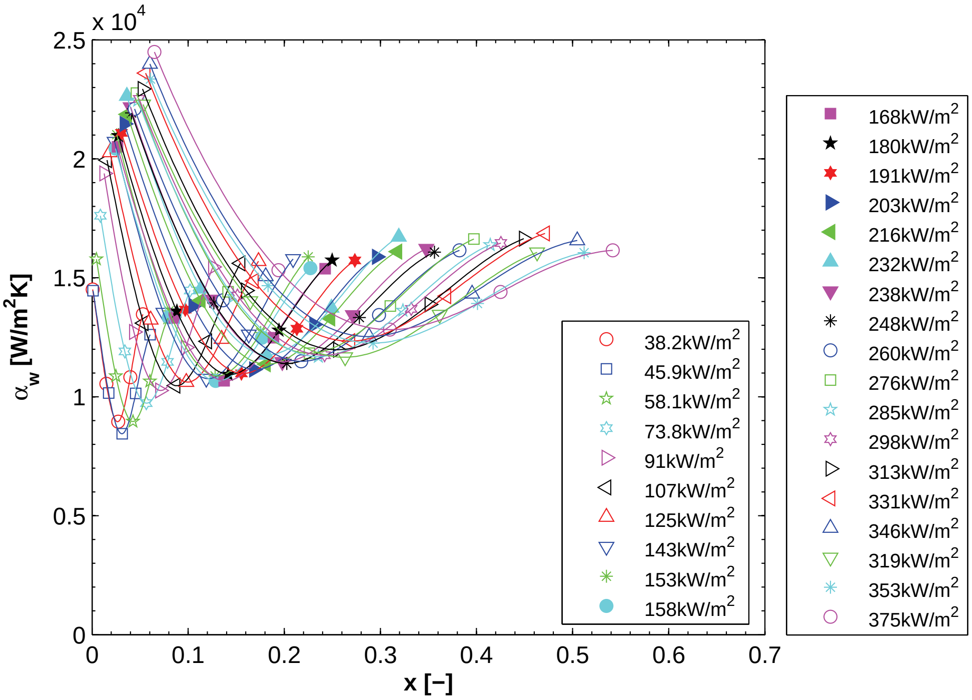

(a) T$_{sat}$: 30.4°C, Error in α_w: 4.7%, RMS: 13.7%

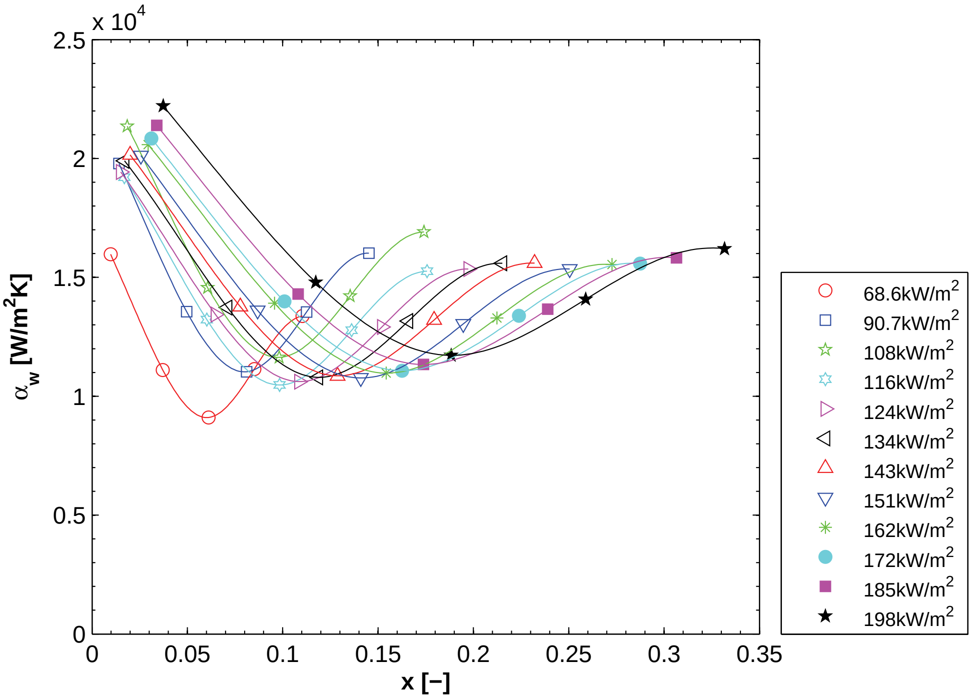

(b) T$_{sat}$: 50.7°C, Error in α_w: 6.1%, RMS: 15%

Figure B.8: α_w for different q$_w$. Copper test section R-134a, 473kg/m^{2}s.

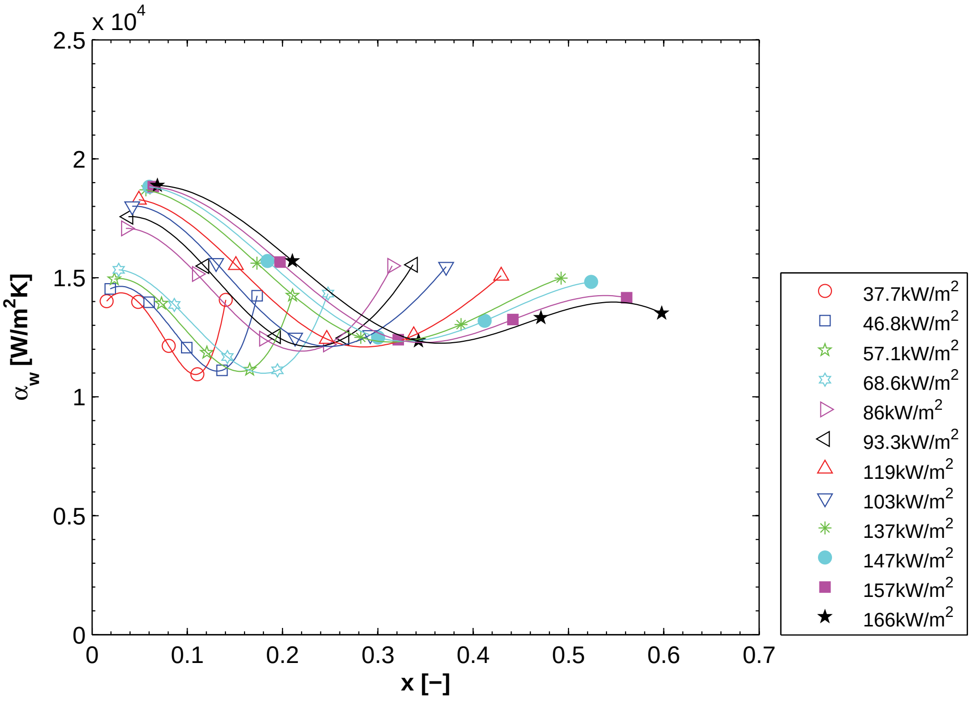

(a) T$_{sat}$: 31.0°C, Error in α_w: 9.0%, RMS: 19.8%

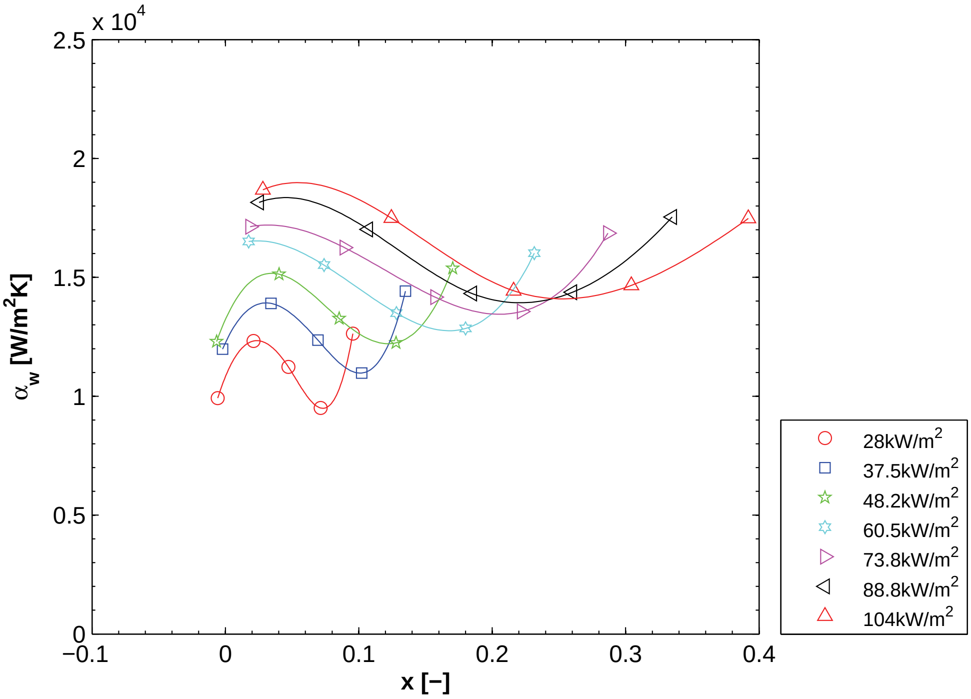

(b) T$_{sat}$: 51.5°C, Error in α_w: 10.0%, RMS: 16.8%

Figure B.9: α_w for different q$_w$. Copper test section R-1234ze(E), 205kg/m^{2}s.

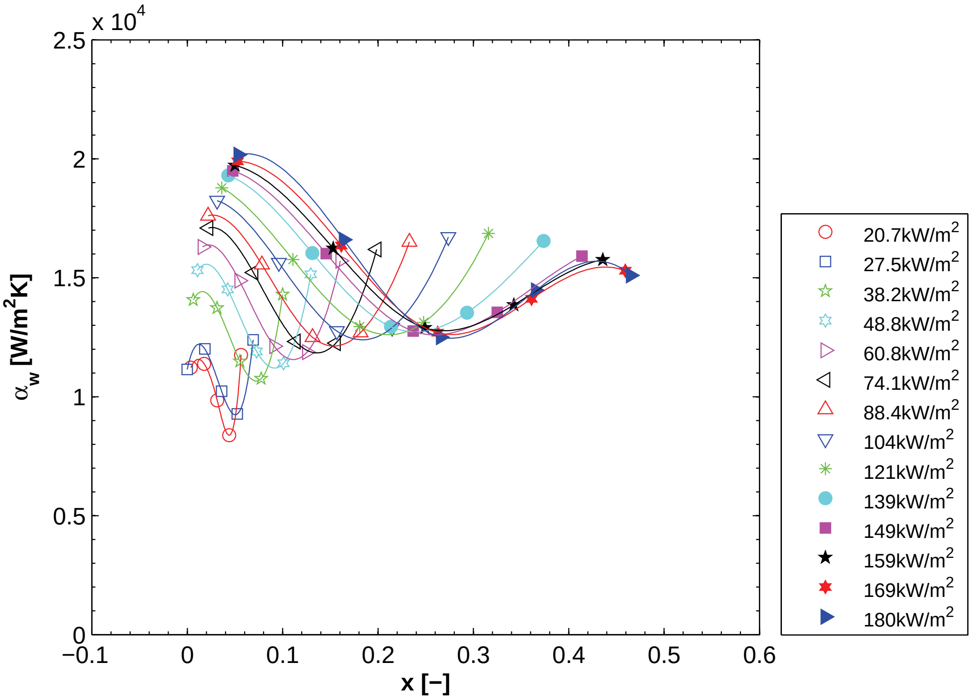

(a) T$_{sat}$: 30.5°C, Error in α_w: 9.6%, RMS: 17.4%

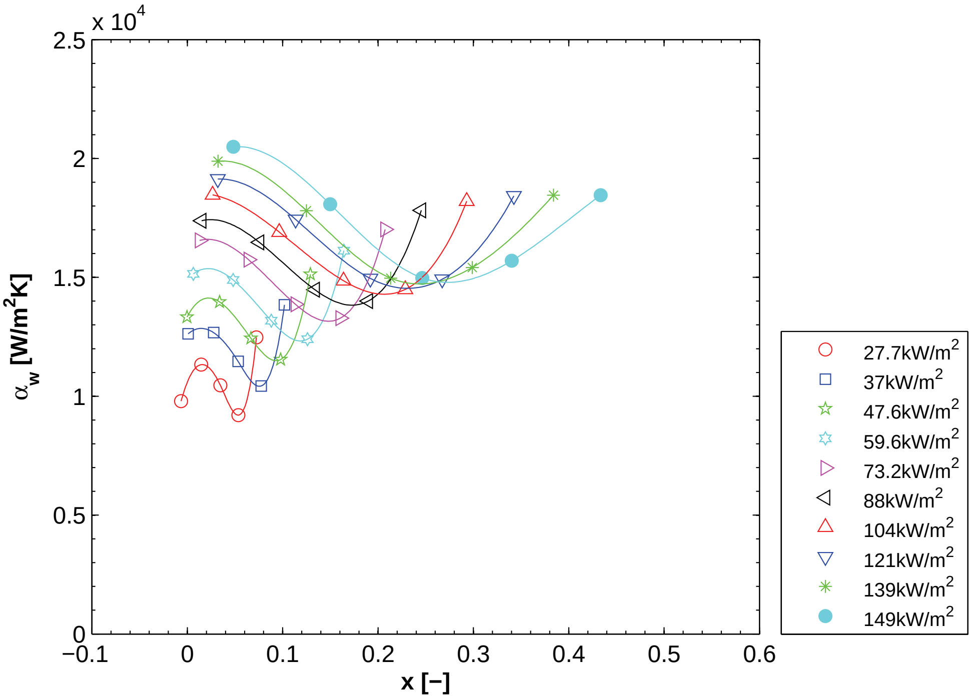

(b) T$_{sat}$: 51.3°C, Error in α_w: 8.7%, RMS: 16.4%

Figure B.10: α_w for different q$_w$. Copper test section R-1234ze(E), 275kg/m^{2}s.

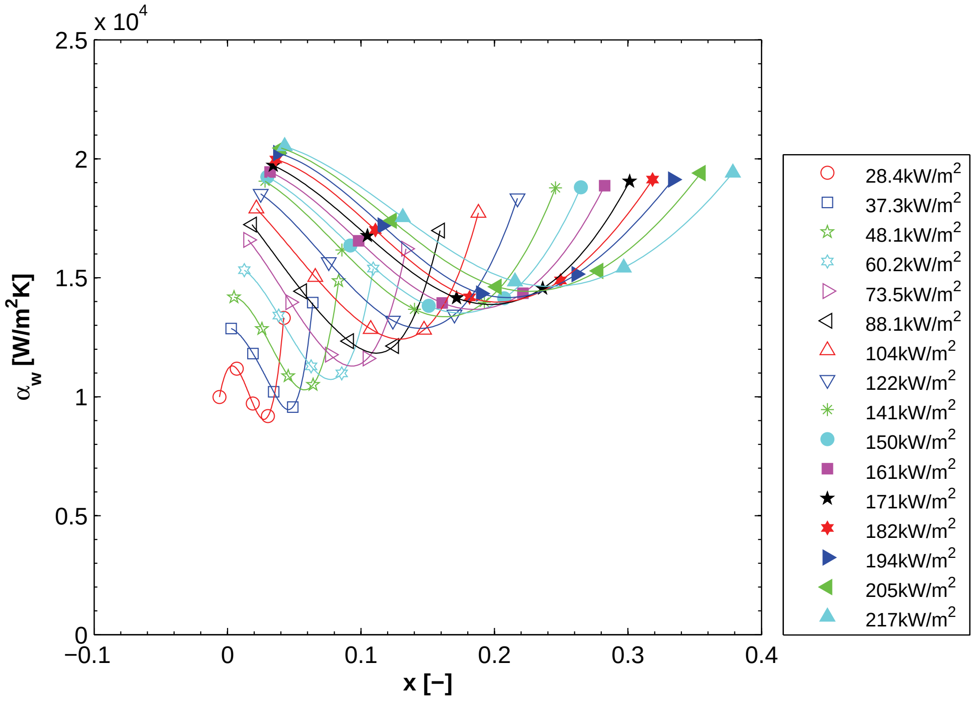

(a) T$_{sat}$: 30.7°C, Error in α_w: 7.1%, RMS: 16.1%

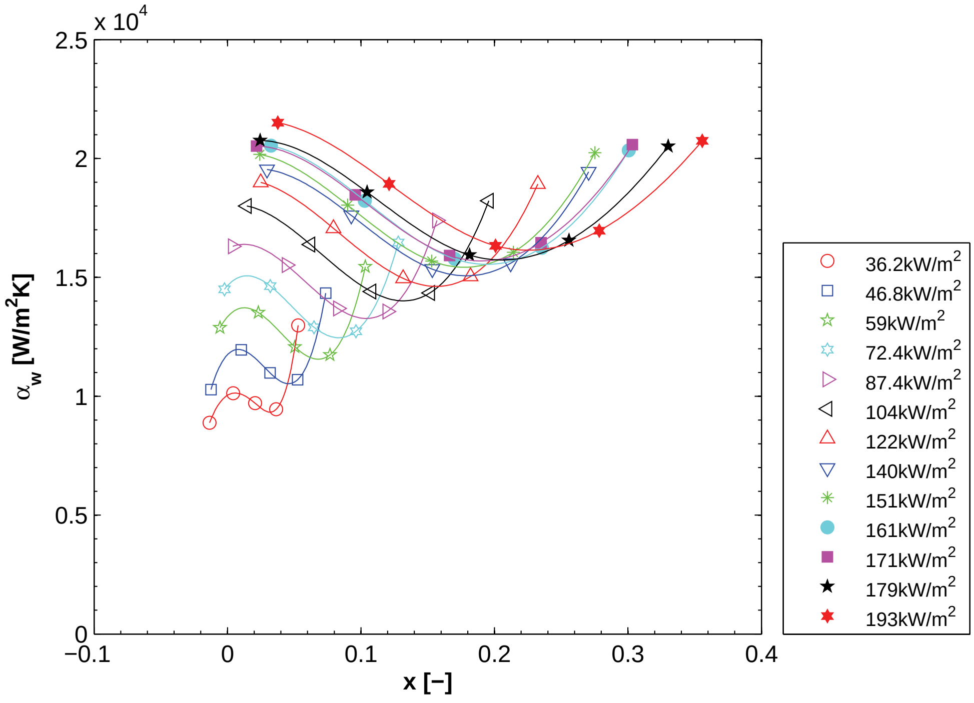

(b) T$_{sat}$: 50.6°C, Error in α_w: 6.3%, RMS: 14.8%

Figure B.11: α_w for different q$_w$. Copper test section R-1234ze(E), 412kg/m^{2}s.

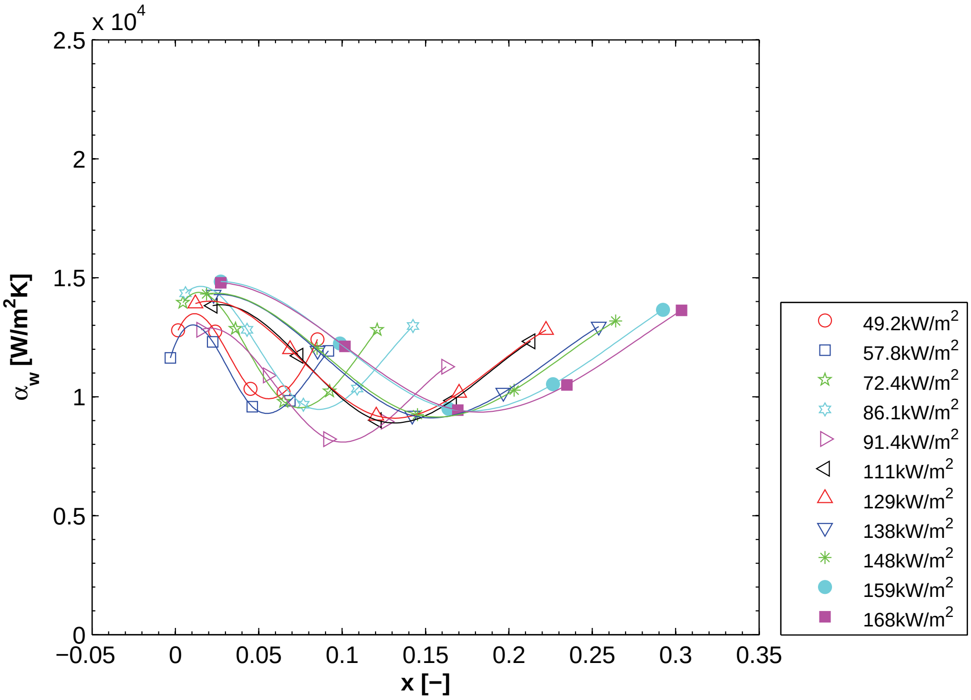

(a) T$_{sat}$: 30.9°C, Error in α_w: 8.5%, RMS: 15.8%

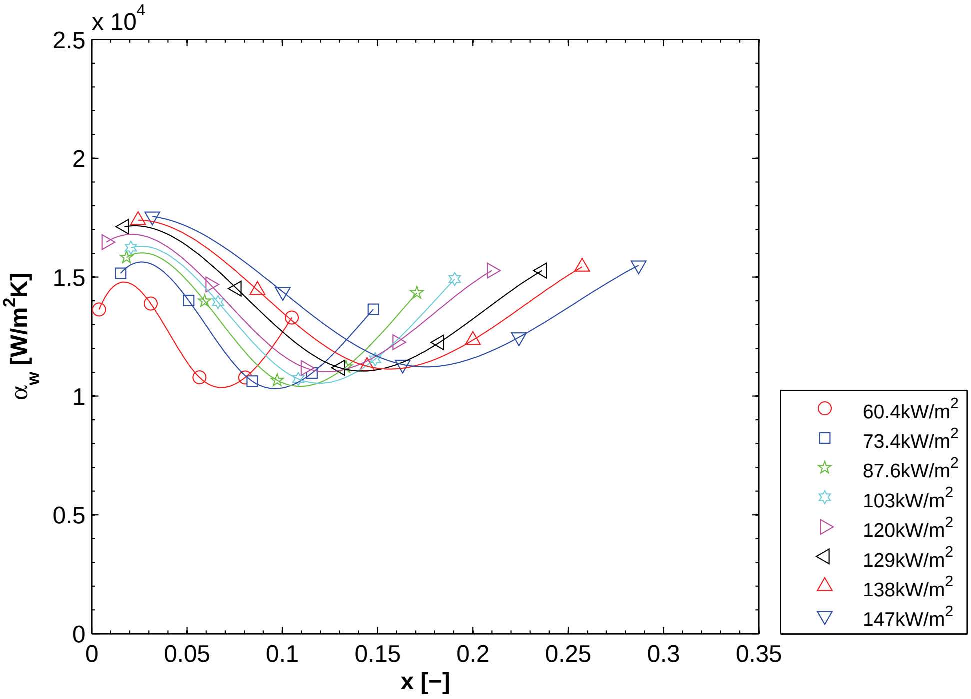

(b) T$_{sat}$: 50.9°C, Error in α_w: 6.8%, RMS: 16.0%

Figure B.12: α_w for different q$_w$. Copper test section R-245fa, 365kg/m^{2}s.

B.3 Non-uniform heat flux

B.3.1 Base heat flux and package thermal conductance

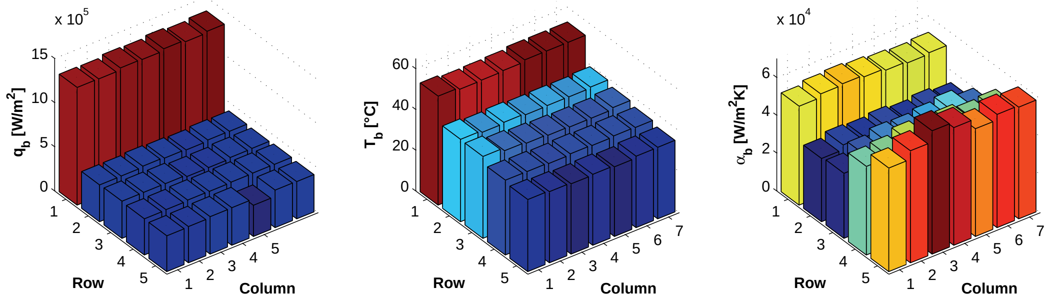

(a) q_b R1H (b) T_b R1H (c) α_b R1H

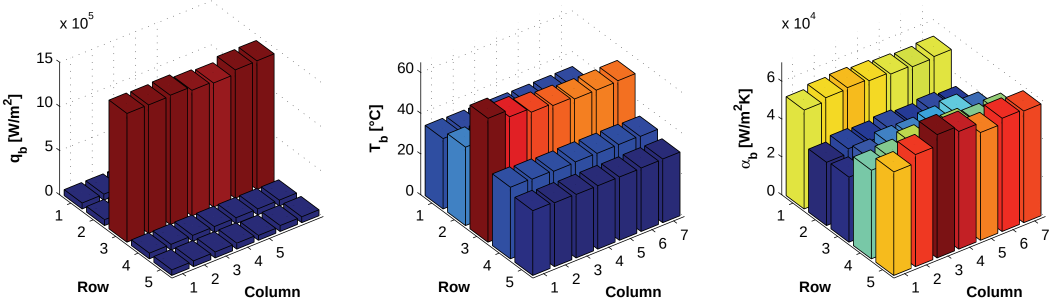

(d) q_b R3H (e) T_b R3H (f) α_b R3H

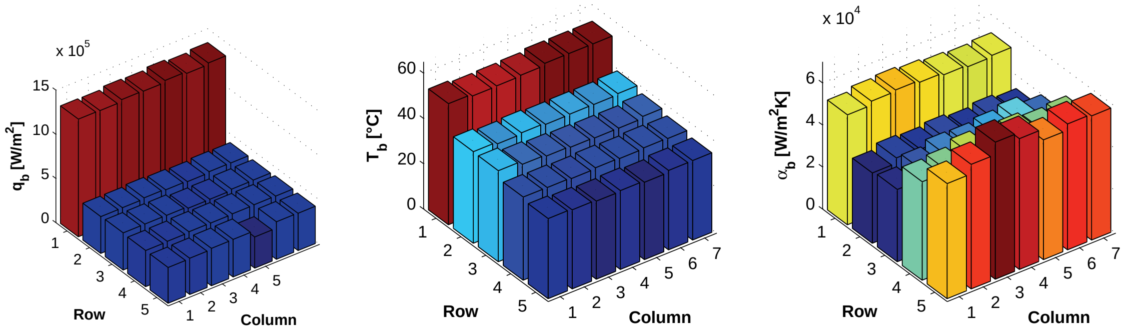

(g) q_b R5H (h) T_b R5H (i) α_b R5H

Figure B.13: Silicon test section: Thermal conductance for row hot-spots in the package for R-245fa, T_{sat}=31°C, 703kg/m^{2}s.

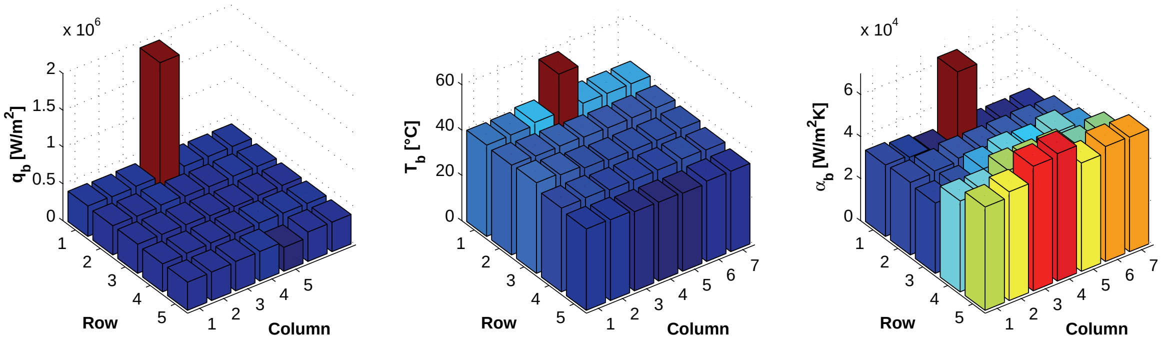

(a) q_b 14H (b) T_b 14H (c) α_b 14H

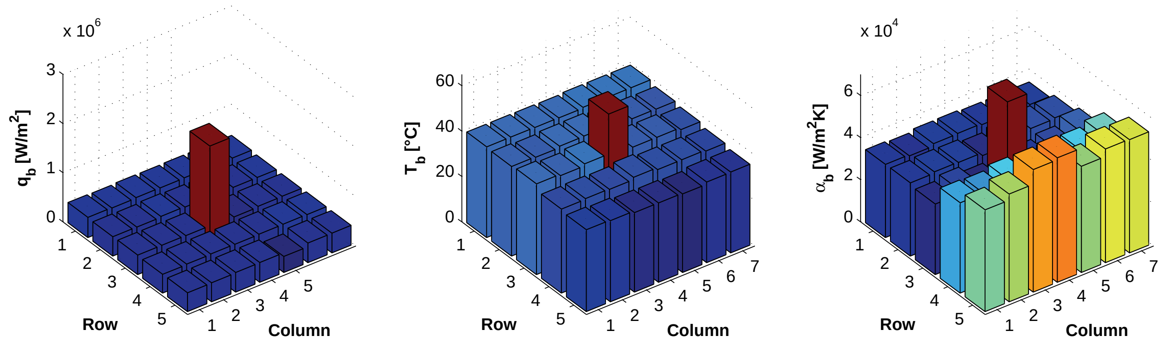

(d) q_b 34H (e) T_b 34H (f) α_b 34H

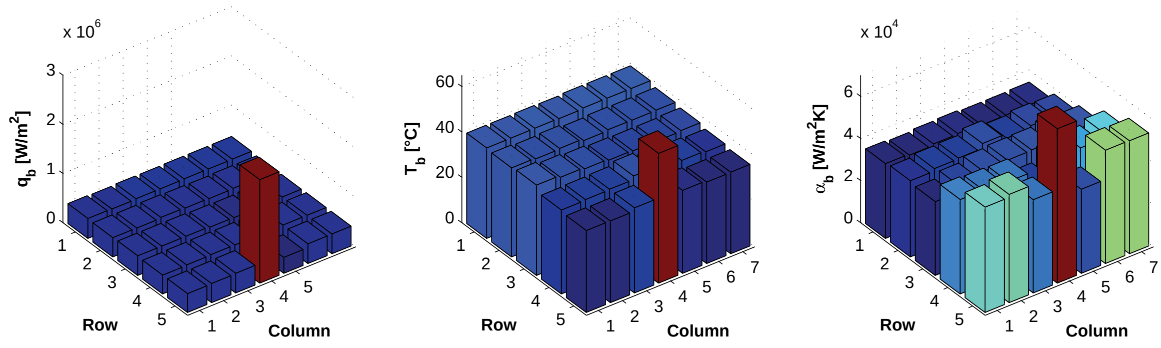

(g) q_b 54H (h) T_b 54H (i) α_b 54H

Figure B.14: Silicon test section: Thermal conductance for point hot-spots in the package for R-245fa, T_{sat}=31°C, 909kg/m^{2}s.

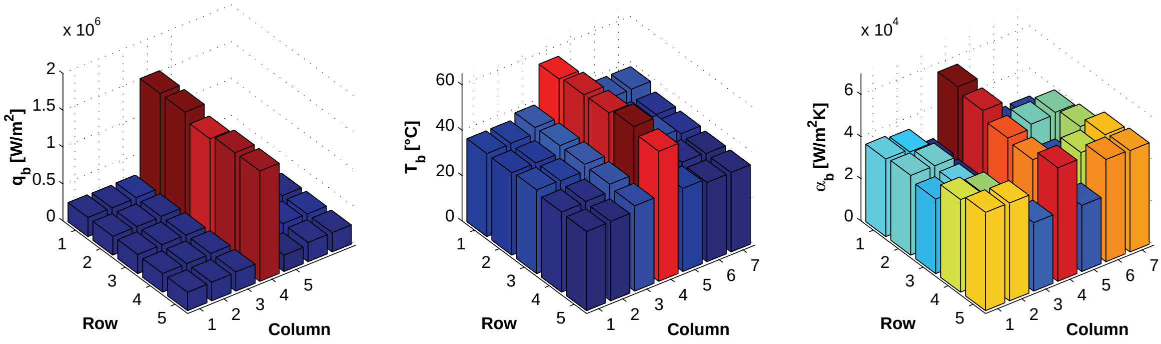

(a) q_b 14H (b) T_b C4H (c) α_b C4H

Figure B.15: Silicon test section: Thermal conductance for column hot-spots in the package for R-245fa, T_{sat}=30°C, 702kg/m^{2}s.

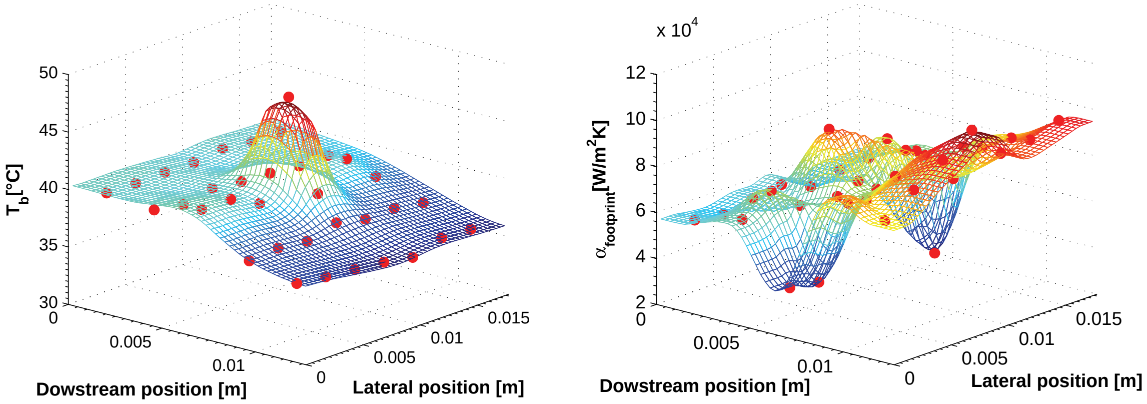

(a) Base temperature (b) Footprint heat transfer coefficient

Figure B.16: Comparison between the three-dimensional thermal conduction data reduction and COMSOL Multiphysics numerical resulzs for the silicon test section with R-245fa for hot-spot at heater 34, q_b[kW/m^2] 1200:400, 909kg/m^{2}s.

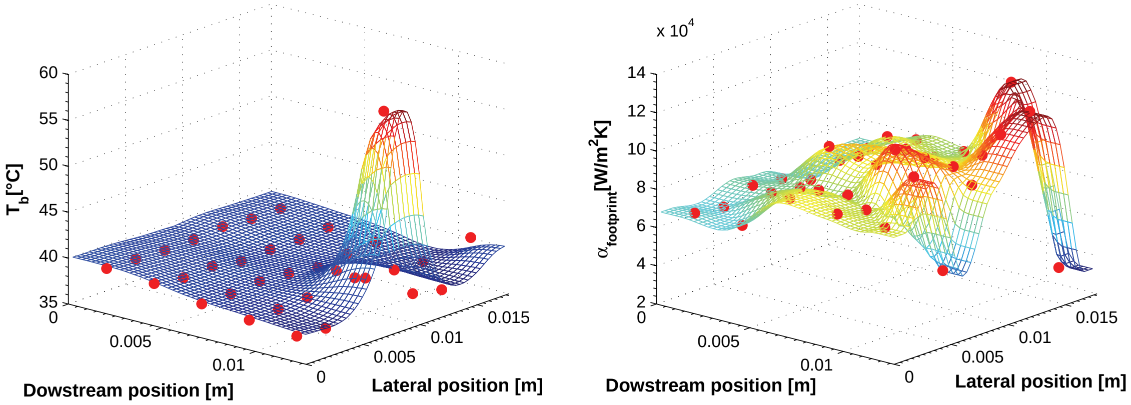

(a) Base temperature (b) Footprint heat transfer coefficient

Figure B.17: Comparison between the three-dimensional thermal conduction data reduction and COMSOL Multiphysics numerical results for the silicon test section with R-245fa for hot-spot at heater 54, q_b[kW/m^2] 1600:400, 715kg/m^{2}s.

B.3.2 Wall heat transfer coefficients for the silicon test section

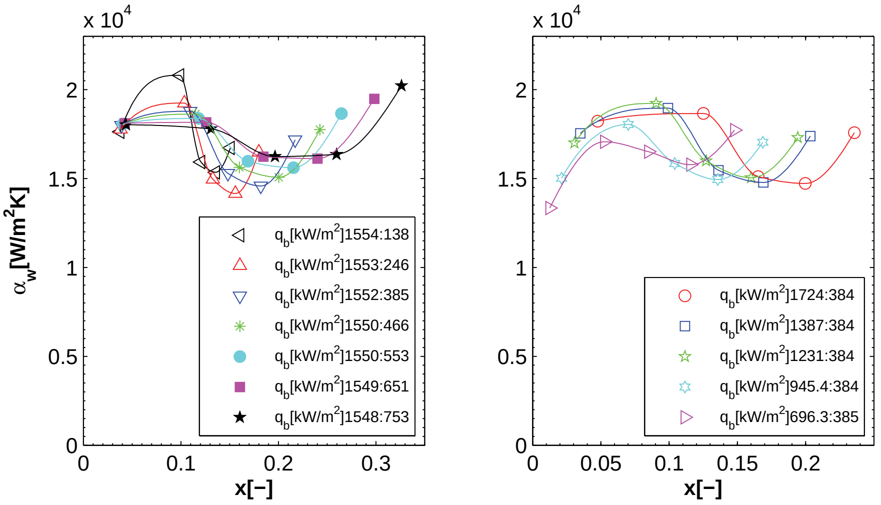

(a) R1H: Error in α_w: 4.6%, RMS: 10.0%, $q_{footprint}/q_b$: 88%

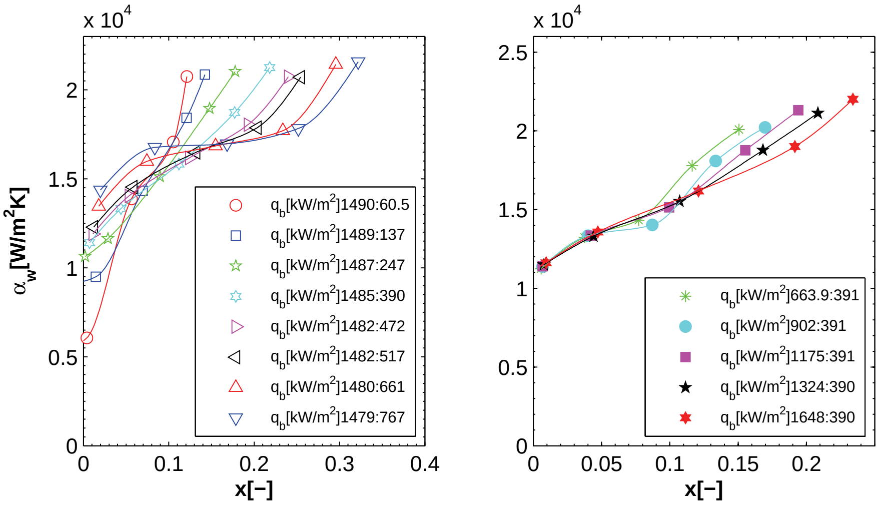

(b) R3H: Error in α_w: 5.1%, RMS: 11.1%, $q_{footprint}/q_b$: 79%

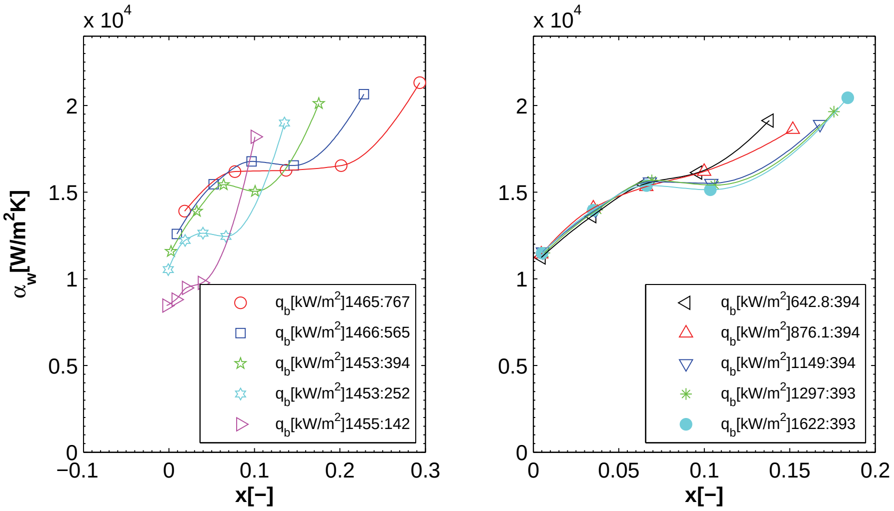

(c) R5H: Error in α_w: 5.1%, RMS: 10.7%, $q_{footprint}/q_b$: 91%

Figure B.18: α_w for row hot-spot in the silicon test section at 503kg/m^{2}s, T$_{sat}$=30°C.

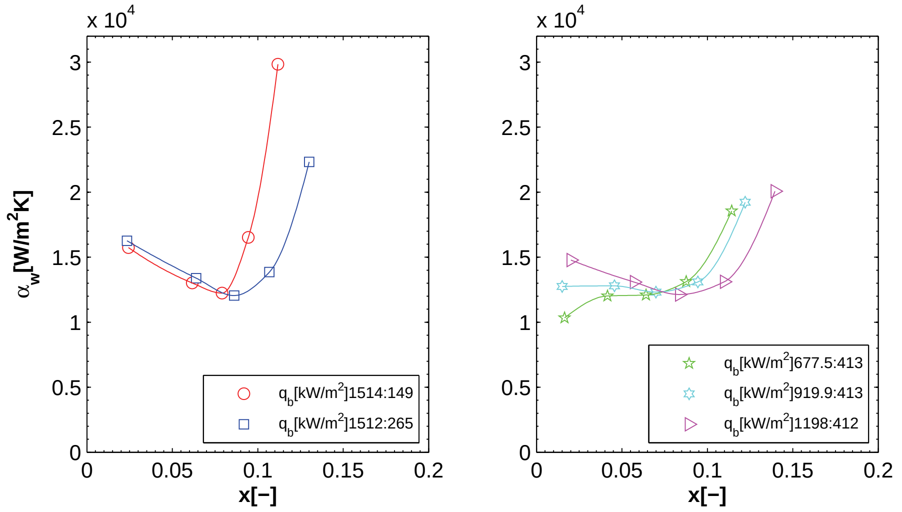

(a) R1H: Error in α_w: 6.3%, RMS: 12.3%, $q_{footprint}/q_b$: 87%

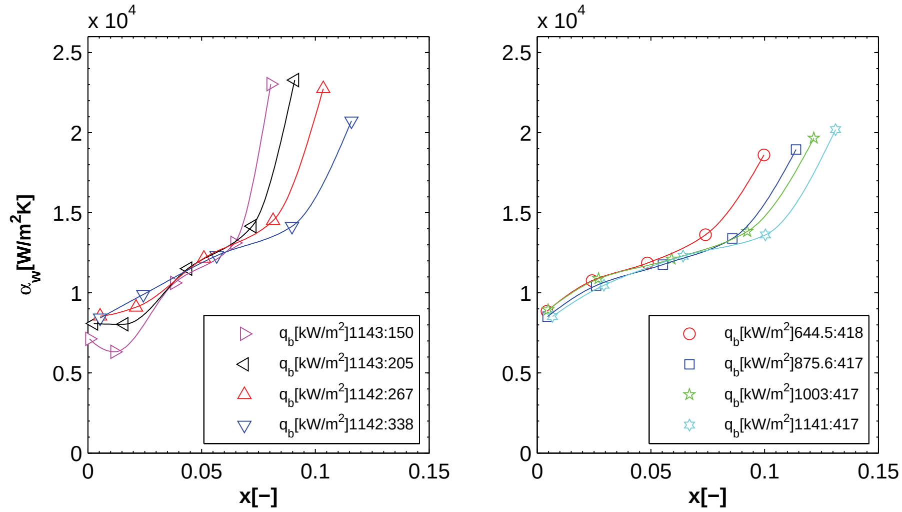

(b) R3H: Error in α_w: 6.2%, RMS: 10.1%, $q_{footprint}/q_b$: 77%

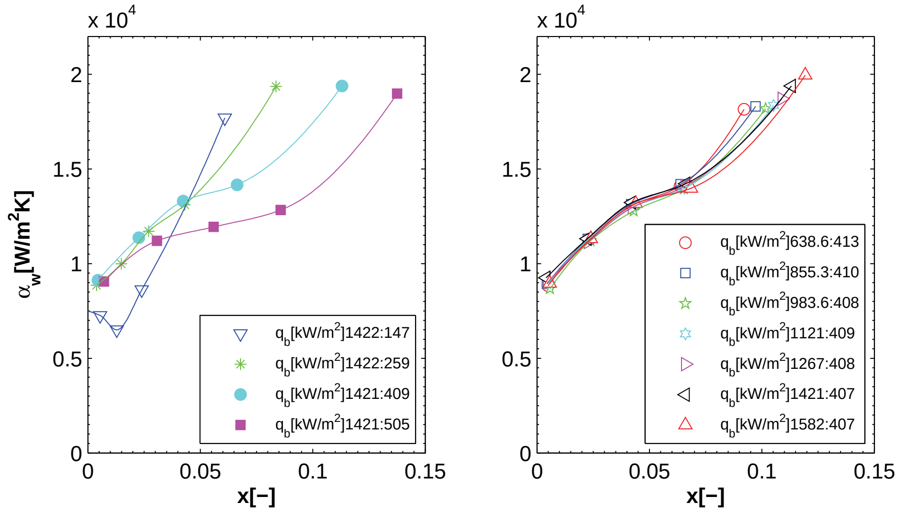

(c) R5H: Error in α_w: 4.6%, RMS: 9.2%, $q_{footprint}/q_b$: 92%

Figure B.19: α_w for row hot-spot in the silicon test section at 900kg/m^{2}s, T_{sat}=30°C.

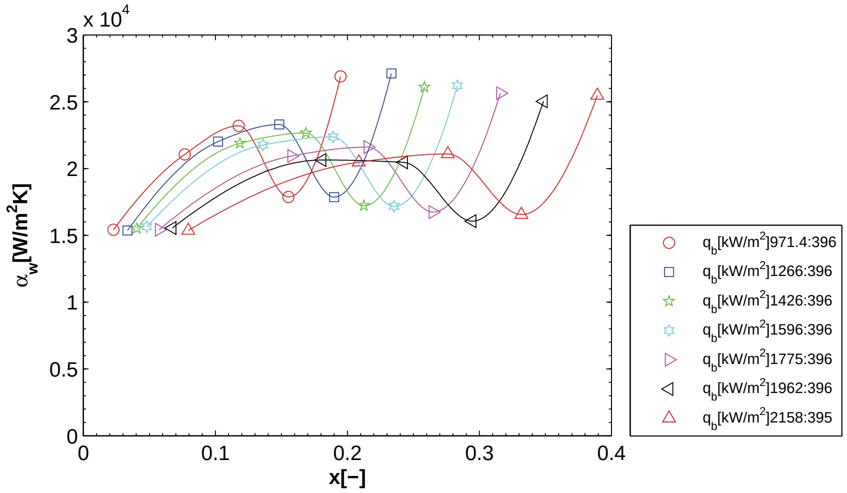

(a) 14H: Error in α_w: 11.8%, q$_{footprint}$/q$_b$: 71%, G$_{min}$/G$_{nom}$: 56%

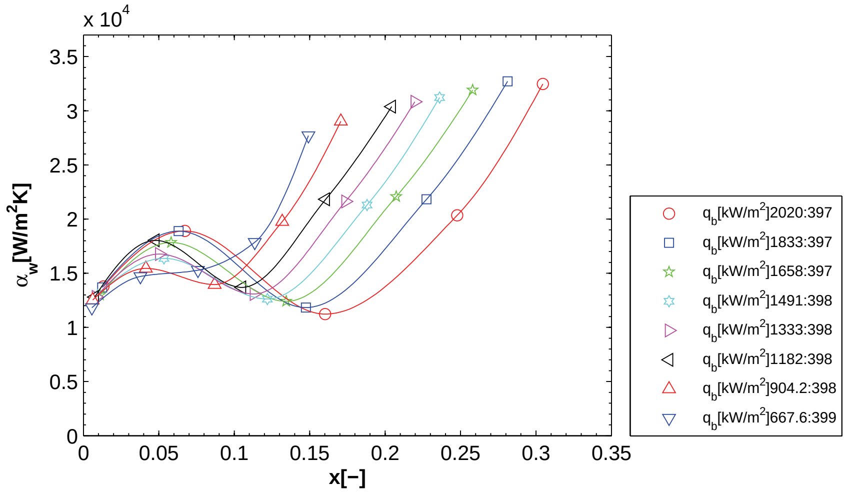

(b) 34H: Error in α_w: 11.5%, q$_{footprint}$/q$_b$: 62%, G$_{min}$/G$_{nom}$: 69%

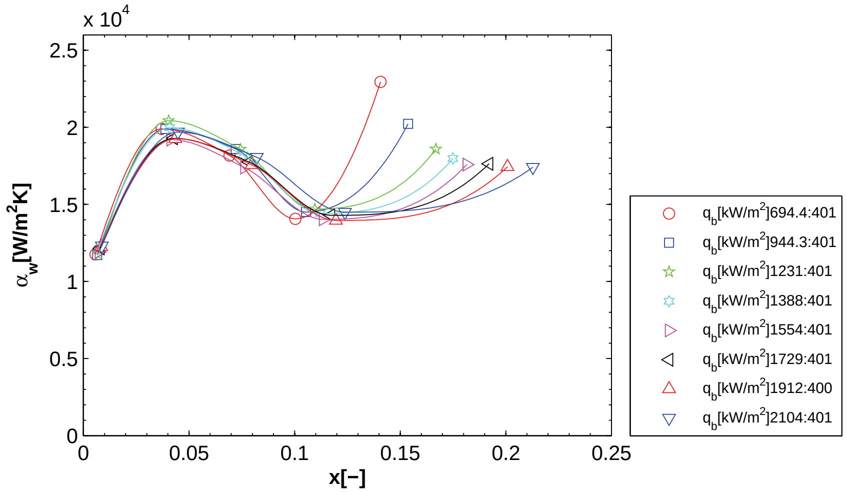

(c) 54H: Error in α_w: 11.6%, q$_{footprint}$/q$_b$: 72%, G$_{min}$/G$_{nom}$: 85%

Figure B.20: α_w along Column 4 for point hot-spot in the silicon test section at 507kg/m^{2}s, T$_{sat}$=30°C.

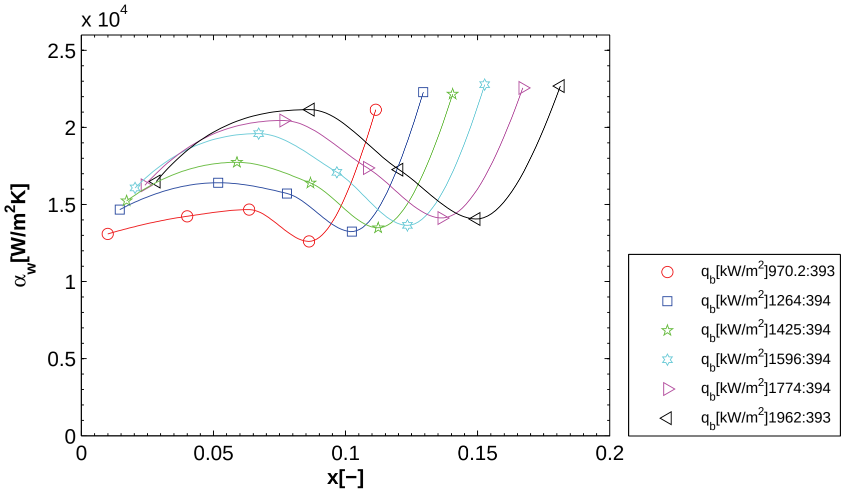

(a) 14H: Error in α_w: 10.4%, $q_{footprint}/q_b$: 74%, G_{min}/G_{nom}: 69%

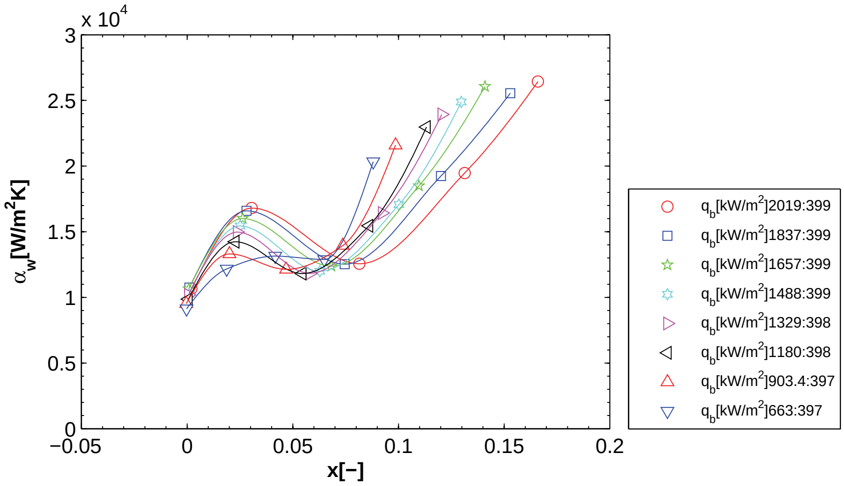

(b) 34H: Error in α_w: 10.6%, $q_{footprint}/q_b$: 63%, G_{min}/G_{nom}: 76%

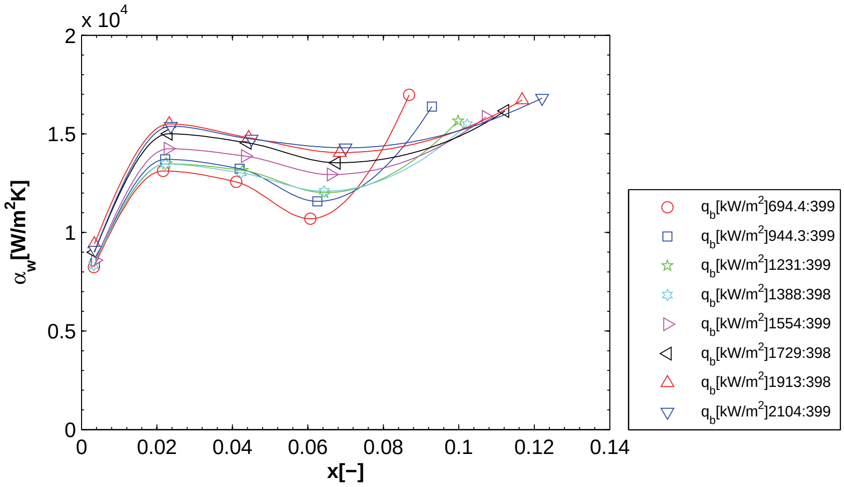

(c) 54H: Error in α_w: 9.9%, $q_{footprint}/q_b$: 71%, G_{min}/G_{nom}: 90%

Figure B.21: α_w along Column 4 for point hot-spot in the silicon test section at 908kg/m^{2}s, T_{sat}=30°C.

B.3.3 Wall heat transfer coefficients for the copper test section

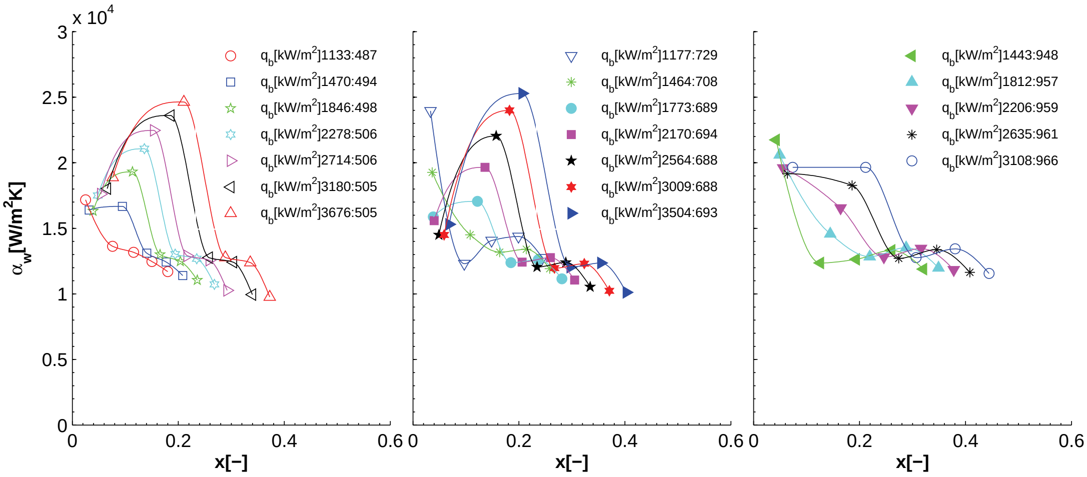

(a) R1H: G=293kg/m^{2}s, Error in α_w: 10.8%, RMS: 19.4%, q$_{footprint}$/q$_b$: 81%

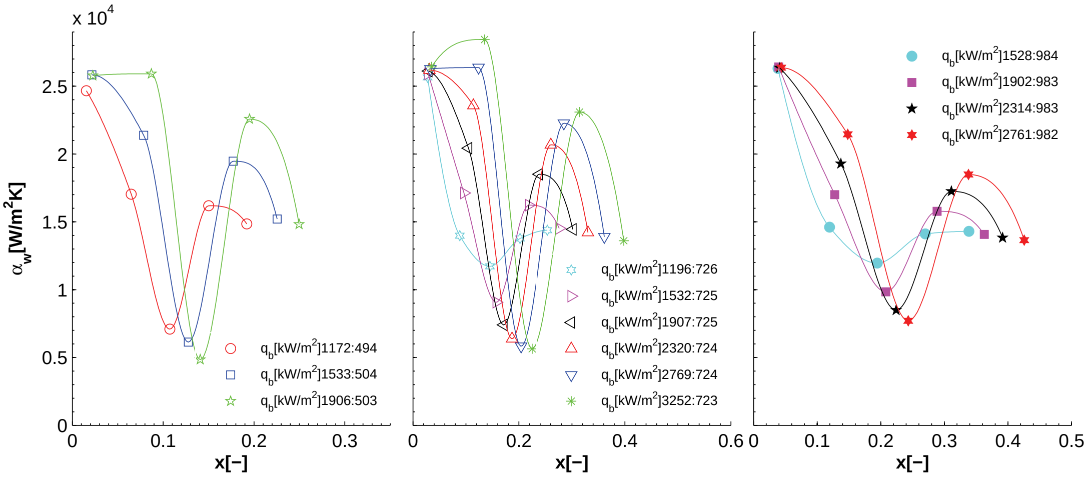

(b) R3H: G=283kg/m^{2}s, Error in α_w: 11.4%, RMS: 20.6%, q$_{footprint}$/q$_b$: 55%

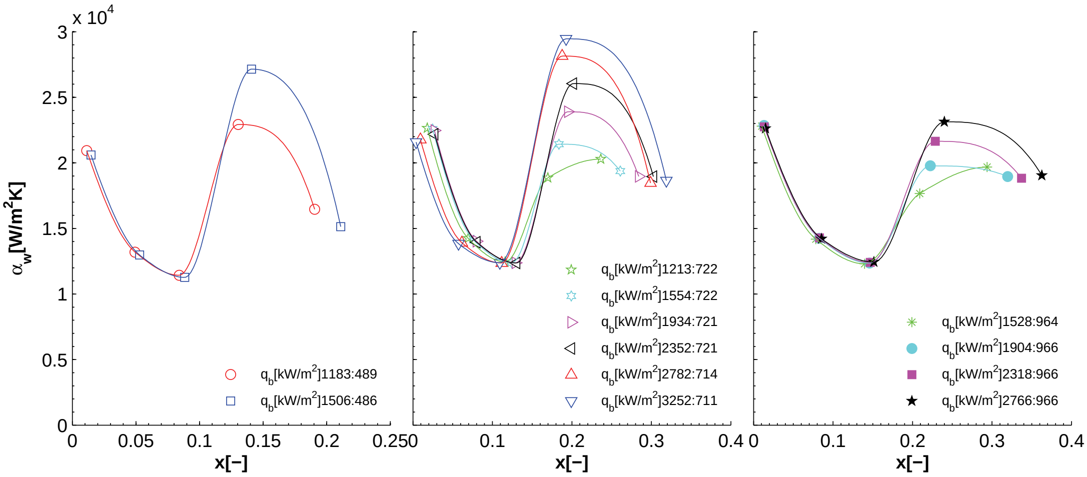

(c) R5H: G=300kg/m^{2}s, Error in α_w: 11.0%, RMS: 20.6%, q$_{footprint}$/q$_b$: 83%

Figure B.22: α_w for row hot-spots with R-134a in the copper test section, T$_{sat}$=30°C.

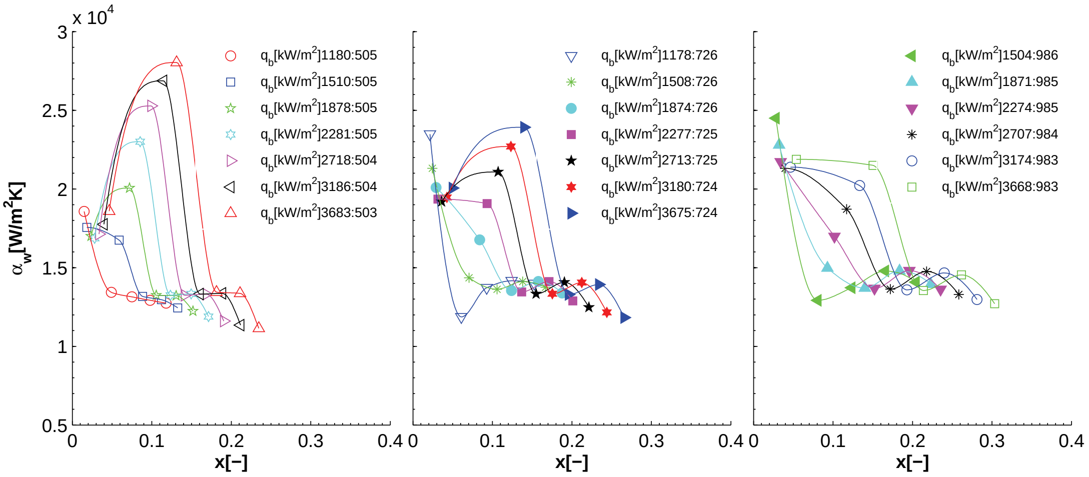

(a) R1H: G=468kg/m^{2}s, Error in α_w: 10.2%, RMS: 19.4%, q$_{footprint}$/q$_b$: 82%

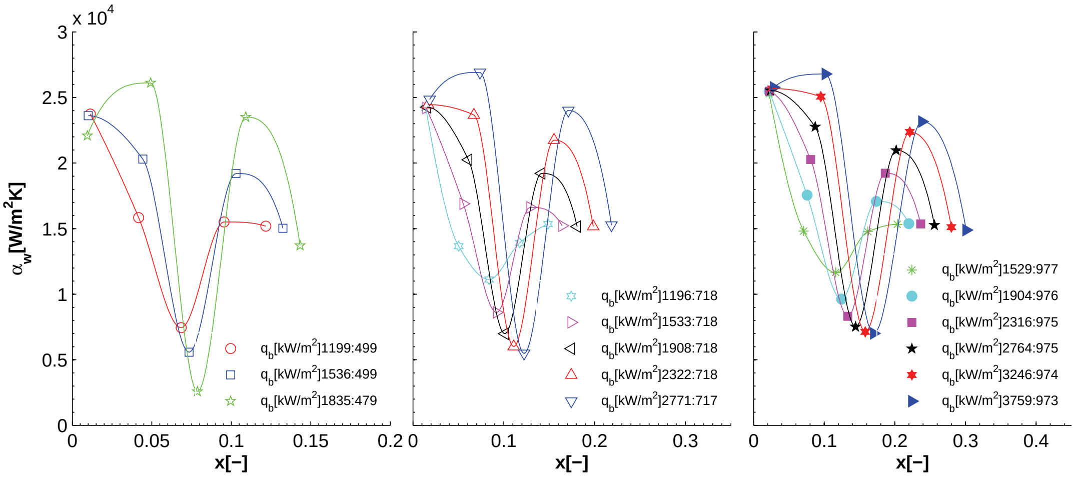

(b) R3H: G=465kg/m^{2}s, Error in α_w: 12.0%, RMS: 20.8%, q$_{footprint}$/q$_b$: 53%

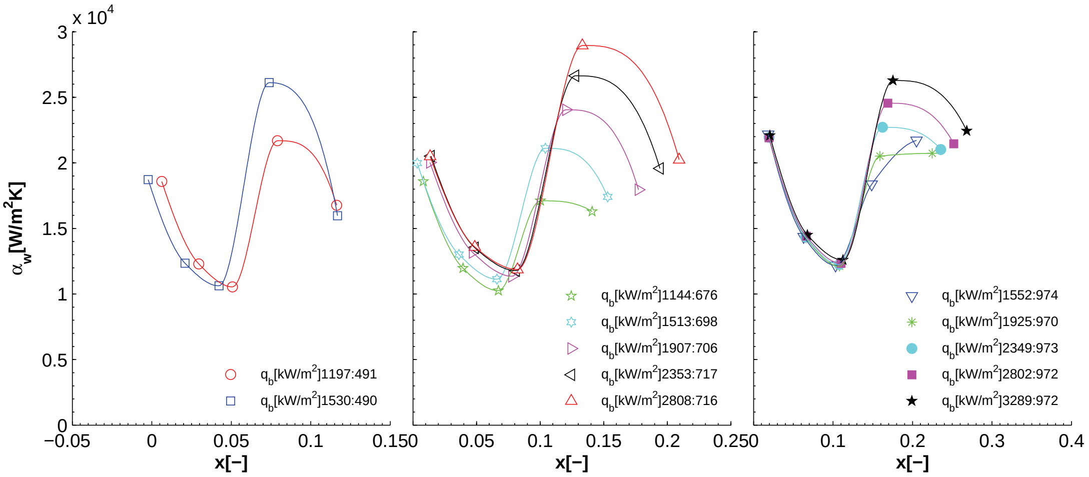

(c) R5H: G=468kg/m^{2}s, Error in α_w: 10.8%, RMS: 20.8%, q$_{footprint}$/q$_b$: 82%

Figure B.23: α_w for row hot-spots with R-134a in the copper test section, T$_{sat}$=30°C.

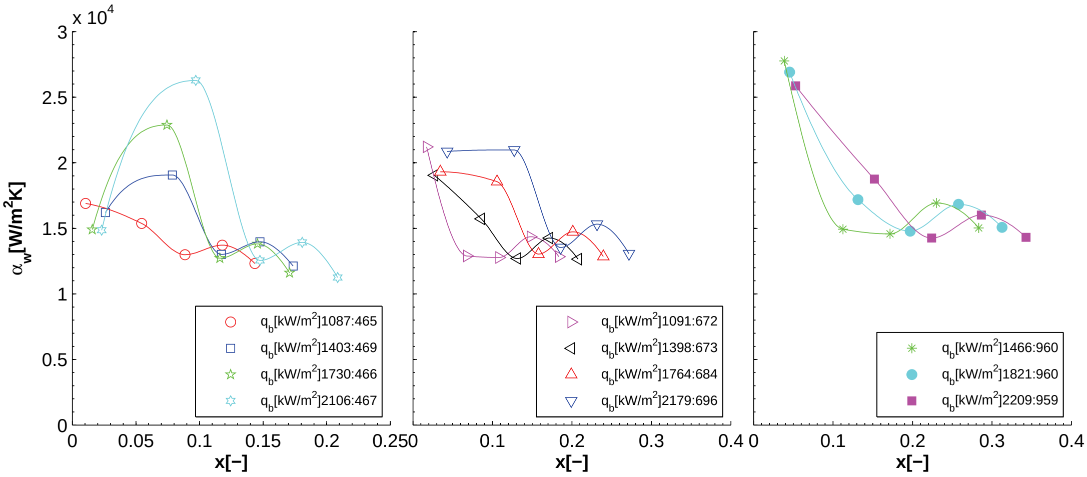

(a) R1H: G=388kg/m^{2}s, Error in α_w: 10.2%, RMS: 18.8%, q$_{footprint}$/q$_b$: 85%

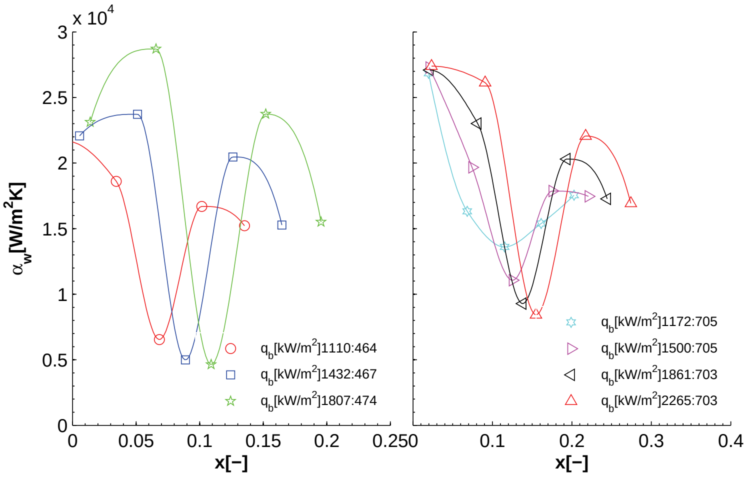

(b) R3H: G=386kg/m^{2}s, Error in α_w: 15.4%, RMS: 19.9%, q$_{footprint}$/q$_b$: 56%

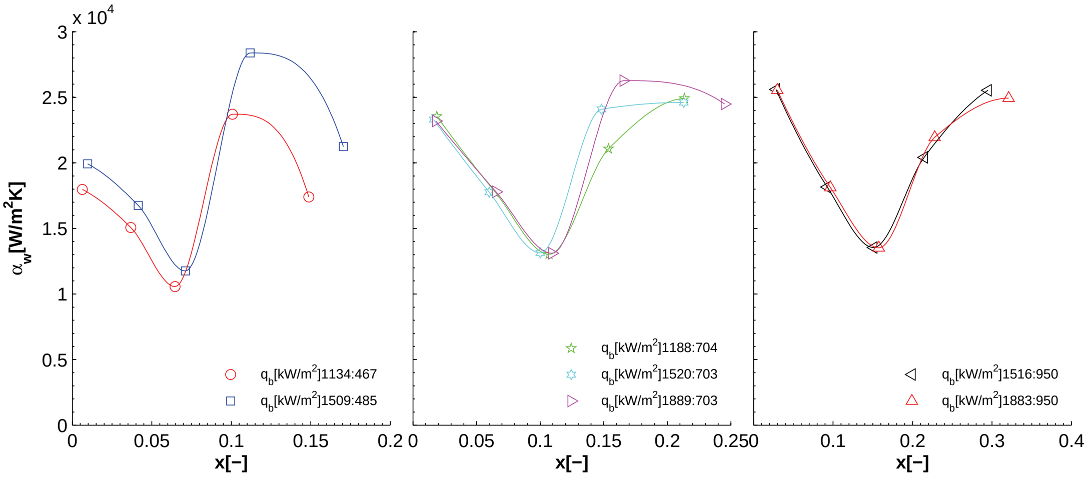

(c) R5H: G=384kg/m^{2}s, Error in α_w: 13.1%, RMS: 19.4%, q$_{footprint}$/q$_b$: 84%

Figure B.24: α_w for row hot-spots with R-134a in the copper test section, T$_{sat}$=50°C.

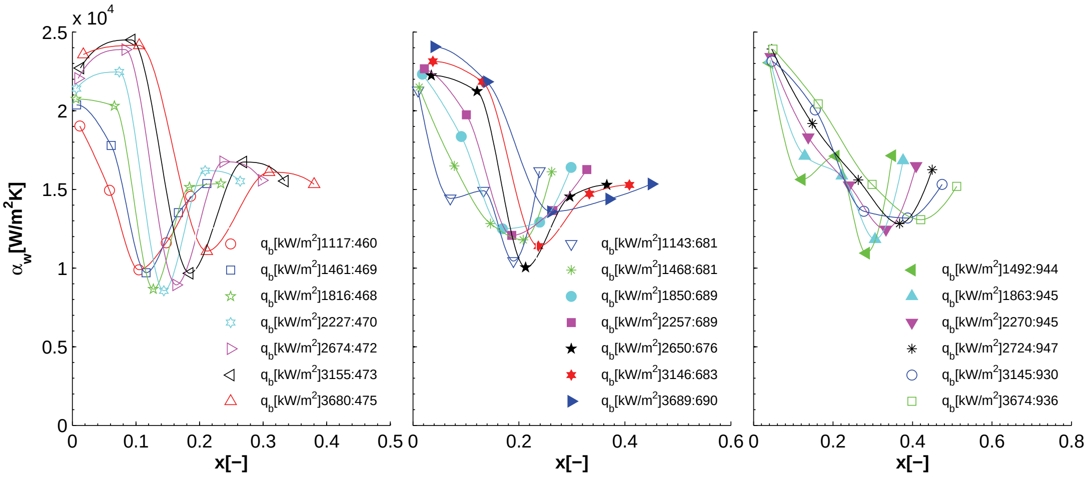

(a) R3H: G=278kg/m^{2}s, Error in α_w: 11.2%, RMS: 21.9%, q$_{footprint}$/q$_b$: 64%

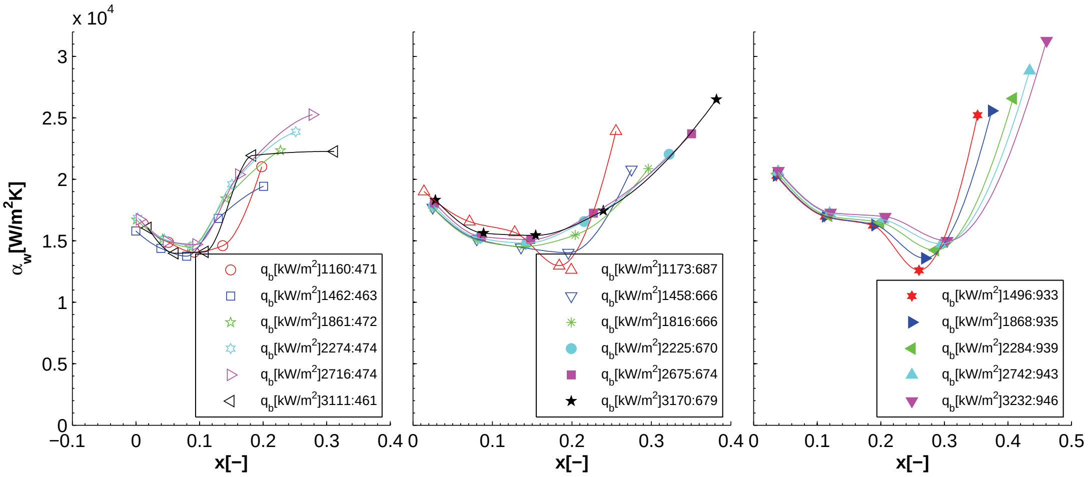

(b) R5H: G=278kg/m^{2}s, Error in α_w: 11.6%, RMS: 21.5%, q$_{footprint}$/q$_b$: 84%

Figure B.25: α_w for row hot-spots with R-1234ze(E) in the copper test section, T$_{sat}$=30°C.

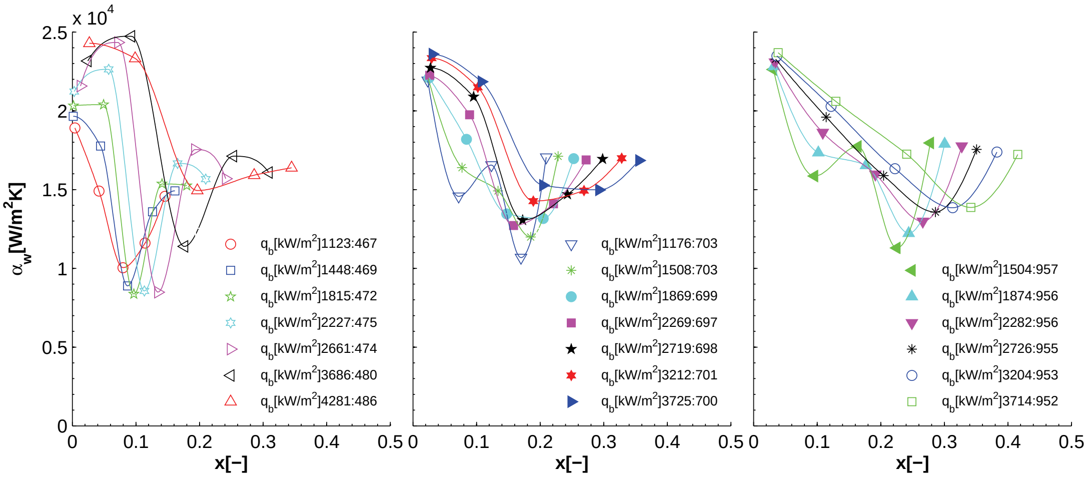

(a) R3H: G=353kg/m^{2}s, Error in α_w: 11.0%, RMS: 22.1%, q$_{footprint}$/q$_b$: 65%

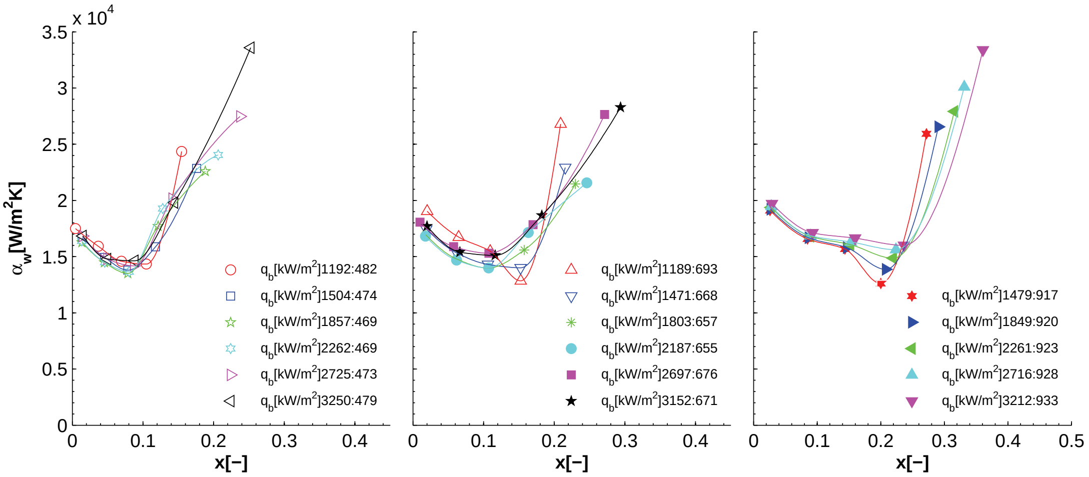

(b) R5H: G=353kg/m^{2}s, Error in α_w: 11.6%, RMS: 21.5%, q$_{footprint}$/q$_b$: 85%

Figure B.26: α_w for row hot-spots with R-1234ze(E) in the copper test section, T$_{sat}$=30°C.

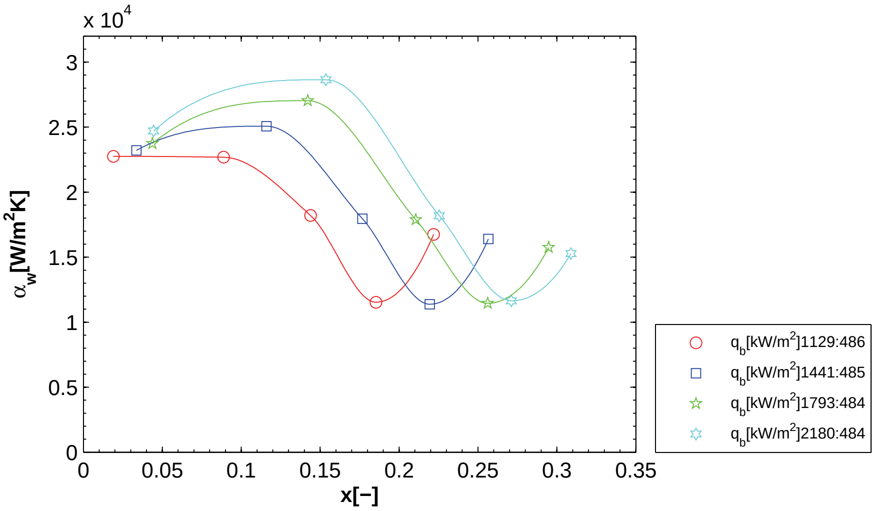

(a) R1H: G=273kg/m^{2}s, Error in α_w: 15.2%, RMS: 26.8%, q$_{footprint}$/q$_b$: 8%

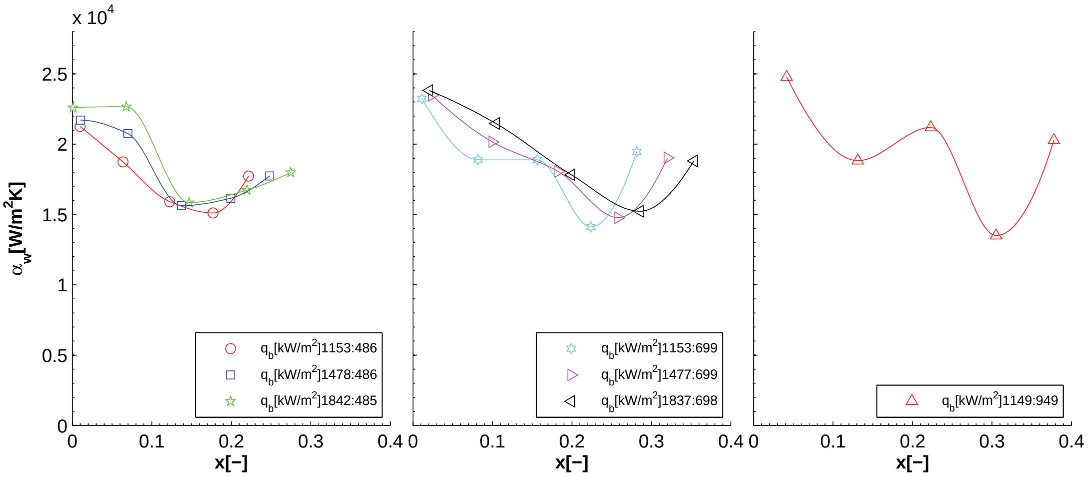

(b) R3H: G=272kg/m^{2}s, Error in α_w: 12.4%, RMS: 24.9%, q$_{footprint}$/q$_b$: 75%

Figure B.27: α_w for row hot-spots with R-1234ze(E) in the copper test section, T$_{sat}$=50°C.

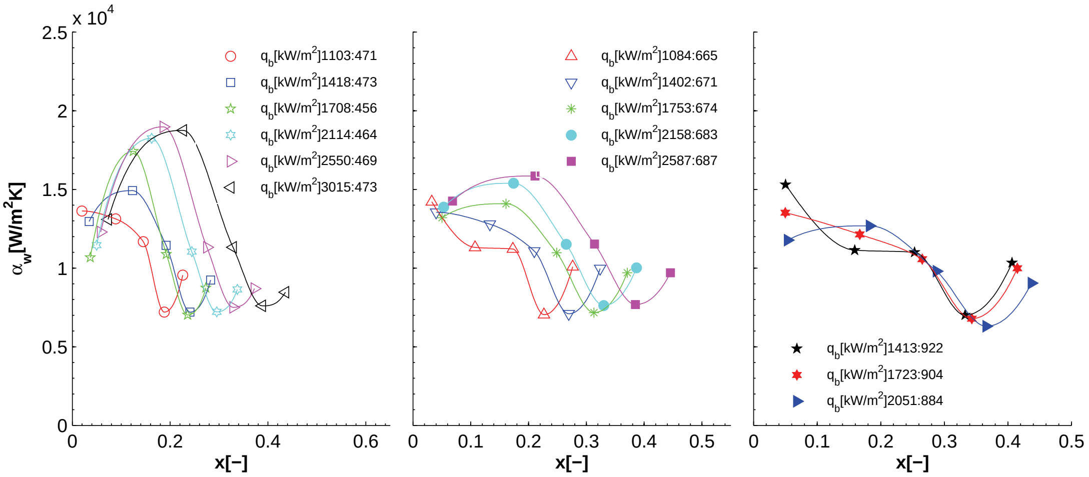

(a) R1H: G=204kg/m^{2}s, Error in α_w: 11.9%, RMS: 25.9%, q$_{footprint}$/q$_b$: 80%

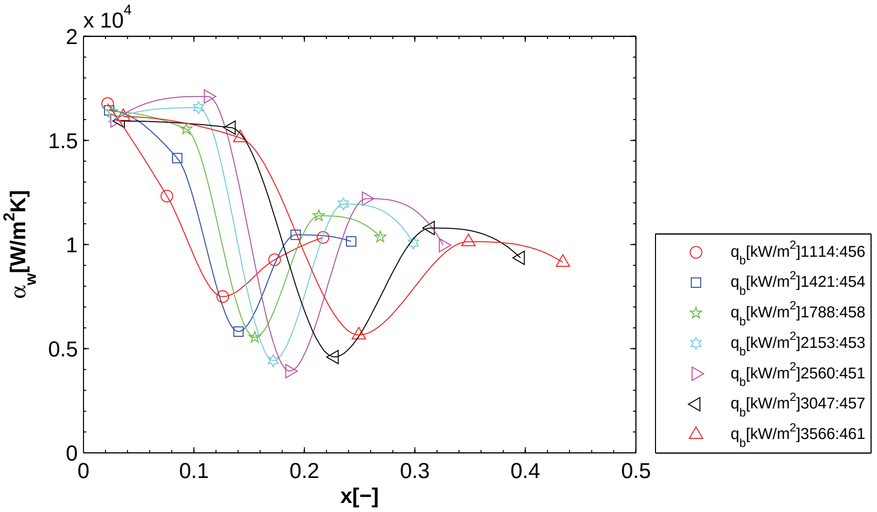

(b) R3H: G=214kg/m^{2}s, Error in α_w: 16.1%, RMS: 17.8%, q$_{footprint}$/q$_b$: 50%

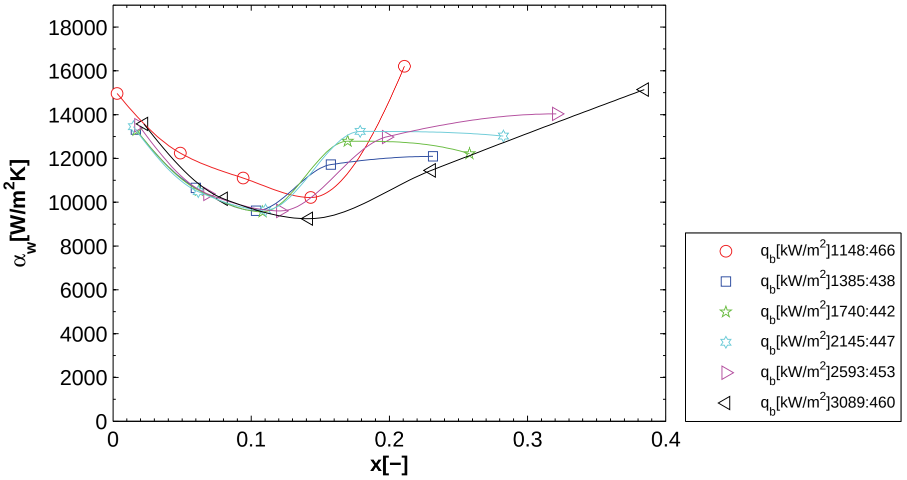

(c) R5H: G=213kg/m^{2}s, Error in α_w: 14.0%, RMS: 18.9%, q$_{footprint}$/q$_b$: 77%

Figure B.28: α_w for row hot-spots with R-245fa in the copper test section, T$_{sat}$=30°C.

B.4 Transient response

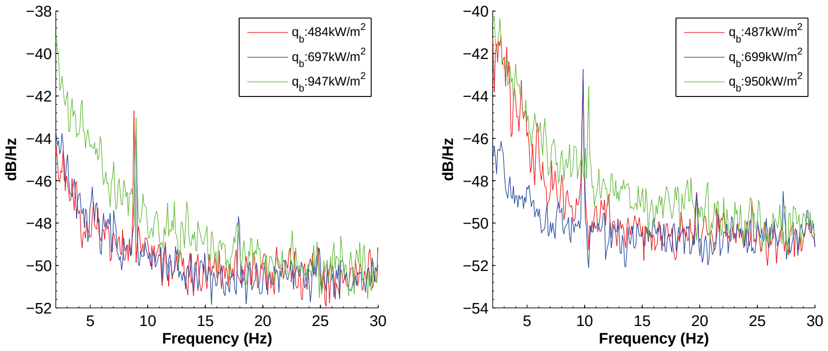

(a) Heater 14, 290kg/m^{2}s (b) Heater 14, 360kg/m^{2}s

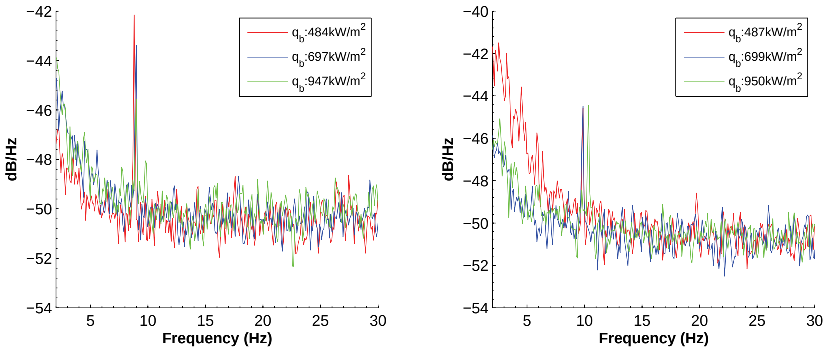

(c) Heater 34, 290kg/m^{2}s (d) Heater 34, 360kg/m^{2}s

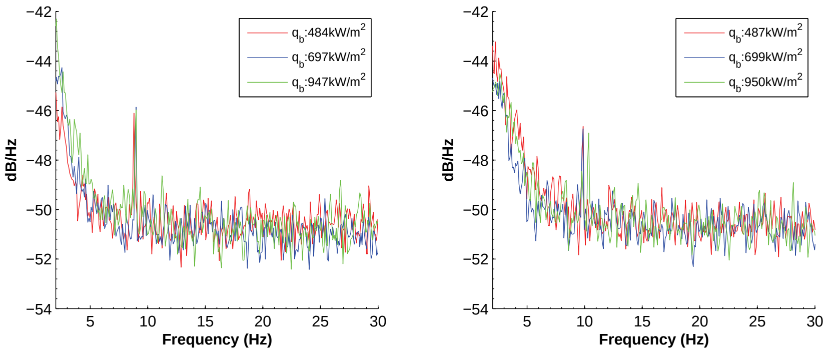

(e) Heater 54, 290kg/m^{2}s (f) Heater 54, 360kg/m^{2}s

Figure B.29: Power spectral density for R-1234ze(E) in the copper test section at T$_{sat}$=30°C

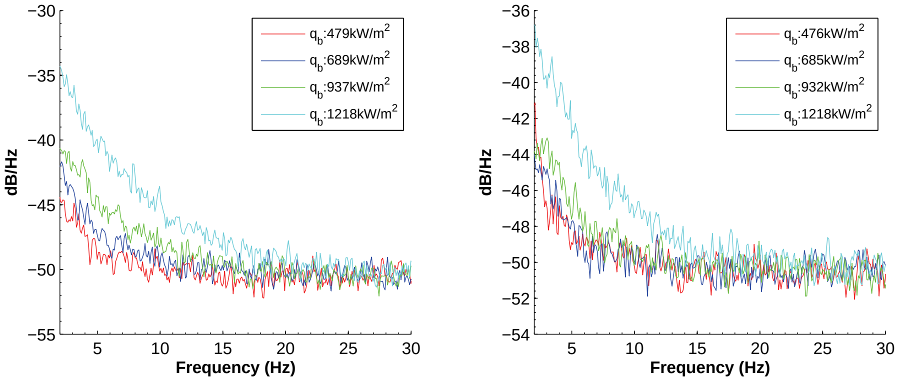

(a) Heater 14, 210kg/m^{2}s (b) Heater 14, 290kg/m^{2}s

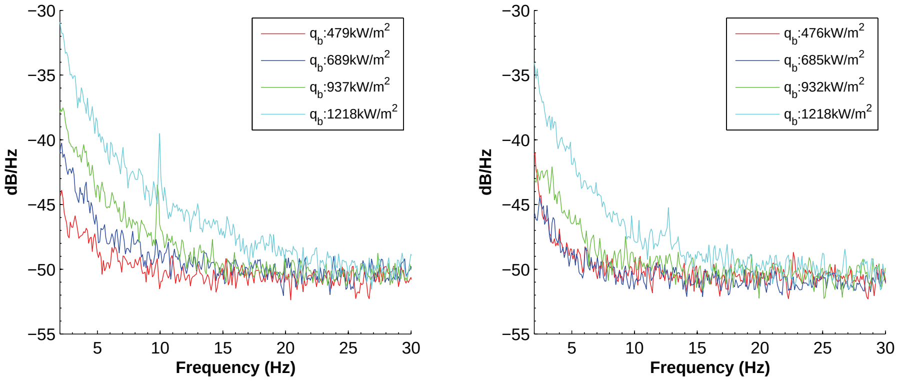

(c) Heater 34, 210kg/m^{2}s (d) Heater 34, 290kg/m^{2}s

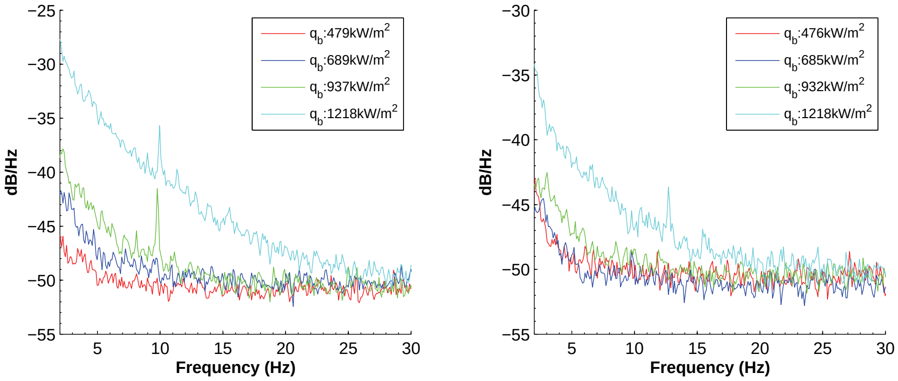

(e) Heater 54, 210kg/m^{2}s (f) Heater 54, 290kg/m^{2}s

Figure B.30: Power spectral density for R-245fa in the copper test section at T_{sat}=30°C

Reference

A., Sridhar, Vincenzi, A., Ruggiero, M., & Atienza, D. 2012. Neural Network-Based Thermal Simulation of Integrated Circuits on GPUs. *IEEE Trans. Computer Aided Design*, **-**, 1–14. xiv, 31

Abu-Eishah, S.I. 2001. Correlations for the Thermal Conductivity of Metals as a Function of Temperature. *Int. J. Thermophysics*, **22(6)**, 1855–1868. 53

Agostini, B., & Bontemps, A. 2005. Vertical flow boiling of refrigerant in small channels. *Int. J. Heat Fluid Flow*, **26**, 296–306. xiii, 19, 20

Agostini, B., Bontemps, A., & Thonon, B. 2006. Effects of Geometrical and Thermophysical Parameters on Heat Transfer Measurements in Small-Diameter Channels. *Heat Transfer Eng.*, **27:1**, 14–24. xiii, 6, 7, 8

Agostini, B., Thome, J.R., Fabbri, M., Michel, B., Calmi, D., & Kloter, U. 2008a. High heat flux flow boiling in silicon multi-microchannels – Part I: Heat transfer characteristics of refrigerant R236fa. *Int. J. Heat Mass Transfer*, **51**, 5400–5414. 13, 24, 25, 28, 100, 104

Agostini, B., Revellin, R., Thome, J.R., Fabbri, M., Michel, B., Calmi, D., & Kloter, U. 2008b. High heat flux flow boiling in silicon multi-microchannels – Part III: Saturated critical heat flux of R236fa and two-phase pressure drops. *Int. J. Heat Mass Transfer*, **51**, 5426–5442. 30

André, J. 2009. *Etude de la conductivité thermique d'un métal liquide.* INP Toulouse ENSEEIHT. 42

Bao, Z.Y., Fletcher, D.F., & Haynes, B.S. 2000. Flow boiling heat transfer of Freon R11 and HCFC123 in narrow passages. *Int. J. Heat Mass Transfer*, **43**, 3347–3358. 22, 23

Barber, J., Brutin, D., Sefiane, K., & Tadrist, L. 2010. Bubble confinement in flow boiling of FC-72 in a "rectangular" microchannel of high aspect ratio. *Exp. Therm. Fluid Science*, **34**, 1375–1388. xiii, 13, 15

Baroczy, C.J. 1965. A systematic correlation for two-phase pressure drop. *In: AIChE 8th National Heat Transfer Conference.* 21, 72, 74, 75

BASU, S., NDAO, S., MICHNA, G.J., PELES, Y., & JENSEN, M.K. 2011. Flow Boiling of R134a in Circular Microtubes – Part II: Study of Critical Heat Flux Condition. *J. Heat Transfer*, **133**. 30

BERGLES, A.E., LIENHARD V, J.H., G.E., KENDALL, & GRIFFITH, P. 2003. Boiling and Evaporation in Small Diameter Channels. *Heat Transfer Eng.*, **24**(1), 18–40. 8

BERTSCH, S.S., GROLL, E.A., & GARIMELLA, S.V. 2008. Refrigerant flow boiling heat transfer in parallel microchannels as a function of local vapor quality. *Int. J. Heat Mass Transfer*, **51**, 4775–4787. 27, 28

BERTSCH, S.S., GROLL, E., & GARIMELLA, S.V. 2009. A composite heat transfer correlation for saturated flow boiling in small channels. *Int. J. Heat Mass Transfer*, **52**, 2110–2118. xviii, 28, 102, 104, 105, 106, 107, 108, 138, 139, 140

BIBER, R.C., & BELADY, L.C. 1997. Pressure Drop Prediction for Heat Sinks: What is the Best Method? *In: INTERpack'97*. 6, 58, 67

BLACK, J.A. 1969. Electromigration-A Brief Survey and Some Recent Results. *IEEE Trans. Electron Devices*, **16, No.4**, 338–347. 2

BLASIUS, H. 1908. Grenzschichten in Flssigkeiten mit kleiner Reibung. *Zeitschr. f. Math. u. Phys.*, **56**, 1–37. 6

BOGOJEVIC, D., SEFIANE, K., WALTON, A.J., LIN, H., CUMMINS, G., KENNING, D.B.R., & KARAYIANNIS, T. 2011. Experimental investigation of non-uniform heating effect on flow boiling instabilities in a microchannel-based heat sink. *Int. J. Thermal Sci.*, **50**, 309–324. 32

BORHANI, N., AGOSTINI, B., & THOME, J.R. 2010. A novel time strip flow visualisation technique for investigation of intermittent dewetting and dryout in elongated bubble flow in a microchannel evaporator. *Int. J. Heat Mass Transfer*, **53**, 4809–4918. xiii, 14, 16, 100

BOURE, J.A., BERGLES, A., & TONG, L.S. 1973. Review of two-phase flow instability. *Nuclear Eng. and Design*, **25**, 165–192. 11

BRUUS, H. 2008. *Theoretical Microfluidics*. Oxford University Press. 6

CAREY, V.P. 2008. *Liquid-Vapor Phase-Change Phenomena*. 2nd edn. Taylor & Francis. 8

CHEN, I.Y., WONGWIES, S., YANG, B.-C., & WANG, C.-C. 2010. Two-Phase Flow Across Small Sudden Expansions and Contractions. *Heat Transfer Eng.*, **31**(4), 298–309. 19

CHEN, J.C. 1966. Correlation for boiling heat transfer to saturated fluids in convective flow. *I&EC Process Des. Dev.*, **5**(3), 322–329. 28

CHENG, P., & WU, H.Y. 2006. Mesoscale and Microscale Phase-Change Heat Transfer. *Adv. Heat Transfer*, **39**, 461–563. 11

Chisholm, D. 1973. Pressure gradients due to friction during the flow of evaporating two-phase mixtures in smooth tubes and channels. *Int. J. Heat Mass Transfer*, **16**, 347–358. 21, 72

Cicchitti, A., Lombardi, C., Silvestri, M., Soldaini, G., & Zavattarelli, R. 1960. Two-phase cooling experiments–pressure drop, heat transfer and burnout measurements. *Energ. Nucl.*, **7**, 407–425. 21, 72

Cioncolini, A., & Thome, J.R. 2011. Algebraic turbulence modeling in adiabatic and evaporating annular two-phase flow. *Int. J. Heat Fluid Flow*, **32**, 805–817. 29, 104, 105, 108, 150

Cioncolini, A., Thome, J.R., & Lombardi, C. 2009. Unified macro-to-microscale method to predict two-phase frictional pressure drops of annular flows. *Int. J. Multiphase Flow*, **35**, 1138–1148. 21, 72, 73, 74, 75, 76, 106, 107, 123, 149

Colgan, E.G., Furman, B., Gaynes, M., Graham, W.S., LaBianca, N.C., Magerlein, J.H., Polastre, R.J., Rothwell, M.B., Bezama, R.J., Choudhary, R., Marston, K.C., Toy, H., Wakil, J., Zitz, J.A., & Schmidt, R.R. 2007. A Practical Implementation of Silicon Microchannel Coolers for High Power Chips. *IEEE Trans. Components and Packaging Tech.*, **30**(2), 218–225. 8

Collier, J.G., & Thome, J.R. 1994. *Convective Boiling and Condensation*. Third edn. Oxford: Oxford University Press. 8, 19, 20, 22, 66, 149

Cooper, M.G. 1984. Heat flow rates in saturated nucleate pool boiling – a wide-ranging examination using reduced properties. *Adv. Heat Transfer*, **16**, 157–239. 22, 28

Cullen, J.M., & Allwood, J.M. 2010. Theoretical efficiency limits for energy conversion devices. *Energy*, **35**, 2059–2069. 1

Dukler, A.E., Wicks, M., & Cleveland, R.G. 1964. Pressure drop and hold-up in two-phase flow Part A – A comparison of existing correlations. *AIChE Journal*, **10** **(1)**, 38–51. 21

Dupont, V., Thome, J.R., & Jacobi, A.M. 2004. Heat transfer model for evaporation in microchannels. Part II: comparison with the database. *Int. J. Heat Mass Transfer*, **47**, 3387–3401. xviii, 105, 142, 144

EPA, U.S. 2007. *Report to Congress on Server and Data Center Energy Efficiency*. 1

Friedel, L. 1979. Improved friction pressure drop correlations for horizontal and vertical two-phase pipe flow. *In: European Two-Phase Flow Group Meeting, Ispra, Italy*. 21, 72, 74, 75

Fritz, W. 1935. Berechnung des Maximal Volume von Dampfblasen. *Phys. Z.*, **36**, 379–384. 9

Garimella, S., Killion, J.D., & Coleman, J.W. 2002. An Experimentally Validated Model for Two-Phase Pressure Drop in the Intermittent Flow Regime for Circular Microchannels. *J. Fluid. Eng.*, **124**, 205–214. 20

GNIELINSKI. 1976. New Equations for Heat and Mass Transfer in Turbulent Pipe and Channel Flow. *Int. Chem. Engineering*, **16**(2), 359–368. 7

HAMANN, H.F, WEGER, A., LACEY, J.A., HU, Z., BOSE, P., COHEN, E., & WAKIL, J. 2007. Hotspot-Limited Microprocessors: Direct Temperature and Power Distribution Measurements. *IEEE J. Solid-State Circuit*, **42(1)**, 56–65. xiv, 31, 32, 33

HAMDAR, M., ZOUGHAIB, A., & CLODIC, D. 2010. Flow boiling heat transfer and pressure drop of pure HFC-152a in a horizontal mini-channel. *Int. J. Refrigeration*, **doi:10.1016/j.ijrefrig.2009.12.006**, 1–12. 22, 23

HARDY, S.C. 1985. The surface tension of liquid gallium. *J. Crystal Growth*, **71**, 602–606. 42

HARIRCHIAN, T., & GARIMELLA, S.V. 2008. Microchannel size effects on local flow boiling heat transfer to a dielectric fluid. *Int. J. Heat Mass Transfer*, **51**, 3724–3735. 22, 23, 101

HARIRCHIAN, T., & GARIMELLA, S.V. 2010. A comprehensive flow regime map for microchannel flow boiling with quantitative transition criteria. *Int. J. Heat Mass Transfer*, **53**, 2694–2702. xiii, 10, 11, 16, 17

HESTRONI, G., MOSYAK, A., POGREBNYAK, E., & SEGAL, Z. 2005. Explosive boiling of water in parallel micro-channels. *Int. J. Multiphase Flow*, **31**, 371–392. 12

HEWITT, G.F., SHIRE, G.L., & BOTT, T.R. 1993. *Process Heat Transfer*. CRC Press. 20

IDELCIK, I.E. 1999. *Memento des pertes de charge*. Paris: Eyrolles. xxi, 19, 61, 63, 64

JACOBI, A.M., & THOME, J.R. 2002. Heat Transfer Model for Evaporation of Elongated Bubble Flows in Microchannels. *J. Heat Transfer*, **124**, 1131–1136. 24

KANDLIKAR, S.G. 2010. Scale effects on flow boiling heat transfer in microchannels: A fundamental perspective. *Int. J. Thermal Sci.*, **49**, 1073–1085. xiii, 9, 10

KANDLIKAR, S.G., & BALASUBRAMANIAN, P. 2004. An Extension of the Flow Boiling Correlation to Transition, Laminar, and Deep Laminar Flows in Minichannels and Microchannels. *Heat Transfer Eng.*, **25**(3), 86–93. 28, 102, 104, 106, 107, 108

KANDLIKAR, S.G., & GRANDE, W.J. 2003. Evolution of Microchannel Flow Passages – Thermohydraulic Performance and Fabrication Technology. *Heat Transfer Eng.*, **24**(1), 3–17. 9, 11

KANDLIKAR, S.G., GARIMELLA, S., LI, D., COLIN, S., & KING, M. 2006. *Heat transfer and fluid flow in minichannels and microchannels*. Elsevier. 6, 8

KARYIANNIS, T.G., SHIFERAW, D., KENNING, D.B.R., & WADEKAR, V.V. 2010. Flow Patterns and Heat Transfer for Flow Boiling in Small to Micro Diameter Tubes. *Heat Transfer Eng.*, **31 (4)**(4), 257–275. xiii, 16, 18, 24, 77

Kattan, N., Thome, J.R., & Favrat, D. 1998. Flow Boiling in Horizontal Tubes: Part 1 – Development of a Diabatic Two-Phase Flow Pattern Map. *J. Heat Transfer*, **120**, 140–147. xiii, 14, 17

Katto, Y., & Ohno, H. 1984. An improved version if the generalized correlation of critical heat flux for forced convective boiling in uniformly heated vertical tubes. *Int. J. Heat Mass Transfer*, **27 (9)**, 1641–1648. 30

Kew, P.A., & Cornwell, K. 1997. Correlations for the prediction of boiling heat transfer in small-diameter channels. *App. Therm. Eng.*, **17 (8–10)**, 705–715. 24, 27

Kline, S.J., & McClintock, F.A. 1953. Describing uncertainties in single-sample experiments. *Mech. Eng.*, **75**, 3–8. 53, 153

Koo, J.-M., Jian, L., Bari, A., Zhang, L., Wang, E., Kenny, T.W., Santiago, J.G., & Goodson, K.E. 2002. Convective Boiling in Microchannel Heat Sinks with Spatially-Varying Heat Generation. *In: Inter Society Conference on Thermal Phenomena*. 31

Koomey, J.G., Belady, C., Patterson, M., Santos, A., & K.D., Lange. 2009. *Assessing trends over time in performance, costs, and energy use for servers*. Tech. rept. Lawrence Berkeley National Laboratory and Stanford University. 1

Kosar, A., & Peles, Y. 2007. Critical Heat Flux of R-123 in Silicon-Based Microchannels. *J. Heat Transfer*, **129**, 844–851. 30

Kosar, A., Kuo, C.J., & Peles, Y. 2006. Suppression of Boiling Flow Oscillations in Parallel Microchannels by Inlet Restrictors. *J. Heat Transfer*, **128**, 251–260. 13

Kreith, F., & Bohn, M.S. 2001. *Principles of Heat Transfer*. Sixth edn. Pacific Grove USA: Brooks/Cole. 60, 142

Laermer, F., & Urban, A. 2003. Challenges, developments and applications of silicon deep reactive ion etching. *Microelectronic Eng.*, **67–68**, 349–355. 43

Lazarek, G.M., & Black, S.H. 1982. Evaporative heat transfer, pressure drop and critical heat flux in a small vertical tube with R-113. *Int. J. Heat Mass Transfer*, **25**(7), 945–960. 22, 23, 24

Lee, J., & Mudawar, I. 2005a. Two-phase flow in high-heat-flux micro-channel heat sink for refrigeration cooling applications: Part I – pressure drop characteristics. *Int. J. Heat Mass Transfer*, **48**, 928–940. 21, 73, 74, 75, 76

Lee, J., & Mudawar, I. 2005b. Two-phase flow in high-heat-flux micro-channel heat sink for refrigeration cooling applications: Part II – heat transfer characteristics. *Int. J. Heat Mass Transfer*, **48**, 941–955. 24, 27, 29, 72, 104, 106, 107, 108

Lee, P.-S., & Garimella, S.V. 2008. Saturated flow boiling heat transfer and pressure drop in silicon microchannel arrays. *Int. J. Heat Mass Transfer*, **51**, 789–806. 19, 21, 72, 74, 75

LIN, S., KEW, P.A., & CORNWELL, K. 2001. Two-phase heat transfer to a refrigerant in a 1 mm diameter tube. *Int. J. Refrigeration*, **24**, 51–56. 24, 25, 77

LIN, S., SEFIANE, K., & CHRISTY, J.R.E. 2002. Prospects of confined flow boiling in thermal management of microsystems. *App. Therm. Eng.*, **22**, 825–837. 5

LOCKHART, R.W., & MARTINELLI, R.C. 1949. Proposed correlation of data for isothermal two-phase, two-component flow in pipes. *Chem. Eng. Prog.*, **45**, 39–48. 21, 72, 73, 74, 75, 76, 123, 149

MAURO, A.W., THOME, J.R., TOTO, D., & VANOLI, G.P. 2010. Saturated critical heat flux in a multi-microchannel heat sink fed by a split flow system. *Exp. Therm. Fluid Science*, **34**, 81–92. 30

MCADAMS, W.H., WOODS, W.K., & BRYAN, R.L. 1942. Vaporization inside horizontal tubes – II – Benzene–oil mixtures. *Trans. ASME*, **64**, 193. 21

MISHIMA, K., & HIBIKI, T. 1996. Some characteristics of air–water two-phase flow in small diameter vertical tubes. *Int. J. Multiphase Flow*, **22**(4), 703–712. 21, 72, 74, 75

MORINI, G.L. 2005. Viscous heating in liquid flows in micro-channels. *Int. J. Heat Mass Transfer*, **48**, 3637–3647. 6

MUELLER-STEINHAGEN, H., & HECK, K. 1986. A Simple Friction Pressure Drop Correlation for Two-Phase Flow in Pipes. *Chem. Eng. Process.*, **20**, 297–308. 21, 72, 74, 75

MUKHERJEE, A. 2009. Contribution of thin-film evaporation during flow boiling inside microchannels. *Int. J. Thermal Sci.*, **48**, 2025–2035. 24

NEBULONI, S., & THOME, J.R. 2010. Numerical modeling of laminar annular film condensation for different channel shapes. *Int. J. Heat Mass Transfer*, **53**, 2615–2627. 29

OGATA, K. 1998. *System Dynamics*. Prentice Hall. 144

OLIVIER, J. 2008. *Single-phase Heat Transfer and Pressure Drop inside Micro-channels*. EPFL LTCM. 7, 83

OLIVIER, J., & COSTA-PATRY, E. 2010. *Report on the Three-zone Model of Thome et al 2004*. LTCM EPFL. 104

OLIVIER, J.A. 2009. *Single-phase heat transfer and pressure drop of water cooled at a constant wall temperature inside horizontal circular smooth and enhanced tubes with different inlet configurations in the transitional flow regime*. Ph.D. thesis, University of Pretoria. 86

ONG, C.L., & THOME, J.R. 2011a. Macro-to-microchannel transition in two-phase flow: Part 1 - Two-phase flow patterns and film thickness measurements. *Exp. Therm. Fluid Science*, **35**, 37–47. 11, 28, 73, 101, 103

ONG, C.L., & THOME, J.R. 2011b. Macro-to-microchannel transition in two-phase flow: Part 2 - Flow boiling heat transfer and critical heat flux. *Exp. Therm. Fluid Science*. xiv, 15, 24, 26, 28, 30, 77, 96, 104

PARK, J.E., & THOME, J.R. 2010. Critical heat flux in multi-microchannel copper elements with low pressure refrigerants. *Int. J. Heat Mass Transfer*, **53**, 110–122. 2, 30, 35

PARK, J.E., THOME, J.R., & MICHEL, B. 2009. Effect of Inlet Orifice on Saturated CHF and Flow Visualization in Multi-microchannel Heat sinks. *In: 25th IEEE SEMI-THERM Symposium*. 13

PETHUKOV, B.S. 1970. Heat Transfer and Friction in Turbulent Pipe Flow with Variable Properties. *In: Adv. Heat Transfer vol.6*. Academic Press. 86

REVELLIN, R., & THOME, J.R. 2007a. Adiabatic two-phase frictional pressure drops in microchannels. *Ex*, **31**, 673–685. xiii, 19

REVELLIN, R., & THOME, J.R. 2007b. A new type of diabatic flow pattern map for boiling heat transfer in microchannels. *J. Micromech. Microeng.*, **17**, 788–796. 15, 30

REVELLIN, R., & THOME, J.R. 2008. A theoretical model for the prediction of the critical heat flux in heated microchannels. *Int. J. Heat Mass Transfer*, **51**, 1216–1225. xiv, 30, 31

REVELLIN, R., DUPONT, V., URSENBACHER, T., THOME, J.R., & ZUN, I. 2006. Characterization of diabatic two-phase flows in microchannels: Flow parameter results for R-134a in a 0.5 mm channel. *Int. J. Multiphase Flow*, **32**, 755–774. xiii, 10, 11, 13, 14, 17, 28, 103

REVELLIN, R., QUIBEN, J.M., BONJOUR, J., & THOME, J.R. 2008. Effect of Local Hot Spots on the Maximum Dissipation Rates During Flow Boiling in a Microchannel. *IEEE Trans. Components and Packaging Tech.*, **31(2)**, 407–416. xiv, 32, 137

RIBATSKI, G., WOJTAN, L., & THOME, J.R. 2006. An analysis of experimental data and prediction methods for two-phase frictional pressure drop and flow boiling heat transfer in micro-scale channels. *Exp. Therm. Fluid Science*, **31**, 1–19. 21

SAITOH, S., DAIGUJI, H., & HIHARA, E. 2005. Effect of tube diameter on boiling heat transfer of R-134a in horizontal small-diameter tubes. *Int. J. Heat Mass Transfer*, **48**, 4973–4984. 27, 28

SHAH, R.K., & LONDON, A.L. 1978. *Laminar Flow Forced Convection in Ducts*. London: Academic Press. 6, 7, 83, 84, 86

SHANKS, H.R., MAYCOCK, P.D., SIDLES, P.H., & DANIELSON, G.C. 1963. Thermal Conductivity of Silicon from 300 to 1400K. *Physical Review*, **130**(5), 1743–1747. 52

THOME, J.R. 2010. *Engineering Databook III*. www.wlv.com/products/databook/. 8

Thome, J.R., & Consolini, L. 2009. Mechanisms of Boiling in Micro-Channels: Critical Assessment. *Heat Transfer Eng.*, **31**(4), 288–297. 22

Thome, J.R., Dupont, V., & Jacobi, A.M. 2004. Heat transfer model for evaporation in microchannels. Part I: presentation of the model. *Int. J. Heat Mass Transfer*, **47**, 3387–3401. xiv, 28, 29, 102, 104, 105, 106, 107, 108, 130, 150

Tran, T.N., Wambsganss, M.W., & France, D.M. 1996. Small circular- and rectangular-channel boiling with two refrigerants. *Int. J. Multiphase Flow*, **22**(3), 485–498. 22, 23, 104, 106, 107, 108

Tran, T.N., Chyu, M.C., Wambsganss, M.W., & France, D.M. 1999. Two-phase pressure drop of refrigerants during flow boiling in small channels – an experimental investigation and correlation development. *In: Int. Conference on Compact Heat Exchangers and Enhancement Technology for Process Industries, Banff, Canada.* 21, 72, 74, 75

Vadgama, B., & Harris, D.K. 2007. Measurements of the contact angle between R134a and both aluminum and copper surfaces. *Ex*, **31**, 979–984. 9

Wang, G., Cheng, P., & Bergles, A.E. 2008. Effects of inlet/outlet configurations on flow boiling instability in parallel microchannels. *Int. J. Heat Mass Transfer*, **51**, 2267–2281. 13

Weaver, A.J., Zickfeld, K., Montenegro, A., & Eby, M. 2007. Long term climate implications of 2050 emission reduction targets. *Geophysical research letters*, **34, L19703**, 1–4. 1

Wojtan, L., Revellin, R., & Thome, J.R. 2006. Investigation of saturated critical heat flux in a single, uniformly heated microchannel. *Exp. Therm. Fluid Science*, **30**, 765–774. 30

Yan, Y.Y., & Lin, T.F. 1998. Evaporation heat transfer and pressure drop of refrigerant R-134a in a small pipe. *Int. J. Heat Mass Transfer*, **41**, 4183–4194. 24, 27

Zhang, T., Tong, T., Chang, J.Y., Peles, Y., Prasher, R., Jensen, M.K., Wen, J.T., & Phelan, P. 2009. Ledinegg instability in microchannels. *Int. J. Heat Mass Transfer*, **52**, 5661–5674. xiii, 12

Zivi, S.M. 1964. Estimation of steady-state stem void-fraction by means of the principle of minimum entropy production. *J. Heat Transfer*, **86**, 247–252. 73

Curriculum Vitae

PERSONAL DATA

Name	**Etienne Costa-Patry**
Date of birth	10th March, 1980
Birthplace	Rivière-du-Loup (Qc), Canada
Nationality	Canadian and Belgian

EDUCATION

2008–2011	**Doctoral Student and Assistant**, Laboratory of Heat and Mass Transfer, Lausanne (EPFL), Switzerland
2003–2005	**Master of Engineering**, McGill University, Montréal, Canada
1999–2003	**Bachelor of Engineering**, McGill University, Montréal, Canada

WORKING EXPERIENCE

2008–2011	**École Polytechnique Fédérale de Lausanne, Laboratory of Heat and Mass Transfer, Lausanne** Doctoral Research Assistant
2006–2008	**Maag Pump Systems Textron, Zurich**, Calculation engineer
2005	**GE Energy, Belfort**, Intern

PUBLICATIONS

E. Costa-Patry, J. Olivier and J. R. Thome. Heat transfer characteristics in a copper micro-evaporator and flow pattern-based prediction method for two-phase flow in microchannels. Submitted for publication to Frontier in Heat and Mass Transfer, 2011.

E. Costa-Patry, S. Nebuloni, J. Olivier and J. R. Thome. On-chip two-phase cooling with refrigerant 85 μm-wide multi-microchannel evaporator under hot-spot conditions. Accepted by IEEE Transactions on Components and Packaging Technologies, 2011.

Y. Madhour, J. Olivier, E. Costa-Patry, S. Paredes, B. Michel and J.R. Thome. Flow Boiling of R134a in a Multi-Microchannel Heat Sink with Hotspot Heaters for Energy-Efficient Microelectronic CPU Cooling Applications. IEEE Transactions on Components and Packaging Technologies, 1(6):873–883, 2011.

E. Costa-Patry, J. Olivier, B. A. Nichita, B. Michel, and J. R. Thome. Two-phase flow of refrigerants in 85μm-wide multi-microchannels. Part I: Pressure drop. International Journal of Heat and Fluid Flow, 32(2):451–463, 2011.

E. Costa-Patry, J. Olivier, B. Michel, and J. R. Thome. Two-phase flow of refrigerants in 85μm-wide multi-microchannels. Part II: Heat transfer with 35 local heaters. International Journal of Heat and Fluid Flow, 32(2):464–476, 2011.

E. Costa-Patry and L. Mydlarski, 2007. Mixing of two scalars emitted from line sources in turbulent channel flow. Journal of Fluid Mechanics, 609: 349-379, 2008.